DEVELOPMENT OF BIOELECTRONIC TECHNOLOGIES FOR THE INVESTIGATION OF EXTRACELLULAR VESICLE FUNCTION AND ANTI-CANCER DRUG DISCOVERY

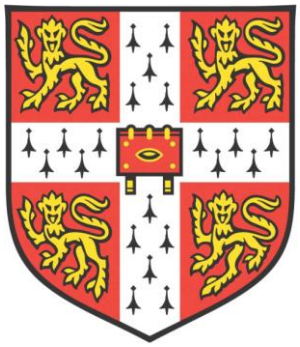

Walther Christensen Traberg
Churchill College

Department of Chemical Engineering and Biotechnology
University of Cambridge

Supervised by Professor Róisín M. Owens

This thesis is submitted for the degree of
Doctor of Philosophy

2022

DECLARATION

This thesis is the result of my own work and includes nothing which is the outcome of work done in collaboration except as declared in the Preface and specified in the text. I further state that no substantial part of my thesis has already been submitted, or, is being concurrently submitted for any such degree, diploma or other qualification at the University of Cambridge or any other University or similar institution except as declared in the Preface and specified in the text. It does not exceed the prescribed word limit for the relevant Degree Committee

Walther Christensen Traberg

August 2022

ABSTRACT

DEVELOPMENT OF BIOELECTRONIC TECHNOLOGIES FOR THE INVESTIGATION OF EXTRACELLULAR VESICLE FUNCTION AND ANTI-CANCER DRUG DISCOVERY

Walther Christensen Traberg

Extracellular vesicles (EVs) are cell-secreted phospholipid bilayer-delimited particles of varying size and composition that facilitate intercellular communication. EVs play a critical role in a wide range of diseases by mediating the transfer of active biomolecules between cells, both in the vicinity of the source cell and at distant sites, to elicit a variety of phenotypic responses. Tumour-derived (T)EVs facilitate the transfer of information between tumour and non-malignant cells to initiate and drive metastasis through a variety of processes, including the epithelial-to-mesenchymal transition (EMT) and angiogenesis. As such, TEVs represent a novel therapeutic target in a field severely lacking in efficacious anti-metastasis treatments. Research into EV biology and function has seen a boom over the last decade owing to their unique features and potential clinical utility, and the demand for new and robust tools to study their functional activity has risen commensurately. However, conventional characterisation methods fail to comprehensively capture the dynamic nature of EV function, and this has obscured the true role of EVs in pathophysiological processes despite their pleiotropic functions *in vitro*. Furthermore, scalable technologies that allow continuous, multiparametric monitoring for identifying metastasis inhibitors are missing.

Here, bioelectronic technologies are utilised as a promising, scalable technology for investigating the dynamics of EV function in a truly quantitative manner using both cell-free and cell-based models. Furthermore, proof of concept drug screening studies demonstrate the applications of these bioelectronic platforms to preclinical drug discovery, addressing the current lack of robust, scalable sensing technologies that facilitate facile translation to *in vivo* outcomes. In this work, organic bioelectronic devices were integrated with cell-free, supported lipid bilayer (SLB) models and a cell-based breast cancer metastasis model. In the case of the former, electronic devices were used to detect virus-membrane fusion, which laid the groundwork for the subsequent study on EV-membrane binding, as viruses and EVs share many similarities in form and function. SLB integration with conducting polymer coated substrates and electronic devices was assessed using optical techniques. Virus hemifusion to both synthetic and natively derived SLBs was detected electrically using electrodes and organic electrochemical transistors (OECTs). Next, a supported biomimetic stem cell membrane incorporating membrane

components from human primary adipose-derived stem cells (ADSCs) was formed to monitor the binding of cancer-derived exosomes (cEXOs) to the plasma membrane and show that this binding can be blocked when an antibody to integrin β1, a component of ADSC surface, is exposed to the membrane surface prior to cEXOs. These SLB platforms used a label-free electronic readout as well as a dual capability of optical (fluorescence) readout.

Lastly, the development of a functional phenotypic screening platform based on OECTs for real-time, non-invasive monitoring of TEV-induced EMT and screening of anti-metastatic drugs is reported. TEVs derived from the triple-negative breast cancer (TNBC) cell line MDA-MB-231 induced EMT in non-malignant breast epithelial cells (MCF10A) over a 9-day period, recapitulating a model of invasive ductal carcinoma metastasis. Epigenetics and immunoblot analysis showed that TEVs modulate TWIST1 protein amount but not DNA methylation level, and dual optical and electrical readouts of cell phenotype using OECTs were obtained. Further, heparin, a competitive inhibitor of cell surface receptors, was identified as an effective blocker of TEV-induced EMT, providing proof of principle that inhibitors of TEV function can be potential anti-metastatic drug candidates.

Together, these results demonstrate the utility of bioelectronic platforms presented here for studying TEV function, both in a cell-based and cell-free manner, and identifying inhibitors of TEV function for drug discovery applications. In additional to being readily scalable, organic electronics facilitate facile modelling of the transient drug response using electrical measurements and are amenable to integration with highly tuneable models systems.

To my mother, Anne-Marie Traberg, whose unrelenting drive and determination in life and love for her children continues to inspire me.

And to my aunt, Gitte Traberg, for her unwavering support.

ACKNOWLEDGEMENTS

First and foremost, I would like to express my enormous gratitude to my supervisor Professor Róisín M. Owens for her guidance and support throughout my PhD. She has helped me keep my efforts focused, while encouraging me to be inquisitive and explore new areas of research. She has provided me with every opportunity to develop myself as a researcher and being a part of her group has been an enriching experience to say the least.

I would like to give my thanks to Dr. Anna-Maria Pappa and Dr. Achilleas Savva for their mentorship and help with understanding the complexities of organic bioelectronics. A big thank you to the Bioelectronic Systems Technology (BEST) group and all its members, with special mention: Aimee Withers, Dr. Chrysanthi-Maria (Anthie) Moysidou, Reece McCoy, Suraj Pavagada, and Zixuan Henry Lu. The group certainly lives up to its name.

My thanks to our collaborators at the Daniel Research Team lead by Professor Susan Daniel at Cornell University, USA, the Organic Bioelectronics Laboratory lead by Professor Sahika Inal at King Abdullah University of Science and Technology (KAUST), SA, and the Salleo Research Group lead by Prof. Alberto Salleo at Stanford University, USA, for their help with this work. And to my advisor Professor Ljiljana Fruk.

A special thank you to Dr. Amberley Stephens and the Molecular Neuroscience group for their guidance and loan of equipment, as well as to the Cambridge Extracellular Vesicle Special Interest Group (EVSIG).

Lastly, I would like to express my eternal gratitude to my wife, Cecilie Steenbuch Traberg, who put up with my long nights at the lab and weekend experiments, and for her help with understanding statistics.

TABLE OF CONTENTS

LIST OF TABLES

List of Figures

List of Abbreviations and Acronyms

AC	Alternating current
ADSC	**Adipose-derived stem cell**
AFM	**Atomic force microscopy**
ASB	**ADSC-supported bilayer**
BHK	**Baby hamster kidney cells**
CE	**Counter electrode**
cEXO	**Cancer exosome**
CL	**Cell lysate**
CM	**Conditioned medium**
CP	**Conducting polymer**
CV	**Cyclic voltammetry**
DLS	**Dynamic light scattering**
EEC	**Equivalent circuit modelling**
EIS	**Electrochemical impedance spectroscopy**
EMT	**Epithelial-to-mesenchymal transition**
EV	**Extracellular vesicle**
FBS	**Foetal bovine serum**
FRAP	**Fluorescent recovery after photobleaching**
FRET	**Förster Resonance Energy Transfer**
HA	**Hemagglutinin**
HEK-293	**Human embryonic kidney cells**
ILV	**Intraluminal vesicles**
MEA	**Multielectrode array**
MoA	**Mode of action**
MV	**Microvesicle**
MVB	**Multivesicular bodies**
nc	**Non-coding**
NTA	**Nanoparticle tracking analysis**
OECT	**Organic electrochemical transistor**
PEDOT:PSS	**Poly(3,4-ethylenedioxythiophene) doped with poly(styrene sulfonate)**
PM	**Plasma membrane**
POPC	**1-oleoyl-2-palmitoyl-sn-glycero-3-phosphocholine**
QCM	**Quartz crystal microbalance**
RE	**Reference electrode**
RUSH	**Retention Using Selective Hook**
SBP	**Streptavidin-binding peptide**
SEC	**Size-exclusion column**
sEV	**Small EV**
SF	**Serum-free**
SLB	**Supported lipid bilayers**
TEM	**Transmission electron microscopy**
TEV	**Tumour-derived extracellular vesicle**
TFS	**Thermo Fischer Scientific**
TGE	**Total ganglioside extract**
TIRFM	**Total internal reflection fluorescence microscopy**
TME	**Tumour microenvironment**
TMP	**Transmembrane protein**
UC	**Ultracentrifugation**
UF	**Ultrafiltration**
VEGF	**Vascular endothelial growth factor**
Vero E6	**African green monkey kidney cells**

τ	**Response time**

“The true delight is in the finding out rather than in the knowing.”

— Isaac Asimov

1 INTRODUCTION

Preamble

This chapter contains work published by A. K. Jayaram, A. M. Pappa, S. Ghosh, Z. A. Manzer, W. C. **Traberg**, T. P. J. Knowles, S. Daniel, R. M. Owens, Biomembranes in bioelectronic sensing. Trends in Biotechnology (2021). Where relevant to this thesis, figures and text have been included, and where not relevant, reference has been made to the publication.

1.1 Motivation and challenges

According to the WHO, cancer is a leading cause of death worldwide, accounting for nearly 10 million deaths, or one in six deaths in 2020 (https://gco.iarc.fr/today). The primary cause of cancer-related mortalities is widespread metastases, which are difficult to treat with therapeutic intervention.[1] Meanwhile, drug development is a slow and costly process,[2] with a failure rate of 96.6% for FDA approvals in clinical trials for oncology,[3] primarily due to insufficient efficacy (48%/55%) or safety (25%/14%; phase II/III).[4] Therefore, the development of reliable preclinical drug screening technologies and disease models is a healthcare imperative. Although metastasis is a hallmark of cancer, it remains poorly understood,[1,5] in part due to challenges in characterising the spatial and temporal progression of this malignancy.[5] Recently, nano-sized particles secreted by tumour cells implicated in intercellular communication, called extracellular vesicles (EVs), have been found to play a pivotal role in metastasis.[6,7] Tumour-derived (T)EVs carry functional biomolecules that confer oncogenic potential[8] and induce malignant transformation[9] to enhance the migratory and invasive properties of recipient cells; a process called the epithelial-to-mesenchymal transition (EMT).[10,11] TEVs may further facilitate premetastatic niche formation,[12] promote angiogenesis,[13] alter host immune response,[14] and induce pro-metastatic inflammatory response.[15] Elucidating the functions and mode of action (MoA) of TEVs could therefore aid the development of therapeutic interventions against TEV-driven metastasis, representing a novel avenue for treating or preventing metastasis.[7]

Research into EV biology and function has seen a boom over the last decade owing to their unique features and potential clinical utility,[16] and the demand for new and robust tools to study their functional activity has risen commensurately.[17] This has obscured the true role of EVs in pathophysiological processes despite their pleiotropic functions *in vitro*.[18] According to a recent worldwide survey, *in vitro* functional EV analyses were among the most common downstream applications in EV research among the researchers surveyed.[19] To date, most *in vitro* EV research has applied cell-based assays accompanied by various microscopy techniques to study the function of EVs and this approach has seen tremendous progress being made towards elucidating the many facets of EV function. Critically, challenges associated with addressing the complexity of EV-cell interactions and EV heterogeneity persist despite the development of intricate reporter systems and labelling strategies.

However, current sensing technologies, often optical-based, and phenotypic screening assays suffer from inherent trade-offs between the density of information gained and the ability to study a complex biological/cellular system in its native state. This is particularly detrimental to the

study of transient biological processes, such as EMT, and hampers the discovery of new pharmacological strategies targeting metastatic drivers, such as TEV regulation pathways.[20] As such, there are three key challenges that must be overcome to accelerate research into EV function in cancer metastasis to advance drug discovery:

1. Inability to non-invasively probe a dynamic system *and* obtain high content (quantitative) information
2. Lack of scalability of current sensing technologies
3. Integration of disease relevant models with novel sensing technologies and validation of the readouts

The field of organic electronics has progressed enormously since the initial discovery of conducting polymers[21] and has recently gained widespread applications in biomedical research. The physiochemical properties of organic electronic materials, often establishing a direct conduit between biological and electrical signals, have enabled the development of novel (bioelectronic) tools/devices to transduce biological signals with the utmost sensitivity. Capitalising on advances in bioengineering and bioelectronics, this work aims to generate *in vitro* bioelectronic platforms integrated with disease-relevant cell-based and cell-free models that will support studies to further enhance current understanding of TEV function and facilitate screens against cancer metastasis initiation and progression.

1.2 Literature review

1.2.1 EV biology and significance

EVs are intercellular signal bearers capable of altering cell function and eliciting a variety of phenotypic responses.[22] These nano-sized carriers have been shown to play a critical role in a range of pathological processes[23] from cancer[24] to infection.[25] EVs were initially thought to be part of a disposal mechanism, removing unwanted substances from cells.[26–28] However, following the discovery that EVs mediate the transport of functional DNA, RNA, and protein between cells as a mechanism of horizontal transfer,[29,30] their role as mediators of intercellular communication in homeostatic[22] and pathological processes[23] quickly attracted attention in the scientific community.[17]

1.2.1.1 EV biogenesis

Nearly all prokaryotic and eukaryotic cells are capable of secreting various types of membrane vesicles. This process is highly conserved across evolution in all species from bacteria and parasites to humans and plants.[22,31–35] The term ‘extracellular vesicle’[36] is a collective term

that covers a range of heterogeneous EV subtypes[37] generally of two subcellular origins (Figure 1.1): EVs derived directly from the outward budding of the plasma membrane (PM) are typically referred to as microvesicles (MVs) or ectosomes[38] (150-1000 nm diameter) but may also include larger vesicles, such as apoptotic bodies and oncosomes.[39] While EVs of endosomal origin[40] are conventionally termed exosomes (30-100 nm diameter).[41] EV cargo is sorted into the vesicles during their biogenesis in a non-random, selective manner,[42] and EV composition reflects the type and physiological/pathological state of the source cell.[16]

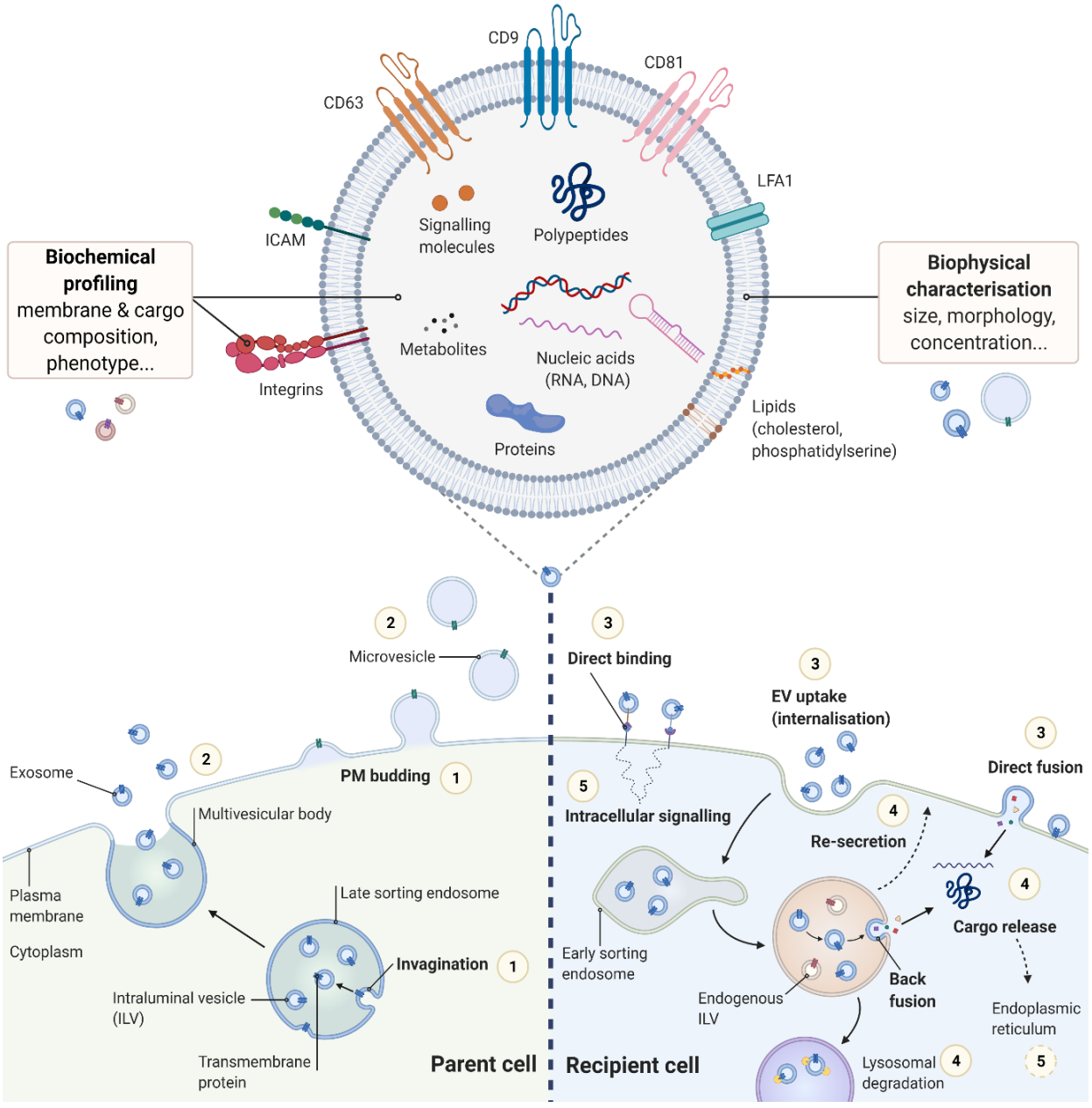

Figure 1.1: EV biogenesis and function. Biogenesis (LHS): MVs are formed by the outward budding of the PM. Intraluminal vesicles (ILVs) formed by the invagination of the limiting membrane of multivesicular bodies (MVBs) become exosomes upon their release following the fusion of late endosomal bodies with the PM. EV-cell interaction (RHS): EVs may interact with recipient cells in a number of ways, including direct binding to surface receptors inducing intracellular signalling cascades and cargo release via either internalisation by various mechanisms or direct

fusion with the PM. Among their intracellular fates, EVs may, once internalised, be degraded by the lysosome or potentially be recycled to the PM preventing any functional activity. EV composition (top): EV membrane and cargo composition is highly complex and heterogeneous between subtypes and reflects that of the parent cell. Functional characterisation is concerned with these active aspects of EV function. Adapted from[43,44] and created with Biorender.com.

1.2.1.2 EV cargo and composition

EV surface composition dictates target cell specificity through specific interactions between EV surface proteins and receptors at the PM of the recipient cell.[43,45] Equally, EV composition and the presence of specific structures on the recipient cell's plasma membrane influence the mechanism of uptake and intracellular fate of EVs and their cargo.[46] Post-internalisation, release of EV cargo in the form of functional proteins,[29,47] lipids,[48] and nucleic acids, including DNA, coding RNAs that encode proteins, and non-coding (nc)RNAs that control gene expression by repressing the translation of target mRNAs into protein,[16] may modulate signalling pathways and/or epigenetically reprogramme recipient cells' transcriptome, thereby altering cell function and triggering phenotypic changes.[16,49]

1.2.1.3 EV function

EVs play a key role in intercellular communication by mediating the transfer of active biomolecules between cells to elicit phenotypic responses that alter the physiological or pathological status of the recipient cell. This process may be broken down thusly: (1) the generation, cargo loading and secretion of EVs from the source cell; (2) EV intercellular movement (egress) and interaction with the recipient cell's membrane; followed by (3) EV uptake and cargo release via different mechanisms leading to a cellular response (Figure 1.1). During biogenesis, EVs are endowed with the active components that determine their targeting specificity and functional potential.[43] Once at the PM of the recipient cell, EVs exert their effect via different mechanisms that include: (i) juxtacrine signalling: activation of surface receptors and initiation of intracellular signalling pathways; (ii) internalisation via endocytic pathways, e.g. phagocytosis, macropinocytosis etc. leading to the release of their contents into the cytoplasm via the endosomal pathway; and (iii) cargo delivery and exchange of transmembrane proteins and lipids by direct membrane fusion.[50] Upon delivery, EV cargo must avoid the lysosomal degradative pathway in order to elicit a functional response in the recipient cell.[51]

1.2.1.4 Pathological role and clinical potential of EVs

In mammals, EVs contribute to normal physiological functions, such as reproduction, embryonic development, tissue repair, bone calcification, neural cell communication, and many other homeostatic processes.[22,52] Importantly, EVs are involved in the pathogenesis and

progression of many diseases,[23] including, *inter alia*, cancer,[24,53] neurodegenerative,[54] diabetes,[55] cardiovascular,[56] and infection,[25]. EVs play a role in regulating immune responses,[57,58] pre-metastatic niche formation, angiogenesis, metastasis,[24] inflammation,[59] and contributing to resistance to therapy,[60] to name a few. Interestingly, EVs can also mediate interspecies and interkingdom communication and are involved in many such pathological processes including host-pathogen interactions,[61] immune response modulation,[62] pathogen virulence,[33,63,64] and even metabolism regulation.[65] The ubiquity of EVs in these interkingdom interactions underscores the importance of (EV)vesicle-mediated processes throughout biology.[34]

Given their function in the genesis and progression of several disease states, strategies to attenuate EV-driven pathologies have been proposed that involve inhibiting the various aspects of EV function[66] – in effect making them therapeutics targets. Moreover, exploring the potential of EVs as therapeutic agents or drug delivery systems,[66,67] as well as diagnostic and prognostic biomarkers,[68] is highly relevant for clinical applications.[23] However, translation to the clinic is currently hampered by the lack of tools to quantify EV function and therapeutic potency,[20] and further progress in unravelling the basic mechanisms of EV function is needed for successful clinical implementation.[16]

1.2.2 Approaches for studying EV function

1.2.2.1 Attributing function

EV functional assays can be defined as systematic *in vivo* or *in vitro* experiments designed to determine the involvement of EVs and their cargo in a particular cellular pathway or biological process,[69] Essentially, an enriched, defined EV preparation is administered to a biological system, e.g. cells, and their functional effect on the system is measured using molecular and functional readouts to reveal changes in cellular expression patterns, cell behaviour etc., that indicate an altered phenotype (Figure 1.2).[70] The activity must be determined to be intrinsic to EVs specifically[71] and not caused by highly active non-EV-associated soluble molecules[70] and/or non-EV components,[72] such as lipoproteins of varying densities,[73] exomeres,[74] and enveloped viruses,[75] which are often co-isolated.[76–78] Furthermore, an observed activity may be specific to a subtype of EVs, however, as separation of EV subtypes has proven difficult,[79] applying preparations of insufficient purity in a functional assay indicates a broader functional relevance of multiple EV subtypes.[80]

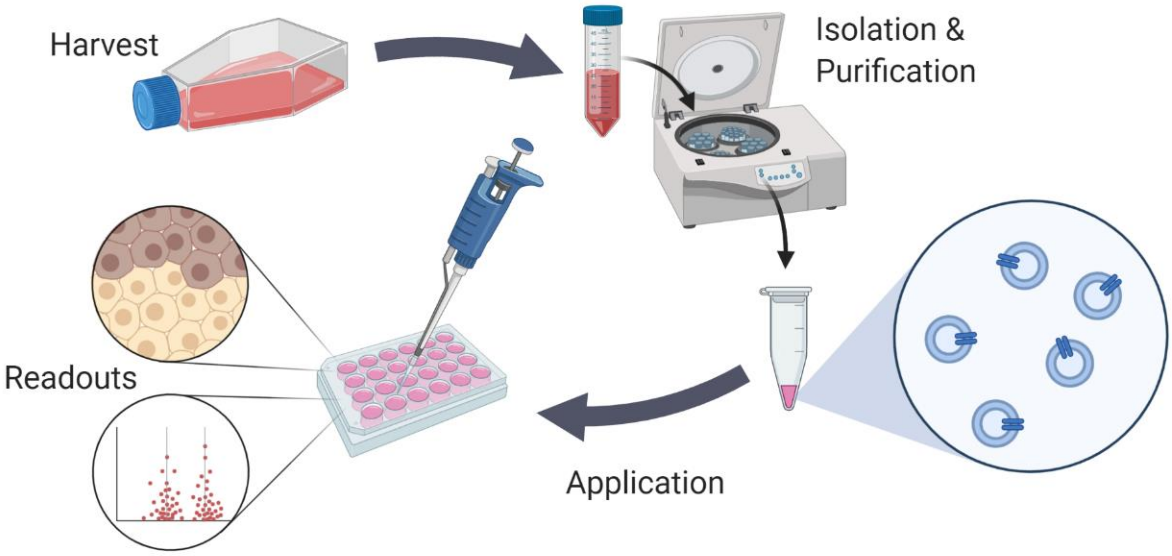

Figure 1.2: A classic EV functional assay. An EV preparation is isolated from a sample, purified, and applied to a biological system at a given dosage and incubation period, after which molecular and functional readouts may reveal the involvement of the EVs in mediating a certain functional activity in the recipient cells. Made with Biorender.com.

The biophysical and biochemical attributes of EVs provide insight into their functional potential, while the actual functional effect EVs mediate in target cells must be studied by determining the fates of EVs and their cargo, and by observing the cellular responses they elicit. Functional studies are highly varied and the outcome measures and methods required to obtain these will largely depend on the scientific question at hand.[81] Equally, the most appropriate combination of analytical tools depends on the applicability, as well as the strengths and limitations of each method.[82]

1.2.2.2 Static vs dynamic approach

Differential gene expression analysis together with gene knockdown or knockout in the model system, or in the EV donor cell, enables researchers to infer how EV cargo modulates cellular signalling pathways and/or expression profiles to elicit a functional response in recipient cells.[70] Analytical techniques that reveal the biochemical/molecular profile of a biological system may be characterised as static methods, as they capture a snapshot of the system at a particular point in time. Together with biophysical characterisation of cells to observe changes in cell behaviour, researchers can determine how EV-mediated modulation of signalling pathways and expression patterns manifests itself on a cell behavioural-level.

As an example, a key function of EVs is the delivery of functional miRNA that may silence its target mRNA, leading to a negative regulation of gene expression in the recipient cell.[16] Demonstration of EV participation may be achieved by rendering the recipient cell[62] or animal

model[83] incapable of expressing the studied miRNA to ensure that the observed miRNA-dependent effect was, in fact, mediated by EV-miRNA transfer, rather than by induction of endogenous miRNA expression by EV components.[79] However, knockdown of miRNAs may lead to changes in the phenotype and/or function of cells[84] and may also result in changes to the quantity or molecular contents of EVs[70], bringing into question the accuracy/credibility of the observed functional effects, and thus, utility of such a model system.

Given the inherent difficulties in attributing function to EVs, it is advisable, or perhaps necessary, to capture the dynamics of EV function in order to determine the specific mechanisms by which an observed effect is mediated. This, in particular, involves revealing the intracellular fates of EVs and their cargo to conclusively demonstrate that a functional biomolecule is being transferred through EVs. As an example, molecular profiling may support the involvement of an miRNA in a particular biological process, but direct demonstration that functional EV-mediated miRNA transfer is the relevant mechanism is difficult to achieve. [79] EV-miRNA must be delivered to the recipient cell's cytosol in order to exercise its function of silencing its target mRNA.[16] EV-cargo delivery by PM fusion offers a direct pathway for the miRNA to enter the cytosol, although evidence for this mechanism is scarce,[85] whereas EV internalisation via the endosomal pathway requires the EV-miRNA to escape the endosome to avoid lysosomal degradation before it can be functionally active. It has been demonstrated that despite successful uptake, EV-delivered mRNA does not always generate functional proteins in recipient cells,[86] suggesting that endosomal escape is critical for EV-RNA function.[16] It is therefore crucial to determine both the mode of action by which EVs deliver their cargo and the fate of that cargo when attributing function.

1.2.2.3 Caught red handed: capturing EV dynamics

Methods for capturing EV dynamics generally include image-based techniques that track the spatiotemporal arrangements of EVs in a biological system. Fluorescence microscopy methods capture EV dynamics in a qualitative or semi/near-quantitative manner,[87] allowing for assessment of spatiotemporal arrangements, visualisation of EV-cell interactions, including EV uptake and cargo release,[82] and quantification of EV kinetics.[88] As illustrated in Figure 1.3, fluorescently labelled EVs and EV-miRNAs allow EV uptake and EV-miRNA release in recipient cells to be tracked using fluorescence microscopy techniques.[89] The functional effect, e.g. downregulation of protein expression, may then be measured using analytical (static) techniques, and the associated cellular response, such as increased cell mobility or proliferation, may also be captured via either approach.

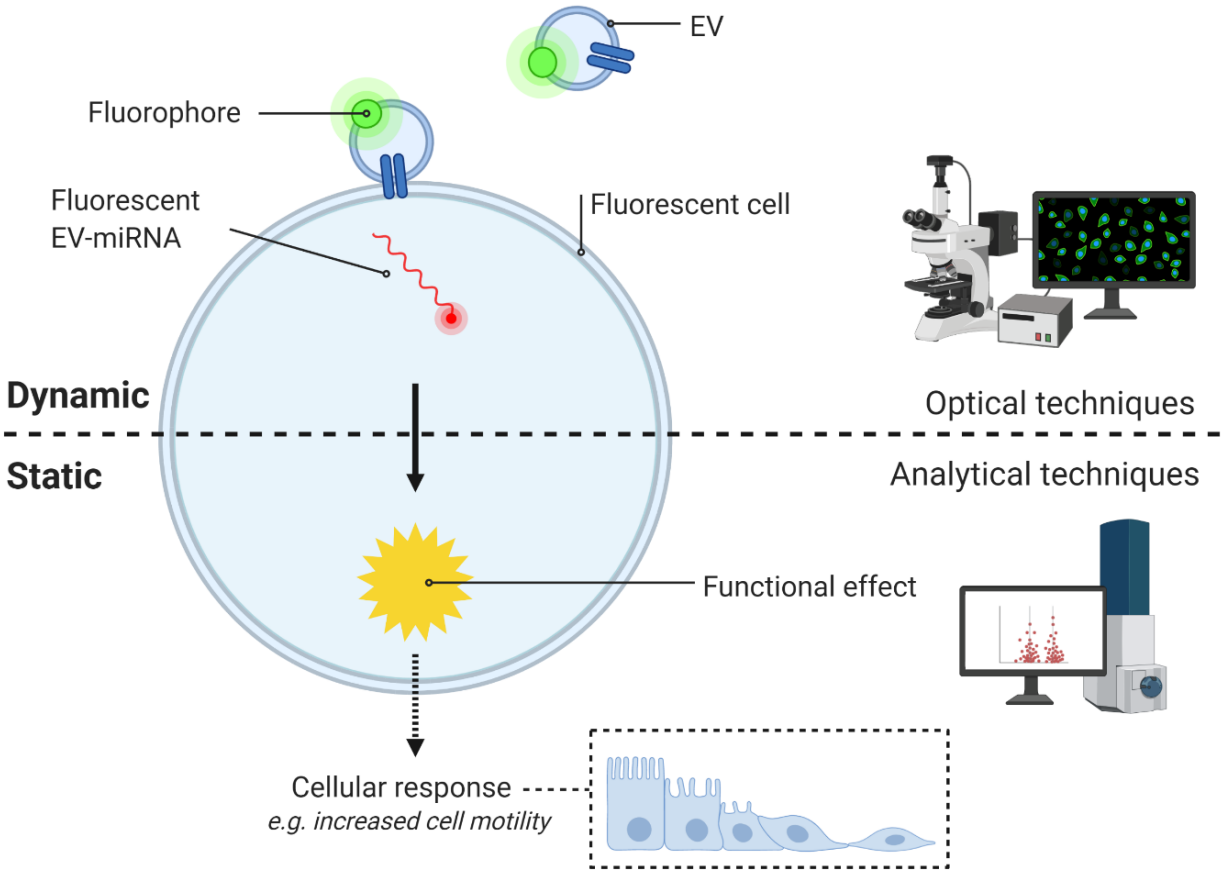

Figure 1.3: Dynamic and static approaches for studying EV function. Top: Optical tracking of a fluorescently labelled EV to observe its uptake and the release of its cargo in the recipient cell. Bottom: Biochemical analysis/molecular profiling reveals the acquisition of functional EV-RNAs and silencing of target mRNA by EV-miRNA. Made with Biorender.com.

As an example, Hoshino et al. demonstrated that exosomal integrins determine organotropism and initiate pre-metastatic niche formation, promoting organ-specific metastasis in the lung, liver, and brain. Mass spectrometry and western blot analysis revealed that integrin expression profiles in TEVs correlate with tissue organotropism. Exosome localisation, quantification, and biodistribution, determined by near-infrared spectroscopy and immunofluorescence imaging, demonstrated that specific tissue-resident stromal cells differentially uptake TEVs in metastatic target organs. Through gene knockdown and overexpression experiments, the researchers showed that specific exosomal integrins, that is, ITGβ4 and ITGβ5, can dictate metastatic organotropism to the lung and liver, respectively.[45]

1.2.2.4 Functional cell-based assays

Considering the "downstream" effects of EVs after eliciting a function in recipient cells, functional assays that allow changes in cell behaviour/function/morphology to be assessed are often based on microscopy or spectrophotometry techniques.[90,91] These include, viability,

proliferation, cytotoxicity, metabolic activity, senescence, and cell death assays. Again, such techniques are either low throughput, required labelling and/or are invasive.

Given the advancement and comprehensiveness of multi-omic technologies to characterise EV contents, it is critical that these data are given proper context and linked to EV function.[81] Methods that capture EV dynamics offer deeper insight into the mechanistic pathways by which EVs deliver their cargo to determine if EV-mediated transfer is the relevant mechanism. Cell-based assays that then measure the resultant functional changes associated with an altered cell phenotype may then shed light on the actual implication of EV function. Studies combining static and dynamic approaches answer the *what* and *how* of EV function, linking the system structures (molecular-level interactions) to the system dynamics (behaviour over time)[92] to paint a complete, systems-level picture of EV function. These allow researchers to better answer key questions regarding EV function, e.g. *do EVs, in fact, mediate the delivery of functional mRNAs in vivo?*[16] and *do TEVs mediate cancer metastasis by conferring oncogenic potential and inducing tumourigenesis in non-tumourigenic cells?*[93]

1.2.3 Current methods for tracking EV dynamics

Cell-based assays paired with microscopy are the most commonly used methods for studying EV dynamics. Microscopy imaging is useful for localising particles and labelled targets and visualising structures in cells or tissues. It is thus ideal for studying the spatiotemporal properties of EVs in biological systems. However, due to their nano-scale size, EVs, and small (s)EVs in particular, fall below the diffraction limit rendering them difficult to track using conventional labelling methods and microscopy techniques. This has required the use of powerful super-resolution microscopy techniques and the development of intricate reporter systems and labelling techniques to capture EV dynamics and determine key mechanisms of EV function. A few examples of the state-of-the-art in capturing EV function are given here.

1.2.3.1 Conventional fluorescence labels and tags

Fluorescence labelling methods are diverse, and the selection of appropriate fluorophores and target molecules enable the imaging of EVs and their interactions with live cells, which may offer critical insight into the mechanisms that govern the different aspects of EV function. The target components may be either ubiquitous or highly specific to particular EV subtypes. Conventional EV labelling strategies typically involve genetically encoding fluorescent proteins enriched in EVs, e.g. CD63,[94] or using organic 'lipophilic' dyes, e.g. PKH ,[95] that work by incorporating their aliphatic portion into the exposed EV lipid bilayer. Many methods opt to label the EV membrane as opposed to EV proteins, as it prevents perturbation of active EV components that are required

for proper function and enables the visualisation of multiple EV subtypes indiscriminately. However, fluorescent dyes for labelling the lipid membrane of EVs, specifically PKH dyes, have been shown to have half-lives outlasting that of EVs *in vivo.* Following EV degradation by cells, recycled dye-labelled membrane or dye residues may be misinterpreted as labelled EVs. Moreover, PKH can associate with other lipid entities for long periods [96] and may also aggregate or form micelles [95] that are almost indistinguishable from PKH-labelled EVs, leading to false-positive signals for EV that misguide spatiotemporal assessment of EV dynamics [97]. This is especially critical as the *in vitro* half-life of PalmGFP$^+$ labelled EVs in recipient cells was shown to be < 24 h [96], while the *in vivo* half-life of intravenously administered EVs has been shown to range from 1.5-2 min [98,99] to 30 min [97]. This begs the question of whether the observed EV half-life is solely a function of EV origin, subtype, *in vivo* model, and pathological state of the system, or the labelling strategy being used, thus further complicating the matter of accurately characterising EV bioactivity and function *in vivo.* Improvements to membrane dyes may help address these issues and Lai et al. developed novel optical reporters that showed improved characteristics compared to traditional PKH dyes. They were able to capture the exchange of EVs between cells by tagging the inner plasma membrane of multiple EV types with fluorescent proteins genetically fused with a palmitoylation signal (Palm), demonstrating that EV exchange is multidirectional,[96] as opposed to solely unidirectional.[100] Increasingly, multiplexed reporters are used to track multiple components simultaneously.

1.2.3.2 Reporter systems

Bioluminescent reporters

Optical reporters have been used for live-cell imaging to confirm the EV-mediated transfer of functional mRNA. Skog et al. used *Gaussia* luciferase (GLuc), a bioluminescent reporter, mRNA to show that RNA incorporated into tumour-derived EVs can be delivered into recipient normal cells and generate a functional protein,[47] thus confirming the initial findings that EVs functionally transfer mRNA.[29,30] It was later shown by multiplexing fluorescent and bioluminescent EV reporters that EV-mRNA encoding a membrane-bound GLuc reporter fused to a biotin accepter domain (*GLucB*) could be translated in recipient cells as early as 1 h post-EV exposure,[96] revealing the rapid dynamics of EV uptake and subsequent translation of EV-delivered mRNAs. Furthermore, as initially demonstrated for viral miRNA-containing sEVs secreted by Epstein-Barr virus-infected cells,[101] luciferase reporter assays have been used to show that EVs transfer functional miRNAs between cells, repressing target gene expression.[101,102]

As pointed out, the resolution limit renders it nearly impossible to distinguish EV binding from cellular uptake using convention microscopy techniques. To solve this, sophisticated

labelling strategies have been employed. As an example, EVs carrying a pair of chimeric reporter proteins DSP1, fused to CD9 or CD63, and DSP2, with the ability to self-associate when present in the same compartment and recover both green fluorescence and luciferase activity, have been used to distinguish EV uptake from binding. When internalised by cells preloaded with a cytopermeable Renilla luciferase substrate, the fully competent Renilla enzyme carried by the EVs is able to elicit a luminescent signal revealing the intracellular localisation of EVs. This system allows for EV uptake to be measured dynamically and quantitatively,[103] and could be used to evaluate the efficacy of molecular inhibitors on EV uptake.

pH-sensitive reporters

The release of EVs of endosomal origin, i.e. exosomes, and the uptake of EVs by cells via endocytosis is associated with transfer to and from endosomal compartments of higher acidity compared to the cytosol and the extracellular space. This presents an opportunity for pH-sensitive reporters to reveal the dynamics of EV intracellular trafficking. *pHLuorin-GFP* is one such pH-sensitive reporter, whose fluorescence is quenched at the acidic late endosomal pH but fluoresces brightly at the neutral pH of the extracellular environment. Conventionally used to visualise exocytosis and endocytosis during synaptic transmission,[104] by inserting this pH-sensitive moiety into the extracellular loop of EV-enriched proteins, e.g. CD63 (*pHLuorin-CD63*), the reporter is ideally suited for identifying exosome secretion sites during live-cell imaging; a process preceded by fusion of MVBs with the PM.[88,105] Sung et al. found that in cells expressing *pHLuorin-CD63* bursts of fluorescence closely preceded adhesion formation; identifying adhesion assembly as a critical exosome function and autocrine mechanism that promotes efficient cell motility in fibrosarcoma HT1080 cell.[105] Later, the same group incorporated a stabilising mutation in the pHLuorin moiety of their reporter (*pHluo_M153R-CD63*) to achieve higher, more stable expression in cells, allowing them to visualise secreted exosomes in 2D and 3D tissue cultures and *in vivo*. They observed that exosomes were secreted at the front of migrating cells and left behind in so-called exosome trails which attracted and promoted migration of follower cells, demonstrating that exosomes secreted from cancer cells promote cancer cell chemotaxis in both an autocrine and paracrine manner.[106,107]

Sung et al. created a dual-colour reporter by incorporating a pH-insensitive tag in their modified pH-sensitive reporter that exhibited fluorescence under both acidic and neutral-pH conditions, allowing them to track MVB trafficking events and visualise cellular interactions with externalised exosomes. They observed that migrating cells detect exosome deposits by touching them with filopodia,[108] then migrate towards these deposits and engulf them. Moreover, as endocytosed exosomes changed colour over time due to loss of the pHluorin signal consistent with

maturation and acidification of endosomes, the kinetics of internalisation and acidification of endocytosed exosome deposits could be quantified;[106] shedding light on the dynamics of intracellular exosome trafficking. The brighter fluorescence and addition of a pH-insensitive tag allowed for the use of confocal microscopy as opposed to total internal reflection fluorescence (TIRF) for tracking MVB trafficking events before fusion with the PM.[106] Combined with inhibitors, molecular interventions and/or other reporters, the dual-colour reporter can be used for studying the endocytic fate of exosomes, directly relevant to the therapeutic application of exosomes.

Using a similar reporter and TIRFM to achieve single-cell resolution, Verweji et al. demonstrated that MVB-PM fusion is controlled by SNARE molecules in the G-protein-coupled receptor signalling pathway, highlighting the modulatory dynamics of MVB exocytosis. This live-imaging approach visualised the effects of interfering agents in real-time, minimising the risk of measuring secondary effects and allowed for the study of the kinetics of exosome release.[88] Moreover, the researchers used dynamic corrective light-EM and 3D tomographic reconstruction to capture the MVB-PM fusion profile and reveal externalisation of ILVs. By correlating fluorescence data with these exosome secretion events, MVB-PM fusion kinetics were found to be distinct from, and more prolonged than, other forms of vesicle-mediated exocytosis.[88]

A strong signal-to-noise ratio is achieved by using the pHLuorin-CD63 probe to observe only extracellular CD63, allowing the dynamic relationship between exosome secretion and cellular structures to be observed. The pH-sensitive approach allows the release of defined subpopulations of exosomes to be tracked and quantified, and the effects of rapid and temporary changes in the local environment to be studied. However, this approach cannot capture vesicles budding from the PM, making it specific to endosome-derived vesicles, nor does it visualise EV subpopulations devoid of the chosen reporter. A different strategy must be deployed for studying MV dynamics.

Tagging fluorescent reporters with a degradation motif

Due to the nature of EV biogenesis, specifically that of the classically termed MVs which bud directly from the PM (ectocytosis), the content of MVs is similar to the membrane and cytoplasm of their donor cell making it difficult to distinguish released vesicles from the plasma membrane of neighbouring cells.[109] MV budding is inhibited by the TAT-5 lipid flippase, resulting in continuous MV release when *tat-5* is knocked down, as first demonstrated statically by electron tomography[110] and later dynamically using a degron-tagged reporter.[18]

Conventionally used as a loss-of-function technique, degron tags are degradation motifs that target specific proteins, such as fluorescent reporters, for controllable degradation by cytosolic factors.[109] Beer et al. demonstrated that both membrane-associated and transmembrane proteins

can be tagged with degrons to specifically label EVs *in vivo*. Once enveloped by the vesicle, the degron-tagged reporter is protected from proteasomal degradation unlike the plasma membrane label which degrades, removing the reporter from the donor cell whilst leaving the EV clearly visible, allowing for the study of autocrine interactions.[109] By using a degron-tagged fluorescent PM reporter ($PH_{PLC1\partial 1}$) to label PM-derived EVs, they could screen for EV release and were able to identify TAT-5 regulators associated with retrograde endosomal recycling that are required for the plasma membrane localisation of TAT-5. This localisation is important to maintain lipid phosphatidylethanolamine (PE) asymmetry and inhibit EV release, pinpointing TAT-5 and PE as key regulators of ESCRT-mediated plasma membrane budding.[18]

Degron-tagged reporters reveal insights on an epifluorescence microscope that are typically limited to super-resolution microscopy or EM on fixed samples.[109] The ability of degron-tagged reporters to specifically label EVs enables *in vivo* tracking and screening for new regulators of EV budding,[18,109] a powerful tool for functional studies. Moreover, degron-tagged reporters reveal topology of tagged protein. However, as before, this method is limited to EV subpopulations by the choice of reporter.

CRISPR-Cas9-based reporter system

de Jong et al. (2020) developed a highly sensitive CRISPR-Cas9-based reporter system that allows direct functional study of EV-mediated transfer of small non-coding RNA molecules at single-cell resolution. To achieve functional RNA delivery, capable of activating high expression of a fluorescent reporter protein, independent of translation of the RNA molecule, the researchers used a CRISPR/Cas9 system. A ~100 nucleotide, 35 kD, single guide RNA, guided the Cas9 protein to a specific genomic sequence, resulting in a specific double-stranded break in the genomic DNA. To visualize the transfer of single guide (sg)RNAs, they designed a fluorescent "Stoplight" reporter system which was permanently activated in EV-acceptor cells upon functional transfer of a specific targeting sgRNA, expressed in EV-donor cells. This allowed them to demonstrate functional intercellular sgRNA transfer using direct co-culture, Transwell inserts, and direct EV-addition experiments at single-cell resolution. This approach addresses a major drawback of mRNA-based systems, where it is inherently impossible to phenotypically distinguish between reporter activation as a result of the delivery of translated protein or the mRNA itself.[111]

Retention Using Selective Hook (RUSH) system

Mathieu et al. (2021) used the RUSH system to follow the EV biomarkers CD9 and CD63 synchronously by live imaging from the ER to their residency compartment.[112] Here, the protein of interest is fused to a fluorescent moiety and a streptavidin-binding peptide (SBP) and co-expressed with another protein localized in the donor compartment, which is fused to streptavidin

and used as a hook (Streptavidin-KDEL for retention in the ER). Upon synthesis, the SBP-fluorescent protein is retained in the ER by its interaction with streptavidin-KDEL. Biotin addition causes the protein of interest to release by binding to streptavidin, inducing the release of the SBP-fused protein that can then follow its normal trafficking route. This allowed the intracellular trafficking of CD9 and CD63 from the endoplasmic reticulum to their residency compartment, the PM and late endosomes, respectively, to be followed, allowing discrimination of exosome vs ectosome secretion.[112]

Förster Resonance Energy Transfer (FRET)

EVs derived from transgenic mice were capable of seeding tau aggregation when assayed with FRET tau biosensor cells. Polanco et al. treated biosensor cells containing a fluorescent protein FRET pair for tau protein capable of detecting tau seeding activity with tau-containing exosome-like EVs derived from transgenic mice. Aggregation of the endogenous tau reporter protein generated a FRET signal detectable by flow cytometry or confocal microscopy. They showed that these EVs induced aggregation of endogenous tau in recipient tau biosensor cells, demonstrating that EVs can transmit tau pathology in neurodegenerative diseases.[113] However, emission in FRET is sensitive to changes of the microenvironment of the fluorescent molecule, while the appropriate combination of emitters needs to be carefully selected and signal-to-noise ratio can be low.[82]

Photoswitchable probes

Specifically for the application of super-resolution methods, by labelling both the exosome membrane and exosomal cargo with photoswitchable probes, dual-colour single-molecule localization microscopy (SMLM)-based dynamic tracking has been used to visualise the release of miR-21 by exosomes in recipient cells and reveal that exosomes protect encapsulated miR-21 from enzymatic degradation. This release process would otherwise be invisible under a wide-field TIRF microscope,[89] demonstrating the ability of super-resolution techniques to track the dynamics of EVs and EV-miRNAs in living cells.

1.2.3.3 Limitations of fluorescence microscopy and optical methods

Fluorescence microscopy is a powerful technique for studying EV function, however current EV labelling methods suffer from some limitations, including the inherent need for labelling, the interference from an intrinsic fluorescence background signal, and the occurrence of photobleaching and quenching by oxygen.[82] Immunofluorescence is highly specific to the target protein being labelled, which may restrict the labelling to certain subpopulations of EVs. Furthermore, EV surface proteins, such as tetraspanins, play a role in EV function:[114] from

biogenesis and release[22,115] to binding and uptake by recipient cells.[116] For example, CD63 is important for sEV secretion and knockdown of CD63 results in decreased sEV secretion.[115] Conversely, overexpression of CD63, when used as a reporter, leads to increased sEV secretion.[106] Thus, is it preferable to minimise perturbation to the EV surface proteome[96] to limit any adverse effects that compromise the validity of the system being studied. Additionally, sEVs may be smaller than 50 nm and tagging them with a 5 nm fluorescent molecule may significantly affect both their biodistribution, kinetics and their functional effects.[81] Furthermore, optical methods often scale poorly and require highly trained operators.

The use of cell-free models may allow facile probing of the molecular mechanisms behind EV function and the integration of both cell-based and cell-free models with organic electronic offer a new sensing technology that addressing many of the issues suffered by optical methods and the phenotypic screening technology field in general.

1.2.4 Supported lipid bilayers: a cell-free system*

The cell membrane compartmentalises the interior of a cell, separating it from the external environment, serving key roles in cellular homeostasis, metabolism, energy harvesting and growth.[74,118,119] Cell membranes across all living kingdoms, animal, plant, and microbial, serve as a protective barrier against invasion or toxicity. Studies of pathogen, toxin, and EV interactions with cells also rely on an understanding of their point of entry, at the external membrane surface.[120,121] Cell membranes have a molecularly complex surface, comprised of lipids, proteins, and glycans, all essential for function. Glycans, for example, are well known for their importance in mediating cell–cell adhesion, macromolecule interactions, and being subverted for pathogen invasion.[122] In many cases, an authentic, functional membrane can be thought of as an alternative to a live cell, providing a robust and scalable alternative to cell-based assays. Cell membranes, being the first point of contact, play an important role in the absorption, distribution, metabolism, and excretion of a drug. Initial cell–drug interactions can dictate the

* This section comprises text and figures published by A. K. Jayaram, A. M. Pappa, S. Ghosh, Z. A. Manzer, W. C. **Traberg** et al. (2021)[117]

fate of the administered drug.[123] Approximately 60% of approved drugs target the cell membrane either via membrane-associated proteins or through direct interaction with the membrane lipids.[124] Despite their significance, the molecular mechanics of cell membranes are not well understood with respect to outside influences, owing to both the complexity of the native membrane and the challenges in recapitulating this while preserving transmembrane protein (TMP) structure/function, and the lack of suitable technologies for efficient, low-cost, and broad spectrum studies.[125] Recent advances in receptor pharmacology, alongside important discoveries in structural biology, have opened new and exciting avenues in drug discovery; however, high-throughput and high-content manner technologies are required to assess interactions at the first point of contact, the cell membrane, to facilitate the drug development process.

1.2.4.1 Supported lipid bilayers: models of the cell plasma membrane

Given the high degree of complexity and diversity of natural membranes, a plethora of biomimetic membrane models have been developed, the choice of which have mainly been dictated by the biological phenomenon at study. The majority of cell membrane mimics consist of lipid vesicles free in solution[126] or self-assembled into a mono-/bilayer format,[127] or surface-tethered lipids (Figure 1.4).[128] Lipid bilayers are potent models for drug/compound permeability studies.[125] Biomembrane sensors use planar lipid bilayer, which allows facile integration with multiple sensing modalities, provided the *in vivo*-like fluidity and mobility can be maintained. Lipid bilayers supported on solid substrates (supported lipid bilayers; SLBs) have become increasingly popular to study fundamental properties of biological membranes and their constituent lipid and protein molecules, as well as other applications, including pathogen diagnostics[129] and drug discovery.[130,131]

SLBs are often produced using Langmuir-Blodgett-Schaeffer transfer,[132] vesicle fusion,[133] or solvent-assisted lipid bilayer formation methods.[134] The hallmark of planar lipid bilayers is that they can be supported on a solid substrate, which in turn can offer a level of tunability by choice of the suitable substrates, an additional advantage for the purpose of biosensing. The majority of the methods to form and subsequently study SLBs rely either on methods that tether the lipids to the surface with a linker to allow the protein to extend below the bilayer, thus limiting the diffusivity of the bilayer, or involve vesicle fusion to surfaces unable to accommodate many functional intracellular domains. The incorporation of proteinaceous or polymeric cushions between the lipids and the substrate has been sought as a way to preserve protein fluidity and functionality.[135,136] The use of electroactive polymeric substrates has therefore emerged as a very promising alternative to seamlessly interface cell membranes, providing a label-free means to directly assess function in a biomimetic environments.[130,137]

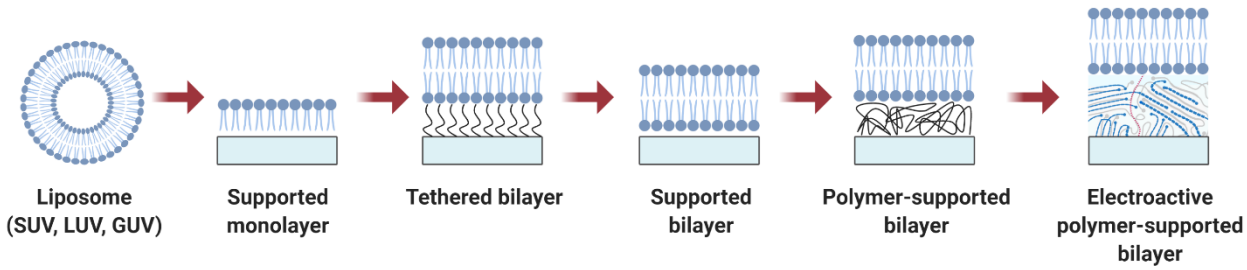

Figure 1.4: SLB progression. Schematic diagram showing the process of bilayer fabrication from liposomes, highlighting the differences between different types of bilayers[117]. Reused with permission from ACS Nano.

The preparation of high-quality planar lipid bilayers with lipid compositions span from single component lipid bilayers to complex systems containing native membrane components (**Figure 1.5**). Emerging applications of SLBs rely increasingly on the incorporation of functional membrane proteins via reconstitution for controlled studies of cellular phenomena.[134] However, the reconstitution process makes it difficult to control protein orientation and there is always a concern about possible denaturation or disruption of essential protein–lipid interactions necessary for preservation of protein activity and function.[125,134,138] In addition, the proximity of the typically rigid solid supports to the lipid bilayer precludes the incorporation of large TMPs with bulky extracellular domains, restricts their mobility (known to be necessary for interaction with key membrane components), and, ultimately, impacts their function.[136,139] To circumvent this, several strategies have been adopted, including the formation of suspended membrane systems, such as black lipid membranes,[140] polymer cushioned lipid bilayers,[135,136] and tethered lipid bilayers.[128,141,142]

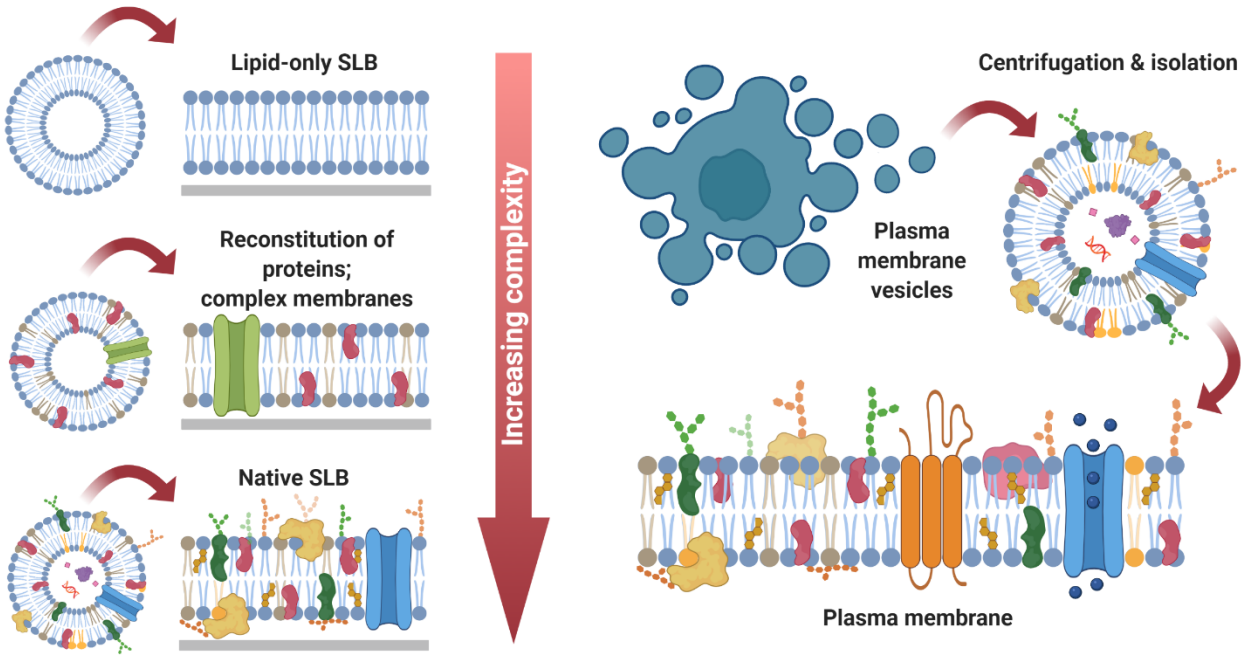

Figure 1.5: Increasing SLB complexity. Schematic diagram highlighting the cell membrane and the planar lipid bilayer model with increasing complexity.[117] Reused with permission from ACS Nano.

Cell-derived vesicles (blebs) are a promising alternative to study native membrane properties and membrane-associated cellular events in a model system (Figure 1.5).[143] Cell blebs are proteoliposomes that protrude and bud from the cell surface and retain the lipid and protein composition of the mother cell membrane.[144] These native membrane vesicles contain a full host of receptors, negating the need to purify and reconstitute membrane proteins. Researchers have developed methods to create SLBs using native cell membranes that maintain mobility and orientation of TMPs,[144–146] an encouraging method for fabrication of biologically complex membranes and a much-needed intermediate between very simple bilayer platforms and whole-cell readouts. A major advantage is that native membrane components are captured with the lipid, protein, and glycan species found in the live cell.[147] Maintaining both protein and lipid mobility in SLBs is important as membrane lipids can regulate the distribution and localisation of peripheral proteins and then participate in numerous important cellular activities, such as protein function, cell adhesion, and cell signalling.[148,149] Recently, formation of SLBs using such naturally occurring membranous vesicles, via vesicle fusion, has enabled studies on ‘authentic’ cell membranes that preserve the structure and composition of the cell membrane.[129–131,137]

1.2.4.2 Surface-sensitive analytical techniques for characterising SLBs

SLBs have a major advantage over vesicles in solution, in that they facilitate integration with surface-based techniques and microscopy due to their planar configuration. For the same reason, they are also preferred for interfacing with planar electronic devices. The choice of the substrate to form the membrane largely dictates the compatibility of techniques to characterise the SLB.

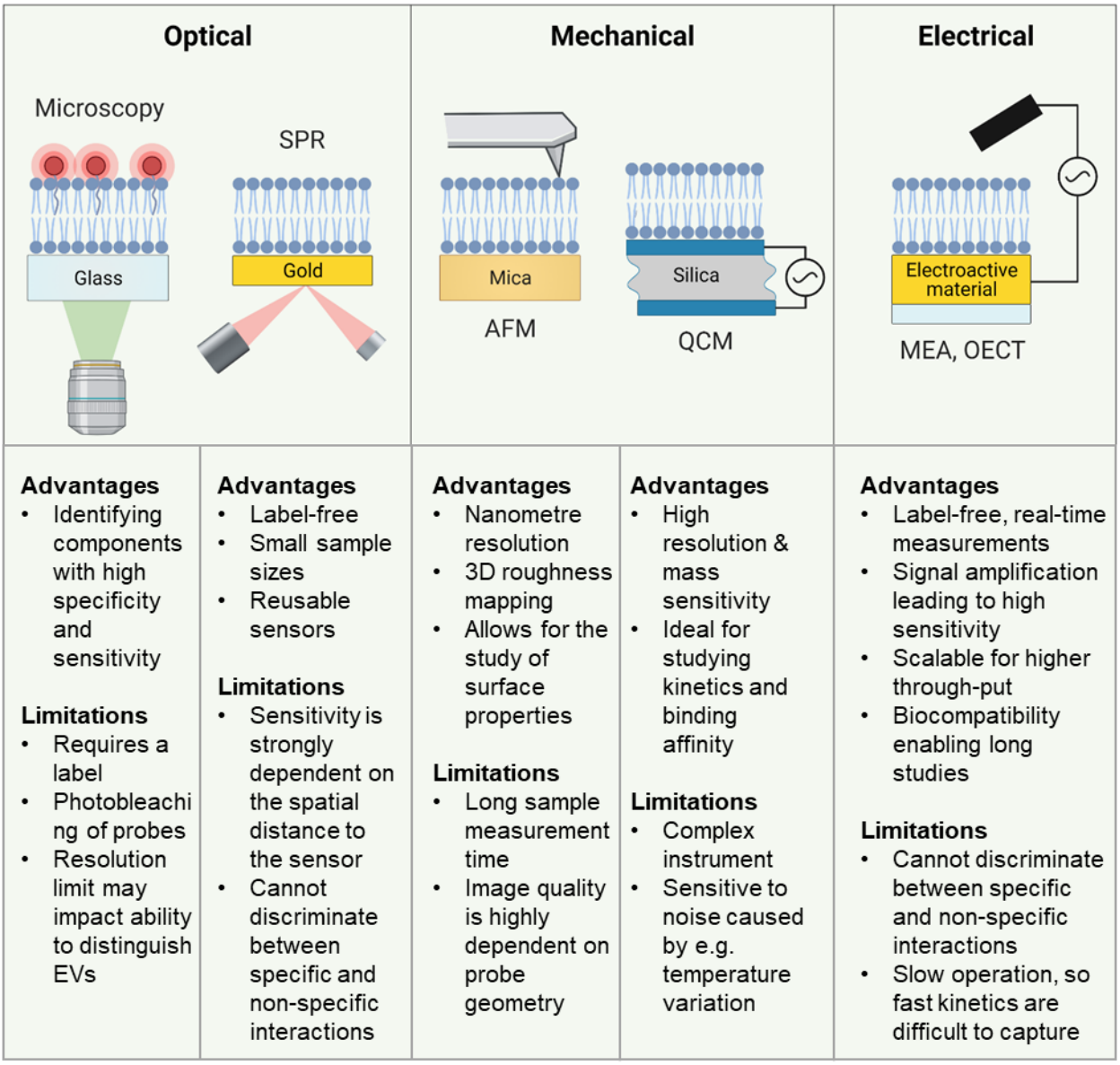

Figure 1.6: Surface-sensitive analytical techniques and their advantages and limitations. Schematic diagram highlighting optical, mechanical, and electrical readout mechanisms that can be used to study biological interactions with SLBs. Abbreviations: AFM, atomic force microscopy; MEA, microelectrode array; OECT, organic electrochemical transistor; QCM, quartz crystal microbalance; SPR, surface plasmon resonance.[117] Reused with permission from ACS Nano.

Various techniques for SLB studies have been developed to date (Figure 1.6), including optical microscopy, atomic force microscopy (AFM),[150] quartz crystal microbalance (QCM),[151] surface plasmon resonance,[128] X-ray reflectivity/scattering,[152] neutron reflectometry,[153] Raman spectroscopy,[154] secondary ion mass spectrometry,[155] and electrical/electrochemical spectroscopy[130], each displaying advantages and disadvantages. In contrast to the large portion of biological assays that involve the use of external probes (e.g., chromophores/fluorophores), many of these techniques are label-free, thus preserving the authenticity of the system at study.

Optical techniques like fluorescent recovery after photobleaching (FRAP) can be carried out on glass, measuring the bilayer fluidity of SLBs,[156] while TIRF is another optical technique that has been used to probe the ordering of lipids in bilayers, which is of paramount importance in enabling representative protein–membrane interactions in model systems.[157] Although these techniques are crucial in ensuring appropriate quality, coverage, and orientation of bilayers, they provide largely qualitative analysis. Moreover, glass as a substrate poses challenges in the formation of SLBs from negatively charged lipids due to electrostatic interactions.[158]

1.2.5 Methods such as electrochemical impedance spectroscopy (EIS), cyclic voltammetry (CV), and transistor-based measurements have been also used to study planar lipid bilayers. A variety of electrically active substrates have been used to interface biomembranes, including inorganic (i.e., gold, silicon oxide, aluminium oxide, and indium tin oxide)[159–162] and organic materials (i.e., graphene, conducting polymers). The latter, in conjunction with surface patterning methods and microfluidics incorporation,[163,164] are being increasingly adopted in biosensing and basic biophysical studies. CV and EIS are commonly used for membrane electrical characterisation,[151,165] with the latter bearing the advantage of quantifying the electrical changes in the membrane, using the appropriate circuit modelling, upon specific interaction.[166] More recently, lipid bilayers have also been incorporated in transistor setups.[129,130] Electrical methods are discussed in further detail in section 1.2.6.Applying SLB models to EV research

A barrier to understanding EV function is the difficulty in studying the EV-cell membrane interactions that precede cargo delivery. Here, a better understanding of membrane biology will help elucidate the mechanisms of EV uptake and contribute substantially towards advancing the field of EV research. Fluorescent reporter systems help elucidate the dynamics of such interactions, but their poor scalability and need for labelling limit their potential, e.g., screens against a large numbers of surface receptors to implicate their involvement in EV binding. Cell membrane models are well suited for multiplex biosensing assays that reveal the dynamics of membrane-related biomolecular interactions.[167] In the context of EVs, utilising SLBs to study EV function is in its nascent stages, but despite the paucity of studies taking this approach, it has already led to some interesting findings. Membrane models in EV research have generally been applied in one of two ways (Figure 1.7): (1) studying the interactions between EVs and a model cell plasma or endosomal membrane; or (2) probing an EV-derived SLB (EV-SLB) to gain information on EV surface constituents and interactions.

1.2.5.1 EV-membrane interactions using SLBs

As an example of the former, host-pathology interaction studies have shown that virus-like proteoliposomes containing the fusion protein hemagglutinin (HA) are able to fuse with HA-containing SLBs [129] and release their fluorescent cargo.[146] Given the inherent similarities between EVs and viruses – both in form and function[75] – the ability to carry out and measure particle fusion events on SLBs holds promise for studying EV-membrane fusion events related to EV-cargo delivery to the cytosol via both direct EV-PM fusion and the endocytic pathway depending on the membrane model deployed. In fact, the majority of EV uptake research has been focused on the endocytic pathways due in part to the difficulty in assessing fusion events.[16]

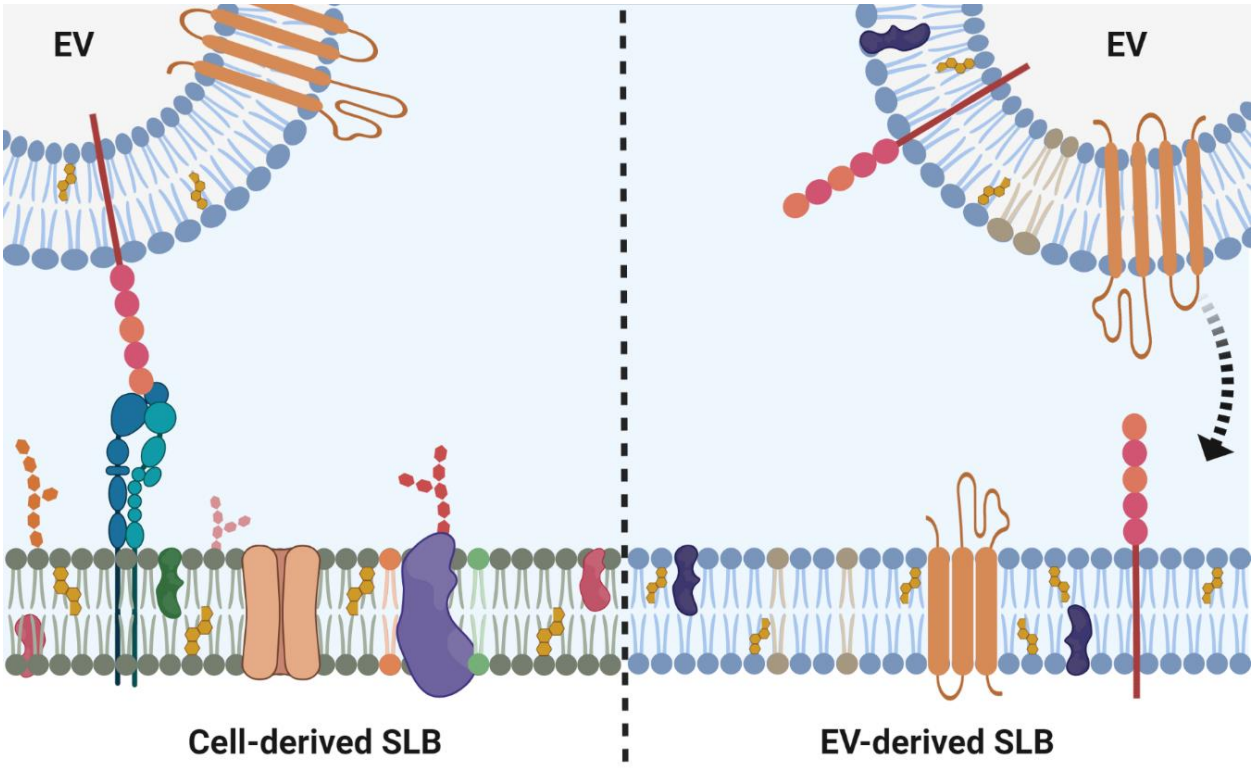

Figure 1.7: Membrane models for studying EV function. LHS: Cell-derived SLB incorporating native plasma membrane components for studying EV-membrane interactions. RHS: EV-derived SLB incorporating EV membrane components for studying the EV membrane and its function. Made with Biorender.com.

In this regard, SLBs represent a novel approach to studying EV-membrane fusion events and have indeed been utilised in this way. Nishio et al. developed an exosome fusion assay based on measuring gramicidin A channel conductance of synthetic SLBs, incorporating external gramicidin A, formed on gold electrodes using spacer and tether molecules. They demonstrated that exosome fusion with the SLB led to modulation of apparent channel activity of gramicidin A, as exosome membrane fusion disturbed the local area of the SLB membrane, increasing the number of gramicidin A molecules inserting into the SLB. This allowed for exosome membrane fusion to be monitored in real-time under different pH conditions. Interestingly, the study found

that the fusion rate of cancer-derived (MCF-7) exosomes was higher than that of exosomes derived from normal (HEK-293) cells.[168] Recently, Perissinotto et al. utilised multiple techniques, including AFM and neutron scattering, to gain structural insight on EV fusion mechanisms with artificial lipid bilayers and showed that ordered lipid compartments mimicking lipid rafts promote EV fusion.[169]

1.2.5.2 EV-derived SLBs

EV-SLBs, on the other hand, have seen their use as either naturally derived "biogenic" SLB mimics of the native cell membrane (as opposed to artificially generating blebs from cells), or as an active substrate for cell culturing to investigate the functional effect that EV membrane constituents elicit in target cells. In the latter case, the functional effect mediated by breast cancer EVs on adipose-derived stem cells has been investigated by culturing these cells on a hybrid supported lipid bilayer incorporating EV membrane material, derived from either exosomes or MVs.[170] Uribe et al. showed that surface interactions between the cells and EV-SLB promoted oncogenic activity, such as angiogenesis and cell proliferation, suggesting that EV membrane constituents confer functional changes in target cells and are thus a key actor in EV function. Interestingly, the SLBs incorporating the classic MVs showed greater oncogenic potential than the SLBs derived from exosomes.[170] This model system presents a strategy for studying the function of EV membrane constituents in absence of EV cargo.

Montis et al. reported the first example of an SLB derived from EVs and highlighted specific structural differences between the EV-SLB and a synthetic SLB.[171] These included lateral inhomogeneity with regions of lipid raft-like domains, a key characteristic of both plasma membranes and EVs, [172] and cushioned patches caused by EV cargo trapped between the support and the SLB, caused by the so-called "parachute" rupture mechanism,[173] whereby the opening vesicles expose their inner leaflet and release their cargo to the side of the support. These features significantly increased the surface roughness of the layer leading to an overall increased surface area.[171] Later, the same group showed that the inherent localised non-flat regions resulted in much stronger interaction with cationic superparamagnetic iron oxide nanoparticles (SPIONs), suggesting that these structural features are relevant in the response of biogenic membranes to nano-objects.[174]

1.2.5.3 Other applications

Larios et al. reported that ESCRT-associated protein ALIX recruits ESCRT-III proteins to endosomes promoting the sorting and delivery of tetraspanins to exosomes *in vivo*. They demonstrated that this recruitment could be fully recapitulated *in vitro* using purified components

incorporated into supported bilayers derived from (synthetic) giant unilamellar vesicles with the phospholipid composition of late endosomes to act as an endosome mimetic.[175]

1.2.5.4 SLB limitations and prospects

Interestingly, the cushioned areas of the EV-SLB in the previous example resulted in a lower coupling of the bilayer with the underlying support, possibly leading to lower bending energy, which rendered these areas more prone to interact with exogenous species, as the membrane was not being hampered by the presence of the support.[174] This highlights an inherent limitation of SLBs incorporated on solid supports in that they do not accurately replicate the native membrane environment nor do they facilitate the incorporation and free movement of transmembrane proteins[135], both of which are crucial for proper membrane function.[173] Bilayer quality is acutely affected by substrate energetics[176] and key issues remain around bilayer fluidity and protein mobility. The proximity of the lipid bilayer to the solid support may inhibit the diffusion of the membrane components through the fluid bilayer.[177] In particular, silica-based surfaces easily foul and denature proteins protruding from underneath the lipid bilayer, and the rigid surface affords limited space (~1 nm) between the lipid headgroups and the silica surface,[178,179] particularly detrimental to the incorporation of transmembrane proteins.[136,139] Various strategies for decoupling the bilayer from the support have been explored, including introducing proteinaceous or polymeric cushions or spacers between the lipids and the substrate,[135,173,180–182] or using functional, interfacial materials[183,184] that accommodate intracellular protein domains, albeit at the expense of sensitivity.

Accurate SLB models allow researchers to, in a sense, zoom in on just the membrane interactions and study that particular facet of EV function. SLBs derived from EVs present an innate link to the phenotype and function of the donor cell,[171] and the ability to derive EV-SLBs from seemingly any EV subtype of any origin holds great potential for the study of interactions between specific EVs and target cells to investigate their functional effect and pathogenic potential. Furthermore, given the difficulty in distinguishing different uptake mechanisms in a complex cellular environment,[185] SLBs may hold the key to unravelling the intricacies of EV-membrane interaction and uptake, offering a less labour intensive and higher throughput method compared to current imaging-based strategies for studying EV uptake mechanisms.

Approach	Cell-based	Cell-free
	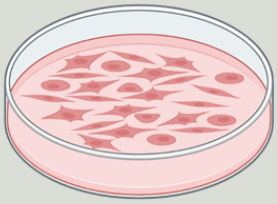	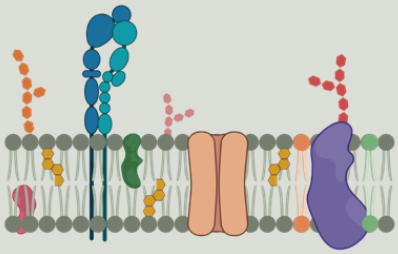
Advantages	• Complete native state • Study intracellular fate • Phenotypic screening	• No need for aseptic conditions • Study membrane molecular mechanisms in isolation • Compatible with scalable sensing technologies
Limitations	• Need for aseptic technique • Highly complex: Difficult to study different cellular parts in isolation • Many complementary sensing techniques are not scalable	• "Only" captures the cell membrane • Cannot study intracellular fate

Figure 1.8: Comparison between cell-based and cell-free approaches for studying EV function. Made with Biorender.com

1.2.6 Organic bioelectronics: a new frontier

The field of organic electronics has progressed enormously since the initial discovery of conducting polymers[22] and has recently gained widespread applications in biomedical research[23–25]. Electroactive polymers have recently come to the fore as a highly promising electrode material providing a biomimetic, hydrogel-like environment, thus merging the critical parameters of 'cushioning' and 'sensing' in one substrate. These materials also have lower impedance, which results in higher conductance. In particular, a class of electroactive material known as organic electronic materials, have been proven to meet key challenges in the biomembrane-sensing arena. Organic electronic materials have proven to be superior to traditional inorganic materials, in improving the communication with biological tissues by providing a more mechanically compliant surface to interface with soft biological structures.[186–188] The integration of biosystems with bioelectronics enables the use of electrical methods for biological sensing and, as such, adds to the toolbox of sensing technologies.[189] Electrical methods for biological sensing are considered advantageous, in particular due to the fact that they are label-free, produce continuous readouts, and are less expensive and time consuming than optical methods.[190] Moreover, they are compatible with highly parallelised microfluidic platforms toward assay multiplexing.[167] Conducting polymers (CPs) have proven to be ideal for bridging the worlds of biology and electronics.[183] The CP poly(3,4-ethylenedioxythiophene) doped with poly(styrene sulfonate) (PEDOT:PSS) has been

by and large the material of choice due to its excellent stability and easy processability.[191] When in contact with aqueous biological environments, PEDOT:PSS swells, providing a biocompatible hydrogel-like interface for biosystems.[190] and exhibiting a large volumetric capacitance,[192] while preserving mechanical and electrical properties.[184,191,193] This property of PEDOT:PSS allows ions from the electrolyte to penetrate into the polymer and compensate electronic charges, changing its doping state over the entire volume and modulating its conductance. As such, PEDOT:PSS exhibits a large volumetric capacitance, a low electrical impedance, and both high ionic and electronic conductivity, which enables the sensing of biological events with great sensitivity.[184,194] Furthermore, the substrates remain compatible with conventional analytical techniques, e.g. QCM, AFM, surface zeta potential, and fluorescence microscopy (given the transparency of the underlying support).[195]

1.2.6.1 Multielectrode arrays (MEAs)

A relatively simple use of CPs for biosensing has been their integration into multielectrode arrays (MEAs) as a coating on the electrode. The MEA electrode serves as the working electrode in a setup with a reference and a counter electrode all in direct contact with a physiologically relevant electrolyte, e.g. PBS (**Figure 3.1b**), and, therefore, are compatible with EIS measurements. In EIS, a small voltage oscillating in a range of frequencies is applied between the counter and working electrodes. This technique measures the frequency-dependent impedance of the electrode and electrolyte, which can be described as their AC response to the voltage-induced ionic flow, typically exhibiting both capacitive and resistive components. Addition of an insulating layer between the counter and the electrode, such as an SLB or cell monolayer, alters the impedance characteristics of the system.

EIS is a useful technique to characterise the functional and physical properties of biosystems. In electrochemistry, impedance, $Z(\omega)$, is the complex resistance encountered when current flows through a circuit made of resistors, capacitors, or a combination of these two. By applying an alternating current (AC), a series of $Z(\omega)$ data are obtained over a range of frequencies, typically between 1×10^{-1} - 1×10^{5} Hz. The obtained impedance data is often treated in two convenient ways: the Nyquist plot, in which the imaginary component of impedance, $Z''(\omega)$, is plotted against the real component, $Z''(\omega)$. The second being the Bode plot, in which absolute values of impedance or phase shift are plotted against the frequency. This data enables the characterisation of the electric properties of these membrane models (surface electrodynamics) elucidating the properties of the interface. Furthermore, the resistance (or inversely the conductance) and capacitance properties of the insulating layer can be extracted using equivalent circuit modelling (EEC).[196] These EEC models are created to reproduce the parameters of the EEC elements and

the electrochemical spectral features. These parameters are compared to the physical properties of the surface systems and processes[197]. In this way, EIS can provide precise and fast monitoring of membrane-compound interactions.

For monitoring EV-membrane interactions, one would expect to see a shift in the Bode plot around the mid-frequency range (Figure 1.9a). This indicates that there is a stronger barrier to the movement of ions through the membrane and into the PEDOT:PSS, which one would expect with EVs bound to the surface of the membrane. In the Nyquist plot (Figure 1.9b), the formation of a semicircle indicates that a barrier is present on the surface of the MEA, i.e. the SLB. The semicircle denotes that the SLB exhibits both resistive and capacitive elements depending on which end of the frequency one observes. The bindings of EVs to the surface of the SLB creates a larger semicircle, which, like on the Bode plot, indicates a more resistive barrier now being present.

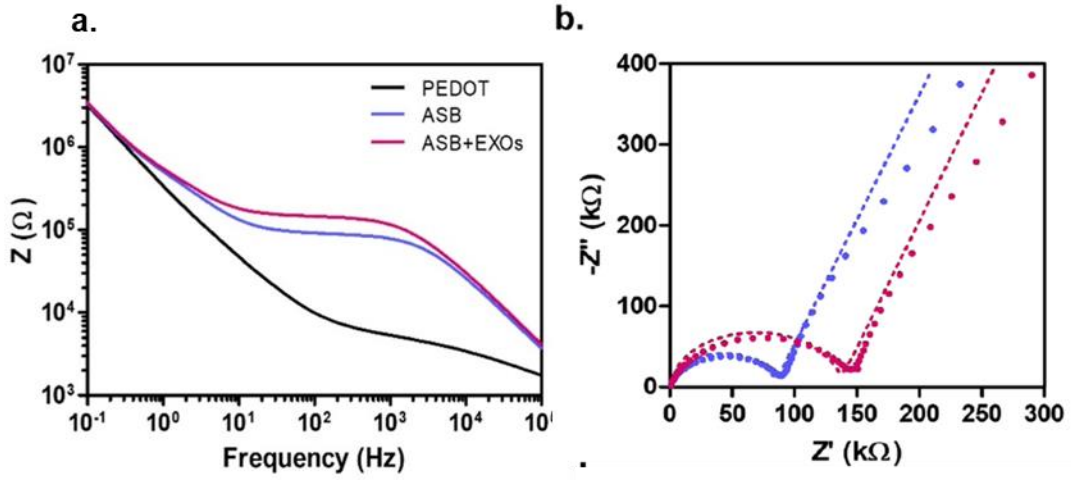

Figure 1.9: Electrical monitoring of EV binding to a supported lipid bilayer (called ASB here) using MEAs. Graphs taken from Chapter 4.

1.2.6.2 The organic electrochemical transistor (OECT)

Another CP device known as the organic electrochemical transistor (OECT) has become increasingly popular for transducing and enhancing biological signals, owing to their signal amplification properties.[198] OECTs adopt a transistor three-terminal configuration consisting of source and drain, on either side of a conducting polymer channel, and one gate electrode that controls the channel conductivity (**Figure 3.1b**). Belonging to the broader class of "electrolyte gated transistors", OECTs operate in direct contact with an electrolyte.[199] Their operation relies on ions being "pushed" into the conducting polymer channel upon application of a gate bias, changing its doping state, hence its conductivity.[200] Application of a positive gate bias promotes the removal of holes from PEDOT chains, which drives cations from the electrolyte to compensate the

negatively charged PSS– chains. The coupling between ionic (from the gate electrode) and electronic (from the drain electrode) charges within the entire volume of the conducting polymer channel is a particularly interesting feature of this device configuration with record high signal amplification values that scale with the volume of the channel.[201] As such, small changes in the ionic current flowing into the polymer channel to modify its doping state result in large changes in the electronic current flowing in the channel. This local signal amplification allows for high sensitivity sensing, which is ideal for unravelling biological information.[190] Hence, OECTs, have been widely considered as especially promising biological signal amplifiers[202] without necessitating the incorporation of external circuits. Moreover, PEDOT:PSS deposited as thin films on transistor channels is optically transparent, making it compatible with microscopy, thereby enabling simultaneous optical and electrical readouts,[129,130,203] pivotal in biological assays. The integration of PEDOT:PSS with bioelectronic devices has unlocked a myriad of biosensing applications.

The addition of an insulating layer (e.g. membrane or cells) between the channel and the gate affects the OECT gating efficiency, rendering the device slower to respond to a given applied gate bias.[204,205] The modulation of the device response time serves as a measure of the resistance of an integrated biosystem which in turn can be correlated to the biological phenomena at play. This is defined as the cut-off frequency, which corresponds to the frequency at 70.7% of the maximum transconductance, g_m,[206] and a figure of merit that defines the regimes of high and low ionic transport.[202] EIS provides a way to study fast events that are hard to measure in the time domain but easy to detect through impedance changes at high frequencies, while OECTs provide a way to miniaturize the devices without losing sensitivity.

1.2.6.3 Membrane-functional sensing using organic electronics

Traditionally, electrical characterisation of cell membranes (in whole-cell studies) has been performed using patch clamp electrophysiology, also used to study pore-forming behaviour of drugs, proteins, and other molecules.[207,208] Patch clamp in whole cells suffers in terms of time efficiency, robustness, and the need for sterility for cell culture, limiting the applications of this method. Patch clamp can be applied to SLBs,[209,210] however, the intricate, technically challenging nature of the method still limits implementation outside of the research laboratory environment.

Measurement of electrical properties of membranes provides a wealth of information on their function. The homeostasis of cells requires control over the ion flux across the membrane and loss of membrane potential leads inevitably to cell death. The highly insulating nature of lipids, combined with mediated flux of different ions by membrane proteins, means that electrical measurements can assay the function of these components. Membrane-targeting drugs, toxins,

pathogens, and EVs exert their effects through blocking ion channels, inserting pores, and binding to receptors in the membrane, all actions that result in electrical changes in the membrane. Electrical properties of cell membranes can be assessed through formation of SLBs on electrically conducting substrate using electronic methods, including EIS.[211]

In the context of membrane sensing, both synthetic and native SLBs have been formed on PEDOT:PSS-based bioelectronic devices, including both electrodes and OECTs, using SALB [189] and vesicle fusion[130,137,184] methods. As the lipid bilayer modulates the ionic current flux sensed by the electrode, the electrical sealing properties of biomimetic lipid bilayers formed on PEDOT:PSS electronic devices may be characterised via EIS to derive the membrane resistance and capacitance. These parameters are a measure of membrane integrity and sealing, and, as such, treatment with lipid bilayer-disrupting agents[189] or pore-forming compounds[184,189] cause a decrease in transmembrane resistance, indicating an increase in bilayer 'leakiness'. OECT-based measurements have also been used as a figure of merit of SLB sealing properties, transducing and quantifying conductance changes of transmembrane protein in native membranes,[204] and offer the added advantage of allowing dual optical and electrical readouts.[130] Given its hydrogel-like properties, PEDOT:PSS acts as a cushion to facilitate the mobility of membrane components and thus preserves, to a greater extent, the native structural and functional properties of the cell membrane,[189] as opposed to rigid, solid supports.[181] In fact, PEDOT:PSS has already proven ideally suited for hosting TMPs within lipid bilayers,[130,184,189] achieving protein mobility comparable to other polymer-cushioned surfaces.[137] Applications include functional readouts of transmembrane proteins in their native environment, including sensing of ATP gating of P2X2 ion channels in mammalian cell-derived lipid bilayers[137] and screening of ligand gated TREK-1 ion channel activity in human-derived membranes.[130] This direct measure of membrane-compound interactions demonstrates the capability of bioelectronic platforms for studying the mechanisms of membrane-interacting agents.

1.2.6.4 Cell-functional sensing using bioelectronics

OECTs have been integrated with *in vitro* models of varying complexity spanning from plasma membranes to 3D complex cell cultures.[129,130,203,212–214] The OECT has been shown to operate stably long term in a variety of different electrolytes, including complex cell media,[190] which makes it suitable for a wide spectrum of biological applications from monitoring barrier tissue integrity,[205,213] cell coverage,[215] and differentiation[194] to biochemical and enzymatic sensors[190] in 2D cultures. In addition, CP scaffolds have been used to support and monitor cell growth in 3D cultures.[216–218] PEDOT:PSS-based OECTs have been used to monitor cell coverage and differentiation, as well as epithelial barrier integrity both in Transwell format and with cells

adhered directly on the device surface.[203,206,213,219] The latter involves the growth of a monolayer of cells on the channel and the gate, which introduces a barrier for ion motion in the electrolyte (cell culture media), directly affecting the transistor output and in effect using the OECT as an impedance biosensor.[213,220] Monitoring tight junction modulation, nephrotoxicity, cancer invasion, wound-healing, and toxicology[212,213,221–223] are only some of the various application areas where impedance-based OECTs interfaced with cell cultures have been successfully used for biomedical research, although biological validation of the electrical readouts has been limited in scope to date.

1.2.6.5 A new tool for EV research

Current applications of electrochemical-based methods to EV research include vesicle isolation strategies[224] and biomarker detection[225] and quantification assays,[226,227] which do provide advantages to conventional analogous techniques.[228] However, the utilisation of electrochemical biosensing techniques to the study of EV function are lacking. To elevate this field and increase impact, focus needs to be placed on improving the sensing capabilities for these models, as well as their translational capabilities, areas where bioelectronic materials and technologies can play a major role.[229,230] Organic electronic devices integrated with cell-based or cell-free models can provide high content information on the function and MoA of EVs. Given the scalability of SLBs integrated with bioelectronic devices, quantifying the dynamics of EV-membrane interactions could help elucidate the prevalent uptake mechanisms of distinct EV subpopulations and implicate the involvement of specific membrane subdomains faster compared to optical methods. This would allow the relationship between the physicochemical properties of EVs and their preferential uptake route to be revealed. This holds promise for the development of therapeutic strategies that act on a defined population of EVs or on a specific EV internalisation channel to block EV uptake in the context of treating EV-associated pathologies. Furthermore, developing phenotypic screening assays using organic electronic devices could provide novel high-content readouts and enable real-time, non-invasive monitoring of EV-induced changes to cell phenotype. Hereto, the potential for high-throughput operation by running multiple devices in parallel simultaneously could allow for rapid screening of therapeutic compounds against EV function in pathologies.

1.3 Aims and objectives of this dissertation

The aim of this thesis was to develop *in vitro* bioelectronic platforms for investigating EV function in cancer metastasis and for drug discovery. To achieve this goal, this dissertation is divided in the following objectives:

1. Compare EV isolation methods by characterising EV samples and identify the most fit-for-purpose method
2. Integrate supported lipid bilayers derived from mammalian cells onto CP-based electronic devices for investigating particle interactions at the plasma membrane and screening compounds that inhibit EV binding
3. Develop a phenotypic screening platform based on OECTs for monitoring TEV-induced EMT in non-malignant cells in real-time and for testing anti-metastasis drugs
4. Orthogonal validation of electrical readouts using established biomolecular assays and fluorescence microscopy

1.4 Supervision and collaborations

The work presented in this dissertation was performed as several projects within the BioElectronic Systems Technology group (BEST group) at the Department of Chemical Engineering and Biotechnology (CEB) of University of Cambridge, UK, under the supervision of Professor Róisín M. Owens.

1.4.1 Publications relevant to this work

1. A.-M. Pappa, H.-Y. Liu, **W. Traberg-Christensen**, Q. Thiburce, A. Savva, A. Pavia, A. Salleo, S. Daniel, R. M. Owens, Optical and Electronic Ion Channel Monitoring from Native Human Membranes. ACS Nano (2020)

   This paper includes the work described in Appendix 1, section 8.8
2. T. Tang, A. Savva, **W. C. Traberg**, C. Xu, Q. Thiburce, H.-Y. Liu, A.-M. Pappa, E. Martinelli, A. Withers, M. Cornelius, A. Salleo, R. M. Owens, S. Daniel, Functional Infectious Nanoparticle Detector: Finding Viruses by Detecting Their Host Entry Functions Using Organic Bioelectronic Devices. ACS Nano 15, 18142–18152 (2021).

   This paper includes the work described in Chapter 3
3. A. K. Jayaram, A. M. Pappa, S. Ghosh, Z. A. Manzer, **W. C. Traberg**, T. P. J. Knowles, S. Daniel, R. M. Owens, Biomembranes in bioelectronic sensing. Trends in Biotechnology (2021)

   This paper includes part of the literature review presented in Chapter 1
4. J. Uribe, **W. C. Traberg**, A. Hama, V. Druet, Z. Mohamed, A. Ooi, A.-M. Pappa, M. Huerta, S. Inal, R. M. Owens, S. Daniel, Dual Mode Sensing of Binding and Blocking of Cancer Exosomes to Biomimetic Human Primary Stem Cell Surfaces. ACS Biomater. Sci. Eng. (2021)

   This paper includes the work described in Chapter 4

5. **W. C. Traberg**, J. Uribe, V. Druet, A. Hama, C-M. Moysidou, M. Huerta, R. McCoy, D. Hayward, A. Savva, A. M. R. Genovese, S. Pavagada, Z. Lu, A. Koklu, A.-M. Pappa, R. Fitzgerald, S. Inal, S. Daniel, R. M. Owens, Bioelectronic platform for real-time phenotypic screening identifies heparin as an inhibitor of extracellular vesicle-driven metastasis. *Submitted*. Preprint available: https://doi.org/10.21203/rs.3.rs-1697648/v1

This paper includes the work described in Chapter 5

1.4.2 Collaborations

The work was performed in collaboration with the Daniel Research Team lead by Professor Susan Daniel at the Robert Frederick Smith School of Chemical and Biomolecular Engineering of Cornell University, USA, the Organic Bioelectronics Laboratory lead by Professor Sahika Inal at King Abdullah University of Science and Technology (KAUST), SA, the Fitzgerald Group lead by Professor Rebecca Fitzgerald at the Early Cancer Institute, University of Cambridge, UK, Dr. Anna-Maria Pappa at the Department of Biomedical Engineering, Khalifa University of Science and Technology, UAE, and the Salleo Research Group lead by Prof. Alberto Salleo at the Department of Materials Science and Engineering at Stanford University, USA. The vast majority of the experimental work presented in this dissertation was carried out at the Department of Chemical Engineering and Biotechnology, University of Cambridge, with some studies conducted at Cornell University. Contribution is stated where any work was conducted and/or results produced in conjunction with collaborators. The following facilities were also used:

- Cambridge Advanced Imaging Centre for transmission electron microscope imaging
- Cambridge Veterinary School for nanoparticle tracking analysis

1.5 Organisation of the thesis

The work described in this dissertation is divided into the following chapter and appendices:

- *Chapter 1*: provides a general introduction of the scope of the project and a literary background content of the work commenced. General administration information is also included.

- *Chapter 2-5*: the central chapters outlining and discussing experimental findings:

  - *Chapter 2*: describes EV isolation method comparison studies and showcases commonly used EV characterisation techniques. A rational for testing and selecting the best fit-for-purpose isolation method is also presented.

- *Chapter 3*: describes the optical assessment of biomembrane formation and the electrical detection of virus fusion to biomembranes using OECTs. Given the inherent similarities between viruses and EVs, this work advances the use of biomembranes integrated with organic electronic devices for investigating particle and molecular interactions at plasma membrane and laid the foundation for the work presented in chapter 4.

- *Chapter 4*: describes the optical assessment of biomembrane formation and the dual optical and electrical detection of binding and blocking of TEVs to biomembranes integrated with organic electronic devices and discusses the utility of cell-free screening.

- *Chapter 5*: describes the real-time monitoring of TEV-induced EMT using OECTs over a 9-day period and the orthogonal validation of the electrical readouts using on-chip and end-point biomolecular techniques and assays. Further, it describes the use of OECT-based phenotypic screening for identifying heparin as a TEV-targeting, anti-EMT drug. It also presents the facile drug response modelling enabled by the platform and provides a rational for using bioelectronic technologies in preclinical drug discovery.

- *Chapter 6*: present final conclusions derived from the current work and plans for future work.

- *Appendix A*: provides a full list of materials and describes the methods used in the experimental work, where such methods were consistent across different projects.

- *Appendix B*: provides additional data to support the main findings presented in chapters 2-5.

“If you wish to make an apple pie from scratch, you must first invent the universe.”

— *Carl Sagan*

2 Comparison of Extracellular Vesicle Isolation Methods

2.1 Introduction

Studying EV function is somewhat curtailed by the technical challenges of working with and successfully isolating EVs, owing to their small size, limited quantities, heterogeneity (size and compositional), and biochemical complexity.[81] EV isolation entails a degree of purification; meaning separation from other EV subtypes and/or non-EV components (i.e. specificity), and enrichment; referring to increasing EV concentration by some metric (i.e. recovery).[70] Conventional isolation protocols are prone to co-isolation of contaminants with comparable features to EVs,[77,78] as well as non-EV-associated soluble factors[76] that may contribute to a suspected EV function[231]. EV proteomic profiles have been found to be highly dependent on the isolation protocol used[22] and some isolation methods may enrich for multiple, functionally distinct EV subtypes[84] with diverse compositions.[232] Furthermore, choice of isolation method and the resultant particle size distribution of EVs seemingly affects their functional potential in terms of rate of cellular uptake and the magnitude of the elicited cellular response.[233] All these factors result in an isolation method-dependent EV function, where observed downstream activities are, in effect, contingent on the isolation strategy employed.[72,234]

2.1.1 EV isolation and purification

As EV subtypes may share similar biophysical and/or biochemical features and given the propensity of non-EV-associated components and molecules to co-isolate,[81] a one-size-fits-all isolation strategy is inadequate when studying EV function. Differential ultracentrifugation (UC)-based isolation protocols remain the most popular among researchers[19,235] despite various flaws,[95,236–238] although UC should not be singled out as the only culprit among the myriad of methods that exist.[72] It should be noted that EVs and soluble factors may have combinatorial effects on cells.[231] Additionally, if it is the case that only a minor subset of EVs facilitate a given functional activity, the abundance of non-functional EVs may undermine the detection of their active role. However, the question remains of whether EV subtypes in isolation function differently from a heterogeneous EV mixture and indeed if such an observed function is even physiologically relevant.[76]

Ultimately, EV isolation is a compromise between recovery and specificity, and choice of isolation protocol depends on the experimental question and EV end use, as well as the complexity of the starting sample, e.g. tissue culture-conditioned media vs. biological fluids.[239] It should be noted that preserving EV function during isolation so as to not negatively impact downstream applications is an important factor to consider as choice of isolation method may impact EV function.[240]

2.1.2 Biophysical and biochemical EV characterisation

EV preparations are typically characterised in a quantitative and/or qualitative manner by multiple, complementary techniques to assess purity and concentration, distinguish subtypes, and attribute function. Biophysical analyses include measures of particle size, concentration and charge, and assessment of structure in bulk preparations (e.g. nanoparticle tracking analysis) and at a single vesicle level (e.g. electron microscopy). Biochemical analysis produces information on EV composition, revealing the presence, topology, and quantity of biomolecular components associated with the EVs.[70] A combination of techniques is preferable to overcome the technical challenges of detecting and characterising EVs,[241] and to increase measurement accuracy.[242] Together, the biophysical and biochemical data shed light on the EV subtype,[232,243–245] i.e. intracellular origin and phenotype,[82,246] which provides information on the functionality of the EVs and is dependent on the cell of origin and its pathological state.[22]

To ascertain the best fit-for-purpose isolation method, a comparison of three different methods was conducted using UC, size-exclusion column (SEC) chromatography, and a commercial precipitation reagent (Exo-kit). EV isolates were characterised by dynamic light scattering (DLS), nanoparticle tracking analysis (NTA), transmission electron microscopy (TEM), and Western blot to assess EV size distributions, particle concentration, protein content, and enrichment of EV biomarker CD9. EVs were derived from non-malignant HEK-293 cells (HEK-EVs).

2.2 Materials and methods

2.2.1 Cell culture

HEK-293 cells were used for the studies described in this chapter. Cell culturing is described in detail in Appendix A, section 8.1.

2.2.2 EV production and harvesting

Once confluent, cells were washed twice in PBS to thoroughly remove foetal bovine serum (FBS)-containing culture medium and replaced with serum-free culture medium to avoid carryover of serum-associated EVs. The conditioned medium (CM) was collected after 48 h and centrifuged at RT; 200 *x g* for 10 min followed by 2 000 x *g* for 10 min to remove intact cells, apoptotic bodies, and cell debris,[247] leaving 0.5 mL liquid after each supernatant extraction.

EV shelf-life and storage: Isolated EVs were used within 3 days of isolation to mitigate the risk of vesicle aggregation and protein degradation. Samples were also imaged fresh to prevent

any perturbation of the vesicle structure caused by freeze-thawing, although studies have shown that prolonged storage at -80 °C and multiple freeze-thaw cycles should not compromise EVs.[248]

2.2.3 Size exclusion chromatography (SEC)

CM was concentrated using an Amicon® Ultra-15 Centrifugal Filter Unit with a 100 kDa nominal molecular weight limit (Millipore). This step also removed non-vesicular macromolecules. The filter units were spun at 3 500 x *g* until ~200 µl liquid remained above the filter. The ultrafiltration (UF) retentate was allowed to remain atop the filter for 30 min to ensure that EVs did not remain stuck to the membrane before collecting the sample. The retentate was passed through a qEVoriginal / 35 nm size exclusion column (Izon Science), as per the manufacturer's instructions, to purify EVs between 35-350 nm. A 1.5 ml fraction was collected after discarding the void volume (3 ml) to obtain the purest sample of EVs with least protein carryover.

2.2.4 Ultracentrifugation (UC)

sEVs were isolated from CM by successive centrifugation at 4 °C; 20 000 x *g* for 1 h to pellet out larger EV, e.g. MVs (150-1 000 nm), and 100 000 x *g* for 4 h to pellet out sEVs, e.g. exosomes (30-150 nm) using a Type 50.2 Ti Fixed-Angle Rotor; Beckmann XL-90 Ultracentrifuge. Pellets were resuspended in 200 µl phosphate buffered saline (PBS).

2.2.5 EV precipitation kit

A precipitation buffer was added to the CM and centrifuged to pellet out EVs, which were resuspended in suspension buffer using miRCURY Exosome Cell/Urine/CSF Kit (Qiagen), as per manufacturers' instructions.

2.2.6 EV characterisation

EV characterisation methods are described in detail in Appendix A, section 8.2

2.3 Results and discussion

2.3.1 Particle size measurement by DLS

The three different EV isolates from HEK cells were characterised by DLS, producing size distribution plots (**Figure 2.1**). The intensity plot describes the amount of light scattered by the particles and is heavily biased towards large particles, as there is a 6^{th} power relationship between intensity of light scattered and particle diameter. The multiple peaks observed in all samples indicate the presence of different sized particles. The volume distribution is a computed value and

shows the volume of particles as a function of their size. Here, the smaller particle size peaks are more prevalent, which indicates that they are more numerous compared to the larger particles. Tellingly, the volume plot for Exo-kit shows only one peak at ~7 nm, most likely caused by the presence of macromolecules, indicating that only a small number of EV-sized particles were present in the isolate.

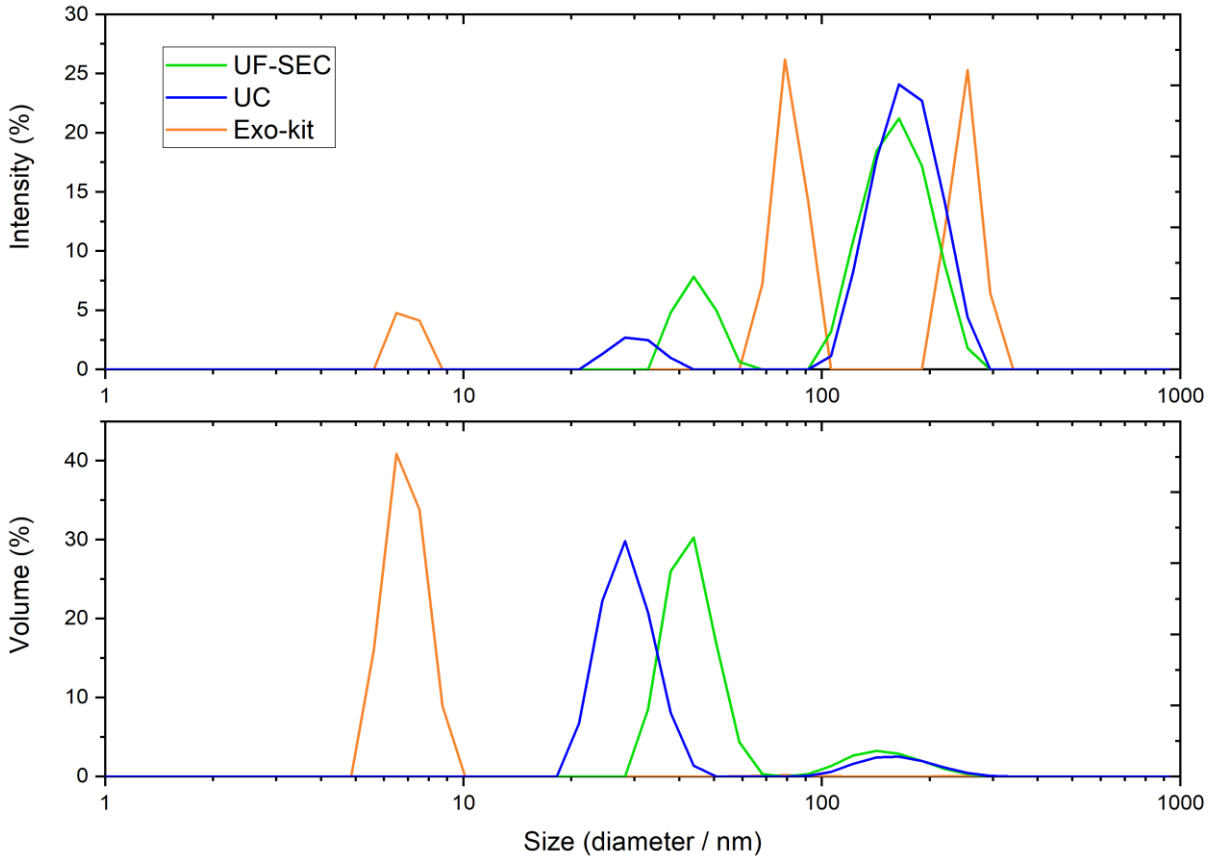

Figure 2.1: Size distribution plots of EV isolates. (**Top**) Size distribution by intensity and (**bottom**) by volume percentage, mean, n=2. Peaks corresponding to EVs at ~30-45 nm and ~155-175 nm for UC and UF-SEC, and at ~80 nm and ~250 nm for Exo-kit. UF-SEC: Ultrafiltration-size exclusion column, UC: ultracentrifugation.

Peaks that could correspond to sEVs and larger EVs are seen for all samples. UC and SEC performed comparatively, whereas the Exo-kit did not. The polydispersity index (PdI) and count rate, measured as kilo counts per second, were assessed for each sample. PdI should be <0.3, where samples with PdI <0.1 are considered to be monodispersed. UC and Exo-kit samples had PdI >0.3, indicating a high degree of heterogeneity in particle sizes, whereas the SEC sample had a PdI of 0.275. UC had the highest count rate with 169.0 kcps, compared to 28.6 kcps and 11.3 kcps for SEC and Exo-kit, respectively, indicating the highest EV yield was obtained by UC.

2.3.2 Protein detection by Western blot

Protein immunoblotting was performed to detect the presence of CD9, an EV biomarker expected to be enriched in EV preparations, and calreticulin, a protein found in endoplasmic reticulum and therefore not expected to be enriched in EV preparations (**Figure 2.2**).

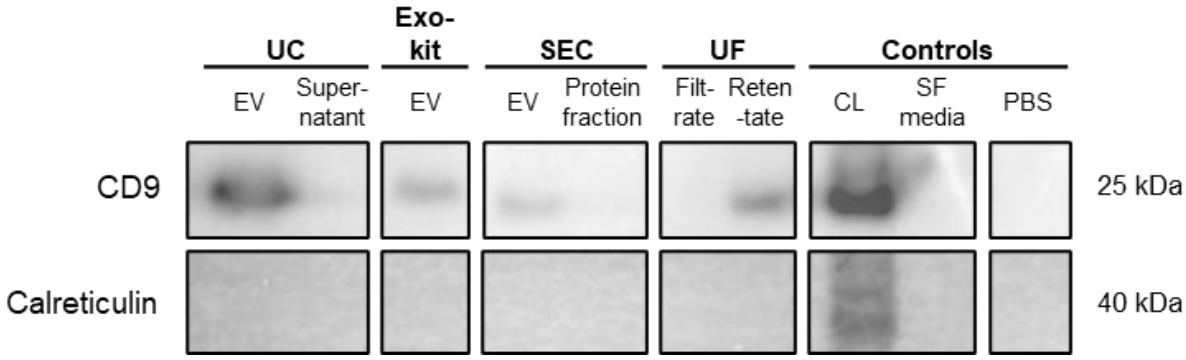

Figure 2.2: Immunoblots of HEK-293 whole-cell lysate and HEK-EV isolates. Equal amounts of protein (25 μg) were loaded and then separated on SDS-PAGE gels and membranes were blotted with indicated antibodies, n=1. CD9, predicted: 25 kDa, and calreticulin, predicted: 55 kDa (other bands may indicate presence of dimers and multimers). Unedited immunoblots are available in Appendix B (Figure S8.3 and Figure S8.4). UC: ultracentrifuge EVs, Exo-kit: Commercial precipitation reagent EVs, SEC: size exclusion column EVs, UF: ultrafiltration, CL: cell lysate, SF: serum-free.

The EV samples (including the UF retentate) show positive bands for EV marker CD9. UC-EVs produces the highest intensity band while SEC-EV produces the lowest. Interestingly, the UF retentate band is not positive for calreticulin indicating that non-EV associated proteins are effectively removed from the CM by UF. As expected, CL is positive for both markers and SF media is not.

2.3.3 Single vesicle characterisation by TEM

Next, EV samples were imaged by TEM to resolve their morphology and size (Figure 2.3), revealing EVs with rounded morphologies that fall under the size ranges expected. UC produced the most numerous amounts of EVs, while the Exo-kit yielded very few EVs. EV aggregates are visible (Figure 2.3**b,e**), which may affect the measured size distribution of these samples and potentially also their bioactivity and bioavailability in the context of uptake and cargo delivery in recipient cells. Interestingly, large artefacts were found in the SEC sample (Figure 2.3**c**), which are much too large to be EVs, while still exhibiting a darkened area around its periphery much like EVs, due to the interaction of the lipid bilayer with the uranyl acetate staining. It is curious that such large structures should pass through the qEV35 size exclusion column. Other odd-shaped/sized vesicles were also found in the SEC isolate (**Figure S8.5**). Particle size is more accurately captured by TEM, but distinguishing EVs from non-extracellular vesicles, such as

liposomes or other lipid structures, is difficult. Size and morphology may aid this to some extent, as lipids structures may have irregular, non-spherical morphology, but immunogold labelling EVs prior to TEM allows vesicle type/origin to be determined more precisely, as only EVs expressing the protein marker are labelled.[249] This was performed for EVs derived from MDA-MB-231 cells showcased in section 5.3.1, **Figure 5.2**.

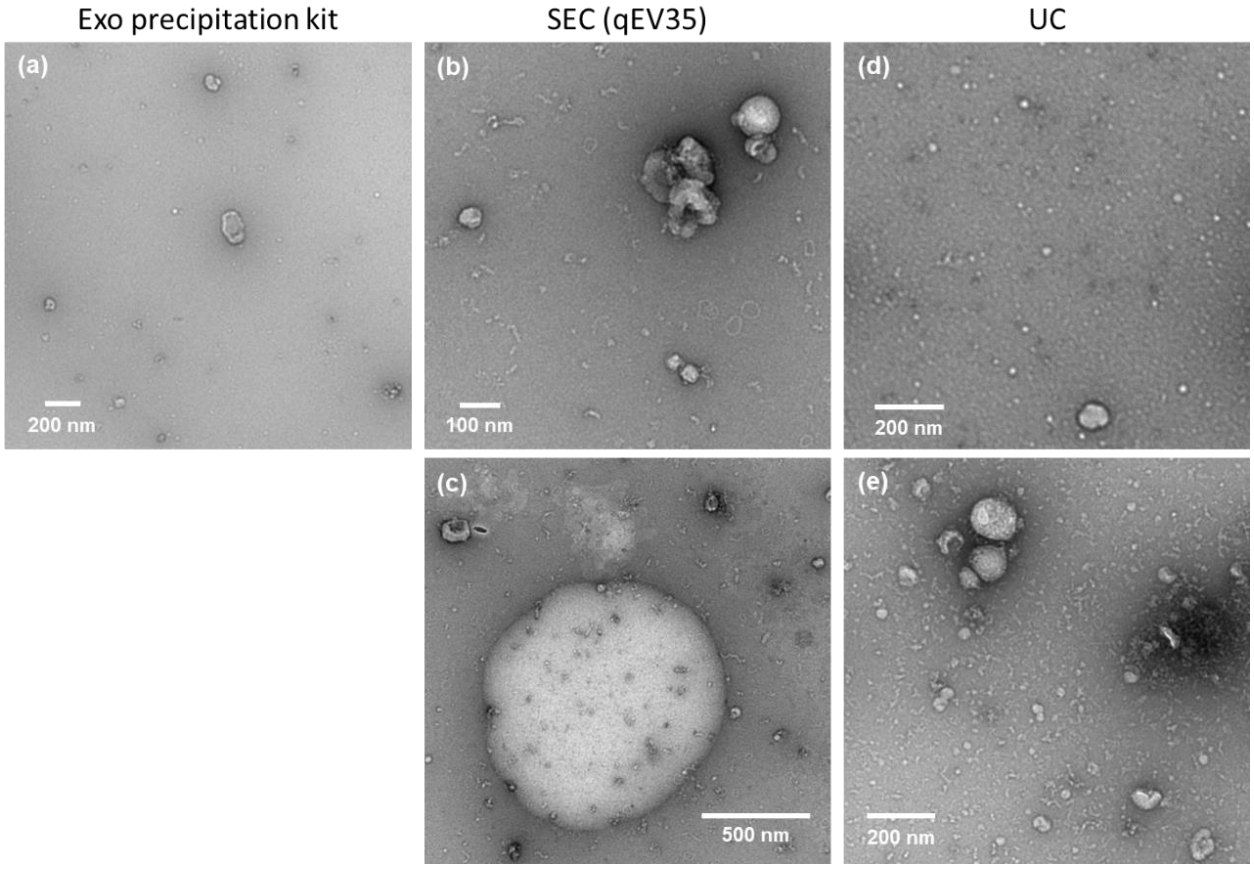

Figure 2.3: TEM micrographs of EV isolates. EVs isolated by Exo-kit (**a**); SEC (qEV35) with close-up of EVs (**b**) and a large artifact >1 μm in diameter (**c**); and UC with a wide-field view (**d**) and a close-up view (**e**) of EVs. n=2.

2.3.4 Yield versus purity: UC versus SEC isolation methods

HEK-EVs isolated by UC and SEC were analysed using NTA and unlysed protein content to compare the relative yield and purity attained by each method. HEK-EVs isolated by SEC exhibit a prominent peak at ~50 nm (Figure 2.4**b**), which is almost absent in the UC sample (Figure 2.4**a**), indicating that SEC isolation leads to purification of sEVs. Interestingly, SEC seemingly produces a much wider distribution of particle sizes compared to UC. From protein quantification (Figure 2.4**c**), it is apparent that the SEC sample contains less protein (~7-fold), while the total EV concentration is ~13-fold higher in the UC sample (Figure 2.4**d**). To assess the sample purity attained by each method, the ratio of protein to particles was compared and found to be 15.4 and 26.9 μg protein to billion particles for UC and SEC, respectively (Table 2.1); a 1.7-fold difference

in protein content. Surprisingly, SEC produced a lower particle-to-protein ratio than UC, although it purportedly should remove more non-EV associated proteins. An explanation could be that the collected samples contained both EV and protein fractions as the protocol was not optimised enough, or that the sEVs more prominent in the SEC isolation are richer in membranous proteins.

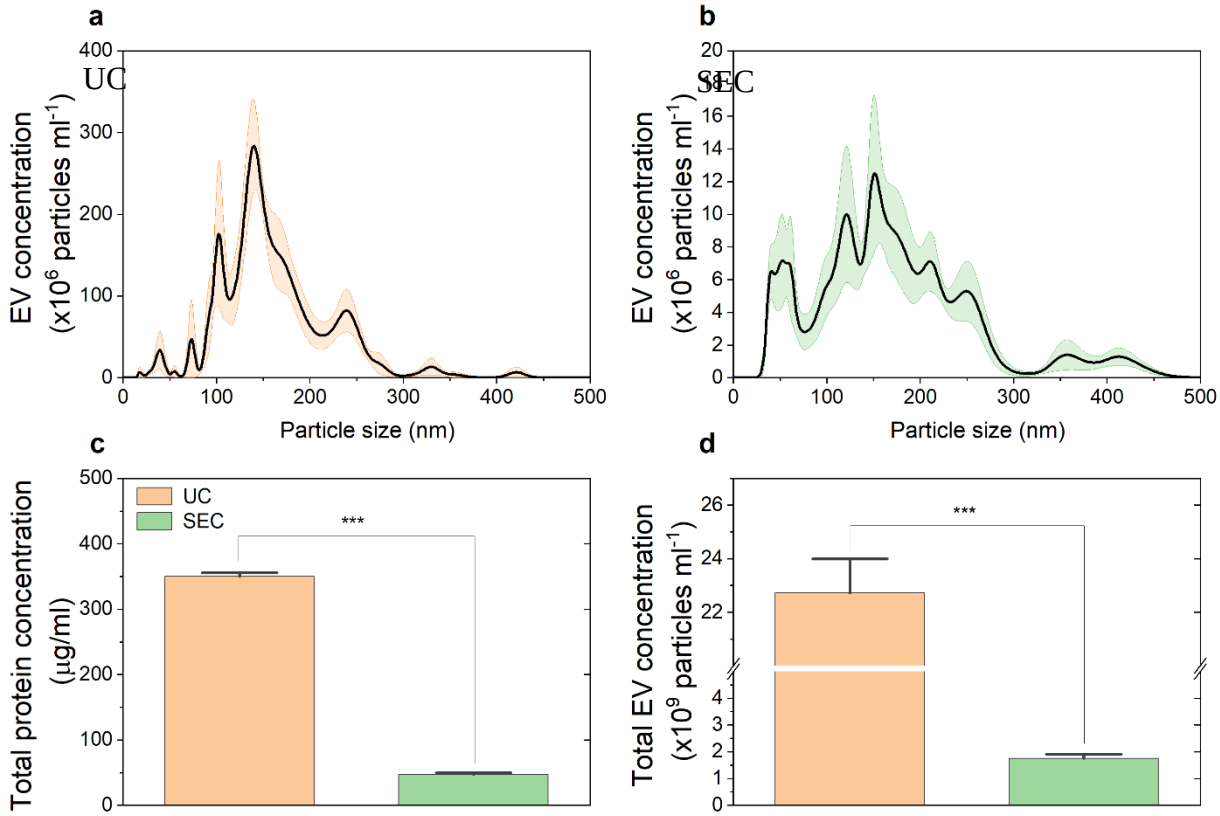

Figure 2.4: Comparison of HEK-EVs isolated by UC and SEC (qEV35). Particle size distribution plots of (**a**) UC- and (**b**) SEC-derived HEK-EVs from NTA, mean ± s.e.m (s.e.m. indicated by shaded areas), n=5 measurements from one sample. (**c**) Total protein concentration of EV samples, mean ± s.e.m, n=3. (**d**) Total EV concentration of EV samples from NTA, mean ± s.e.m. *** p≤0.001.

Isolation method (HEK-EVs)	**Size (nm)**	**Concentration (particle ml^{-1})**	**Protein content (µg ml^{-1})**	**Ratio of million particles to µg protein**
UC	**161.9 ± 3.5**	**2.27 x 10^{10} ± 8.48 x 10^{8}**	**350.0 ± 3.5**	**64.9**
SEC (qEV35)	**174 ± 9.8**	**1.75 x 10^{9} ± 1.06 x 10^{8}**	**47.1 ± 2.1**	**37.2**

Table 2.1: Comparison data of HEK-EVs isolation by UC and SEC.

2.4 Conclusion

A comparison of Exo-kit, UC, and SEC by particle size distribution, immunoblot, and TEM micrographs reveals that the Exo-kit isolates a very low number of EVs and likely co-isolates macromolecules. UC and SEC, on the other hand, isolate EV samples within expected sizes ranges

that are enriched in the EV biomarker CD9. TEM also showed EVs with expected morphology, although SEC curiously led to isolation of giant vesicle-like structures. Immunoblotting against CD9 revealed that UC had the highest intensity band while SEC had the lowest, indicating a higher concentration of EVs in the UC isolate. This is further supported by the higher count rate from DLS measurements, but here UC had a higher polydispersity index than SEC.

Excluding the Exo-kit from contention, particle concentration and total protein amount was assessed in UC and SEC isolates. Surprisingly, SEC produced samples with higher protein-to-particle ratios than UC. Furthermore, the particle concentration was more than one order of magnitude greater in the UC sample (~13-fold) compared to the SEC samples. The only caveat being that physical-based isolation techniques, where high forces are applied, such as UC, may cause vesicle deformation, breakage, and aggregation. This may in turn adversely affect downstream applications where EVs must be functionally active, but studies indicate that enough EVs do remain functional.[247,250] For subsequent functional studies, EVs were required to elicit an effect in recipient cells and compromising EV yield may prevent detection of any such effect. Therefore, UC was selected as the preferred EV isolation method going forward to ensure that large quantities of EVs were obtained.

“The Stone Age didn't end because the World ran out of stones”

— Niels Bohr

3 ELECTRICAL DETECTION OF VIRUS FUSION TO SLBS

Preamble

This chapter contains work published by T. Tang, A. Savva, W. C. **Traberg**, C. Xu, Q. Thiburce, H.-Y. Liu, A.-M. Pappa, E. Martinelli, A. Withers, M. Cornelius, A. Salleo, R. M. Owens, S. Daniel, Functional Infectious Nanoparticle Detector: Finding Viruses by Detecting Their Host Entry Functions Using Organic Bioelectronic Devices. ACS Nano. 15, 18142–18152 (2021). Where relevant to this thesis, figures and text have been included, and where not relevant, reference has been made to the publication.

3.1 Introduction

EVs and virus share many similarities, both in form and function. Structurally, enveloped viruses and EVs are both lipid-delimited particles with complex membrane and cargo compositions of proteins and nucleic acids.[75] Their initial interactions with the cell membrane constitute the first step in eliciting a functional effect in recipient cells and is thus of great interest to the study of their function and for the development of attenuation/blocking strategies. For this reason, the development of a bioelectronic platform integrated with biomembranes for detecting virus fusion was pursued. Furthermore, this chapter introduces synthetic SLBs and SLBs derived from native biomembranes as models of the cell plasma membrane and describes the development of such membranes on electrical devices for functional studies of interactions at the membrane. SLBs integrated onto planar substrates are compatible with several surface-sensitive analytical techniques. In the studies described here, the optical methods used were FRAP for bilayer fluidity characterization[145,156] and total internal reflection fluorescence microscopy (TIRFM) to detect interactions such as nanoparticle binding[251–254] and blocking virus binding.[129,255,256] Lateral diffusion of components within the cell membrane is a fundamental process involved in many biological functions including binding and fusion of external particles[257–260]. For proper mimicking of the cell plasma membrane, the SLB should retain the fluidity of the cell membrane because it allows diffusion within its 2D plane,[260] influences binding avidity,[261] and facilitates lateral rearrangement of ligands to optimize binding.[262] Therefore, its assessment in SLBs is a crucial figure of merit for the utility of these models. Additional characterisation data of synthetic and native SLBs formed on PEDOT:PSS-coated surfaces and devices, as well as glass substrates is presented in Appendix B, chapter 8.8.

For membrane-enveloped viruses (e.g., influenza, SARS-CoV-2, ebolavirus, zika virus, etc.) to infect human cells, they must first bind to a specific receptor on the host cell surface, and then when triggered by an environmental cue, the viral membrane fuses with the host cell membrane to transfer the viral genome into the cell (**Figure 3.1a**).[263] This fusion process is facilitated by the glycoproteins embedded within the viral membrane envelope. While the details of viral entry are virus and cell-type specific, there are general themes surrounding entry mechanisms.[264] During membrane fusion, the composition of the host cell membrane changes as lipids and proteins from the viral envelope are mixed with the host membrane during hemifusion. Hemifusion is when the outermost leaflets of both membranes merge and form a connected stalk structure.[265] After the stalk structure ruptures forming a pore, the viral genome can be transferred across the host membrane and into the cytosol.

Recapitulating the conditions *in vitro* that support virus infection of a host cell and being able to detect these entry process-related changes on chip is an interesting approach for detecting an active virus based on its entry "signature". This signature is specific in that it depends on the presence of the right host receptor, the fusion trigger(s), and other environmental factors, such as proteases and ions present, which all depend on the particular virus. For example, influenza fusion occurs with membranes containing a sialic acid receptor and when triggered by a drop in pH. This represents the endosomal uptake pathway, where the low pH of the endosomal compartment triggers this fusion. Other viruses in this class, for example, coronavirus, bind different receptors and are triggered to fuse by specific proteases and require calcium ions. In contrast to nucleic acid detection approaches like PCR, which detect viruses based on genetic content, this approach detects for viral function and introduces a hitherto unseen level of specificity, as it can distinguish fusion competent virus particles from fusion incompetent particles. The ability to distinguish competent from noncompetent viruses is a key feature here and enables applications beyond detection, such as screening antiviral compounds for their ability to block virus entry in a highly sensitive and specific manner.

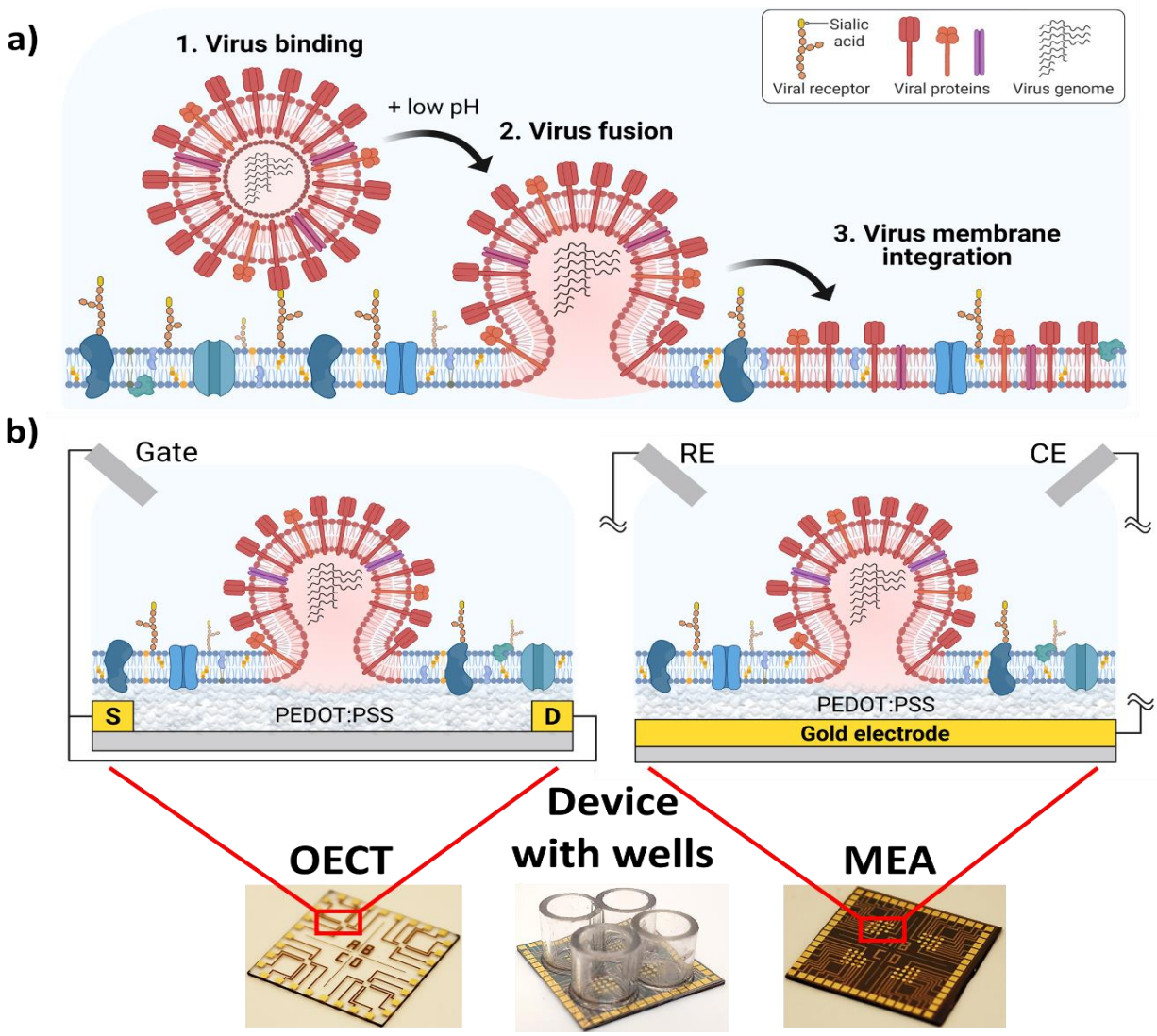

Figure 3.1: Diagram of virus fusion sensing strategy. (**a**) Schematic representation of enveloped viral entry processes, using influenza as the prototypical example.[266,267] Influenza binds a sialic acid receptor (yellow) on the host membrane, and influenza hemagglutinin (HA) proteins are triggered to induce viral–host cell membrane fusion upon exposure to low pH. During this fusion event, the viral envelope lipids and proteins (red) are mixed with the host cell membrane (blue), allowing the virus to release its genome. Note: image not drawn to scale. (**b**) Images of the electroactive platforms used in this study, OECTs (left) and MEAs (right), for scale, each device measures 2 cm × 2 cm. The OECT arrays, fabricated on glass, contain four different working areas that can be isolated with glass wells attached on the surface as shown in the image in the middle. Each working area contains four OECT channels covered with PEDOT:PSS, 50 µm length × 50 µm width. The MEAs were made on Si/SiO_2 glass with a similar design. Each of the four different working areas contained 15 round electrodes with 500 µm in diameter. The inset shows a schematic of the OECT and electrode sensing mechanism. The OECT consists of a CP channel in between a source (S) and drain (D) electrodes in contact with an electrolyte in contact with a gate electrode. The MEA has a CP formed on top of it and is in a setup with a reference electrode (RE) and a counter electrode (CE) all in direct contact with an electrolyte. In both setups, the biomimetic membrane is formed on top of the CP to probe virus interactions.[129]

Biomembrane bioelectronic technology – both electrode and OECTs – was deployed to electrically monitor virus-host membrane interactions and fusion (**Figure 3.1b**). For the OECT, the coupling between ionic (from the gate electrode) and electronic (from the drain electrode) charges within the entire volume of the conducting polymer channel produces record high signal amplification values that scale with the volume of the channel[35]. This is a key feature that allows OECTs to be smaller than electrodes to achieve the same sensitivity. OECTs have historically been integrated with cell systems to monitor tissue integrity, effectively using the device as an impedance biosensor (see Chapter 5). The same principle is applied here to monitor the interaction of virus particles with a membrane. The OECTs used in this study used planer source and drain electrode and a gate electrode that was suspended in the solution. It is also possible to use the "built in" planar gate electrode and this is done for the studies in Chapter 5. The choice does not impact the electrical readout and comes down to the application at hand.

3.2 For this proof-of concept demonstration, influenza H3N2, strain X-31, was used, as its sialic acid receptor, pH fusion trigger, and entry mechanism are well characterized.[226] Two approaches to present viral receptors in SLBs were used: (1) reconstituted lipid bilayers with receptors, and (2) assembly of native cell membrane vesicles into planar membranes. Membranes were formed on the surfaces of PEDOT:PSS-based OECTs and electrodes and changes in electrical signals after triggering virus fusion on SLBs with viral receptors were detected. These changes are not observed when receptors are not present, the virus has been inactivated, or in the absence of the fusion trigger. The combination of both OECT pulse response time and electrode impedance measurements provide two distinct ways to electrically monitor changes in membrane properties induced by viral fusion. Materials and methods

3.2.1 Cell culture

Vero E6 (Vero) and baby hamster kidney (BHK) cells were used for the studies described in this chapter. Cell culturing is described in detail in Appendix A, section 8.1

3.2.2 Preparation of liposomes

A variety of liposome compositions were used in this study. Synthetic lipids 1-oleoyl-2-palmitoyl-sn-glycero-3-phosphocholine (POPC) and total ganglioside extract (TGE) (Avanti Polar Lipids) and oregon green DHPE (OG) (Molecular Probes). Purified influenza X-31 A/Aichi/68 H3N2 (Charles River, Wilmington, MA) live virus was purchased for this study and stored at −80 °C. For inactivation studies, virus was inactivated by incubating it at 80 °C for >6 h. POPC/OG is composed of POPC and OG at a 0.999:0.001 molar ratio. Lipids were mixed in a cleaned scintillation vial and dried under high-purity nitrogen gas to remove the bulk chloroform solution. Afterward, the vial was placed in a desiccator under vacuum for 3 h. The dried lipid film was resuspended with PBS to a final concentration of 4 mg/ml. Liposomes were then frozen overnight and extruded 10 times through a 50 nm pore size polycarbonate filter (Sigma) and stored at 4 °C.

3.2.3 Preparation of cell blebs and formation of SLBs

Vero and BHK blebs were prepared and SLBs formed as described in Appendix A, section 8.4

3.2.4 Electrochemical impedance spectroscopy (EIS)

The fabrication of electronic devices [†] and a detailed description of the electrical measurements is provided in Appendix A, section 8.6. In brief, to monitor the viral fusion, EIS measurements were taken on individual electrodes after each step as follows. First, the bare PEDOT:PSS electrodes, followed by SLB formation. After the SLB was formed on the MEAs, the pH of the buffer was lowed to 4.5 by exchanging PBS with a citric acid/MES buffer solution. This was done to evaluate the influence of the pH change on the EIS response due to the membrane lipids confirmation changes. Then the buffer was reversed back to PBS with pH 7.2. After that, 10^9 influenza X-31 virus particles were dispersed in 200 µl of PBS and incubated for 5 min on top of the SLB-functionalized devices (no dye in viral or SLB membrane). The virus was then triggered to fuse by lowering the pH again using the same citric acid/MES buffer. To capture as many virus fusion events as possible, the virus was treated with the acidic buffer at least 10 min before EIS measurements were taken for all samples studied. Nova software was then used for data analysis and modelling to extract the membrane resistance values.

3.2.5 Organic electrochemical transistor (OECT) measurements

OECTs were characterized using a dual-channel source-meter unit (NI-PXI) with custom-written control code in LabVIEW. All measurements were performed using an Ag/AgCl pellet (D = 2 mm × H = 2 mm – Warner instruments) as the gate electrode. The channels studied were 50 µm in length and 50 µm in width. A drain voltage −0.5 V was continuously applied and the OECT response time was calculated by applying square-shaped pulses at the gate electrode, 0.5 V in

[†] Electronic devices were provided by colleagues from the Salleo Research Group at Department of Materials Science and Engineering, Stanford University, USA

magnitude and 5 ms in width. These measurements were taken after each step of the SLB formation and virus fusion as described above in the EIS section.

3.3 Results and discussion

Before electrically detecting virus fusion on conducting polymer electrodes, virus fusion on synthetic SLBs on PEDOT:PSS surfaces was first confirmed optically. Optical detection of influenza virus fusion at the single particle level is possible using a fluorophore reporter embedded in the viral membrane imaged using TIRFM. This resolution is possible because the setup illuminates just a few 100 nm distance at the buffer/surface interface, effectively removing any signal from labelled viruses in the bulk solution that are not bound to the host membrane. TIRFM confirmed that virus fusion to SLBs can be triggered on PEDOT:PSS surfaces in a similar manner as done on glass surface and that the receptor is important for ensuring virus specificity (Figure 3.3). Moreover, fusion kinetics were similar for both systems.[129‡]

‡ Work performed by Tang, available in the published paper

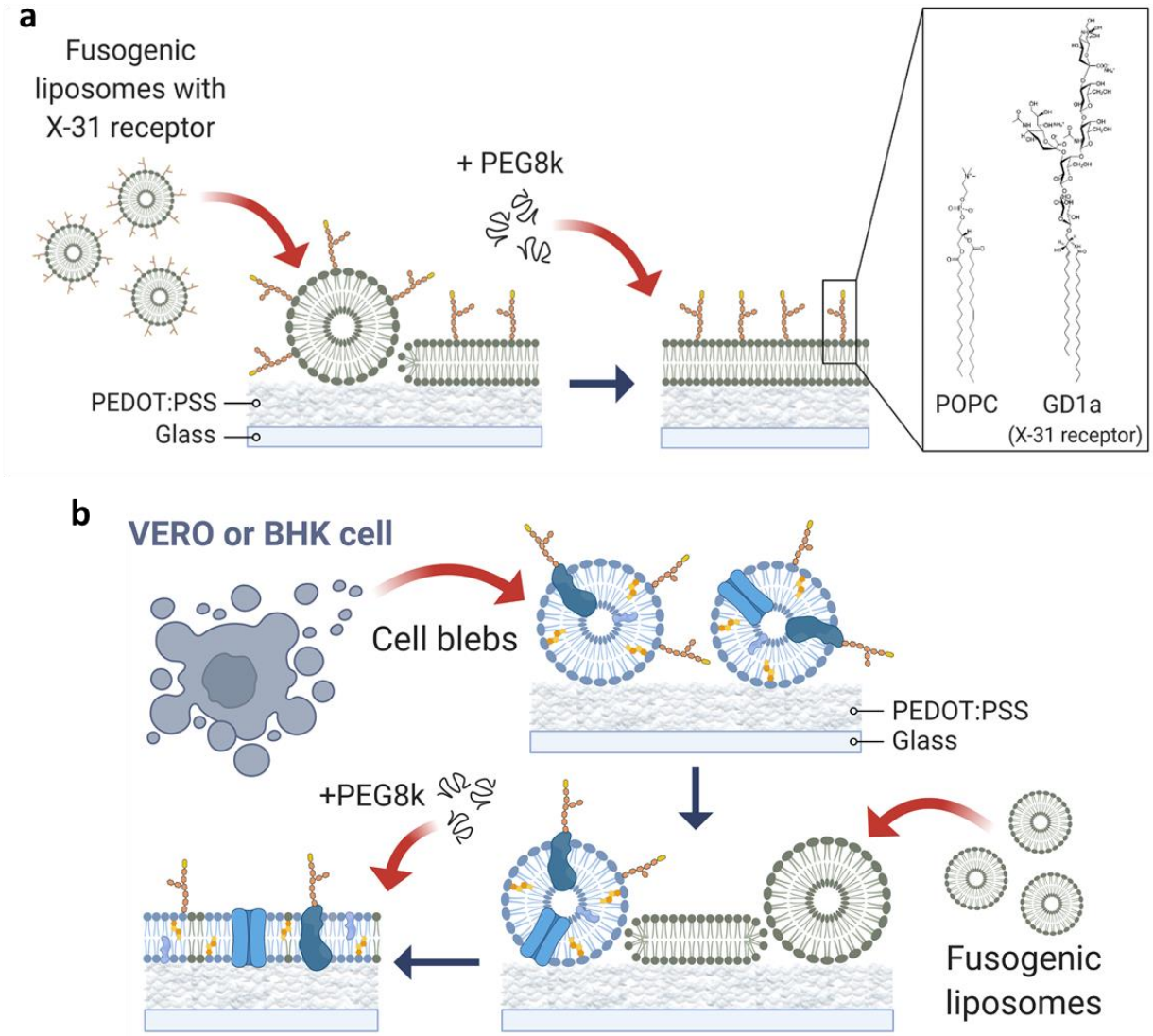

Figure 3.2: Schematic of SLB formation. Liposomes consisting of 95 mol % POPC and 5 mol % TGE were adsorbed onto PEDOT:PSS-coated glass surfaces. Rupture was induced via addition of 30 wt % PEG8K to form a SLB with the influenza sialic acid receptor. Inset show chemical structures of POPC and the GD1a molecules, obtained from Avanti ChemDraw Files. (**b**) Blebs (blue) from Vero E6 or BHK cell line were adsorbed on PEDOT:PSS-coated bioelectronic devices. Rupture was induced by adding POPC liposomes (green) and 30 wt % PEG8K sequentially to form an SLB.[129] Made with Biorender.com.

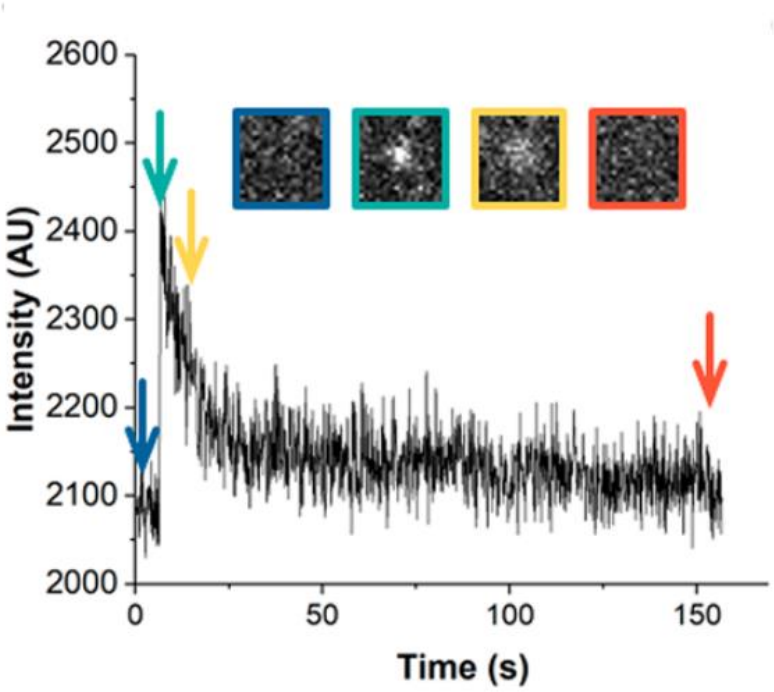

Figure 3.3: Fluorescence trace of a single fusion event captured in a 4 × 4 μm region with t = 0 the time when the system was acidified. The hemifusion lag time is determined by calculating the difference between when the peak occurs and when the system is acidified. Inset images show R18 labelled X-31 viruses. Images are colour-coded to match the time point as indicated by the arrows.[§]

3.3.1 Formation of synthetic and native SLBs**

To form the bilayer for these studies, liposomes composed of POPC and TGE were generated. TGE contains glycolipids containing sialic acid that serve as the receptor for X-31, as successfully used in previous studies.[268,269] The liposomes were adsorbed on a PEDOT:PSS-coated glass surface in and ruptured via addition of exogeneous poly(ethylene glycol) (PEG), which serves as an osmotic shock step previously seen to induce better SLB formation on PEDOT:PSS surfaces (**Figure 3.2a**).[270] To demonstrate the feasibility of this approach to capture viral receptors directly

[§] Results collected by Tang, available in the published paper

[**] Work performed by Tang, Savva, and Traberg

from a permissive cell line, blebs from the African green monkey kidney cells (Vero E6) and baby hamster kidney cells (BHK) were generated. These cell lines were chosen because influenza readily infects them, and they express the sialic acid receptors to which the X-31 HA proteins can bind.[268,271] Blebs from these cells were collected and adsorbed onto PEDOT:PSS OECTs and electrodes. Blebs were then induced to rupture into planar supported bilayers on these surfaces with the addition of pure POPC liposomes, followed by a final osmotic shock step using PEG solution (**Figure 3.2b**).[130,137] The formation of single lipid bilayers, as opposed to multiple stacked bilayers, was confirmed as we attained diffusion coefficient values comparable to those in the literature and this SLB formation protocol has previously been confirmed to produce single bilayers on top of a substrate[173,189].

3.3.2 Detection of virus fusion on reconstituted SLBs using OECT and electrode measurements††

The ability to electrically detect virus fusion after triggering on POPC/TGE bilayers formed on both the OECTs and electrodes (**Figure 3.1b**) was assessed. The first step was to show that the "host" SLBs can form on the device surfaces. FRAP measurements verify the formation of SLBs on top of the devices with $D = 0.41 \pm 0.03$ μm^2/s, $MF = 0.91 \pm 0.04$ (**Figure 3.4a**). These values are in line with previously reported diffusivity values of bilayers with similar lipid compositions using R18 probes.[145,146] Importantly, lipid diffusion is essential in this application because, without it, the mixing of the viral and host membrane during virus fusion is impossible.

Although optical measurements provide semiquantitative characterization of membrane quality by reporting its fluidity, electrical measurements can provide a higher degree of quantitation by determining the electrical properties of the membrane that reflect the ability of the SLB to block ionic flow to the conducting polymer. These "permeability" characteristics come in the form of changes in transient time constants in response to a voltage pulse in the OECTs and impedance measurements in the electrodes. On the OECTs, the response time (τ) serves as a figure of merit, in line with previous studies using insulating biolayers.[205,213] τ was determined by fitting

†† Savva and Traberg

with an exponential function, the evolution of the drain current after a short voltage pulse at the gate (**Figure S8.7a**), with representative output, transfer, and transconductance curves also shown (**Figure S8.7b,c**). As τ is indicative of the time it takes for the device to respond to a given gate bias (i.e., response time), any layer on top of the device that impedes ion flow slows down the device, thus increasing τ. Upon the application of a short gate voltage pulse (0.5 V for 2 ms), τ increases from 29 ± 9 to 144 ± 21 µs and from 32 ± 7 to 152 ± 14 µs when the OECTs are functionalized with POPC/TGE and POPC SLBs, respectively (**Figure 3.4c,d**), corroborating the FRAP data showing SLB formation on the OECT.

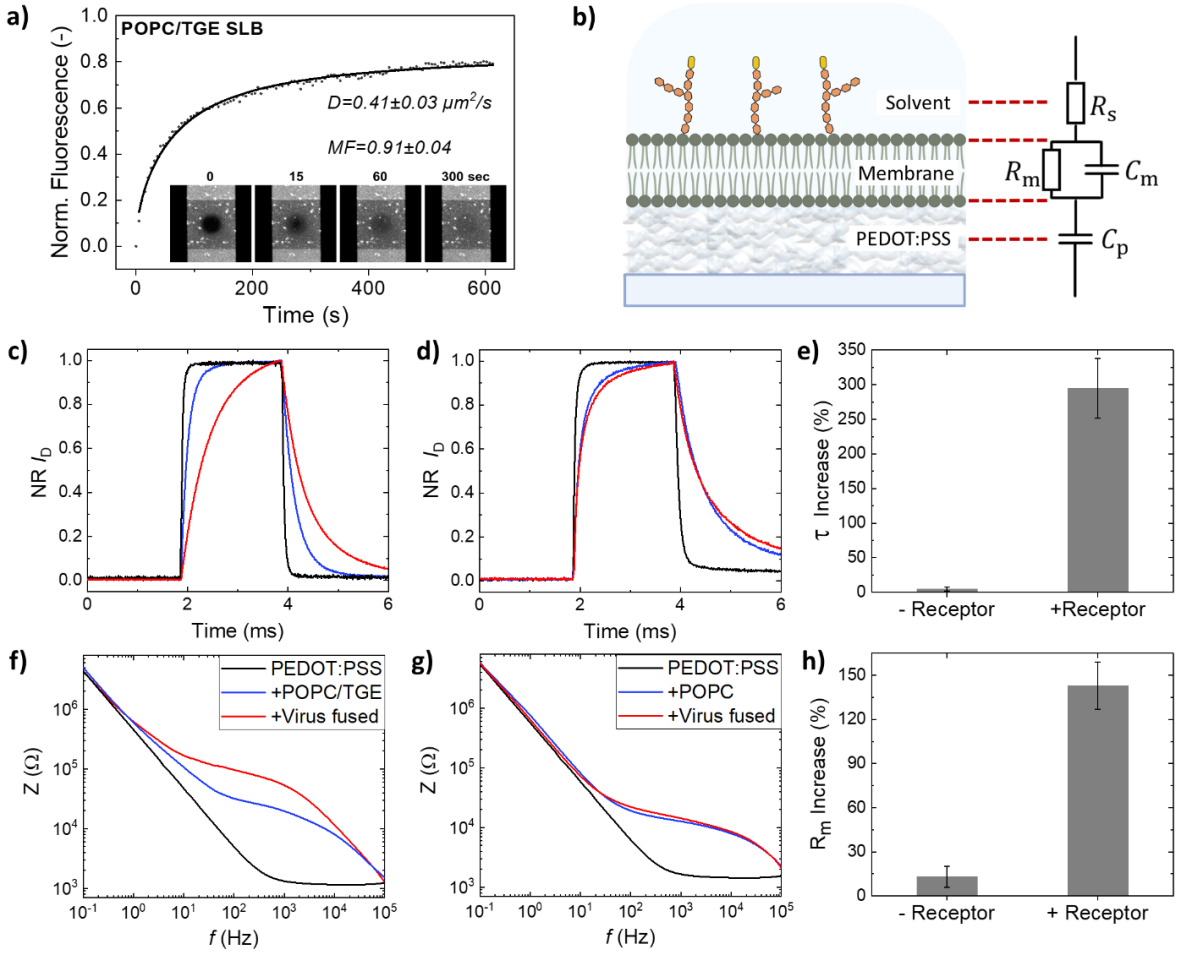

Figure 3.4: OECT and EIS measurements of X-31 fusion on POPC/TGE (+ receptor) and POPC (− receptor). (**a**) Representative FRAP measurement from POPC/TGE synthetic membranes formed on top of PEDOT:PSS OECT channels. D = 0.41 ± 0.03 µm²/s, MF = 0.91 ± 0.04. n=4. (**b**) Schematic drawing of SLB on electrodes and the equivalent circuit used to model the EIS data. The electrolyte resistance is modelled as a resistor (R_s) in series, the membrane is modeled as a resistor and capacitor in parallel (R_m– C_m), and PEDOT:PSS is modeled as a capacitor (C_p), as its resistance is much smaller than that of the electrolyte and may be neglected. Made with Biorender.com. (**c**) Response time of the OECTs before and after virus fusion is shown for POPC/TGE (+ receptor) and (**d**) POPC (− receptor) membranes. (**e**) Absolute increase in the response times of OECTs when the X-31 virus is fused to

reconstituted membranes (mean ± s.e.m.) n=4. (**f**) EIS measurements on MEAs functionalized with POPC/TGE (+ receptor) membranes and (**g**) POPC (− receptor) reconstituted membranes before and after viral fusion. (**h**) Absolute increase in the membrane resistance (R_m) as calculated by fitting the data into an equivalent circuit model after the flu virus is fused to reconstituted membranes mean ± s.e.m.) n=4.[129]

Next, influenza virus X-31 was incubated with the membrane-functionalized devices and virus fusion was triggered by lowering the pH from 7.0 to 4.5. After acidification, a dramatic increase of the response time of the OECTs functionalized with POPC/TGE SLB to 569 ± 32 μs (**Figure 3.4c**) is observed. This corresponds to a ∼290% increase in the response time compared with the response time of the POPC/TGE functionalized OECT before viral fusion (**Figure 3.4e**). Almost no change was observed in the response time of the POPC functionalized OECTs (− receptor) when virus fusion was triggered, showing that the viral receptor is a critical component of detectable fusion events in these devices and provides specificity.

To gain additional assessment of the bilayer electrical properties, EIS measurements were performed on PEDOT:PSS electrodes. Here, the figures of merit are the impedance magnitude, Z, as a function of frequency, and the fitted resistance values derived from the SLB. This impedance response can be captured in a Bode plot (**Figure 3.4f,g**). In these figures, an increase in Z is observed when the POPC/TGE and POPC SLBs are formed, indicative of the presence of an insulating layer, i.e. the SLB. The experimental data were fitted to an equivalent circuit model. The electrolyte resistance is modelled as a resistor (R_s) in series and PEDOT:PSS is modelled as a capacitor (C_p), as its resistance is much smaller than that of the electrolyte and can thus be neglected, while the membrane is modelled as a resistor and capacitor in parallel ($R_m - C_m$) (**Figure 3.4b**). The membrane resistance (R_m) values were calculated to be 0.067 and 0.024 kΩ cm^2 for POPC/TGE- and POPC SLB-functionalized electrodes, respectively, which when taken with the optical assessment (**Figure 3.4a)** confirms that SLBs have formed on these electrodes. The R_m values obtained here are slightly lower compared to previously published R_m values for both native and synthetic SLBs on PEDOT:PSS supports;[130,137] however, these previous reports used lipid formulations that contain positively charged lipids. Here, zwitterionic lipids were used in the rupture liposomes, and as such, this change, along with different device design and dimensions, could impact the R_m values making them lower than previously reported values. Nonetheless, this current formulation and design yield signals in a range that still allow observable changes while eliminating non-native lipids that could promote nonspecific interactions. Upon triggering influenza fusion with low pH, a large increase in the R_m is observed from 0.067 to 0.167 kΩ cm^2 on POPC/TGE SLBs (+ receptor) but almost no increase on the POPC SLB (− receptor).

The average increase of the R_m was calculated at ~141% and ~12% for POPC/TGE (+ receptor) and POPC (− receptor) functionalized electrodes, respectively (**Figure 3.4h**).

To relate the electrical signal to the number of viral fusion events occurring at the membrane and to offer some preliminary thoughts on determining the limit of detection (LOD), the following calculations were carried out. On average, about 30 viral fusion events are observed from TIRF in a 6.72×10^{-7} mL imaging volume (82 μm length × 82 μm width × 100 μm height). The concentration of the virus used in TIRF experiments is $\sim 6.25 \times 10^9$ particles/ml, resulting in ~4200 particles in the imaging chamber. At maximum, 30–40% of particles are active (determined from influenza virus-liposome lipid mixing experiments), suggesting that roughly 2% of active viruses hemifused (30 fusion events/1500 active viruses) in this imaging volume. Since the membrane resistance increase measured in an electrode is ~50 kΩ per 0.19635 mm^2, each viral fusion event increased the membrane resistance by ~55 Ω, assuming that the electrode response has a linear relationship to fusion events. Based on the EIS signal recorded from multiple electrodes, an increase in the range of 1000 Ω in the frequency range between 100–1000 Hz is clearly detectable, suggesting that at least 20 fusion events are needed for EIS detection if each event changes the resistance by 55 Ω on average. With 2% of active viruses hemifusing, this suggests the device needs at least 1000 active particles in the solution to detect fusion. Of course, future studies will be needed to accurately determine the LOD.

3.3.3 Detection of virus fusion on native membranes incorporating virus receptors derived from host cell plasma membranes using OECT and electrode measurements[‡‡]

The work above establishes a platform for detecting viral fusion function so long as the viral receptor can be reconstituted in a liposome for SLB formation. However, this limits applications to viruses with lipid receptors that can be easily reconstituted, such as those bearing sialic acid for the influenza virus. As viruses can recognize other cell surface moieties, most notably proteins, it is important to capture other types of viral receptors to demonstrate the versatility of this platform.

[‡‡] Savva and Traberg

By blebbing from a host cell plasma membrane, not only is the viral receptor included but also the other features of the host membrane that more closely mimic the host cell surface and its components (**Figure 3.5a**) that can be integrated into this platform. Again, the first step was to show that the "host" native membranes can form on the device surfaces. FRAP measurements verify the formation of SLBs on top of the devices with $D = 0.41 \pm 0.03$ μm^2/s, $MF = 0.91 \pm 0.04$ (**Figure 3.5b;** see also **Figure S8.1**). These values are in line with previously reported diffusivity values of bilayers with similar lipid compositions using R18 probes.[145,146]

To assess membrane fluidity, FRAP measurements of both Vero and BHK bleb bilayers using R18 as the reporter were performed, yielding the following values: $D = 0.32 \pm 0.07$ μm^2/s, $MF = 0.90 \pm 0.03$ and $D = 0.43 \pm 0.03$ μm^2/s, $MF = 1.07 \pm 0.02$, for Vero E6 and BHK-derived membranes, respectively (**Figure 3.5b** and **Figure S8.1**). These values are comparable to those obtained on glass surfaces with R18 probes, with $D = 0.32 \pm 0.01$ μm^2/s, $MF = 1.01 \pm 0.02$ and $D = 0.31 \pm 0.03$ μm^2/s, $MF = 1.10 \pm 0.02$, for Vero and BHK-derived membranes, respectively (**Figure S8.1**).[135,145,272]

Electrical characterization using OECTs showed that τ increased from 54 ± 12 to 107 ± 18 μs and from 45 ± 6 to 123 ± 20 μs after formation of the Vero and BHK SLBs on the devices, respectively (**Figure 3.5c,d**). Following incubation and triggering of virus fusion via addition of pH 4.5 buffer, a clear ~100% and ~130% increase in the OECT response time (**Figure 3.5e**) to 208 ± 24 and 243 ± 23 μs on Vero and BHK SLB, respectively, is seen. The effect of pH change (from 7.0 to 4.5) is negligible compared to the signal caused by virus fusion. Additionally, heat-inactivated X-31 virus cannot fuse, as observed on TIRFM, nor does it change the response time of the BHK-membrane functionalized OECTs.[129]s

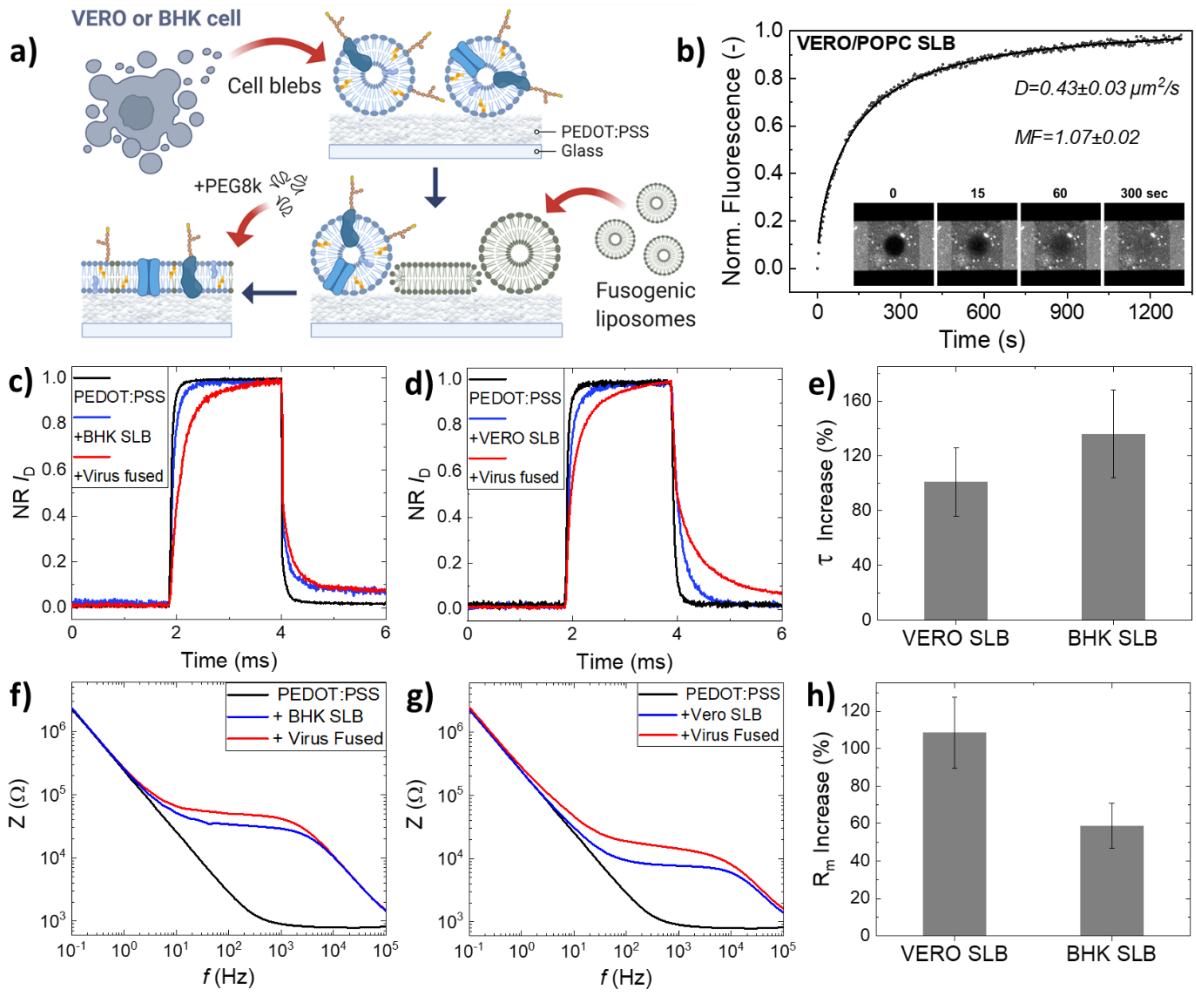

Figure 3.5: OECT and EIS measurements of X-31 fusion on native membranes. (**a**) Schematic drawing of bleb SLB formation. Blebs (blue) from Vero E6 or BHK cell line were adsorbed on PEDOT:PSS-coated bioelectronic devices. Rupture was induced by adding POPC liposomes (green) and 30 wt % PEG8K sequentially to form an SLB. Made with Biorender.com. (**b**) FRAP measurements from Vero membranes formed on top of PEDOT:PSS OECT channels. D = 0.43 ± 0.03 μm^2/s, MF = 1.07 ± 0.02, n=3 (see **Figure S8.1** for additional FRAP measurements of Vero and BHK membranes). Response time of the OECTs before and after virus fusion is shown for (**c**) BHK and (**d**) Vero SLBs. (**e**) Absolute increase in the response times of OECTs when flu virus is fused to native membranes (mean ± s.e.m.), n=4. EIS measurements on microelectrode arrays functionalized with (**f**) Vero native membranes and (**g**) BHK native membranes before and after viral fusion. (**h**) Absolute increase in the membrane resistance (R_m) as calculated by fitting the data into an equivalent circuit model after the virus is fused to native membranes (mean ± s.e.m.), n=4.[129]

These OECT results are corroborated by EIS measurements on the native SLBs on PEDOT:PSS electrodes. An increase in impedance magnitude Z is observed after Vero and BHK SLBs are formed, indicative that the SLB had formed. The R_m values were calculated to be 0.064 and 0.015 kΩ cm^2 for BHK and Vero SLB-functionalized electrodes, respectively. After triggering virus fusion, an increase of R_m values is observed (**Figure 3.5f,g**), showing a ~110% and ~60% increase after virus fused to Vero and BHK host membranes, respectively (**Figure 3.5h**). The

OECT and electrode measurements confirm that we can use the blebbing technique as a method to capture viral receptors for these devices and detect viral fusion.

One possible cause for the increased OECT response times and impedance magnitudes is that the fusion event adds viral lipids and proteins to the SLB, which can patch up defects, resulting in a more compact and dense membrane. As a result, the ionic flow is further impeded, resulting in increased OECT response time and electrode impedance. A greater increase in both OECT response time and MEA impedance magnitude is also observed when membrane fusion is triggered on the POPC/TGE membrane compared with fusion on the Vero E6 or the BHK membranes. We suspect that the greater increase in POPC/TGE measurements is because there are no proteins or other biological matter in the membrane. Native SLBs have been shown to capture ion channels that can allow ions to pass through more easily,[130,137] compared to their pure lipid counterpart. Regardless, the native SLBs still have a notable change in electrical measurements and is a viable method for detection if the viral receptor cannot be easily isolated.

Both sets of measurements, conducted on OECTs and electrodes, demonstrate the ability to detect electrical responses resulting from viral fusion and that these responses are specific to bilayers with the viral receptor and environmental conditions, and are not due to nonspecific virus–lipid or virus–protein interactions. This suggests that the viruses cannot fuse to any SLB; it can only fuse to SLBs with the viral receptor and appropriate environmental conditions.

3.4 Outlook

Current diagnostic methods focus on detecting virus related biological matter, such as viral nucleic acids or antibodies. However, detecting biological matter can be misleading as they are not necessarily indicative of an active infection. Thus, an innovative approach to viral detection was developed, by creating a label-free platform that leverages electrical signals to sense viral biological function, specifically the ability of an enveloped virus to bind and fuse to a host cell membrane. Using influenza virus as the proof-of-principle demonstration, the triggering of influenza virus fusion with low pH on host membrane mimics formed on PEDOT:PSS-coated OECTs and electrodes resulted in quantifiable changes in electrical properties without the use of label probes.The ability of this platform to detect viral function has both basic science and applied uses. On the basic science end, this platform can be used as a research tool to further characterize viral fusion. Since the OECTs are transparent, it would be interesting to explore simultaneous TIRFM and response time measurements to better correlate the response time increases with visible viral fusion events. This can unlock knowledge about virus fusion signatures that can complement fusion kinetic data obtained from just TIRFM. On the applied end, this platform can

complement current approaches for high-throughput detection of enveloped viruses (i.e., SARS-CoV-2) and inhibition screening. For viral detection, researchers can develop bilayers with a variety of viral receptors, run appropriate fusion triggers, and observe whether fusion occurs to confirm the presence of active virus in the sample. Future development in this area would determine the feasibility of using clinically complex samples as opposed to using purified viral samples. For inhibitor screening, antivirals can be screened for their ability to block the viral entry function and it is expected that successful candidates would dampen the response time increases associated with successful viral entry. As current approaches to screen viral function involve performing live cell-based assays, this *in vitro* approach could expedite screening processes by providing functional data without the complications of working with live cells. Overall, developing a platform to detect viral functionality would provide additional approaches toward viral diagnostics and therapeutics that are much needed in addressing current and future viral outbreaks.

Building on the platform and knowledge gained from this work, native SLBs integrated with organic electronic devices were applied to the study of EV-plasma membrane interactions, which is described in section 4.

“Nature makes penicillin; I just found it.”

— Alexander Fleming

4 DUAL MODE SENSING OF BINDING AND BLOCKING OF CANCER EXOSOMES TO BIOMIMETIC HUMAN PRIMARY STEM CELL SLBS

Preamble

This chapter contains work published by J. Uribe, **W. C. Traberg**, A. Hama, V. Druet, Z. Mohamed, A. Ooi, A.-M. Pappa, M. Huerta, S. Inal, R. M. Owens, S. Daniel, Dual Mode Sensing of Binding and Blocking of Cancer Exosomes to Biomimetic Human Primary Stem Cell Surfaces. ACS Biomater. Sci. Eng. (2021). Where relevant to this thesis, figures and text have been included, and where not relevant, reference has been made to the publication.

4.1 Introduction

Recently, TEVs have been reported to transfer miR-630 to fibroblasts, promoting their differentiation to carcinoma-associated fibroblasts and ovarian cancer invasion and metastasis.[273] Similarly, several studies have implicated TEVs in cancer development and progression in other types of cancers.[274–276] In particular, a subset of TEVs, cancer exosomes (cEXOs), are known to mediate transfer of information between cells within the tumour and to distal sites contributing to tumour growth and formation of premetastatic niches.[277,278] For instance, interactions with breast cancer-derived cEXOs induced proangiogenic behaviour, indicated by the upregulation of vascular endothelial growth factor (VEGF) in adipose-derived stem cells (ADSCs) and their subsequent differentiation to myofibroblasts.[279,280] Both outcomes favour tumourigenesis by promoting tumour vasculature formation and high levels of inflammation at the tumour microenvironment (TME).[281–283] Therefore, hindering interactions between cEXOs and healthy cells is expected to reduce these types of negative outcomes and possibly mitigate the progression of cancer.

ADSCs are an important cell group in the TME with a critical role in cancer progression and aggressiveness.[283,284] ADSCs secrete inflammatory biomarkers, such as VEGF, that promote angiogenesis and a TME with high levels of inflammation, fostering tumourigenesis.[281,285] Notably, surface interactions between cEXOs and ADSCs are known to stimulate VEGF secretion in ADSCs contributing to their angiogenic potential.[170] Because of these malignant implications, it is imperative to study cEXO−ADSC binding and to find treatments to block it as a means to decrease ADSC angiogenic properties. Toward this end, an ADSC membrane model was developed and integrated with PEDOT:PSS-based MEAs to create a cell-free and label-free tool for studying cEXO-ADSC binding events.

Blocking specific interactions as a route to inhibit the transfer of information between cEXOs and cells and subsequent outcomes is an important emerging avenue for cancer therapeutics. However, given the complexity of the plasma membrane surface and all the possible targets for cEXOs to bind to and deliver their cargo, screening for such interactions is a challenge that could benefit from new models and tools. These types of screening studies are complex because the molecular interactions between cEXOs and cells are specific to each type of cEXO–cell pair and are determined by the surface composition of both entities.[286–288] All possible cEXO–target cell interactions are expected to begin by surface contact that involves binding of at least two surface components, one from the cEXO surface and one from the cell plasma membrane.[286,287] Subsequently, cEXOs can take different routes to transfer of

information, including binding-induced activation of signaling pathways at the plasma surface that leads to downstream cellular responses, cellular internalization via various endocytosis pathways that leads to delivery of contents to various organelles, and direct fusion with the cell plasma membrane that leads to the direct release of cargo into the cytosol.[121,286,287] Being able to assess binding isolated from these subsequent biological processes, with an easy readout that can be scaled up to integrate technologies for high-throughput screening, is a current need in the field. To create a model system to study and visualize cEXO–cell binding, a planar and tuneable *in vitro* ADSC plasma membrane model system was developed. The central element of this platform consists of a hybrid SLB, incorporating native ADSC membrane components derived from plasma membrane blebs from human primary stem cells to create an ADSC-supported bilayer (ASB).

By adapting previously published protools,[130,137] the ASB maintained much of the authenticity of the plasma membrane of ADSCs, preserving native constituents, molecular complexity, and lateral diffusivity of the membrane. Because this platform is a representative mimic of the plasma membrane that is free of the dynamism of live cells, it is useful for isolating and focusing on cEXO binding and blocking without competing effects of cEXO uptake and cargo delivery. Using both optical and electrical sensing modes, cEXO binding to ASBs, and subsequent blocking by an antibody to integrin β1/CD29 on the surface of ADSCs, was detected. Finally, as a means to corroborate the platform's results, in the context of live cells, this antibody blocking strategy was applied to cell-based assays to demonstrate that cEXO blocking stops the upregulation of VEGF and cell proliferation in ADSCs.

4.2 Materials and methods

4.2.1 Cell culture

Human adipose-derived stem cells (ADSCs) and MDA-MB-231 cells were used for the studies described in this chapter. Cell culturing is described in detail in Appendix A, section 8.1.

4.2.2 Preparation of ADSC blebs

ADSC blebs were prepared as described in Appendix A, section 8.4

4.2.3 cEXO isolation

MDA-MB-231 cells were cultured on a 150 cm^2 cell culture flask (TFS) in 15 ml complete media until they reached 75-85% confluency. To avoid the presence of serum-derived EVs during isolation, cells were incubated in serum-free media for 18-48 hours at 37 °C and 5% CO_2. The medium was collected and centrifuged at 280 x *g* for 12 min at 21 °C to remove cells, followed by a second centrifugation at 10 000 x *g* for 25 min at 21 °C to remove cell debris. The cleared media was vacuum filtered using a 0.22 μm Millipore Steriflip PVDF-filter (Millipore) to separate bigger particles from exosomes. The filtrate generated in the vacuum tubes was transferred to ultracentrifuge tubes followed by ultracentrifugation at 100 000 x *g* at 4 °C for 4 h. The cEXO pellet was resuspended in 1 ml of PBS, pH 7.4 supplemented with 1% P/S. cEXOs were kept at 4 °C until needed.

4.2.4 Preparation of liposomes

POPC (Avanti Polar Lipids, Sigma) and 1,2-distearoyl-sn-glycero-3-phosphoethanolamine-N-[methoxy (polyethylene glycol)-2000], PEG2000-PE, (Avanti Polar Lipids, Sigma) were used to create liposomes. POPC–PEG2k liposomes were made with 99.5% (mol/mol) POPC and 0.5 (% mol/mol) PEG2000 (PEG2k). The lipid mixture was prepared by adding appropriate ratios to a clean glass vial and drying them with nitrogen gas, followed by desiccation in a vacuum chamber for 3 h. The lipid film was resuspended in PBS pH 7.4 solution to a final concentration of 2 mg/ml and stored at −20 °C overnight. After thawing, liposomes were extruded through a 100 nm membrane 12 times (Sigma) and kept at 4 °C for up to 2 weeks.

4.2.5 Formation of SLBs

Formation of phosphatidylcholine-SLBs. SLBs self-assembled on a clean coverslip using the well-established vesicle fusion method as shown previously.[144,145] 100 μl of a 2.0 mg/ml liposome solution (POPC–PEG2k) was added into a well and incubated for 20 min at RT. Wells were thoroughly washed with PBS pH 7.4 to remove excess lipid vesicles remaining in the bulk phase after bilayer formation.

Formation of the ASB. For ASB formation, 100 μL of ADSC membrane blebs (2.48 × 10^8 blebs/ml) in GPMV buffer were added to a well and incubated at RT for ∼10 min. Then, the well was thoroughly rinsed with PBS pH 7.4 to remove unabsorbed blebs. Formation of the bilayer was induced by adding 100 μl of 2 mg/ml POPC–PEG2k into the well and incubating for 20 min at RT, followed by rinsing with PBS.

The rupture of fluorescently labelled ADSC blebs was observed using an inverted Zeiss Axio Observer.Z1 microscope with α Plan-Apochromat objectives, a Hamamatsu EM-CCD camera (Image EM, model C9100-13, Bridgewater, NJ), and an X-Cite 120 microscope light source (Lumen Dynamics Group Inc., Canada). To accumulate the fluorescence emitted by the fluorophores (R18), an ET MCH/TR filter cube (49008, c106274, Chromatech Inc.) was used. Labelled ADSCs blebs were first incubated on the coverslips or PEDOT:PSS-coated coverslips as described above, followed by the addition and incubation of POPC–PEG2k vesicles (unlabelled) to rupture them. The process was recorded with the camera and complete rupture observed, further corroborated by FRAP.

4.2.6 Testing integrin β1/CD29 presence in the ASB

The ASB was incubated with 70 µl of 20% normal goat serum (GS, Thermo Fisher Scientific) for 30 min at RT. The well was thoroughly washed with PBS to remove excess GS. 100 µl of 1:100 anti-integrin β1/CD29 antibody solution (MAB1778, R&D Systems) was added to the well and incubated for 2 h at RT. The well was thoroughly washed with PBS to remove the excess primary antibody and incubated with 100 µl of 1:2000 Donkey Anti-Mouse IgG NorthernLights (NL009, R&D Systems) conjugate antibody for 1 h at RT in the dark. After that, the bilayer was washed one last time with PBS to remove the excess secondary antibody and imaged using a TIRF microscope to detect specific binding of integrin β1/CD29 antibody to the ASB. As a negative control, an ASB was treated just with the secondary conjugated antibody to show non-specific binding of integrin β1/CD29 to the ASB with the absence of the primary antibody. Additionally, treatment with both antibodies was repeated with a POPC–PEG2k SLB (no ADSC material) as a negative control to show non-specific binding of integrin β1/CD29.

4.2.7 Binding of cEXOs to the ASB

The ASB was formed as stated above and blocked using 70 µl of 20% normal GS for 30 min at RT to prevent non-specific binding. After thoroughly washing the well with PBS to remove excess GS, 100 µl of R18 labelled cEXOs were added to the ASB and incubated for 30 min in the dark to allow binding. Finally, the well was thoroughly washed with PBS to rinse unbound vesicles. Binding of cEXOs to the ASB was imaged using TIRFM and quantified by ImageJ software.

4.2.8 Blocking binding of cEXOs to the ASB using integrin β1/CD29

The ASB was incubated with 100 µL of 20% normal GS for 30 min at room temperature, followed by a thorough wash with PBS to remove excess GS. 100 µL of 1:100 anti-integrin β1/CD29 were added to the well and incubated for 2 h at RT. The well was thoroughly washed with PBS to remove the primary antibody, followed by incubation with 100 µL of R18-labeled cEXOs at room temperature for 30 min to allow binding. The ASB was washed with PBS to rinse unbound cEXOs, and images were captured using TIRFM.

4.2.9 TIRFM setting and operation

TIRFM was conducted on an inverted Zeiss Axio Observer.Z1 microscope with an α Plan-Apochromat 100 × objective; 488 and 561 nm wavelengths from solid-state lasers were used to excite the samples. A Laser TIRF 3 slider (Carl Zeiss, Inc., Oberkochen, Germany) was used to adjust the angle of incidence at approximately 68.2° generating an evanescent wave at 100 nm and total internal reflection. The excitation light was filtered using a Semrock LF488-B-ZHE filter cube and sent to the electron-multiplying CCD camera (ImageEM C9100-13, Hamamatsu).

4.2.10 Electrochemical impedance spectroscopy (EIS)

The fabrication of multielectrode arrays[*] and a detailed description of the electrical measurements is provided in Appendix A, section 8.6. In brief, ASBs were formed on PEDOT:PSS-coated MEAs and cEXO binding and blocking experiments were carried out in the same manner as described for glass substrates. ASBs were prepared fresh on the devices and were stable for 48 h, meaning device performance did not decrease during this time nor did the membrane resistance change. To monitor cEXO binding, EIS measurements were taken on individual electrodes after each step as follows: (1) bare PEDOT:PSS electrodes, (2) the ASB formed on top, (3) after incubation with the anti-CD29 antibody, in the case of blocking,

[*] Devices were provided by Victor Druet from the Organic Bioelectronics Laboratory at KAUST, SA

and (4) after addition of cEXOs. Nova software was then used for data analysis and EEC modelling to extract the membrane resistance values.

4.2.11 Statistical Analysis

For all experiments performed in this study, variance analysis was performed using a t-test with unequal variances to find significant differences between substrates and conditions. All data were plotted and analysed using Microsoft Excel and they were presented as mean ± s.e.m. Statistical significance levels were determined as follows: *$p \leq 0.05$, **$p \leq 0.01$, ***$p \leq 0.001$, and ****$p \leq 0.0001$.

4.3 Results & discussion

ASBs were deployed to investigate cancer cEXOs−ADSCs binding and blocking strategies. First, optical means were used to characterize the formation of an ASB and the binding of cEXOs, followed by assessment of blocking plasma membrane bound β1/CD29 with a specific antibody to reduce cEXOs binding. Next, an electrical approach was used to demonstrate the label-free binding and blocking of cEXOs to ASBs. Lastly, to corroborate the results obtained using the cell-free ASB platform, a cell culture assay was used to investigate the effect of cEXO-blocking and demonstrate that this prevents the upregulation of VEGF secretion and cell proliferation, which are direct outcomes of cEXO and ADSC binding.[170,279]

4.3.1 Characterisation of ADSCs blebs and cEXOs

The characterisation data for ADSCs blebs and MDA-MB-231-derved cEXOs used in this study is available in Appendix B, chapter 8.11.1.

4.3.2 Formation and characterization of ASBs†

ADSC blebs labelled with R18 were incubated and adsorbed on a glass slide. The fluorophore, R18, was initially confined to cell blebs and visualized as bright dots, as shown in the left image of the fluorescence images (**Figure 4.1a**). Next, fusogenic POPC–PEG2k liposomes were added to the well to induce rupture of blebs, as seen in the middle image of the fluorescence images.[144,146] After 30 min of incubation, followed by thorough PBS rinsing, a contiguous supported bilayer was formed and the R18 signal from blebs uniformly spreads out, diffusing freely within the planar bilayer surface as seen in the right fluorescence image.

† Work by Uribe

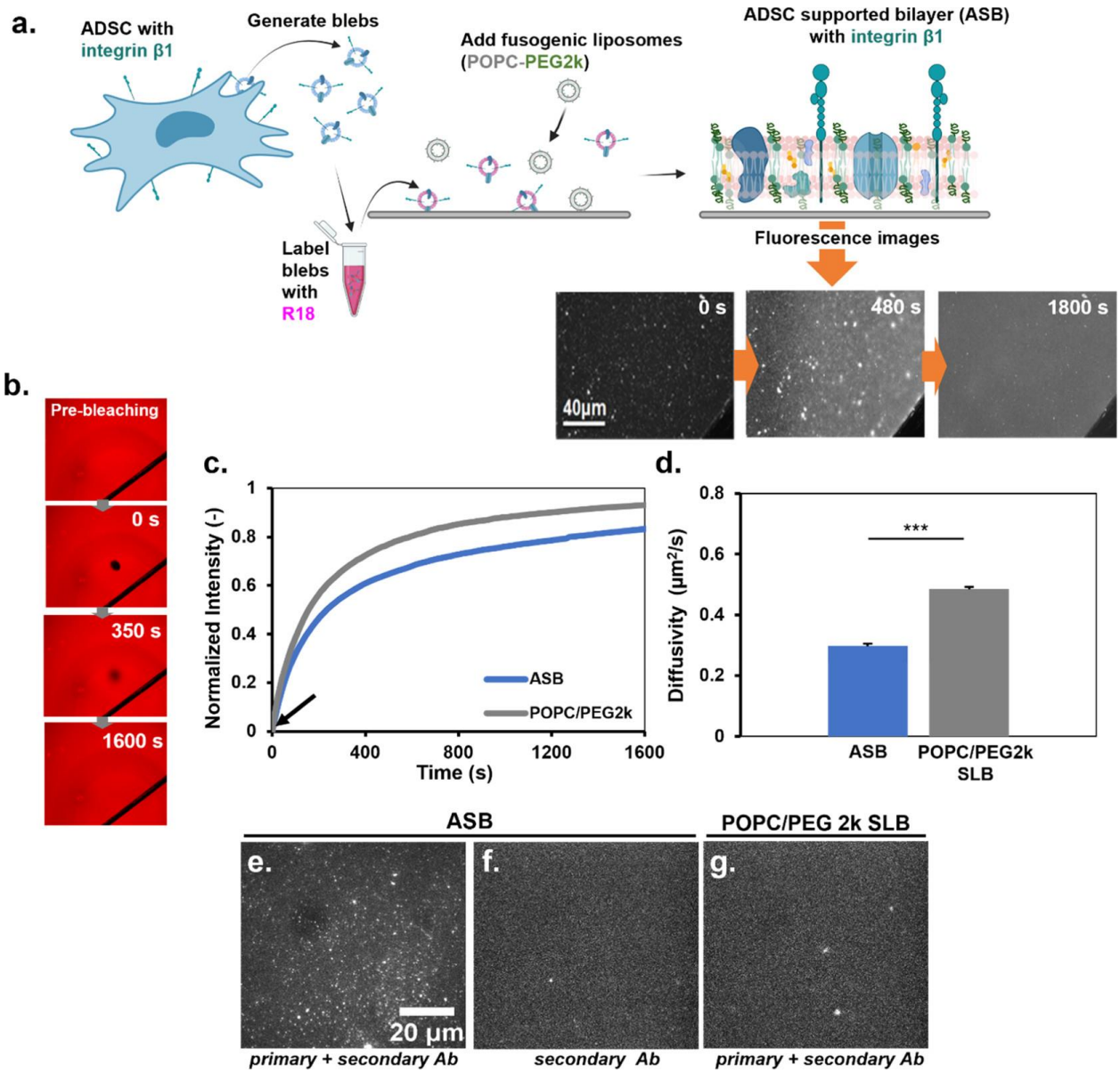

Figure 4.1: ASB formation and optical characterization. (**a**) Diagram and fluorescence images of ASB formation. (**b**) Using a laser beam, a 22 μm diameter circle was photobleached in the bilayer at time zero, as shown in the top fluorescence image. Partial recovery of the photobleached circle can be visualized at around 350 s for ASB. Lastly, final recovery of the photobleached circle was achieved at about 1600 s for ASB, as shown in the fluorescence recovery graph in **c** and in the bottom fluorescence image in **b**. Images depicting prebleached, photobleached, partially recovered, and completely recovered ASB. (**c**) ASB and POPC-PEG2k FRAP curve. (**d**) Coefficient of diffusivity for the ASB and the POPC/PEG2k SLBs (mean ± s.e.m.; n=4). (**e**) TIRF microscopy images of ASB treated with anti-CD29/integrin β1 antibody showing specific binding of CD29/integrin β1 to the ASB and its presence in it. (**f**) ASB treated with a conjugated secondary antibody in the absence of a primary antibody. (**g**) POPC/PEG2k-SLB is treated with primary and secondary antibodies, and no presence of integrin β1 is detected because it is a synthetic and inert bilayer that does not contain adhesion molecules such as integrins. n=4. ***$p \leq 0.001$.[131]

The diffusivity of R18 in the 2D plane of ASB was assessed using FRAP (**Figure 4.1b**). The ability of the ASB to undergo fluorescence recovery with a high mobile fraction value of 90% confirms the formation of a diffusive and mobile supported bilayer, minimally free of defects. The ASB was found to be less diffusive (0.297 ± 0.035 $\mu m^2/s$) than the POPC/PEG-2k SLB (0.486 ± 0.096 $\mu m^2/s$). These results were expected because the POPC-PEG-2k SLB contains only lipids, and the ASB contains ADSC membrane proteins from ADSC blebs in addition, which have been established to reduce the diffusion within the bilayer.[139] Therefore, the ASB conserves the characteristic fluidity properties of cell membranes. Additionally, ASB formation on PEDOT:PSS-coated glass slides was assessed using FRAP (**Figure 4.2**), which yielded slightly higher diffusivity values.

To recapitulate the plasma membrane of ADSC, the ASB should retain its native components. Integrin β1 is a protein highly expressed in the plasma membrane of ADSCs and is implicated in several biological functions including cell adhesion, wound repair, tumour-directed angiogenesis, and tumour cell growth.[289,290] Here, the presence of integrin β1 in the ASB was confirmed by probing with an anti-integrin β1/CD29 antibody, directed to recognize the extracellular portion of this transmembrane protein, and using a fluorescent secondary antibody to allow detection by TIRFM. **Figure 4.1e** depicts the bright spots associated with antibody binding, confirming the presence of integrin β1 in an ASB. Importantly, given that the antibodies bound to the appropriate epitope that faces away from the membrane, it suggests that the orientation of the integrins is also intact, which is in agreement with previously reported observations.[144,173] Additionally, two negative controls were performed to reassure that detection was specific and not reflective of non-specific adsorption (**Figure 4.1f, g)**. Collectively, these results indicate that the ASB preserves native membrane components with correct orientation, confirming its validity as a model to study cEXOs interactions with ADSCs.

4.3.3 Optical and electrical characterisation of ASB on PEDOT:PSS-coated substrates and devices‡

ASBs formed on PEDOT:PSS-coated glass slides and electrodes were characterised optically by FRAP and electrically by EIS (**Figure 4.2**). The formation of native cell membranes on PEDOT:PSS is readily achievable using a vesicle fusion protocol and membrane mobility is comparable to state-of-the-art values obtained on glass substrates.[144] For the ASB, the reported coefficient of diffusivity of the ASB on PEDOT:PSS (0.500 ± 0.022 $\mu m^2/s$) (**Figure 4.2d**) was slightly higher than on glass (0.297 ± 0.035 $\mu m^2/s$) (**Figure 4.1d**). This may be due to the ability of PEDOT:PSS to swell in aqueous medium, creating a hydrogel-like surface that acts as a cushion for the ASB, as has been previously observed for other hybrid-SLBs formed on polyelectrolyte cushions.[135] The presence of a bilayer on top of the PEDOT:PSS electrode induces a shift in the measured impedance in the $10\text{-}10^4$ frequency range (**Figure 4.2a**), as well as change in the phase shift (**Figure 4.2b**). The presence of a semicircle in the Nyquist plot (**Figure 4.2c**), characteristic of a membrane, is also observed. By applying an equivalent circuit to the Nyquist plot, the membrane resistance and capacitance can be extracted. This is described in detail in **chapters 4.3.5** and **3.3.2**.

‡ Work by Traberg

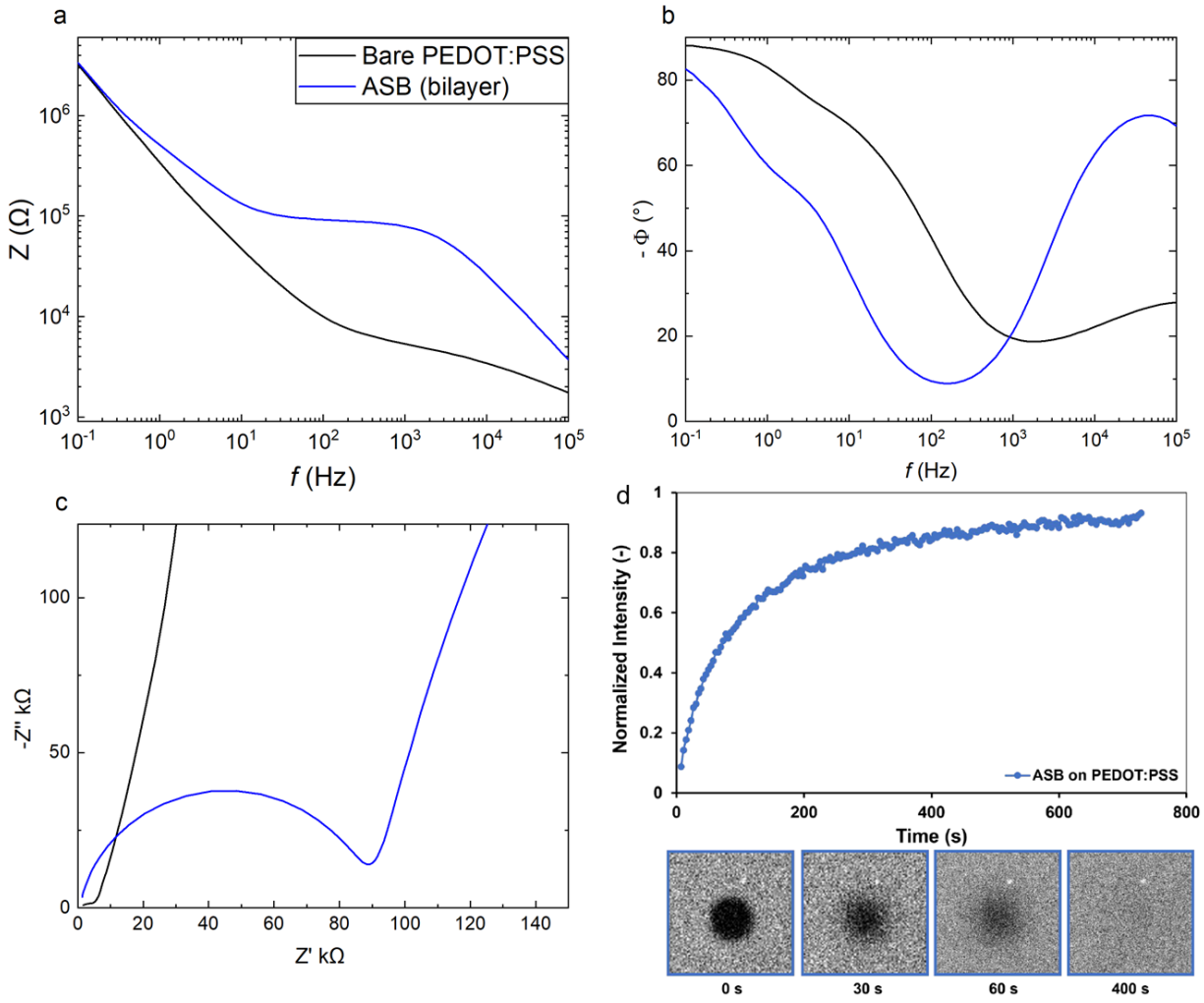

Figure 4.2: Electrical and optical characterisation of the ASB on PEDOT:PSS-coated glass slides and electrodes. EIS measurements taken before (PEDOT:PSS/bare electrode) and after ASB formation, showing Bode plots (**a**) impedance and (**b**) phase shift, Φ, as a function of frequency, and (**c**) Nyquist plot with the complex imaginary (Z'') and real (Z') impedances. (**d**) Typical FRAP measurement of ASB on PEDOT:PSS-coated glass slide. Images depicting (from left to right) photobleached, initial recovery, partial recovery, and complete recovery, with D = 0.500 ± 0.002 μm^2/s and MF = 0.99 ± 0.03. n=3.[131]

4.3.4 Optical detection of cEXO binding/blocking to the ASB[§]

Independent of the route taken by cEXOs after initial contact with the cell membrane, binding is a common initial step for all mechanisms of EV function. Therefore, targeting binding represents a therapeutic strategy for inhibiting malignant outcomes of cEXO–cell interactions. To detect binding to the ASB, R18-fluorescently labelled cEXOs were incubated with an ASB, and their initial interactions were captured using a TIRF microscope. cEXO binding to the ASB was observed within 3 min of contact, with some particles being stably bound and others binding and detaching from the ASB. Images captured using TIRFM after 30 additional minutes of incubation show that cEXOs remained attached to ASBs (**Figure 4.3a**), indicating stable binding after this time. In contrast, **Figure 4.3c** shows a negligible amount of cEXOs binding to POPC/PEG2k-SLB, as expected since POPC/PEG2k-SLBs are inert, non-fouling surfaces and do not contain adhesion proteins to mediate binding. This also suggests that in the ASB, the cEXO binding specificity comes from the incorporated ADSC membrane components.

Binding between cEXO and ADSCs is known to be mediated by at least two proteins, one on the surface of each entity. Since it is established that integrins, including β1, α3, and α5, have been involved in binding of different types of exosomes to recipient cells,[50,57] integrin β1 is likely one of the proteins involved in cEXO–ADSC binding. To assess the potential of blocking integrin β1 as a strategy to decrease cEXO binding, the surface of the ASB was treated with an anti-integrin β1/CD29 primary antibody (referred to as CD29-Ab hereinafter) prior to incubation with cEXOs. Treatment resulted in significantly reduced cEXO binding compared to the untreated ASB (**Figure 4.3a,b,d)** with a similar number of cEXOs binding to the POPC/PEG2k-SLB. These results indicate that integrin β1 plays a specific role in cEXO–ADSC binding, recapitulated in ASB, and its blockage decreases attachment of cEXOs to ASB. A key advantage of SLBs is their high amenability to scale up, through rapid functionalization

[§] Work by Uribe

and patterning of surfaces and integration with microfluidic and electrical components. Toward this end, the ASB was integrated with electrical devices to create a bioelectronic screening platform for label-free and sensitive detection of cEXO binding/blocking.

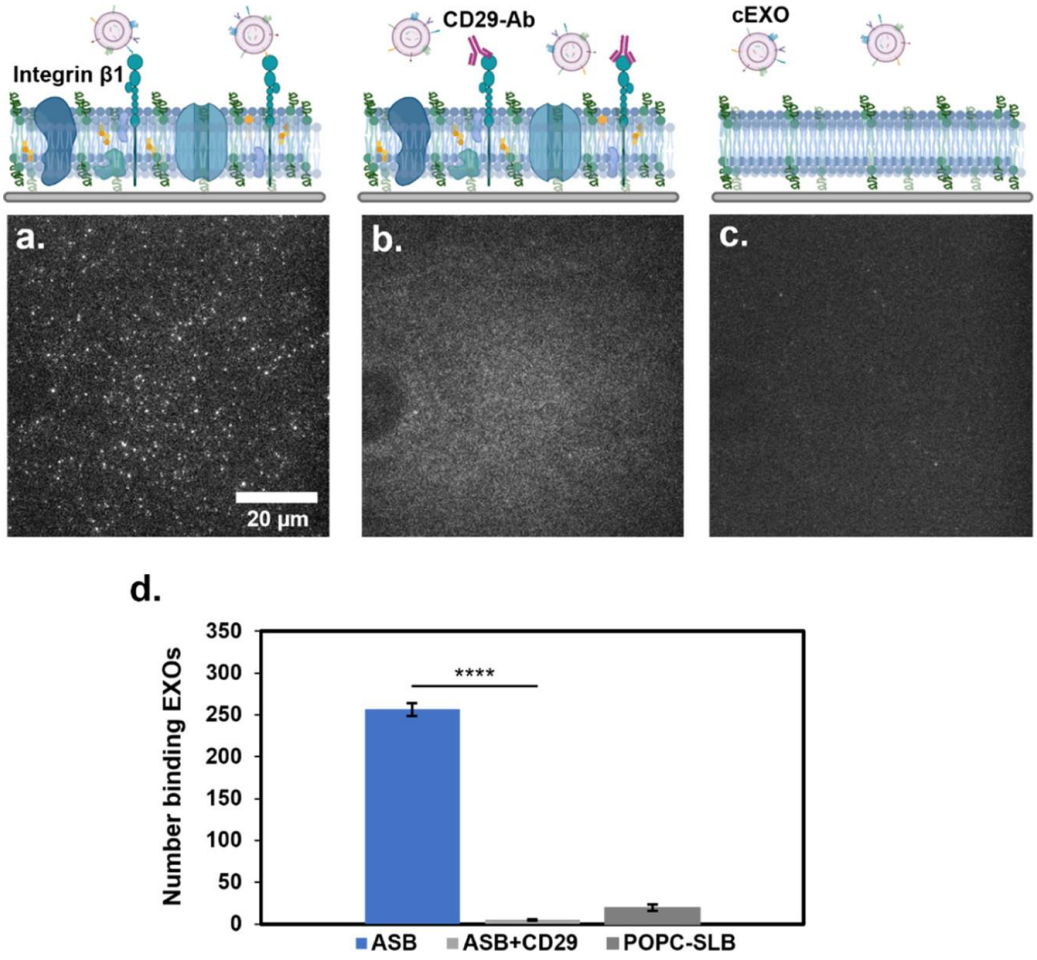

Figure 4.3: Integrin β1/CD29 plays a role in cEXOs binding to ASBs. TIRFM images of cEXOs binding to (**a**) ASB with no treatment. (**b**) ASBs treated with CD29/integrin β1 antibody. (**c**) POPC-PEG2k SLB. (**d**) Quantification of cEXOs bound to ASBs, non-treated, and treated with integrin β1/CD29 antibody, and the POPC-PEG2k SLB after 30 min of incubation (mean ± s.e.m.; n= 3). ****$p \leq 0.0001$.[131]

4.3.5 Electrical monitoring of cEXO binding to ASBs

By coupling the ASBs with MEAs, changes in the electrical signals resulting from modifications of the membrane properties associated with the binding of cEXOs can be probed. The capability of electrical methods for monitoring biological events at the cell plasma membrane have previously been demonstrated.[130,137,291] ASBs were formed on PEDOT:PSS-based MEAs (**Figure 4.4a**) and characterised using EIS.

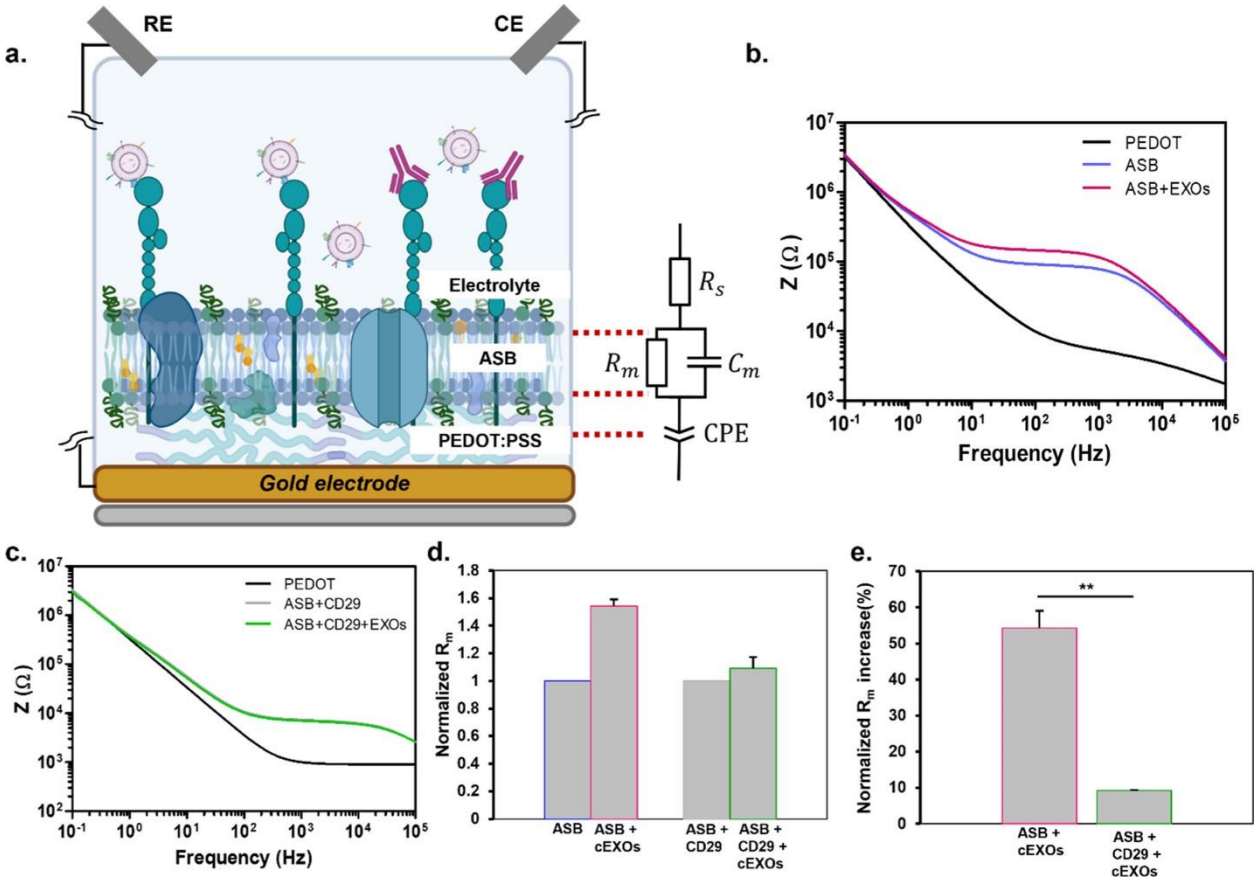

Figure 4.4: Electrical readouts support the role of integrin β1/CD29 in cEXO binding to ASBs. (**a**) Experimental setup showing ASB formed on top of the PEDOT:PSS-coated Au electrode with reference electrode (RE) and a counter electrode (CE) all in direct contact with an electrolyte. The EEC is shown with R_s being the solvent/electrolyte (PBS), R_m and C_m being the membrane resistance and capacitance, respectively, and the PEDOT:PSS modeled as a constant phase element (CPE). Made with Biorender.com. Representative Bode plots of cEXOs binding to the ASB (**b**) and cEXOs binding to the CD29-Ab-treated ASB (**c**). (**d**) Normalised R_m of ASB prior to cEXOs binding showing ASB + cEXOs in the absence and presence of CD29-Ab treatment (mean ± s.e.m.; n= 5). (**e**) Comparison of the normalized percentage increase in R_m between the ASB + cEXOs addition and between the ASB + CD29 + cEXOs addition, as defined by equation 1 (mean ± s.e.m.; n= 5). **p ≤ 0.01.[131]

The impedance magnitude, Z, as a function of frequency, is captured in the Bode plots shown in **Figure 4.4b,c** and the complex impedance, comprising real (Z') and imaginary (Z'') impedance, is captured in the Nyquist plots shown in **Figure 4.5**. EEC modelling was performed to extract membrane resistance (R_m) values, which were used as figures of merit. The magnitude of the calculated membrane resistance relates to the membrane ion permeability and has thus been successfully used in similar setups as a measure of the membrane "leakiness" or the membrane "integrity". Previous studies demonstrate that membrane-binding events result in an increase in the membrane resistance, whereas membrane events that could potentially result in membrane "leakiness" (i.e., disruption, pore formation, and ion channel

opening) result in a decrease in membrane resistance.[129,130] R_m was calculated for the ASB and the ASB with integrin β1 blocking (ASB + CD29), and again after the addition of cEXOs (+cEXOs) for each condition.

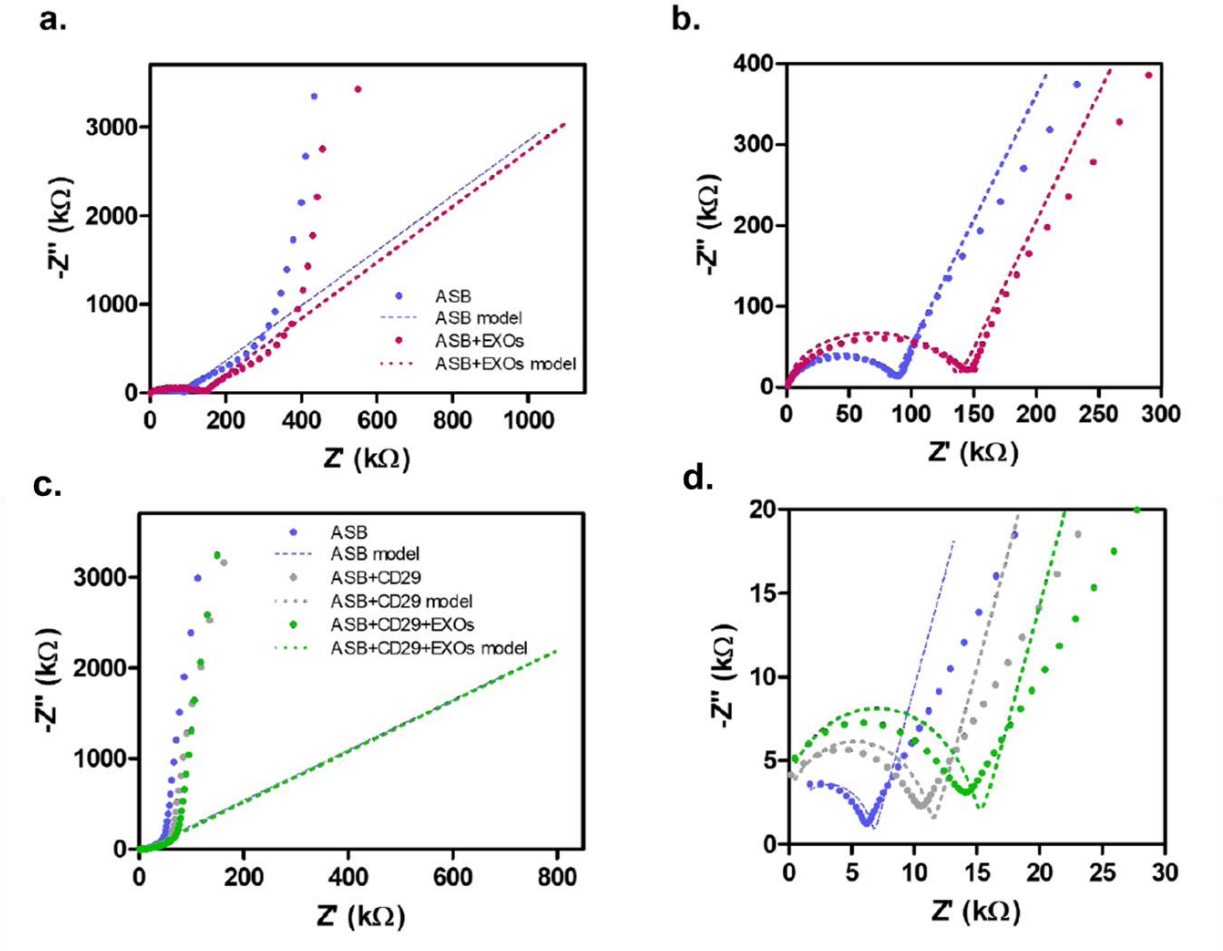

Figure 4.5: Representative Nyquist plots of cEXO-ASB binding/blocking. (a, b) cEXO binding to ASB, and (c, d) CD29-Ab blocking cEXOs binding to ASB. b and d are zoomed in views of a and c, respectively. The capacitance of bare PEDOT: PSS is $C_{m,PEDOT:PSS} = 1.09\ nF\ \text{cm}^2$. The EEC model (Figure 4.4a) fitted to the raw impedance data was used to extract membrane resistance R_m and is denoted by the dashed lines in each plot. This data complements the Bode plots presented in Figure 4.4b,c and is further evidence that cEXOs binding results in a detectable electrical change and that blocking CD29 with antibodies inhibits cEXO binding.[131]

The experimental protocol was carried out using multiple single MEAs for each condition to control for MEA batch-to-batch variability. Measurements were taken from multiple electrodes within the same MEA (i.e., of the same ASB) for each condition to control for electrode-to-electrode variability and to ensure that measurements were only collected from electrodes, where there was good coverage of the ASB. The ASB sealing quality was assessed based on the increase in impedance compared to the bare PEDOT:PSS impedance, as observed in the Nyquist and Bode plots and as determined from the increase in the derived R_m value. It

was typical to achieve a 25–50% success rate of electrodes whose R_m reflected a tightly sealed lipid bilayer and were thus qualified for cEXO binding studies. The calculated $R_m$values were normalized to the baseline SLB readout for each measurement due to the variability in absolute R_m between MEAs, which ranged between 0.01 and 1.02 kΩ cm^2. This range in R_m values was likely caused by small differences in the ASBs, as the MEAs are very sensitive to defects found in the bilayer. These values are comparable to values obtained from similar setups that used mammalian cell-derived SLBs.[129,130,137] Thus, the relative change in magnitude of R_m before and after cEXOs binding for each condition was assessed (**Figure 4.4d,e**). This allows cEXO binding to be inferred from changes in R_m, essentially rendering R_m a function of the abundance of cEXOs binding to the membrane and allows comparison across multiple experiments performed on different MEAs, regardless of the baseline R_m obtained. In the case of the CD29-Ab blocking condition, R_m of the ASB after treatment with CD29-Ab was used as a reference for cEXO binding. The addition of anti-CD29 Ab to the ASB resulted in a small increase in $R_m \sim$ 14% (from 0.010 to 0.011 kΩ cm^2; **Figure S8.9**). The relative change in normalized R_m, ΔR_m , is defined in equation 1.

$$\boldsymbol{\Delta R_m = \frac{R_{m,cEXO} - R_{m,ASB^*}}{R_{m,ASB^*}}} \quad \textbf{(1)}$$

where R_{m,ASB^*} is either ASB or ASB+CD29. The addition of cEXOs caused an average increase in normalized R_m of ~54% and ~9% for the non-treated and anti-CD29 Ab-treated conditions, respectively (**Figure 4.4e**). Preparations containing no EVs were also tested on the ASBs as a control, which yielded no change in the electrical readouts. These results align with the ones from the optical experiments and provide further proof that blocking integrin β1 receptors with anti-CD29 antibodies reduces cEXOs binding to the ASB.

In summary, using optical and electrical analytical approaches, the ASB platform enables the detection of cEXO binding to the plasma membrane and verification of the mediating role of integrin β1 in this process. Fluorescence/label-based methods are more established in this field, and by confirming the optical data with the novel electrical readouts, the ability to detect cEXO binding to native cell membranes in a label-free manner was demonstrated for the first time. To validate these results and implicate cEXO function in tumourigenesis, a cell-based assay was performed to investigate the biological outcome of blocking integrin β1 in ADSCs by measuring changes in proangiogenic behaviour. Results from this study were obtained by co-author Johana Uribe and are presented in Appendix B, section 8.11.3. In brief, exposure to cEXOs promotes cell proliferation and upregulation of vascular endothelial growth factor

(VEGF), a marker of cancer-associated angiogenesis, in ADSCs. Blocking cEXO binding with CD29-Ab treatment results in a decrease in both proliferation and VEGF secretion. This indicates that integrin β1 plays an important role in cEXO–ADSC binding in live cells (adding further credibility to the ASB platform) and blocking it is a strategy with therapeutic potential to decrease cEXO-induced proangiogenic activity that occurs from VEGF upregulation and proliferation of ADSCs in the TME.

4.4 Outlook

The ASB platform conserved the lateral fluidity and the presence of integrin β1, important characteristics of the ADSC surface, making a relevant *in vitro* model of the human primary ADSC plasma membrane. This system was used to recapitulate cEXO binding to the ADSC plasma membrane, isolating it from subsequent cEXO internalization and cargo delivery, in a cell-free manner. The planar nature of the stem cell membrane model renders it amenable to surface-sensitive analytical techniques, optical and electrical, which hold potential for extracting valuable information regarding cEXOs' binding and function that would otherwise remain elusive to cell-based systems and its complementary analytical techniques. This geometry facilitated the integration of the ASB with a PEDOT:PSS-based MEA and detection of cEXO binding using optical (TIRFM) and electrical (EIS) techniques, allowing visualization and label-free monitoring of such an interaction. Moreover, a significant decrease of cEXO binding to the ASB was demonstrated post anti-CD29 Ab treatment (as a means to block integrin β1) with both optical and electrical readouts. These results suggest that integrin β1 receptors were bound to CD29 Ab and not available to interact with cEXOs, supporting the initial hypothesis that integrin β1 facilitates cEXO binding to ADSCs. Likewise, treatment of cultured ADSCs with CD29 Ab prior to cEXO addition led to a small change in VEGF secretion and cell proliferation, both processes highly upregulated in ADSCs treated with cEXOs in the absence of CD29 Ab. This validates the results obtained with the bilayer model, demonstrating the ability of CD29 Ab to reduce cEXO binding to ADSCs and its malignant outcomes, and it further corroborates an important role of integrin β1/CD29 in cEXO–ADSC binding.

The detection of low levels of remaining cEXOs-ASB binding, particularly by electrical detection, and some increase in VEGF secretion and cell proliferation in ADSCs despite CD29 blocking suggests the involvement of other molecules in this binding. This possibility opens a new avenue to use this ASB system and study the role of other ADSC and cEXO surface components in cEXO–ADSC interactions and investigate strategies to inhibit this through drug

screening. Furthermore, the ASB will facilitate the study of cEXO binding kinetics and the mechanisms behind it to further attain its complete inhibition along its malignant outcomes.

Next, the development of a cell-based, bioelectronic phenotypic screening platform for monitoring a cancer EV-driven metastatic process, called the epithelia-to-mesenchymal transition, in real-time is described.

“Success is not final, failure is not fatal: it is the courage to continue that counts.”

— *Winston S. Churchill*

5 BIOELECTRONIC PHENOTYPIC SCREENING PLATFORM FOR MONITORING TEV-INDUCED EMT

Preamble

This chapter contains work submitted for peer-review by W. C. **Traberg**, J. Uribe, V. Druet, A. Hama, C-M. Moysidou1, M. Huerta, R. McCoy, D. Hayward, A. Savva, A. M. R. Genovese, S. Pavagada, Z. Lu, A. Koklu, A.-M. Pappa, R. Fitzgerald, S. Inal, S. Daniel, R. M. Owens, Bioelectronic platform for real-time phenotypic screening identifies heparin as an inhibitor of extracellular vesicle-driven metastasis.

5.1 Introduction

Recently, TEVs have been found to play a pivotal role in metastasis[6,7] by conferring oncogenic potential[8] and inducing malignant transformation in recipient cells via the transfer of their active cargo[9]. TEVs drive a process called the epithelial-to-mesenchymal transition (EMT), which is a central component of metastasis[7]. EMT is a reversible process by which epithelial cells at the invasive front of carcinoma acquire a mesenchymal phenotype[10] and develop the ability to migrate, invade[11], and disseminate via circulation to form metastases in distal organs[12]. Post-internalisation of TEVs, recipient cells exhibit physiological changes associated with alterations of their transcriptome and proteome.[299,300] TEV exposure results in increased expression of several mesenchymal markers, including vimentin and TWIST1,[301,302] decreased expression of epithelial markers, including reciprocal changes in E-cadherin and N-cadherin expression[299] – the so-called cadherin switch. Functionally, TEVs enhance the migratory and invasive properties of recipient cells.[10,11] Targeting TEVs with therapeutic intervention could represent a novel avenue for preventing EMT, and thereby metastasis.

Phenotypic drug discovery approaches incorporating cell-based disease models have the potential to address the incompletely understood complexity of diseases, compared to target-based drug discovery. Although phenotypic screening can be an attractive proposition for efficiently identifying functionally active hits that lead to first-in-class drugs,[292] current readouts rely on sensing technologies that are invasive; perturbing the system of study (e.g. omics), produce discrete data, and/or scale poorly (e.g. microscopy imaging).[90,91] This makes it difficult to investigate the temporal relationship between measured pharmacodynamic response and pharmacokinetics for quantitative translation to *in vivo* outcomes.[293] Moreover, utilising low-throughput technologies to screen thousands of potential hits during the early stages of drug discovery is cost- and time-prohibitive.[294] Thus, there is a pressing need to integrate disease-relevant cell-based models with novel, scalable sensing technologies that produce unbiased high-content and multiparametric readouts, ideally in a continuous manner, without disrupting the native state of the system of study.[292] Here, we present a platform based on organic bioelectronic technology that fulfils these requirements.

The OECT has been integrated with *in vitro* models of varying complexity spanning from plasma membranes to 3D complex cell cultures[26–31], possible due to its widely reported biocompatibility[32]. PEDOT:PSS-based OECTs have been used to monitor cell coverage and differentiation, as well as epithelial barrier integrity both in Transwell format and with cells adhered directly on the device surface[26,28,39,40]. The latter involves the growth of a monolayer of

cells on the channel and the gate, which introduces a barrier for ion motion in the electrolyte (cell culture media), directly affecting the transistor output and in effect using the OECT as an impedance biosensor[28,41]. Monitoring tight junction modulation, nephrotoxicity, cancer invasion, wound-healing, and toxicology[27,28,42–44] are only some of the various application areas where impedance-based OECTs interfaced with cell cultures have been successfully used for biomedical research, although biological validation of the electrical readouts has been limited in scope to date.Capitalising on its key attributes, interfacing OECTs with a cell-based EMT-disease model could address current issues facing sensing technologies and unlock higher throughput phenotypic screening for drug discovery. We propose utilising OECTs and electrical measurements to continuously monitor EMT *in vitro* and to produce high-content, quantitative time-series data that can be correlated with cell phenotype. We integrated OECTs with MCF10A cells; a normal, non-tumuorigenic, pre-neoplastic mammary cell line,[295,296] and exposed these to TEVs derived from MDA-MB-231 cells; a highly aggressive and invasive triple-negative breast cancer (TNBC) cell line,[297] to recapitulate a model of invasive ductal carcinoma (**Figure 5.1** and supplementary discussion 1). Key features of this work are: (i) isolating and characterising EVs; (ii) investigating the ability of TEVs to induce EMT in MCF10A cells using combined electrical and biological readouts, providing mechanistic insight using an epigenetics approach; and (iii) developing a robust and scalable platform for the functional, phenotypic screening of anti-cancer/anti-metastatic drugs, e.g. heparin.

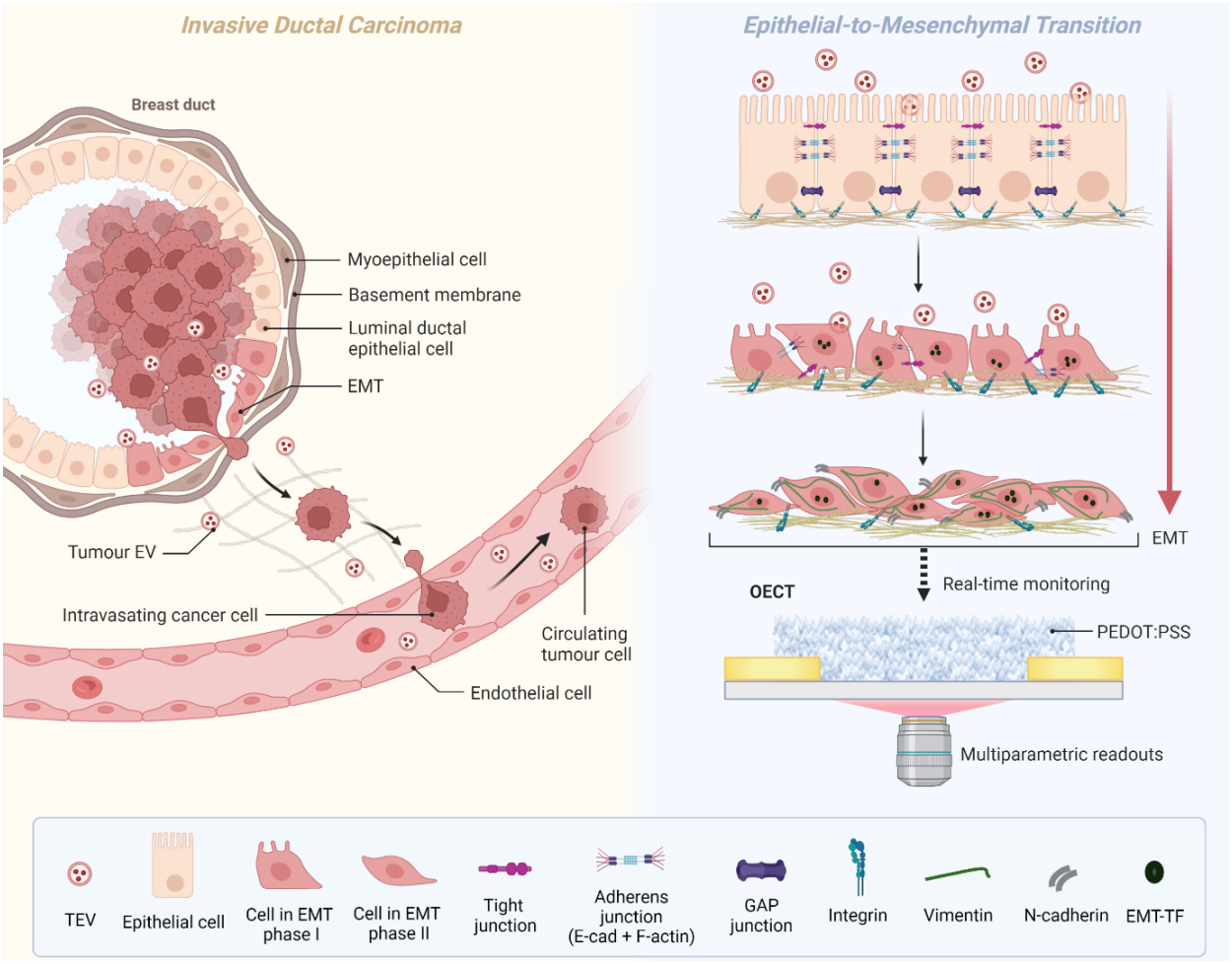

Figure 5.1: A model to recapitulate invasive ductal carcinoma integrated with an OECT platform for monitoring TEV-induced EMT. EMT has been implicated in the initiation of metastasis, as epithelial cells at the invasive front of carcinomas acquire migratory and invasive properties to break through the basement membrane and disseminate via circulation to form metastases in distal organs.[298] By integrating a highly relevant model of breast cancer metastasis associated EMT on OECTs, this malignant process can be monitored in real-time with multiparametric readouts and the effect of TEV-targeting drugs can be assessed.

Here, we demonstrate the ability of the OECT to monitor TEV-induced EMT in real-time, without compromising compatibility with conventional end-point assays. We leverage the capabilities of OECT devices to provide a continuous, label-free, non-disruptive, and *quantitative* measure of EMT *in vitro*, using electrical measurements as a novel functional readout of a metastatic process, as well as of TEV function. We correlate the electrical readouts with molecular biology and optical microscopy techniques to validate the OECT-based measurements. Finally, we demonstrate that we can dynamically monitor therapeutic response and find that heparin, a competitive inhibitor of cell surface receptors, effectively abrogates TEV-induced EMT in MCF10A cells, showcasing the drug screening capabilities of the platform.

5.2 Material and methods

5.2.1 Study Design

The objectives of this study were (i) to develop a phenotypic screening platform based on bioelectronic technology to dynamically monitor TEV-induced EMT, (ii) validate the electrical readouts with biomolecular assays, and (iii) to test the blocking effect of heparin on TEV function and provide proof of principle that OECT phenotypic screening can identify potential anti-metastatic drug candidates. The effects of different treatments on MCF10A phenotype and EMT status was assessed in a controlled laboratory experiment using continuous OECT-based measurements and a range of *in vitro* assays. The treatments included exposure to EVs derived from MDA-MB-231 and HEK-293 cells (from more than four different cell passages), TGF-β1, and heparin. MDA-TEV, non-treated, heparin, and heparin + MDA-TEV experiments were performed three times and TGF-β1, HEK-EV, and transient heparin experiments were performed twice with different MCF10A cell passages. Experiments were performed on both OECTs and in cell culture plates in parallel and stopped at prospectively defined study endpoints.

5.2.2 Cell culture

MDA-MB-231, HEK-293, and MCF10A cells were used for the studies described in this chapter. Cell culturing is described in detail in Appendix A, section 8.1.

5.2.3 Extracellular vesicle isolation

For EV harvesting, MDA-MB-231 and HEK-293 cells were cultured until 80% confluent, washed twice with phosphate-buffered saline (PBS; TFS), and incubated with serum-free culture medium for 48 hours before the conditioned medium (CM) was collected for further processing. CM from MDA-MB-231 and HEK-293 cells was processed using a protocol adapted from.[303] CM was centrifuged at 4 °C, 3 000 *x g* for 30 min to remove cells and cellular debris. The supernatant was centrifuged at 4 °C, 100 000 x *g* for 4 h (Type 50.2 Ti Fixed-Angle Rotor, Beckmann XL-90 Ultracentrifuge) to pellet out EVs. The pellet was resuspended in 500 µL MCF10A cell culture medium or PBS (depending on the downstream application) and stored at 4 °C. For cell experiments, EVs were used within 2 days of isolation, and for particle imaging (TEM) and size analysis, EVs were analysed on the same day.

5.2.4 EV characterisation

EV characterisation is described in Appendix A, section 8.2.

5.2.5 Immunoblot analysis

Cultured cells were washed twice with cold PBS and solubilised in 1 mL radio immunoprecipitation assay buffer (RIPA) Lysis and Extraction Buffer supplemented with 10 μL Halt Protease Inhibitor Cocktail and 10 μL EDTA (TFS) immediately before use. Samples were incubated on ice for 5 min with agitation (20-30 min for MCF10A cells), aspirated buffer was collected into a microcentrifuge tube and centrifuged at 4 °C; 14 000 x *g* for 15 min to pellet cell debris. The supernatant contained the whole-cell lysate and was quantified using a Qubit 4 Fluorometer (TFS) per manufacturer's instruction.

Samples were diluted in lithium dodecyl sulfate (LDS) sample buffer (4X Bolt; Invitrogen), denatured by heating for 10 min at 70 °C, and subjected to electrophoresis using precast NuPAGE Novex 4-12% Bis-Tris Proteins Gels (Invitrogen) in NuPAGE MES SDS Running Buffer (Invitrogen) under non-reducing conditions at constant 200 V for 30 min. The same amount of protein (between 10-25 μg) from each sample was loaded into the gel wells. Proteins were electrotransferred onto PVDF Transfer Membranes (TFS) using NuPAGE Transfer Buffer (Invitrogen). Membranes were blocked with 5% (w/v) BSA in PBS (TFS, Oxoid) with 0.1% (v/v) Tween-20 (PBST; TFS) for 1 h. For MCF10A blots: Membranes were probed with mouse anti-vimentin (abcam; 1:1 000), mouse anti-F-actin (abcam, 1:500), rabbit anti-E-cadherin (abcam; 1:1 000), mouse anti-N-cadherin (1:1 000), mouse anti-TWIST1 (1:250), and mouse anti-GADPH (Sigma-Aldrich; 1:25 000) monoclonal primary antibodies for 1 h in PBST. This was followed by incubation with HRP-conjugated anti-mouse IgG H&L (Invitrogen; 1:10 000) and anti-rabbit IgG H&L (abcam; 1:10 000) secondary antibodies in PBST for 1 h. All incubations were carried out on a shaker at RT or 4 °C. Western blots were washed 3-5 times in PBST for 5 min after each incubation step and were visualised using Pierce enhanced chemiluminescence (ECL) Western Blotting Substrate (TFS) on a G:BOX Chemi XX6 (Syngene). Band intensity was quantified using ImageJ Software Band function and normalised with GADPH to compare relative protein expression between conditions.

5.2.6 Enzyme-linked immunosorbent assay (ELISA)*

To investigate the expression of mesenchymal marker N-cadherin in MCF10A cells before and after treatment with MDA-TEVs, an ELISA assay was done. Following the manufacturer's protocol, a Human N-cadherin DuoSet ELISA kit (R&D Systems) was utilized to measure the concentration of N-cadherin in MCF10A lysates on day 7 of treatment. Absorbance at 450 nm, as recommended, was measured for all samples, and the concentration of N-cadherin was found using the absorbance and concentration of the protein standards and the absorbance of the unknown concentration samples. The concentration of N-cadherin protein present in MCF10A lysates was normalized by total protein content.

5.2.7 Cell density from IF micrographs†

IF images were analysed using ImageJ software. Cell count was performed using the software. Images were converted to 8-bit, and the threshold was adjusted to minimise noise and amplify contrast. The binary tools Fill Holes and Watershed were used to automatically determine cell borders. Cells were automatically counted using the Analyze Particles tool. Both cell counts including and excluding image borders were performed, and their mean was used as the final cell count.

5.2.8 DNA extraction and methylation qPCR‡

QIAamp DNA mini kit (Qiagen) was used to extract DNA from TEV-treated un-treated MCF10A cells according to the manufacturer's protocol. A total DNA input of 300 ng was bisulfite converted using the EZ DNA Methylation Gold kit (Zymo) following manufacturer's protocol. For the qPCR assay, a TaqMan approach was used involving gene-specific primers and probe targeting the methylated sequences. No amplification detected was considered to be non-methylated DNA for the target. Each sample was run in triplicate for the two genes; TWIST1 and

* Work conducted by Uribe

† Work conducted by Genovese

‡ Work conducted by Hayward

TFPI2, and for the house-keeper gene B-actin used to control for variances in DNA input. A standard curve was initially established using fully methylated DNA (Merck), and each subsequent qPCR run included a calibrator (1:100 dilution) to allow for quantification and negative controls.

Each PCR contained a final concentration of 1x LightCycler Probes (Roche), 0.6 µM each primer, 0.2 µM probe, 2.5% DMSO, 1M betaine and 2 µL bisulfite converted DNA in a final reaction volume of 10 µL. Reactions were carried out using a LightCycler 480II (Roche) using the following qPCR thermal cycling conditions; 95ºC for 10 mins, 50 cycles of 95ºC for 15 sec, 60 ºC for 60 sec including data acquisition. Methylation was determined as previously described by Chettouh et al., (2018), equation 2.

$$\boldsymbol{Total\ Methylation}\ (\%) = \sum \frac{(\frac{\boldsymbol{A}}{\boldsymbol{B}})}{(\frac{\boldsymbol{C}}{\boldsymbol{D}})} \qquad (\mathbf{2})$$

A= methylation value of gene of interest in each sample; B = methylation value of the gene of interest in the calibrator; C= amplification value of β actin in each sample; and D= amplification value of β actin in the calibrator.

Sequence Name	Nucleotide Sequence
TWIST1_Forward	CGTCTACAACTCCTCGTAAAACTACG
TWIST1_Reverse	TCGGGTAGTTCGGTTTAGGGTAAG
TWIST1_Probe	[6FAM]ACTCCCGCCGCCGCTACTACTACC[TAM]
TFPI2_Forward	TGTAGGGGGTCGGGCGGTTC
TFPI2_Reverse	CGCTCGCCCCGCATAAAACG
TFPI2_Probe	[6FAM]CGTTTGGCGGGAGGAGGTGCGCGGTT[TAM]
Beta-actin_Forward	TGGTGATGGAGGAGGTTTAGTAAGT
Beta-actin Reverse	AACCAATAAAACCTACTCCTCCCTTAA
Beta-actin_Probe	[6FAM]ACCACCACCCAACACACAATAACAAACACA[TAM]

Table 5.1: Nucleotide sequences for the genes tested

5.2.9 Cell-based EMT experiments on OECTs

OECTs were cleaned thoroughly with Milli-Q water and isopropanol prior to sterilising by immersion in 70% ethanol for 24 hours. The devices were left in a sterile MSC to promote evaporation of ethanol before incubating with normal culture medium overnight. Cloning cylinders with an area of 0.5 cm^2 doubled as culture wells which were stuck onto OECT devices with PDMS. The wells defined the area in which the cells were cultured, with 3-6 channels and a gate electrode accessible within each well. MCF10A cells were then seeded at $1x10^4$ cells/cm^2 and cultured for 3 days until cell coverage was ~70-80%, covering all channels fully, at which point the cells displayed a polygonal morphology, characteristic of an epithelial phenotype (**Figure 5.3A**). MCF10A cells are usually serum-starved for EMT studies[304] but the normal culture medium does not contain serum, therefore, the base medium was kept the same for all conditions. Treatment was started on culture day 3 (called treatment day 0) and cell culture medium either pre-supplemented

with 200 μg MDA-TEVs, 185 μg HEK-EVs, 10 ng/ml TGF-β1, heparin, or without supplementation. The discrepancy in dose between MDA-TEVs and HEK-EVs is due to the slight difference in protein-to-vesicle ratio of each EV type (see **Table 5.2**). EV dose, as measured by total protein content and correlated with vesicle concentration (see **Table 5.2**), was normalised to the number of MCF10A cells seeded to ensure that an equal number of cells were exposed to an equal number of EVs (in this case 12 x 10^9 vesicles per 5,000 cells seeded), regardless of culture area and medium volume. EV doses of 50-200 μg are typical[302,305,306] and a 5 ng/ml dose of TGF-β1 induces EMT in MCF10A cells.[304] but prolonged treatment with 5 ng/ml TGF-β1 (6 days) is necessary to induce EMT in MCF10A cells,[307] therefore the dose was increased to 10 ng/ml[308] to accelerate this process. Supplemented exogenous EVs were isolated from their respective cell lines every 2 days and used fresh to prevent degradation of EV function by prolonged storage times. Electrical measurements were performed prior to medium changes. Cells in the OECTs were fixed for immunofluorescence (IF) staining, lysed to collect whole-cell lysates for immunoblot analysis, or used to assess cell viability on treatment day 9 (after 12 days of culture).

5.2.10 Heparin treatment

Cells were incubated with or without 200 μg MDA-TEVs in the presence or absence of 10 μg/ml[10,11,309] heparin sodium salt from porcine intestinal mucosa (Sigma-Aldrich). Heparin treatment was refreshed every 48 h concurrently with medium changes (supplemented with MDA-TEVs or not). In the transient heparin treatment study, cells were treated with MDA-TEVs and heparin concurrently until day 3, after which time the cells were washed thoroughly with PBS three times[309] and treated with MDA-TEVs for the remainder of the experiment.

5.2.11 OECT measurements

The fabrication of OECTs[§] and a detailed description of the electrical measurements is provided in Appendix A, section 8.6. In brief, OECTs were characterized using a dual-channel source-meter unit (NI-PXI) with custom-written control code in LabVIEW. All measurements

[§] Electronic devices were provided by Victor Druet from the Organic Bioelectronics Laboratory at KAUST, SA

were performed using the integrated planar gate electrodes. The channels studied were either 50x50 μm or 100x100 μm in length and width.

5.2.12 Extraction of cell layer resistance from Z vs frequency plots

The electrochemical impedance spectra (EIS) was obtained from the OECT channels using the source, drain and gate as the three electrode setup and a custom made MATLAB code as described earlier by Rivnay et al.[215] EIS was performed at a frequency range between 100 kHz to 0.1 Hz at V = 0 V *vs* V_{OC} with an AC amplitude of 10 mV. We extracted the resistance value for each condition by using equation 3 and the impedance magnitude value at 2 kHz, assuming that capacitance contribution to the overall signal is negligible.

$$\boldsymbol{Z = \sqrt{R^2 + \frac{1}{\omega^2 C^2}}} \qquad (\mathbf{3})$$

5.2.13 OECT data analysis

Cut-off frequency (*CF)* was normalised to treatment start date using the following equation: $Normalised\ CF = CF_n/CF_{n=0}$, where n is treatment day and $CF_{n=0}$ refers to the cut-off frequency on treatment day 0.

5.2.14 Confocal Microscopy**

Viability assay: the viability of cells growing on the OECT platform was checked by evaluating plasma membrane intactness and enzymatic activity via a two-colour fluorescence cytotoxicity/viability assay (LIVE/DEAD™ Viability/Cytotoxicity Kit, for mammalian cells, Invitrogen). The assay was performed at the end of the experimental period (treatment day 9; culture day 12), by removing cell growth medium, washing thoroughly with PBS and adding the reagents. After 1-hour incubation, the reagent was replaced with PBS before visualization with a confocal microscope.

** Work conducted together with Moysidou

Immunofluorescence staining: All samples were fixed with 4% paraformaldehyde (PFA, TFS) for 10 min, at room temperature; then, samples were thoroughly washed with PBS and stored at 4 ^{o}C until ready to use. Prior to immunofluorescently labelling the samples, cells were permeabilized in 0.1% v/v Triton X-100 (Fisher) for 10 min and then blocked for nonspecific binding with 1% wt/v BSA (TFS) and 0.1% v/v Tween-20 (TFS) in PBS for 1 hour at room temperature. The primary and secondary antibodies used are: Phalloidin-iFluor 594 Reagent (abcam), Bisbenzamide H (Hoechst 33342) (abcam). Images were obtained using an epifluorescence/confocal microscope (Axio Observer Z1 LSM 800, Zeiss), using 10x/0.45 and 20x/0.8, (Plan-Apochromat, Zeiss) objective. The 2D micrographs shown are representative of three different frames/locations of each. *Z-stacks and cell height*: For each condition/treatment, z-stacked confocal images were acquired from at least one channel of the respective OECT devices (independent samples). After acquiring these, the height of cells on the OECT channel was measured using the ortho-view (x/z and y/z planes) and graphic features/tools of the confocal microscope software (Axio Observer Z1 LSM 800, Zeiss; ZEN blue edition 3.4). The mean cell height for each condition/channel/sample was calculated from at least eight measurements: the z plane was fixed in the middle/center of each cell layer on the respective OECT channel, as identified by the z-stack series data, and x and y locations were varied within this frame to account for variations of the cell layer height on this surface/plane.

5.2.15 Statistical Analysis

For all experiments performed in this study, variance analysis was performed using a one-way or two-way ANOVA, depending on the number of factors, to find significant differences between conditions. F- and p-value were reported using the following convention: F(df regression, df residual) = [F-value], p = [p-value]). All data were plotted and analysed using Microsoft Excel and OriginLab Pro and they were presented as mean ± s.e.m. Statistical significance levels were determined as follows: *$p \leq 0.05$, **$p \leq 0.01$, and ***$p \leq 0.001$. Each independent experiment corresponds to a biological replicate where cells from different passages were used; n = total number of biological replicates.

5.3 Results

5.3.1 Characterisation of extracellular vesicles

In the present study, MCF10A cells were exposed to either MDA-TEVs or EVs derived from non-tumuorigenic human embryonic kidney (HEK)293 cells (HEK-EVs), to demonstrate that the associated EMT-inducing effect was caused by TEVs specifically, rather than EVs in general – a

so-called specificity check. EVs were isolated by ultracentrifugation, but without further purification to avoid compromising particle yield and may therefore be described as crude EVs. EVs were characterised following the guidelines of The International Society for Extracellular Vesicle (ISEV) for EV research,[70] which include EV quantification by particle number and total protein content, detection of protein markers expected and not expected to be present in enriched EV samples, and single vesicle analysis. Samples were enriched in the classic EV protein biomarkers CD9 and CD63 and did not contain calreticulin; a protein located in the endoplasmic reticulum, nor annexin A1; a microvesicle (150-1,000 nm sized EVs) biomarker (**Figure 5.2**),[310] as expected. Nanoparticle tracking analysis (NTA) revealed heterogenous EV populations, with peak particle sizes of 153 ± 5.1 nm and 112 ± 12.7 nm for MDA-TEVs and HEK-EVs, respectively **(**Fig. 2B**)**. Although such EVs may qualify as exosomes, without confirmation of their endosomal origin, they should be characterised as CD63/CD9-positive EVs [70]. Interestingly, EV particle concentration varied by a factor of >6 between the cell types, with 145 ± 2.3 x 10^9 MDA-TEVs and 23 ± 0.8 x 10^9 HEK-EVs derived from the same number of cells. This is consistent with reports that cancer cells produce an overabundance of EVs compared to healthy cells,[311,312] with their biogenesis possibly enhanced by hypoxic conditions prevalent in the tumour microenvironment (TME).[313] This difference was equally reflected in the total protein content of intact vesicles (**Table 5.2**). EVs had particle zeta potentials of -12.6 ± 0.62 mV for MDA-TEVs and -6.2 ± 0.25 mV for HEK-EVs, as expected [131]. EVs displayed characteristic spherical and cup-shaped morphologies on transmission electron microscopy (TEM) micrographs, and size heterogeneity is apparent with vesicles ranging from 50-200 nm in diameter (Fig. 2C). Immunogold labelling of MDA-TEVs was performed to confirm the presence of CD63 on the EV's surface (Fig. 2Cii).

EV	Size (nm)	ζ-potential (mV)	Concentration (particles/ml)	Protein content (µg/ml)	Ratio of µg protein to billion particles
MDA-TEV	**153 ± 5.1**	**-12.6 ± 0.62**	**145 ± 2.3 x 109**	**2,411 ± 23.2**	**16.6**
HEK-EV	**112 ± 12.7**	**-6.2 ± 0.25**	**23 ± 0.8 x 109**	**350 ± 3.5**	**15.4**

Table 5.2: EV characterisation data. Mean ± s.e.m.; values calculated from measurements of EVs collected from n=2 and 3 different cell passages for each cell line for NTA/zeta potential and protein concentration, measured using a Qubit 4 fluorometer, respectively.

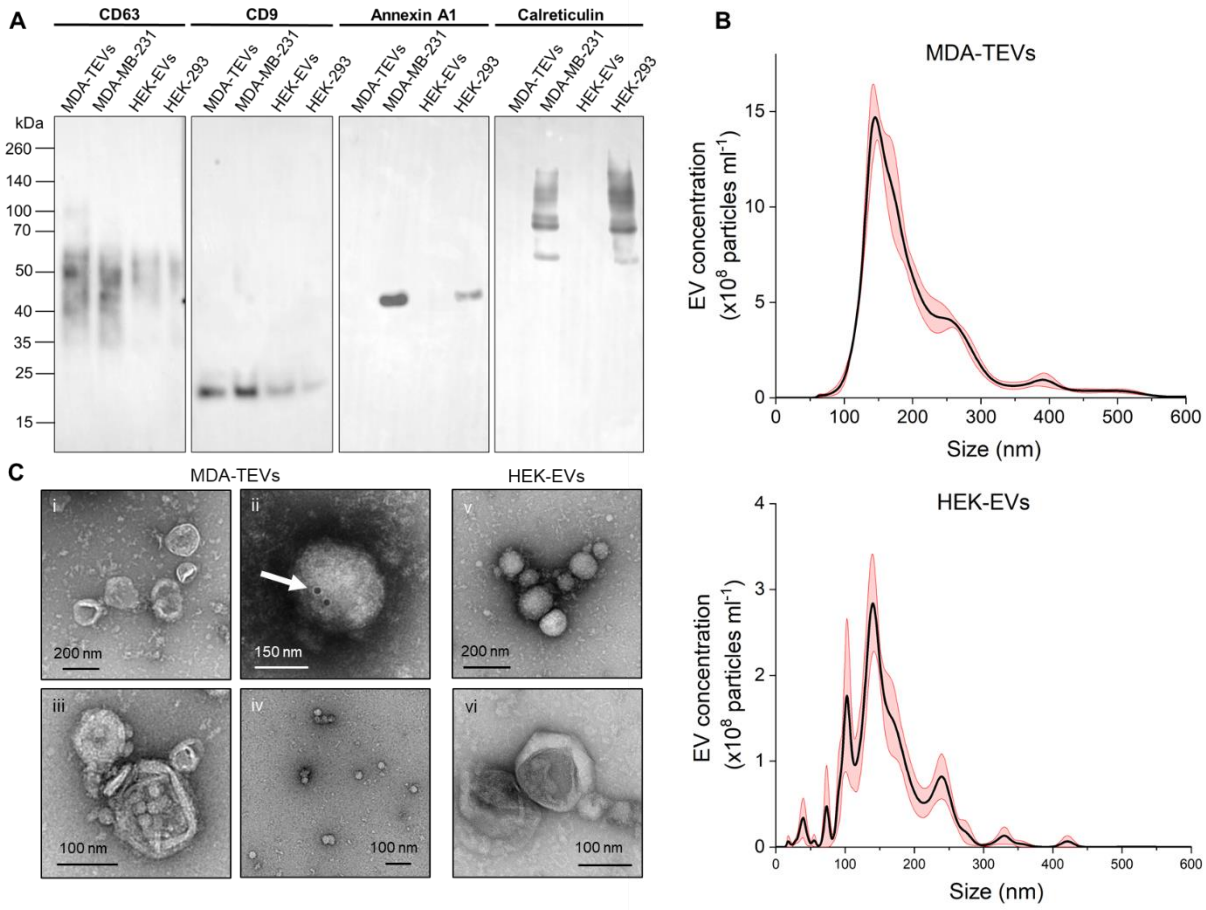

Figure 5.2: EV physical and biochemical characterisation. (**A**) Immunoblots of MDA-MB-231 and HEK-293 whole-cell lysates and (T)EV samples. Proteins were separated on SDS-PAGE gels and membranes were blotted with indicated antibodies. CD9, predicted: 25 kDa; CD63: smeared band between 35-60 kDa (multiple glycosylated forms influence gel migration, therefore CD63 appears as a smear in the 30-60 kDa range, as expected [314]); annexin A1, predicted: 38 kDa; calreticulin, predicted: 55 kDa (other bands may indicate presence of dimers and multimers). Unedited immunoblots are available in fig. S1. (**B**) Concentration and size distribution, calculated by NTA, of EVs (mean ± s.e.m.; n=2 per EV type), with peak particle sizes of 153 ± 5.1 nm and 112 ± 12.7 nm for MDA-TEVs and HEK-EVs, respectively. (**C**) Representative negative stain TEM micrographs of indicated EVs (n=3). (**C.i.**) MDA-TEVs. Scale bar, 200 nm. (**C.ii.**) MDA-TEV with 20 nm gold nanoparticles conjugated via CD63 antibody (white arrow). Scale bar, 150 nm. (**C.iii**) Close-up of MDA-TEV. Scale bar, 100 nm. (**C.iv**) Smaller MDA-TEVs. Scale bar, 100 nm. (**C.v**) HEK-EVs. Scale bar, 200 nm. (**C.vi**) Close-up of HEK-EV. Scale bar, 100 nm.

5.3.2 Continuous OECT-based monitoring of TEV-induced EMT

Current cell-based approaches and accompanying sensing technologies suffer from limitations that result in the loss of useful information and hamper the development of therapeutic interventions against EMT. End-point assays that yield discrete data require multiple time-points to be incorporated into the experimental design to track the dynamic changes that occur during EMT. While functional assays, such as migration or invasion assays, allow functional changes to be assessed, these are often limited to optical techniques, which are inherently low-throughput and

semi-quantitative at best. To address this, we developed a novel functional readout of EMT using dynamic impedance-based monitoring on OECTs to probe changes in epithelial cell barrier integrity resulting from malignant transformation. The electrical "tightness" of a cellular monolayer reflects the ionic conductance of the paracellular and transcellular pathways in an epithelial monolayer.[315] Although strictly speaking this should be a measured on a Transwell format, the resistance of cells adhered on substrates has previously been measured and correlates with barrier cell differentiation to epithelial phenotypes.[206] Additionally, the integration of cells directly onto an electroactive substrate allows for better compatibility with biomolecular assays. Resistance of the cell layer is a quantitative measure of barrier integrity and permeability, and, as such, can be correlated to the EMT status of cells (**Figure 5.1**). We postulated that the ability to continuously and non-invasively monitor cell phenotype during EMT could help shed light on the incidence and implication of EMT hybrid states in metastasis and elucidate the timescales of TEV function; a crucial insight for developing potent therapeutic interventions (see supplementary discussion 2**)**.

To achieve this, we had to adapt our OECT platform to ensure that it was compatible with long-term monitoring studies and could be integrated seamlessly with the EMT-model. Previous studies had functionalised the OECT surface with collagen type I to promote cell adhesion.[212,222] However, collagen type I promotes EMT and tumour invasion in cancer cells.[316,317] Therefore, to avoid any confounding variables, we forewent any surface functionalisation and instead incubated the OECTs with normal MCF10A culture media overnight prior to cell seeding to promote adherence of cells. Moreover, the commonly used external Ag/AgCl electrodes[222,223] are cytotoxic[318–320] and thus inappropriate for long-term studies. Instead, we opted to use a planar gold gate electrode to ensure that the devices produced stable outputs over extended periods of time. The absence of any external electrode also reduced the risk of contamination considerably and improved data acquisition times.

The addition of an insulating cell layer between the channel (**Figure 5.3a**) and the gate affects the OECT gating efficiency, rendering the device slower to respond to a given applied gate bias[129]. The modulation of the device response time serves as a measure of the epithelial barrier integrity and is defined as the cut-off frequency, which corresponds to the frequency at 70.7% of the maximum transconductance.[206] The cut-off frequency is a figure of merit that defines the regimes of high and low ionic transport.[202] Another important readout relevant to cells undergoing EMT can be derived from impedance measurements of the OECT channel as a function of frequency. As shown in the inset of **Figure 5.3b**, the impedance of the channels increases for frequencies over ~2 kHz. At this frequency range, the impedance of our system is dominated by the resistance of

the cell layer with the effect of capacitance being negligible.[215] Therefore, we can directly correlate this increase of impedance with the cell layer resistance.

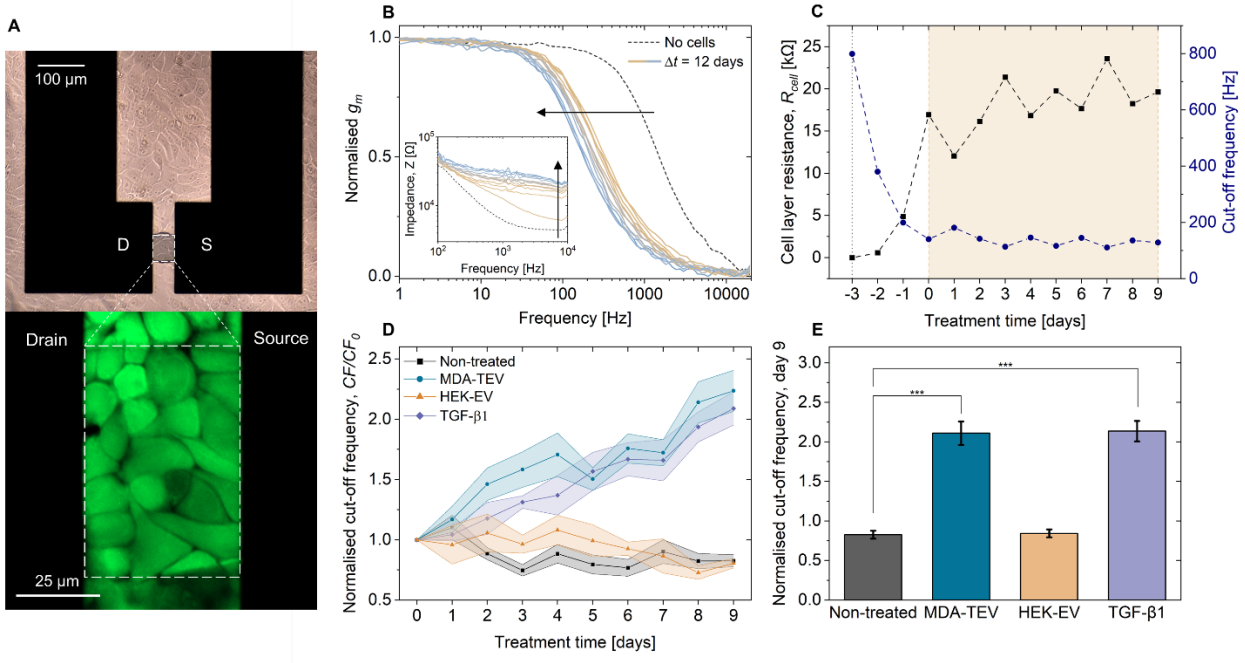

Figure 5.3: Real-time, OECT-based monitoring of EMT. (**A**) Brightfield image of MCF10A cells on the OECT device and zoomed in view of the channel with cells stained with calcein AM (green-LIVE). The black boxes are the source and drain electrodes and the darkened area between them is the PEDOT:PSS channel. (**B**) Typical time evolution of the OECT frequency-dependent response as cells grow and form a confluent layer under normal culture conditions (non-treated). Inset graph shows the evolution of the impedance for non-treated cells. A confluent layer of cells grown on the transistor channel induces a shift in the OECT cut-off frequency, from 860 Hz (dashed black line) to 140 Hz (solid blue line), and an increase in impedance from 4.9 kΩ to 26.4 kΩ. (**C**) Typical in-line monitoring of the cut-off frequency, as derived from the transconductance vs frequency plot; and the cell layer resistance (R_{cell}), as derived from the impedance vs frequency plot for non-treated cells. The vertical dotted line represents the baseline without cells on the device and the shaded area represents the equivalent treatment window. Representative cut-off frequency and R_{cell} plots are available for all conditions in fig. S3. (**D**) Cut-off frequency normalised to day 0 (treatment start day) over time for the four experimental conditions: non-treated; 200 µg MDA-TEVs; 185 µg HEK-EVs; and 10 ng/ml TGF-β1 (mean ± s.e.m.; indicated by lightly coloured areas; n=3 and 2 for non-treated/MDA-TEV and TGF-β1/HEK-EV, respectively). Data points before treatment day 0 are omitted for clarity. (**E**) Normalised cut-off frequency on treatment day 9 compared across the four conditions (mean ± s.e.m). Two-way ANOVA. *** $p \leq 0.001$.

To assess the ability of MDA-TEVs to promote EMT in MCF10A cells, four experimental conditions were tested: (1) non-treated cells cultured with normal medium; (2) cells treated with MDA-TEVs representing the treatment condition; (3) cells treated with transforming growth factor beta 1 (TGF-β1) representing a positive control, as TGF-β1 is commonly used to induce EMT in epithelial cells;[321] and (4) cells treated with HEK-EVs representing a negative control and a specificity check. The culture medium (normal or supplemented with MDA-TEVs, HEK-EVs, or

TGF-β1) was refreshed every 48 hours, thereby exposing the cells to fresh EVs or TGF-β1 every two days (see schematic S1). Throughout the experimental period, the activity of cells growing on the devices was monitored via daily OECT measurements. **Figure 5.3a** (see also Figure S8.12) illustrates highly viable cells on the devices at the end of the experimental period, assessed by cytotoxicity/viability assays (LIVE/DEAD), revealing an exceedingly high ratio of live-to-dead cells. This also highlights the added benefit of using the OECT which has a transparent channel that can be used to image the cells. Cells present on the transistor channel and the gate electrode induce a shift in the cut-off frequency (**Figure 5.3c**), which decreases as the cells continue to grow and differentiate, creating a barrier to the ion flux and slowing the response of the device. This is equally reflected in the extracted cell layer resistance (R_{cell}) data, which increases over time (**Figure 5.3c** and **Figure S8.13**). The cut-off frequency was normalised to treatment day 0 for each condition (**Figure 5.3d**), as the treatments were started at this time and to account for device-to-device performance variation.

Statistical analyses were performed to analyse the effect of treatment condition and treatment time on cut-off frequency. Within conditions, a two-way ANOVA showed that there was not a statistically significant difference in mean normalised cut-off frequency between day 0 and day 9 for non-treated cells ($F(1,45)=54.88$, $p=.92$) with $M_{diff}=0.17$ (-17%) and cells treated with HEK-EVs ($F(1,45)=54.88$, $p=.86$) with $M_{diff}=0.20$ (-20%). A small decrease in normalised cut-off frequency is observed in both conditions, which may be caused by the tightening of the lateral cell-cell junctions, as cells continue to differentiate and form an insulating barrier on the device. An asymptotic regression analysis revealed that the normalised cut-off frequency of non-treated MCF10A cells tended towards 0.88 ± 0.034 (**Figure S** 8.14). There was, however, a statistically significant difference in mean normalised cut-off frequency between day 0 and day 9 for cells treated with MDA-TEVs ($F(1,45)=54.88$, $p<.000$) with $M_{diff}=1.24$ (+124%) and cells treated with TGF-β1 ($F(1,45)=54.88$, $p<,000$) with $M_{diff}=1.09$ (+109%). This increase in cut-off frequency indicates an increase in the "leakiness" of the cell monolayer. This is in line with the degradation of cell-cell junctions,[322] characteristic of cells undergoing EMT, leading to an increase in paracellular ion flux into the PEDOT:PSS channel.[323] Optical imaging illustrates that cells are present and alive on the channel (**Figure 5.3a** and **Figure 5.4b**), and although the changes in paracellular ion flux are not visible, the highly sensitive OECT-based measurements reveal these changes in paracellular flux caused by EMT, enabling real-time monitoring of cell phenotype transition. Interestingly, it appears that MDA-TEVs initially promote degradation of epithelial barrier integrity faster than TGF-β1, during treatment day 0 to 4, after which point the effect of

both treatments is comparable. This is in line with previously reported timescales of TEV and TGF-β1-indued EMT.[301,302]

Additionally, mean normalised cut-off frequency was compared between treatment conditions on day 9 (**Figure 5.3e**). A two-way ANOVA showed that there was a statistically significant difference in mean normalised cut-off frequency on day 9 between non-treated cells and cells treated with either MDA-TEVs ($F(3,45)=35.20$, $p<.000$) with $M_{diff}=1.41$ (171%) or TGF-β1 ($F(3,45)=35.20$, $p<.000$) with $M_{diff}=1.27$ (153%). Whereas there was not a statistically significant difference in mean normalised cut-off frequency on day 9 between non-treated cells and cells treated with HEK-EVs ($F(3,45)=35.20$, $p=1.$) with $M_{diff}=0.021$ (-3%). This demonstrates our ability to compare different treatment conditions conducted on different OECT devices to one another, which holds promise for scaled-up operation and confirms that the observed effect is caused by the intervention (MDA-TEV or TGF-β1). Lastly, a simple linear regression was used to test if MDA-TEV treatment time significantly predicted the mean normalised cut-off frequency (**Figure S8.15**). The fitted regression model is shown in equation 4.

$$\textit{Normalised cut-off frequency} = 1 + 0.134\ (\pm\ 0.008) \times \textit{MDA-TEV treatment time} \quad \textbf{(4)}$$

The overall regression was statistically significant ($R^2=.978$, $F(1,69)=1527.60$, $p<.000$) and it was found that MDA-TEV treatment time significantly predicted mean normalised cut-off frequency ($\beta=0.134$, $p<.000$). This indicates that the kinetics of the degradation of epithelial barrier integrity in this regime (0-9 days of MDA-TEV treatment) can be represented by a linear approximation. We would assume that the linear regime only represents a slice of the epithelial barrier degradation process, as the cells progress through EMT. The overall kinetics could potentially be represented by a logistic regression model (with its characteristic S-shape) with a maximum (plateau) corresponding to the cut-off frequency when no cells are present in the channel, i.e., after the cells have migrated away. As cell barrier integrity invariably is associated with cell phenotype[206] and by extension EMT status,[1,322] our platform is thus able to provide insight into the kinetics governing TEV-mediated EMT. This is highly applicable to predicting therapeutic response and modelling the relationship between TEV/drug treatment dose/time and epithelial barrier integrity.

Compared to previous studies, which assessed the effects of MDA-TEVs up to 48 hours post treatment,[301,302] we demonstrate continuous monitoring of MDA-TEV-induced EMT over a 9 day period and establish a linear relationship between MDA-TEV treatment time and epithelial barrier integrity and thus EMT status. The ability to continuously monitor a transient process in a dynamic

system is ideal for assessing drug response over time. To validate the electrical readouts, biomolecular assays were carried out to assess the change in cell phenotype and determine EMT.

5.3.3 Biological validation of OECT measurements by immunofluorescence and immunoblots

In our study, to validate the electrical readouts and establish cut-off frequency and impedance as a credible figure of merit for EMT, we assessed cell phenotype and determined EMT status by analysis and quantification of gene expression of classic EMT markers using immunoblots and ELISA. Additionally, we performed IF confocal imaging to assess protein abundance and location profiles and measure cell height and assess morphology. IF confocal imaging was performed both on samples fixed 48 hours after treatment, as previous studies report TEV-induced changes within this timeframe,[301,302] and on samples fixed on treatment day 9. An N-cadherin based ELISA was performed on treatment day 7 and whole-cell lysates were collected on treatment day 9 for immunoblot analysis.

After 48 hours of exposure to MDA-TEVs or TGF-β1, vimentin expression markedly increased in the treated cells and remodelling of F-actin is apparent with the appearance of actin stress fibres inside the cells, as opposed to the cortical thin actin bundles in the non-treated cells (**Figure 5.4a** and supplementary discussion 3). Additional confocal IF images of MCF10A cells stained for E-cadherin, N-cadherin, and nuclei are available in **Figure S8.16**. After 9 days of treatment, F-actin stress fibres were still present (**Figure 5.4b**). Cell density, as measured by the number of nuclei per area, decreased by 23% and 44% with MDA-TEV and TGF-β1 treatment, respectively (**Figure 5.4c**). This is caused by individual cells occupying a larger area, which indicates a flattening of the cells, consistent with the transformation from the apical-basal polarity of epithelial cells to the back-front polarity of migratory mesenchymal cells.[322] Cells with a rounded morphology were also observed in the transistor channel (**Figure 5.4b**). The accompanying functional changes to the cells was captured by the OECT measurements, as cut-off frequency increased in the same 48-hour period (**Figure 5.4d**), indicating that changes to lateral cell-cell adhesion have already begun and is readily detectable by the OECT. This holds promise for the utilisation of the OECT platform to provide better temporal resolution of TEV-induced EMT.

To further substantiate these findings and demonstrate the multiparametric readout capabilities of the OECT platform, confocal microscopy was employed to evaluate the height of cells hosted on the OECT channel, as changes in cell height can be used to imply phenotypic switching during EMT.[324] Z-stacked confocal images of cells in the OECT channel, labelled for F-actin and nuclei, were obtained on day 9 of the experimental period (**Figure 5.4b**, **Figure S8.17**,

and supplementary videos 1-3). Cell height varied between non-treated and treated cells, mirroring the trend of cell layer resistance derived by OECT monitoring (**Figure 5.4e**), and clearly demonstrating the unique ability of our platform to directly correlate a biological event with a corresponding electrical readout, both occurring in the channel. To assess the degradation of cell-cell junctions and determine EMT status, the samples were probed for several hallmark EMT proteins. MDA-TEV and TGF-β1 treatment increased the abundance of vimentin, N-cadherin, and fibronectin, (mesenchymal markers) and decreased the abundance of E-cadherin (epithelial marker), while F-actin remained constant (**Figure 5.4f,g,h**). This evidences the occurrence of the cadherin switch (from E- to N-cadherin) and corroborates vimentin upregulation as seen on the confocal images (**Figure 5.4a**). ELISA-based N-cadherin protein quantification revealed that N-cadherin on treatment day 7 in the MDA-TEV- and TGF-β1-treated cells was 19- and 15-fold higher, respectively, compared to the non-treated cells (**Figure 5.4f**). TWIST1, a marker of EMT, was also more abundant in MDA-TEV treated cells (**Figure 5.5a,d**). Cells treated with HEK-EVs did not exhibit differential abundance of these proteins (**Figure 5.4g,h**), indicating that it is specifically MDA-TEVs that mediate EMT.

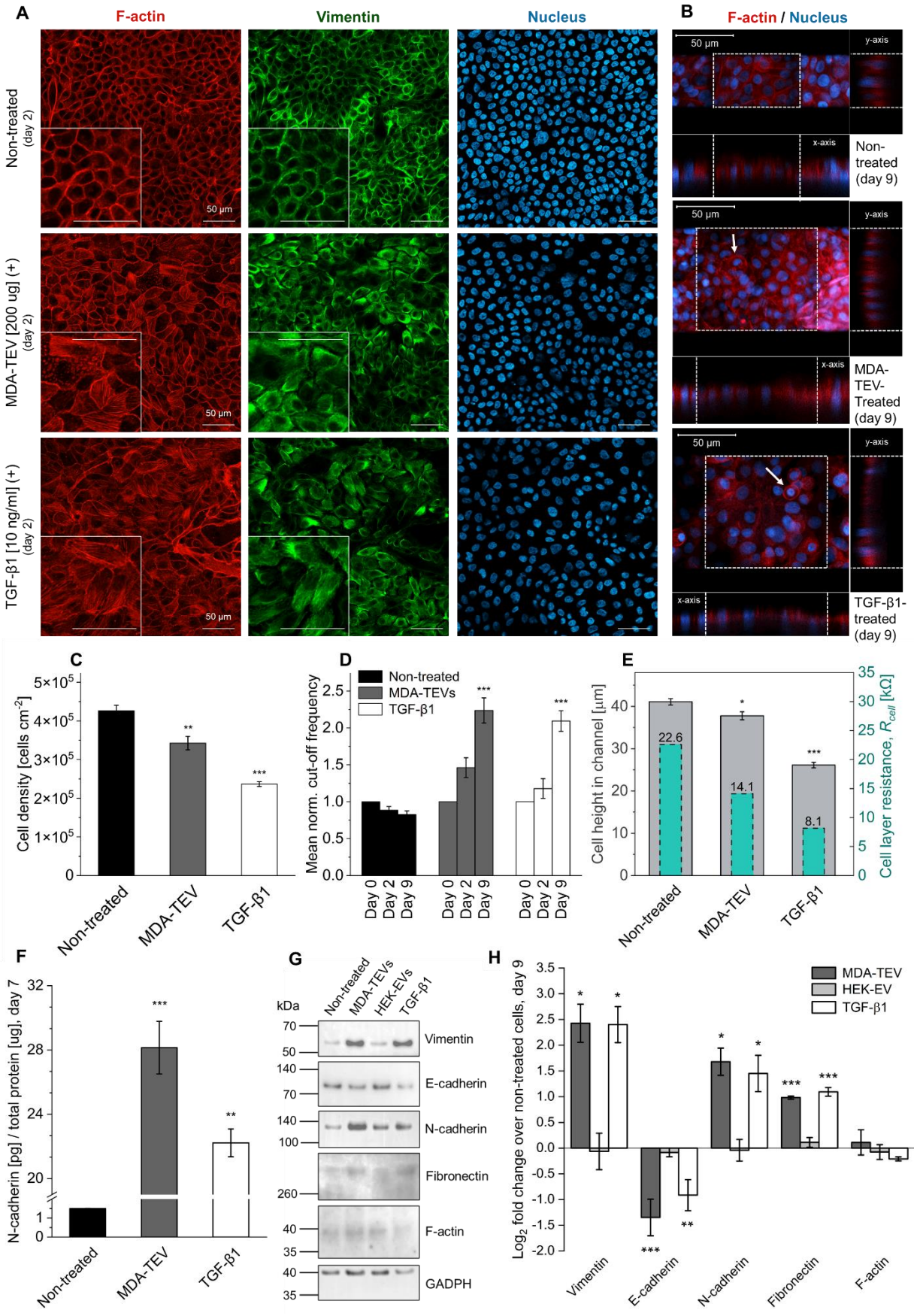

Figure 5.4: Biological validation of OECT-based measurements to determine EMT status. (A) Representative confocal images of immunofluorescently labelled MCF10A cells on treatment day 2. Cells were stained for F-actin,

vimentin, and nuclei. Insets show a close-up of cells. Scale bars, 50 μm. (B) Representative x/z and y/z orthogonal views (ortho-views, right) of each cell layer in the OECT channel (treatment day 9), obtained by z-stacked confocal images. PEDOT:PSS channel is indicated by white dotted lines. Cells were stained for F-actin and nuclei. Scale bars, 50 μm. White arrows indicate cells with a rounded morphology. (C) Cell density on treatment day 2 across conditions. Cell number was determined by counting cell nuclei from 5 frames (mean ± s.e.m.). (D) Normalised cut-off frequency from treatment day 0, 2, and 9 across conditions (mean ± s.e.m.; n=3 and 2 for non-treated/MDA-TEV and TGF-β1, respectively). (E) Cell height in channel derived from orthogonal projections (mean ± s.e.m.; min. 8 measurements taken from different x- and y-positions; see fig. S7 and supplementary videos 1-3) and the cell layer resistance measured in each specific channel as derived from impedance (*Z*) plots. (F) ELISA-based N-cadherin protein on treatment day 7 across conditions (mean ± s.e.m.; n=1). (G) Immunoblots of whole-cell lysates collected on treatment day 9. Equal quantities of protein were separated on SDS-PAGE gels and membranes were blotted with indicated antibodies. Vimentin, predicted: 54-75 kDa; E-cadherin, predicted: 97 kDa; N-cadherin, predicted: 125-135 kDa; fibronectin (slightly smeared due to glycosylation [325]), predicted: 262-285 kDa; F-actin (slightly smeared), predicted: 42 kDa; and GADPH, predicted: 37 kDa. Unedited blots are available in fig. S8. (h) Quantitative values of protein expression derived from immunoblots presented as Log_2 fold-change versus non-treated condition expression level (mean ± s.e.m.; n=3). One-way ANOVA: C, E and F; two-way ANOVA: D. * $p \leq 0.05$, ** $p \leq 0.01$, *** $p \leq 0.001$.

Our biological validation data strongly indicate that MDA-TEV treatment induces EMT in MCF10A cells. Additionally, we demonstrate the multiplexing capability of the OECT platform by correlating the height of cells in the transistor channel to the cell layer resistance, R_{cell}, measured in the same channel, as well as compatibility with end-point assays. This ability to directly correlate an electrical signal with a biological readout is highly beneficial for furthering our understanding of EMT and crucial for establishing OECT-based measurements as credible figures of merit for phenotypic drug screening applications.

5.3.4 MDA-TEVs do not influence TWIST1 and TFPI2 DNA methylation levels

Next, to further support the validation of the model, we sought to gain mechanistic insight into the mode of action (MoA) of MDA-TEV-induced EMT via epigenetics analysis. Epigenetic remodelling is prevalent during breast cancer metastasis[326] and DNA methylation of tumour and metastasis suppressor genes is a hallmark of circulating tumour cells.[327] Gene promoters, especially key tumour suppressor genes, are unmethylated in normal tissues and highly methylated in cancer tissues.[328] In this way, gene promoter hypermethylation is a pathway for repression of gene transcription (transcriptional silencing), and conversely, gene promotor hypomethylation (loss of DNA methylation) may promote gene expression.[329] Oncogene BCR-ABL1-positive EVs released from leukaemia cells have been demonstrated to increase global DNA methylation levels in recipient cells.[330] With this in mind, we sought to determine whether MDA-TEVs influence DNA methylation by analysing the methylation status of the tumour suppressor gene *tissue factor pathway inhibitor 2* (*TFPI2*) and the pro-metastatic transcription factor *TWIST1*. TWIST1

represses E-cadherin and promotes EMT[301] and *TWIST1* transcripts were reportedly upregulated after MDA-TEV treatment.[301,302] TWIST1 is negatively associated with TFPI2 in breast cancer patients, as TFPI2 suppresses breast cancer progression through inhibiting TWIST-integrin α5 pathway.[331] TFPI2 is downregulated in breast cancer cells lines compared to MCF10A cells and methylation in the *TFPI2* promotor has been found in highly invasive breast cancer cells.[332] We observed upregulation of TWIST1 protein between MDA-TEV and non-treatment conditions (**Figure 5.5a**), which likely caused E-cadherin repression (**Figure 5.4g,h**). However, MDA-TEVs do not appear to carry TWIST1 (**Figure 5.5b**).

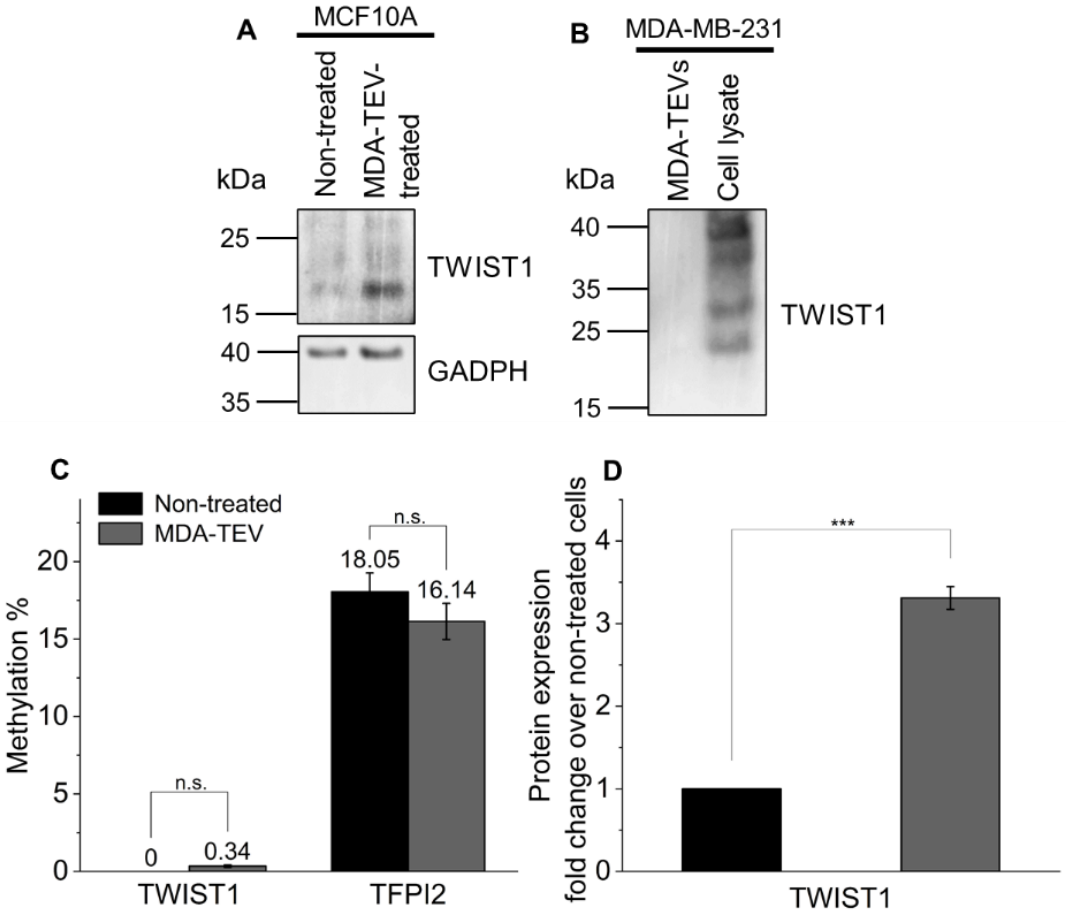

Figure 5.5: MDA-TEVs modulate TWIST1 protein abundance but not DNA methylation level. (A) Immunoblots of whole-cell lysates collected on treatment day 9. (B) Immunoblot of MDA-TEVs and MDA-MB-231 whole-cell lysate. Equal quantities of protein were separated on SDS-PAGE gels and membranes were blotted with indicated antibodies. TWIST1, predicted: 21 kDa; GADPH, predicted: 37 kDa. Unedited blots are available in fig. S9. (C) Total methylation (%) relative to house-keeping gene *β-actin* (mean ± s.e.m.; n=1). (D) Quantitative values of protein expression derived from immunoblots presented as fold-change versus non-treated expression level (mean ± s.e.m.; n=3). *** $p \leq 0.001$, n.s. = non-significant.

A MethyLight-based approach was used to determine the methylation of these markers.[333] This was based on previous work published by Chettouh et al (2018), which looked at markers of Barrett's oesophagus for methylation.[334] We found that neither *TFPI2* nor *TWIST1* was significantly differentially methylated between non-treated and MDA-TEV-treated cells (**Figure 5.5c**). Surprisingly, *TFPI2* displayed higher levels of methylation compared to *TWIST1* across both conditions. This raises the question of whether *TFPI2* (and *TWIST1*) methylation status in MCF10A cells could potentially contribute to the cell line's intrinsic phenotypic plasticity for mesenchymal transition.

Interestingly, immunoblot analysis revealed that TWIST1 protein was present in different amounts between the two conditions (**Figure 5.5a,d**), which could suggest that *TWIST1* is being repressed post-transcriptionally in non-treated MCF10A cells, which further supports the evidence that EMT is occurring, e.g. by CPEB1/2 and miR-580.[335] miR-580 acts as a negative regulator of *TWIST1* expression in MCF10A cells and is downregulated in MCF10A cells which have undergone EMT.[335] As MDA-TEVs increase the abundance of TWIST1 protein, *TWIST1* could be upregulated post-transcriptionally by other regulatory mechanisms, e.g. MDA-TEV-delivered miR-580-siliencing circular RNAs,[336] or even be induced by upregulation of transcriptional factors, e.g. HMGA2.[337] Further immunoblot analysis revealed that TWIST1 was not part of MDA-TEV cargo, although highly abundant in MDA-MB-231 cells (**Figure 5.5b**). These results collectively indicate that MDA-TEVs are dysregulating endogenous TWIST1-repression in MCF10A cells via mechanisms other than epigenetic remodelling or direct protein transfer.

5.3.5 OECT-based screening reveals that heparin treatment prevents TEV-induced EMT

Given that EMT determines the most lethal feature of cancer, metastasis, it represents an attractive target in oncology. However, direct targeting of EMT effector molecules is, in most cases, pharmacologically challenging.[338] Previous anti-EMT strategies have targeted signalling pathways, molecular drivers, or the mesenchymal cells themselves,[339] and several clinical trials targeting EMT are ongoing.[340] Recent efforts using nitrofen and its analogues to interfere with the process of EMT have proven efficacious in blocking triple-negative breast cancer (TNBC) metastasis and invasiveness both *in vivo* and *in vitro*.[341] Such reports underscore the importance of identifying pharmacological targets against EMT to prevent metastasis. Moreover, as EMT increases drug resistance,[342] targeting EMT could also attenuate cancer cell stemness and increase the effectiveness of more classic chemotherapeutics.[343] There is therefore an imminent need to elucidate the role of TEVs in EMT to identify new anti-cancer strategies that target TEVs.

We selected heparin as a possible TEV-targeting, anti-EMT treatment and leveraged our platform to screen this candidate drug. Heparin is a glycosaminoglycan commonly used as an anticoagulant drug. However, it is reported to have anti-cancer effects in humans[344–346] and has been shown to decrease metastasis in animal models.[347] The mechanism for heparin's anti-metastatic effect has been proposed to be a blocking function in tumour cell/platelet interactions.[348,349] In addition to this mechanism, heparin's anti-cancer role may involve regulating TEV uptake into recipient cells.[309] EVs depend on cell-surface heparan sulphate proteoglycans (HSPGs) for their internalisation and functional activity, and heparin is a competitive inhibitor of cell surface receptors dependent on HSPG coreceptors.[11,309,350] Heparin treatment of cells and/or EVs is known to interfere with TEV binding to the cell surface (**Figure 5.6a**), [11,309,350] and heparin has been reported to partially block EV-transfer of EGFRvIII mRNA into recipient cells[309] and significantly reduce EV-mediated stimulation of cancer cell migration and invasion.[10,11] This function makes HSPGs a potential target for inhibition of TEV-mediated tumour invasion and metastasis. To test the efficacy of heparin in preventing MDA-TEV-induced EMT, a two-factor factorial experiment was designed, where cells were incubated with or without MDA-TEVs in the presence or absence of heparin **(Figure 5.6b**).

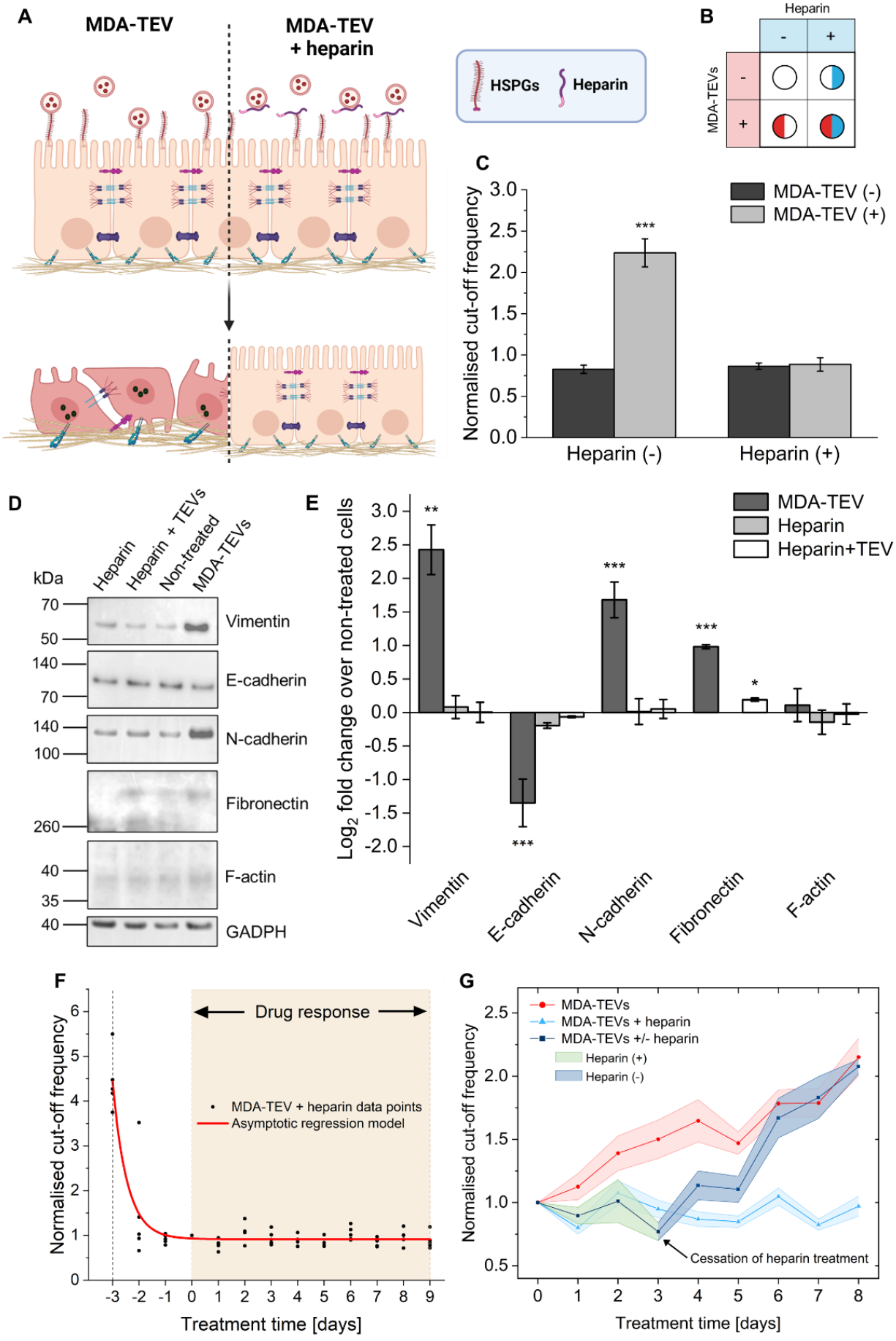
A
MDA-TEV
MDA-TEV + heparin
HSPGs
Heparin
B
Heparin
MDA-TEVs
C
MDA-TEV (-)
MDA-TEV (+)
Normalised cut-off frequency
Heparin (-)
Heparin (+)
D
kDa
Heparin
Heparin + TEVs
Non-treated
MDA-TEVs
Vimentin
E-cadherin
N-cadherin
Fibronectin
F-actin
GADPH
E
MDA-TEV
Heparin
Heparin+TEV
Log2 fold change over non-treated cells
F
Drug response
MDA-TEV + heparin data points
Asymptotic regression model
Normalised cut-off frequency
Treatment time [days]
G
MDA-TEVs
MDA-TEVs + heparin
MDA-TEVs +/- heparin
Heparin (+)
Heparin (-)
Cessation of heparin treatment
Normalised cut-off frequency
Treatment time [days]

Figure 5.6: OECT-based phenotypic screening of heparin as a TEV-targeting, anti-EMT drug. (A) Schematic showing the proposed mechanism by which heparin binds to spike glycoproteins to out compete cell surface HSGPs and prevent TEV adhesion and uptake. (B) Two-factor factorial design to assess the effect of heparin treatment on MDA-EV-induced EMT. (C) Comparison of the normalised cut-off frequency on treatment day 9 between cells treated with MDA-TEVs in the absence (-) or presence (+) of heparin (mean ± s.e.m.; n=3). (D) Immunoblots of whole-cell lysates collected at the end of the experiment. Equal quantities of protein were separated on SDS-PAGE gels and membranes were blotted with indicated antibodies (same antibodies as listed in Fig. 4). Unedited immunoblots are available in fig. S8. (E) Quantitative values of protein expression derived from immunoblots presented as Log_2 fold-change versus non-treated expression level (mean ± s.e.m.; n=3). (F) Asymptotic regression model fitted to the drug response cut-off frequency data points. (G) Cells were treated with heparin between day 0 and 3 (green coloured area) while exposed to MDA-TEVs. Washing with PBS and subsequently exposing cells to MDA-TEVs lead to an increase in cut-off frequency (dark blue coloured area). Data points before treatment day 0 are omitted for clarity (mean ± s.e.m.; s.e.m. indicated by lightly coloured areas; n=2 and 3 for the transient heparin treatment condition (dark blue data points) and MDA-TEV (+/-) heparin (red and light blue data points), respectively). Two-way ANOVA. * $p \leq 0.05$, ** $p \leq 0.01$, *** $p \leq 0.001$.

Heparin treatment of cells effectively ablated the EMT-promoting effect of MDA-TEVs and heparin itself does not appear to adversely affect the barrier forming properties of the MCF10A cells (**Figure 5.6c** and **Figure S8.20**), the abundance of several mesenchymal and epithelial markers (**Figure 5.6d,f,e**), nor the viability of cells (Figure S8.12). We hypothesize that if heparin treatment blocks MDA-TEV binding to cells and thereby prevents MDA-TEV-induced EMT, then it may have an impact on cancer metastasis and could therefore be a putative starting point in developing an effective new drug for treating metastatic TNBC. To demonstrate the facile drug response modelling enabled by the OECT time-series data, an asymptotic regression was used to test if heparin treatment time significantly predicted the normalised cut-off frequency (**Figure 5.6f**). The fitted regression model is given by equation 5:

$$\text{Normalised cut-off frequency} = \alpha - \beta \times \gamma\text{^}(MDA - TEV\ treatment\ time) \quad (5)$$

The overall regression was statistically significant (R^2=.872, F(2,62)=210.63, p<.000) and it was found that heparin treatment time significantly predicted normalised cut-off frequency (α=0.92, β=-3.52, γ=0.16, p=0.0013), which compares well with the same model applied to the non-treated condition (**Figure S** 8.14). This demonstrates our ability to readily model the transient drug response and compare it to a control condition.

Furthermore, it has been reported that persistent heparin treatment is necessary to abrogate the malignant effects of TEVs and inhibit TEV-induced tumour progression.[351] To test the transient effect of heparin treatment, cells were concurrently treated with heparin and MDA-TEVs for 3

days, after which the cells were washed in PBS and heparin treatment was ceased while MDA-TEV treatment continued (**Figure 5.6g**). Our results confirm the transient effect of heparin treatment and demonstrate that persistent treatment of cells with heparin concurrently with exposure to MDA-TEVs is necessary to prevent MDA-TEV-induced EMT. This also demonstrates the ability of the OECT to continuously monitor a dynamic drug response and investigate the temporal relationship between measured pharmacodynamic response and pharmacokinetics non-invasively and in a facile manner.

5.4 Discussion

EMT is a crucial turning point in cancer progression, facilitating the invasion and spread of cancer cells throughout the body to form metastases, which carries with it a poor prognosis. Therefore, interventions that target EMT drivers may be useful therapeutic strategies against cancer metastasis. A few successful clinical trials in human patients using EMT-targeting drugs provide proof of principle that such interventions have translational implications [340]. However, there are limitations associated with these existing drugs (such as lack of specificity and adverse effects) and a shortage of phenotypic screening technologies by which to rapidly identify new and more effective molecular entities with high potential for translation to *in vivo* outcomes. Here, we report the development of a new phenotypic screening platform based on bioelectronic technology for the real-time monitoring of TEV-induced EMT and testing of anti-metastatic drugs. Current phenotypic screening technologies suffer from limitations that hitherto have frustrated adoption for preclinical development,[292] and often the choice is between dynamic monitoring or high throughput. In contrast, our platform offers dynamic, multiparametric monitoring of a pathogenic process *in vitro* and has a direct path towards scaling and massive parallelization. We hypothesised that using the OECT as an impedance biosensor to monitor cell barrier integrity could unlock real-time tracking of EMT. By integrating OECTs with a disease-relevant model of TEV-driven invasive ductal carcinoma, we achieved real-time, label-free, non-invasive monitoring of MDA-TEV-induced EMT over a 9-day period, which is almost 5-fold longer than previous reports.[301,302] Through validation of the electrical signal with on-chip and end-point biomolecular assays, we established OECT-based electrical measurements as a novel figure of merit for determining EMT status. To demonstrate its preclinical utility, we used our platform to identify heparin as a candidate anti-metastatic drug that acts by blocking TEV function to prevent EMT. These data provide proof of principle that TEV blocking compounds can be identified with OECT-based functional phenotypic screens targeting EMT and confer benefit in the treatment of TEV-mediated,

metastasis-initiating EMT. Furthermore, our screening platform opens up the possibility of discovering similar compounds that prevent EMT by targeting TEV function.

On the other hand, functional, electrical monitoring represents a new tool for elucidating the role of TEVs in EMT and metastasis that readily facilitates the kinetics governing TEV-driven epithelial barrier disruption to be extracted. Such readouts have the potential to implicate specific EV subtypes, reveal TEV dose-response relationships, and explore the function of EVs derived from cancerous/non-cancerous cell lines and clinical samples. Here, unravelling the MoA of TEVs has implications for finding therapeutic targets and we show that MDA-TEVs dysregulate endogenous TWIST1-repression in MCF10A cells via mechanisms other than epigenetic remodelling or direct protein transfer. Drugs that target epigenetic modulation during EMT are gaining increasing attention[339] and it would be interesting to see if TEVs play a part in this pathway. Lastly, our platform is amenable to integration with models recapitulating other pathologies where epithelial barrier function serves as a functional readout of pathogenesis/disease progression.

"In my view, all that is necessary for faith is the belief that by doing our best we shall succeed in our aims: the improvement of mankind."

– Rosalind Franklin

6 Conclusion and Outlook

The aim of this thesis was to develop *in vitro* bioelectronic platforms for investigating EV function in cancer metastasis and to advance preclinical drug discovery technologies to address the clinical need for more efficacious anti-cancer treatments. To describe how I achieved this goal, I have broken down this dissertation into the following objectives:

1. Comparison of EV isolation methods by characterising EV samples and identifying the most fit-for-purpose method
2. Integration of supported lipid bilayers derived from mammalian cells onto CP-based electronic devices for investigating particle interactions at the plasma membrane and screening compounds that inhibit EV binding
3. Development of a phenotypic screening platform based on OECTs for monitoring TEV-induced EMT in non-malignant cells in real-time and for testing anti-metastasis drugs
4. Validation of electrical readouts using established biomolecular assays and fluorescence microscopy

A comparison of EV isolation methods revealed that UC yielded 13-fold higher particle concentrations than SEC, whilst also producing EV isolates with lower protein-to-particle ratios than SEC. Given the requirement to elicit a measurable, functional effect in recipient cells, a higher EV yield was favoured, therefore UC was selected without further purification steps. Such EV isolates may be described as crude, with the descriptor CD63/CD9-positive EVs, and it is thus not possible to implicate specific EV subtypes in the observed functional effect. However, given the role of multiple EV subtypes in eliciting functional effects in recipient cells,[80] it may be more physiologically accurate/relevant to use such crude preparations to replicate EV function *in situ*, especially in the context of identifying drugs that target EV function.

Next, cell-free, SLB models were integrated with organic electronic devices for investigating interactions at the plasma membrane. Two studies were carried out, the first was based on detecting virus fusion to a SLBs, both fully synthetic and natively derived, and the second investigated cancer exosome binding to a native cell membrane, with screens to block this interaction using CD29 Ab. As discussed, EVs and viruses share many similarities, both in form and function,[75] hence the advancement of SLBs integrated with bioelectronic devices for detecting such particle interactions at the membrane is highly relevant for research into EV function.

OECTs and MEAs integrated with synthetic and natively derived SLBs were deployed to detect pH-triggered virus hemifusion. The formation of mobile bilayers on top of PEDOT:PSS-coated glass slides and OECTs was demonstrated by FRAP. Here, the optical transparency of the

OECT channel confers a crucial benefit in that it enables dual monitoring of biological interactions occurring at the membrane. Using influenza virus as the proof-of-principle demonstration, the triggering of influenza virus fusion with low pH on host membrane mimics formed on PEDOT:PSS coated OECTs and electrodes resulted in quantifiable changes in electrical properties without the use of label probes. The mixing of the virus membrane material with the SLB results in a tighter packing of the membrane components on top of the active sensing area, which in turn leads to a membrane with higher sealing properties that is readily detectable. The ability to investigate the hemifusion of viruses using biomembranes integrated with organic electronic devices has a direct path to studying EV hemifusion with the plasma membrane and/or endosomal compartments to further elucidate these uptake routes. Additionally, correlating electrical signals to optical readouts could help determine LOD for these platforms, as demonstrated for virus fusion, but it could also be utilised to gather more in-depth information on the mechanisms at play, e.g. by optically tracking the release of fluorescently stained EV cargo into a bilayer to discern differences in binding vs fusion, as detected electrically. Building on the platform and knowledge gained from this work, biomembrane bioelectronics were applied to the study of EV-plasma membrane interactions.

ASBs derived from ADSCs incorporating native membrane components, including integrin β1/CD29 were characterised by TIRFM and FRAP. These were integrated with PEDOT:PSS-coated glass slides and MEAs for the electrical detection of cEXO binding. Blocking of this binding was possible by treating the ASB with CD29 Ab, which was readily detectable by both optical and electrical methods. The ASB platform allows the recapitulation of the human primary ADSC plasma membrane and the monitoring of cEXO binding in a simpler manner than the available conventional methods such as optical tweezers[352] and immunofluorescence[353]. Although previous groups have used native cell membrane models to screen virus binding inhibitors[255,256], this is the first time biomimetic membrane models incorporating native components of human mammalian cells have been used to screen strategies for blocking cEXO binding to cells. These results support blocking cEXO binding as a potential therapeutic strategy and validates the utility of this ASB-sensing platform in identifying successful targets that reduce cEXO binding and reduce proangiogenic outcomes when applied to cells. Furthermore, cEXO interactions with the cell plasma membrane can be studied in isolation, as cEXO internalization by cells is absent, to target that conserved aspect of cEXO–cell interactions. Lastly, the ASB can be tuned to generate model systems of the plasma membrane of different types of cells to investigate their binding to diverse types of EVs. This model would facilitate the study of different types of cancer and other diseases for which the prognosis is worsened as communication between diseased and healthy cells progresses via EVs. Importantly, this platform is a scalable tool for screening EV-cell

inhibitors and the development of therapeutics to mitigate the strong effect that cEXOs have on tumourigenesis and metastasis.

The SLB systems offers several advantages including the following: (i) it is free of the complexity of cells; (ii) it does not need the aseptic conditions required in cell culture; (iii) the ability to use complementary analytic techniques, such as TIRFM and EIS, for visual detection in real time and for label-free and sensitive electrical monitoring of membrane interactions. This versatility makes SLB systems an excellent option for screening potential therapeutic molecules, as it is compatible with scale-up and multiplexing, with the option to be label-free. The ability of these platforms to detect EV function has both basic science and applied uses. On the basic science end, the platforms can be used as a research tool to further characterize EV interactions with the plasma membrane and elucidate the receptors required for binding. On the applied end, these platforms can be utilised for high-throughput drug screening against TEV function. For EV binding, a multitude of bilayers with a variety of receptors and/or derived from different cell types can be developed to identify which receptors can be inhibited to block EV binding, and thus curtail EV function. Future work should explore the purification of EVs to further distinguish subtypes and apply these preparations to the platform, which could advance understanding of preferential receptor binding by EV subtype. Future development in this area would determine the feasibility of using clinically complex samples as opposed to using purified samples derived from cell cultures. As current approaches to screen EV function involve performing live cell-based assays, this *in vitro* approach could expedite screening processes by providing functional data without the complications of working with live cells. Overall, developing a platform to detect EV interactions with the plasma membrane would provide additional approaches toward EV-targeted therapeutics that are much needed in addressing current need for anti-metastatic drugs.

Although these SLB models generate highly useful information regarding potential therapeutic targets, identified hits should be tested using live cell-based assays to ensure that the target is still relevant in a live biological system with all the extra- and intracellular mechanisms/complexities intact. To this end, the development of a cell-based phenotypic screening platform based on OECTs for investigating TEV-driven EMT in cancer metastasis and testing anti-metastatic drugs was reported. A model of TEV-driven invasive ductal carcinoma was integrated on OECTs to facilitate the continuous, non-invasive monitoring of TEV-driven EMT *in vitro* over a 9-day period. OECT-based readouts were validated with on-chip and end-point biomolecular assays to establish a novel figure of merit for determining EMT status. Furthermore, the platform was used to identify heparin as a candidate anti-metastatic drug that acts by blocking TEV function to prevent EMT. TEVs represent a novel and potentially more specific target for anti-EMT therapies and by using the OECT platform, this new therapeutic window between cancer and

normal cells can be explored. The compatibility of the platform with on-chip optical imaging and end-point assays for multiparametric readouts is crucial for establishing OECT-based measurements as a functional and robust figure of merit for EMT status. This feature is necessary for validation and qualification of analytical performance and biological *in vivo* relevance, and for adoption by industry and regulatory agencies.[294] Further, the platform facilitates quantitative translation to *in vivo* outcomes, as it readily allows modelling of pharmacokinetic/pharmacodynamic (PK/PD) relationships, crucial for elucidating the causative relationship between drug exposure and response.[354] Although the platform improves upon current phenotypic screening technologies, positive hits must still be screened in animal models prior to clinical trials. Here, the facile drug response modelling enabled by the platform may help inform appropriate dosage and dose timings, reducing the reliance on animal studies in line with the three Rs principle for more ethical animal testing. Additionally, by integrating patient-derived samples with our platform, we may decrease the risk of failure, especially due to lack of efficacy, at the clinical phase, as such systems would allow us to measure the drug response on the cells/tissue we wish to target *in situ.*

Several limitations of the work presented should be addressed going forward to further substantiate and validate the findings described. These include:

Using EVs derived from different isolation methods and comparing the functional readouts

Conducting dose-response studies to correlate the magnitude of the functional readouts with the amount of EVs used

Using EVs derived from other tumour cells, e.g. the non-invasive MCF-7 cell line, to compare their EMT-promoting effect

Furthermore, other potential applications of the technology should be explored. In particular, the OECT EMT-monitoring platform would be ideal for studying blood brain barrier disruption associated with metastasis initiation. Here, the TEVs derived from MDA-MB-231 cells present an intriguing actor, as breast cancer preferentially metastasises to the lungs and brain. Recapitulating a disease model for studying priming of the pre-metastatic niche by TEVs would be of great interest. Lastly, this technology is poised to accelerate preclinical drug discovery and as such efforts to facilitate the technology transfer process should be made, herein validating the model with patient derived samples, either TEVs or the tissues being treated.

In terms of the devices used, both MEAs and OECTs were used throughout the different studies conducted. The optical transparency of the OECT channel lends itself to dual readout studies – relating the optical images to the electrical signals. This was especially important for the EMT study to illustrate the power of the OECT in monitoring epithelial barrier integrity. This is a clear advantage of the OECT compared to MEAs, especially when conducting quality control to

ensure that what is being measured on the electroactive area is, in fact, the biosystem of interest rather than a defect or similar abnormality. Lastly, their high signal amplification enables the use of smaller devices and thereby less material usage, which has implications for applications requiring mass produced devices.

Developing this technology for commercial applications requires further validation of the electrical signal across established disease models and proof-of-scale studies that showcase the higher-throughput and facile operation of numerous devices operating in parallel. Crucially, the ability to mass produce these devices and attain replicable results with these will determine if this technology has the potential to contribute to the toolbox of pre-clinical and clinical drug screening assays.

In summary, the functional, bioelectronic phenotypic screening platform described here demonstrates the feasibility to monitor TEV-induced EMT in real-time and rapidly identify potent compounds that act on TEV function and are effective in the treatment of metastasis-initiating EMT in preclinical models. This platform should facilitate the efforts to target TEV-driven EMT and aid the development of first-in-class anti-metastatic drugs. Future work using this platform should explore other TEV-targeting drugs, potentially those with higher specificity than heparin, e.g. CD29, and test identified hits in animal models to determine the utility of this platform. Furthermore, a scaled-up platform comprising multiple OECTs should be developed to test various different treatments simultaneously to enable rapid screening. Lastly, integration with patient samples, either blood-derived (T)EVs or tissue samples (e.g. epithelial breast tissue), constitutes an important step in ensuring that screened hits are physiological/pathologically relevant and that drugs developed are efficacious.

Organic electronic technologies have the potential to address the limitations of current tools for characterising EV function and aid in the preclinical research arena. As described, integration of both cell-free and cell-based models recapitulating various pathologies with organic electronic devices enables real-time monitoring of a dynamic system in its native state. Here, compatibility with other surface-sensitive methods, such as microscopy in the case of the OECT, facilitates facile validation of the electrical signals by orthogonal analytical techniques. Lastly, and crucially for drug discovery, CP-based electronic devices have direct path towards scaling and massive parallelization for high throughput screening applications. It is anticipated that the application of multifunctional techniques employing these innovative technologies will lead to a deeper understanding of EV function and could accelerate the development of TEV-targeting therapeutics.

7 REFERENCES

1. Fares, J., Fares, M. Y., Khachfe, H. H., Salhab, H. A. & Fares, Y. Molecular principles of metastasis: a hallmark of cancer revisited. *Sig Transduct Target Ther* **5**, 1–17 (2020).
2. Wouters, O. J., McKee, M. & Luyten, J. Estimated Research and Development Investment Needed to Bring a New Medicine to Market, 2009-2018. *JAMA* **323**, 844–853 (2020).
3. Wong, C. H., Siah, K. W. & Lo, A. W. Estimation of clinical trial success rates and related parameters. *Biostatistics* **20**, 273–286 (2019).
4. Harrison, R. K. Phase II and phase III failures: 2013–2015. *Nature Reviews Drug Discovery* **15**, 817–818 (2016).
5. Gui, P. & Bivona, T. G. Evolution of metastasis: new tools and insights. *Trends in Cancer* **8**, 98–109 (2022).
6. Hasan, H. *et al.* Extracellular vesicles released by non-small cell lung cancer cells drive invasion and permeability in non-tumorigenic lung epithelial cells. *Sci Rep* **12**, 972 (2022).
7. Syn, N., Wang, L., Sethi, G., Thiery, J.-P. & Goh, B.-C. Exosome-Mediated Metastasis: From Epithelial–Mesenchymal Transition to Escape from Immunosurveillance. *Trends in Pharmacological Sciences* **37**, 606–617 (2016).
8. Rodríguez, M. *et al.* Exosomes enriched in stemness/metastatic-related mRNAS promote oncogenic potential in breast cancer. *Oncotarget* **6**, 40575–40587 (2015).
9. Melo, S. A. *et al.* Cancer Exosomes Perform Cell-Independent MicroRNA Biogenesis and Promote Tumorigenesis. *Cancer Cell* **26**, 707–721 (2014).
10. Franzen, C. A. *et al.* Urothelial cells undergo epithelial-to-mesenchymal transition after exposure to muscle invasive bladder cancer exosomes. *Oncogenesis* **4**, e163–e163 (2015).
11. Christianson, H. C., Svensson, K. J., van Kuppevelt, T. H., Li, J.-P. & Belting, M. Cancer cell exosomes depend on cell-surface heparan sulfate proteoglycans for their internalization and functional activity. *Proceedings of the National Academy of Sciences* **110**, 17380–17385 (2013).

12. Costa-Silva, B. *et al.* Pancreatic cancer exosomes initiate pre-metastatic niche formation in the liver. *Nature Cell Biology* **17**, 816–826 (2015).
13. Mao, Y. *et al.* Hypoxic exosomes facilitate angiogenesis and metastasis in esophageal squamous cell carcinoma through altering the phenotype and transcriptome of endothelial cells. *Journal of Experimental & Clinical Cancer Research* **38**, 389 (2019).
14. Clayton, A., Al-Taei, S., Webber, J., Mason, M. D. & Tabi, Z. Cancer Exosomes Express CD39 and CD73, Which Suppress T Cells through Adenosine Production. *The Journal of Immunology* **187**, 676–683 (2011).
15. Fabbri, M. *et al.* MicroRNAs bind to Toll-like receptors to induce prometastatic inflammatory response. *Proc. Natl. Acad. Sci. U.S.A.* **109**, (2012).
16. O'Brien, K., Breyne, K., Ughetto, S., Laurent, L. C. & Breakefield, X. O. RNA delivery by extracellular vesicles in mammalian cells and its applications. *Nature Reviews Molecular Cell Biology* 1–22 (2020) doi:10.1038/s41580-020-0251-y.
17. Roy, S., Hochberg, F. H. & Jones, P. S. Extracellular vesicles: the growth as diagnostics and therapeutics; a survey. *J Extracell Vesicles* **7**, (2018).
18. Beer, K. B. *et al.* Extracellular vesicle budding is inhibited by redundant regulators of TAT-5 flippase localization and phospholipid asymmetry. *PNAS* **115**, E1127–E1136 (2018).
19. Gardiner, C. *et al.* Techniques used for the isolation and characterization of extracellular vesicles: results of a worldwide survey. *Journal of Extracellular Vesicles* **5**, 32945 (2016).
20. Lener, T. *et al.* Applying extracellular vesicles based therapeutics in clinical trials – an ISEV position paper. *J Extracell Vesicles* **4**, (2015).
21. Twenty-five years of conducting polymers. *Chemical Communications* **0**, 1–4 (2003).
22. Yáñez-Mó, M. *et al.* Biological properties of extracellular vesicles and their physiological functions. *J Extracell Vesicles* **4**, (2015).

23. De Toro, J., Herschlik, L., Waldner, C. & Mongini, C. Emerging Roles of Exosomes in Normal and Pathological Conditions: New Insights for Diagnosis and Therapeutic Applications. *Front. Immunol.* **6**, (2015).

24. Rajagopal, C. & Harikumar, K. B. The Origin and Functions of Exosomes in Cancer. *Front. Oncol.* **8**, (2018).

25. Schwab, A. *et al.* Extracellular vesicles from infected cells: potential for direct pathogenesis. *Front. Microbiol.* **6**, (2015).

26. Pan, B.-T. & Johnstone, R. M. Fate of the transferrin receptor during maturation of sheep reticulocytes in vitro: Selective externalization of the receptor. *Cell* **33**, 967–978 (1983).

27. Harding, C., Heuser, J. & Stahl, P. Receptor-mediated endocytosis of transferrin and recycling of the transferrin receptor in rat reticulocytes. *J Cell Biol* **97**, 329–339 (1983).

28. Johnstone, R. M., Adam, M., Hammond, J. R., Orr, L. & Turbide, C. Vesicle formation during reticulocyte maturation. Association of plasma membrane activities with released vesicles (exosomes). *J. Biol. Chem.* **262**, 9412–9420 (1987).

29. Ratajczak, J. *et al.* Embryonic stem cell-derived microvesicles reprogram hematopoietic progenitors: evidence for horizontal transfer of mRNA and protein delivery. *Leukemia* **20**, 847–856 (2006).

30. Valadi, H. *et al.* Exosome-mediated transfer of mRNAs and microRNAs is a novel mechanism of genetic exchange between cells. *Nature Cell Biology* **9**, 654–659 (2007).

31. Robinson, D. G., Ding, Y. & Jiang, L. Unconventional protein secretion in plants: a critical assessment. *Protoplasma* **253**, 31–43 (2016).

32. Nawaz, M., Malik, M. I., Hameed, M. & Zhou, J. Research progress on the composition and function of parasite-derived exosomes. *Acta Tropica* **196**, 30–36 (2019).

33. Woith, E., Fuhrmann, G. & Melzig, M. F. Extracellular Vesicles—Connecting Kingdoms. *Int J Mol Sci* **20**, (2019).

34. Deatherage, B. L. & Cookson, B. T. Membrane Vesicle Release in Bacteria, Eukaryotes, and Archaea: a Conserved yet Underappreciated Aspect of Microbial Life. *Infection and Immunity* **80**, 1948–1957 (2012).

35. Samuel, M., Bleackley, M., Anderson, M. & Mathivanan, S. Extracellular vesicles including exosomes in cross kingdom regulation: a viewpoint from plant-fungal interactions. *Front. Plant Sci.* **6**, (2015).

36. György, B. *et al.* Membrane vesicles, current state-of-the-art: emerging role of extracellular vesicles. *Cell. Mol. Life Sci.* **68**, 2667–2688 (2011).

37. Zijlstra, A. & Di Vizio, D. Size matters in nanoscale communication. *Nature Cell Biology* **20**, 228–230 (2018).

38. Tricarico, C., Clancy, J. & D'Souza-Schorey, C. Biology and biogenesis of shed microvesicles. *Small GTPases* **8**, 220–232 (2017).

39. Meehan, B., Rak, J. & Di Vizio, D. Oncosomes – large and small: what are they, where they came from? *J Extracell Vesicles* **5**, (2016).

40. Ostrowski, M. *et al.* Rab27a and Rab27b control different steps of the exosome secretion pathway. *U61* (2010) doi:http://dx.doi.org/10.1038/ncb2000.

41. Colombo, M., Raposo, G. & Théry, C. Biogenesis, Secretion, and Intercellular Interactions of Exosomes and Other Extracellular Vesicles. *Annual Review of Cell and Developmental Biology* **30**, 255–289 (2014).

42. Nolte-'t Hoen, E. N. M. *et al.* Deep sequencing of RNA from immune cell-derived vesicles uncovers the selective incorporation of small non-coding RNA biotypes with potential regulatory functions. *Nucleic Acids Res* **40**, 9272–9285 (2012).

43. van Niel, G., D'Angelo, G. & Raposo, G. Shedding light on the cell biology of extracellular vesicles. *Nature Reviews Molecular Cell Biology* **19**, 213–228 (2018).

44. Kalluri, R. & LeBleu, V. S. The biology, function, and biomedical applications of exosomes. *Science* **367**, eaau6977 (2020).

45. Hoshino, A. *et al.* Tumour exosome integrins determine organotropic metastasis. *Nature* **527**, 329–335 (2015).

46. Mulcahy, L. A., Pink, R. C. & Carter, D. R. F. Routes and mechanisms of extracellular vesicle uptake. *Journal of Extracellular Vesicles* **3**, 24641 (2014).

47. Skog, J. *et al.* Glioblastoma microvesicles transport RNA and protein that promote tumor growth and provide diagnostic biomarkers. *Nat Cell Biol* **10**, 1470–1476 (2008).

48. Skotland, T., Sagini, K., Sandvig, K. & Llorente, A. An emerging focus on lipids in extracellular vesicles. *Advanced Drug Delivery Reviews* (2020) doi:10.1016/j.addr.2020.03.002.

49. Quesenberry, P. J., Aliotta, J., Deregibus, M. C. & Camussi, G. Role of extracellular RNA-carrying vesicles in cell differentiation and reprogramming. *Stem Cell Research & Therapy* **6**, 153 (2015).

50. McKelvey, K. J., Powell, K. L., Ashton, A. W., Morris, J. M. & McCracken, S. A. Exosomes: Mechanisms of Uptake. *Journal of Circulating Biomarkers* **4**, 7 (2015).

51. Eitan, E., Suire, C., Zhang, S. & Mattson, M. P. Impact of lysosome status on extracellular vesicle content and release. *Ageing Research Reviews* **32**, 65–74 (2016).

52. Desdín-Micó, G. & Mittelbrunn, M. Role of exosomes in the protection of cellular homeostasis. *Cell Adhesion & Migration* **11**, 127–134 (2017).

53. Vader, P., Breakefield, X. O. & Wood, M. J. A. Extracellular vesicles: emerging targets for cancer therapy. *Trends in Molecular Medicine* **20**, 385–393 (2014).

54. Thompson, A. G. *et al.* Extracellular vesicles in neurodegenerative disease — pathogenesis to biomarkers. *Nature Reviews Neurology* **12**, 346–357 (2016).

55. Noren Hooten, N. & Evans, M. K. Extracellular vesicles as signaling mediators in type 2 diabetes mellitus. *American Journal of Physiology-Cell Physiology* **318**, C1189–C1199 (2020).

56. Ailawadi, S., Wang, X., Gu, H. & Fan, G.-C. Pathologic function and therapeutic potential of exosomes in cardiovascular disease. *Biochimica et Biophysica Acta (BBA) - Molecular Basis of Disease* **1852**, 1–11 (2015).

57. Robbins, P. D. & Morelli, A. E. Regulation of immune responses by extracellular vesicles. *Nature Reviews Immunology* **14**, 195–208 (2014).

58. Robbins, P. D., Dorronsoro, A. & Booker, C. N. Regulation of chronic inflammatory and immune processes by extracellular vesicles. *J Clin Invest* **126**, 1173–1180 (2016).

59. Chan, B. D. *et al.* Exosomes in Inflammation and Inflammatory Disease. *PROTEOMICS* **19**, 1800149 (2019).

60. Steinbichler, T. B. *et al.* Therapy resistance mediated by exosomes. *Mol Cancer* **18**, 58 (2019).

61. Schorey, J. S., Cheng, Y., Singh, P. P. & Smith, V. L. Exosomes and other extracellular vesicles in host–pathogen interactions. *EMBO reports* **16**, 24–43 (2015).

62. Buck, A. H. *et al.* Exosomes secreted by nematode parasites transfer small RNAs to mammalian cells and modulate innate immunity. *Nature Communications* **5**, 1–12 (2014).

63. Correa, R., Caballero, Z., De León, L. F. & Spadafora, C. Extracellular Vesicles Could Carry an Evolutionary Footprint in Interkingdom Communication. *Front Cell Infect Microbiol* **10**, 76 (2020).

64. Coakley, G., Maizels, R. M. & Buck, A. H. Exosomes and Other Extracellular Vesicles: The New Communicators in Parasite Infections. *Trends in Parasitology* **31**, 477–489 (2015).

65. Zhang, L. *et al.* Exogenous plant MIR168a specifically targets mammalian LDLRAP1: evidence of cross-kingdom regulation by microRNA. *Cell Research* **22**, 107–126 (2012).

66. EL Andaloussi, S., Mäger, I., Breakefield, X. O. & Wood, M. J. A. Extracellular vesicles: biology and emerging therapeutic opportunities. *Nature Reviews Drug Discovery* **12**, 347–357 (2013).

67. György, B., Hung, M. E., Breakefield, X. O. & Leonard, J. N. Therapeutic Applications of Extracellular Vesicles: Clinical Promise and Open Questions. *Annu Rev Pharmacol Toxicol* **55**, 439–464 (2015).

68. Li, W. *et al.* Role of exosomal proteins in cancer diagnosis. *Molecular Cancer* **16**, 145 (2017).

69. Simpson, J. C. Functional Assays. in *Encyclopedic Reference of Genomics and Proteomics in Molecular Medicine* 617–620 (Springer, 2006). doi:10.1007/3-540-29623-9_3700.

70. Théry, C. *et al.* Minimal information for studies of extracellular vesicles 2018 (MISEV2018): a position statement of the International Society for Extracellular Vesicles and update of the MISEV2014 guidelines. *Journal of Extracellular Vesicles* **7**, 1535750 (2018).

71. Lötvall, J. *et al.* Minimal experimental requirements for definition of extracellular vesicles and their functions: a position statement from the International Society for Extracellular Vesicles. *Journal of Extracellular Vesicles* **3**, 26913 (2014).

72. Taylor, D. D. & Shah, S. Methods of isolating extracellular vesicles impact down-stream analyses of their cargoes. *Methods* **87**, 3–10 (2015).

73. Karimi, N. *et al.* Detailed analysis of the plasma extracellular vesicle proteome after separation from lipoproteins. *Cell. Mol. Life Sci.* **75**, 2873–2886 (2018).

74. Zhang, H. *et al.* Identification of distinct nanoparticles and subsets of extracellular vesicles by asymmetric flow field-flow fractionation. *Nat. Cell Biol.* **20**, 332–343 (2018).

75. Nolte-'t Hoen, E., Cremer, T., Gallo, R. C. & Margolis, L. B. Extracellular vesicles and viruses: Are they close relatives? *Proc Natl Acad Sci U S A* **113**, 9155–9161 (2016).

76. Shu, S. L. *et al.* Purity and yield of melanoma exosomes are dependent on isolation method. *J Extracell Vesicles* **9**, (2019).

77. Deun, J. V. *et al.* The impact of disparate isolation methods for extracellular vesicles on downstream RNA profiling. *Journal of Extracellular Vesicles* **3**, 24858 (2014).

78. Brennan, K. *et al.* A comparison of methods for the isolation and separation of extracellular vesicles from protein and lipid particles in human serum. *Scientific Reports* **10**, 1039 (2020).

79. Tkach, M. & Théry, C. Communication by Extracellular Vesicles: Where We Are and Where We Need to Go. *Cell* **164**, 1226–1232 (2016).

80. Mathieu, M., Martin-Jaular, L., Lavieu, G. & Théry, C. Specificities of secretion and uptake of exosomes and other extracellular vesicles for cell-to-cell communication. *Nature Cell Biology* **21**, 9–17 (2019).

81. Ramirez, M. I. *et al.* Technical challenges of working with extracellular vesicles. *Nanoscale* **10**, 881–906 (2018).

82. Panagopoulou, M. S., Wark, A. W., Birch, D. J. S. & Gregory, C. D. Phenotypic analysis of extracellular vesicles: a review on the applications of fluorescence. *Journal of Extracellular Vesicles* **9**, 1710020 (2020).

83. Alexander, M. *et al.* Exosome-delivered microRNAs modulate the inflammatory response to endotoxin. *Nature Communications* **6**, 1–16 (2015).

84. Mateescu, B. *et al.* Obstacles and opportunities in the functional analysis of extracellular vesicle RNA – an ISEV position paper. *J Extracell Vesicles* **6**, (2017).

85. Russell, A. E. *et al.* Biological membranes in EV biogenesis, stability, uptake, and cargo transfer: an ISEV position paper arising from the ISEV membranes and EVs workshop. *Journal of Extracellular Vesicles* **8**, 1684862 (2019).

86. Hung, M. E. & Leonard, J. N. A platform for actively loading cargo RNA to elucidate limiting steps in EV-mediated delivery. *Journal of Extracellular Vesicles* **5**, 31027 (2016).

87. Chuo, S. T.-Y., Chien, J. C.-Y. & Lai, C. P.-K. Imaging extracellular vesicles: current and emerging methods. *Journal of Biomedical Science* **25**, (2018).

88. Verweij, F. J. *et al.* Quantifying exosome secretion from single cells reveals a modulatory role for GPCR signaling. *J Cell Biol* **217**, 1129–1142 (2018).

89. Chen, C. *et al.* Visualization and intracellular dynamic tracking of exosomes and exosomal miRNAs using single molecule localization microscopy. *Nanoscale* **10**, 5154–5162 (2018).

90. Menyhárt, O. *et al.* Guidelines for the selection of functional assays to evaluate the hallmarks of cancer. *Biochimica et Biophysica Acta (BBA) - Reviews on Cancer* **1866**, 300–319 (2016).

91. Kumar, N., Afjei, R., Massoud, T. F. & Paulmurugan, R. Comparison of cell-based assays to quantify treatment effects of anticancer drugs identifies a new application for Bodipy-L-cystine to measure apoptosis. *Sci Rep* **8**, 16363 (2018).

92. Kitano, H. Systems Biology: A Brief Overview. *Science* **295**, 1662–1664 (2002).

93. Liu, H. *et al.* Colorectal cancer-derived exosomal miR-106b-3p promotes metastasis by down-regulating DLC-1 expression. *Clinical Science* **134**, 419–434 (2020).

94. Hurwitz, S. N. *et al.* CD63 Regulates Epstein-Barr Virus LMP1 Exosomal Packaging, Enhancement of Vesicle Production, and Noncanonical NF-κB Signaling. *Journal of Virology* **91**, (2017).

95. Pužar Dominkuš, P. *et al.* PKH26 labeling of extracellular vesicles: Characterization and cellular internalization of contaminating PKH26 nanoparticles. *Biochimica et Biophysica Acta (BBA) - Biomembranes* **1860**, 1350–1361 (2018).

96. Lai, C. P. *et al.* Visualization and tracking of tumour extracellular vesicle delivery and RNA translation using multiplexed reporters |. *Nature Communications* **6**, 7029 (2015).

97. Lai, C. P. *et al.* Dynamic Biodistribution of Extracellular Vesicles in Vivo Using a Multimodal Imaging Reporter. *ACS Nano* **8**, 483–494 (2014).

98. Morishita, M. *et al.* Quantitative Analysis of Tissue Distribution of the B16BL6-Derived Exosomes Using a Streptavidin-Lactadherin Fusion Protein and Iodine-125-Labeled Biotin Derivative After Intravenous Injection in Mice. *Journal of Pharmaceutical Sciences* **104**, 705–713 (2015).

99. Takahashi, Y. *et al.* Visualization and in vivo tracking of the exosomes of murine melanoma B16-BL6 cells in mice after intravenous injection. *Journal of Biotechnology* **165**, 77–84 (2013).

100. Mittelbrunn, M. *et al.* Unidirectional transfer of microRNA-loaded exosomes from T cells to antigen-presenting cells. *Nature Communications* **2**, (2011).

101. Pegtel, D. M. *et al.* Functional delivery of viral miRNAs via exosomes. *Proc Natl Acad Sci U S A* **107**, 6328–6333 (2010).

102. Kosaka, N. *et al.* Secretory Mechanisms and Intercellular Transfer of MicroRNAs in Living Cells. *J. Biol. Chem.* **285**, 17442–17452 (2010).

103. Toribio, V. *et al.* Development of a quantitative method to measure EV uptake. *Scientific Reports* **9**, 10522 (2019).

104. Martineau, M. *et al.* Semisynthetic fluorescent pH sensors for imaging exocytosis and endocytosis. *Nature Communications* **8**, 1–10 (2017).

105. Sung, B. H., Ketova, T., Hoshino, D., Zijlstra, A. & Weaver, A. M. Directional cell movement through tissues is controlled by exosome secretion. *Nature Communications* **6**, 1–14 (2015).

106. Sung, B. H. *et al.* A live cell reporter of exosome secretion and uptake reveals pathfinding behavior of migrating cells. *Nature Communications* **11**, 1–15 (2020).

107. Sung, B. H. & Weaver, A. M. Exosome secretion promotes chemotaxis of cancer cells. *Cell Adhesion & Migration* **11**, 187–195 (2017).

108. Heusermann, W. *et al.* Exosomes surf on filopodia to enter cells at endocytic hot spots, traffic within endosomes, and are targeted to the ER. *J Cell Biol* **213**, 173–184 (2016).

109. Beer, K. B. *et al.* Degron-tagged reporters probe membrane topology and enable the specific labelling of membrane-wrapped structures. *Nature Communications* **10**, 1–16 (2019).

110. Wehman, A. M., Poggioli, C., Schweinsberg, P., Grant, B. D. & Nance, J. The P4-ATPase TAT-5 Inhibits the Budding of Extracellular Vesicles in C. elegans Embryos. *Current Biology* **21**, 1951–1959 (2011).

111. de Jong, O. G. *et al.* A CRISPR-Cas9-based reporter system for single-cell detection of extracellular vesicle-mediated functional transfer of RNA. *Nat Commun* **11**, 1113 (2020).

112. Mathieu, M. *et al.* Specificities of exosome versus small ectosome secretion revealed by live intracellular tracking and synchronized extracellular vesicle release of CD9 and CD63. *bioRxiv* 2020.10.27.323766 (2020) doi:10.1101/2020.10.27.323766.

113. Polanco, J. C., Scicluna, B. J., Hill, A. F. & Götz, J. Extracellular Vesicles Isolated from the Brains of rTg4510 Mice Seed Tau Protein Aggregation in a Threshold-dependent Manner. *J. Biol. Chem.* **291**, 12445–12466 (2016).

114. Andreu, Z. & Yáñez-Mó, M. Tetraspanins in Extracellular Vesicle Formation and Function. *Front. Immunol.* **5**, (2014).

115. Hurwitz, S. N., Conlon, M. M., Rider, M. A., Brownstein, N. C. & Jr, D. G. M. Nanoparticle analysis sheds budding insights into genetic drivers of extracellular vesicle biogenesis. *Journal of Extracellular Vesicles* **5**, 31295 (2016).

116. Escrevente, C., Keller, S., Altevogt, P. & Costa, J. Interaction and uptake of exosomes by ovarian cancer cells. *BMC Cancer* **11**, 108 (2011).

117. Jayaram, A. K. *et al.* Biomembranes in bioelectronic sensing. *Trends in Biotechnology* (2021) doi:10.1016/j.tibtech.2021.06.001.

118. Zhao, Y. *et al.* Patch clamp technique: Review of the current state of the art and potential contributions from nanoengineering. *Proceedings of the Institution of Mechanical Engineers, Part N: Journal of Nanoengineering and Nanosystems* **222**, 1–11 (2008).

119. Bakheet, T. M. & Doig, A. J. Properties and identification of human protein drug targets. *Bioinformatics* **25**, 451–457 (2009).

120. van Niel, G. *et al.* Challenges and directions in studying cell–cell communication by extracellular vesicles. *Nat Rev Mol Cell Biol* 1–14 (2022) doi:10.1038/s41580-022-00460-3.

121. Buzás, E. I., Tóth, E. Á., Sódar, B. W. & Szabó-Taylor, K. É. Molecular interactions at the surface of extracellular vesicles. *Semin Immunopathol* **40**, 453–464 (2018).

122. Moremen, K. W., Tiemeyer, M. & Nairn, A. V. Vertebrate protein glycosylation: diversity, synthesis and function. *Nat Rev Mol Cell Biol* **13**, 448–462 (2012).

123. Overington, J. P., Al-Lazikani, B. & Hopkins, A. L. How many drug targets are there? *Nat Rev Drug Discov* **5**, 993–996 (2006).

124. Hauser, A. S., Attwood, M. M., Rask-Andersen, M., Schiöth, H. B. & Gloriam, D. E. Trends in GPCR drug discovery: new agents, targets and indications. *Nat Rev Drug Discov* **16**, 829–842 (2017).

125. Knobloch, J., Suhendro, D. K., Zieleniecki, J. L., Shapter, J. G. & Köper, I. Membrane–drug interactions studied using model membrane systems. *Saudi Journal of Biological Sciences* **22**, 714–718 (2015).

126. Fusco, G. *et al.* Structural basis of synaptic vesicle assembly promoted by α-synuclein. *Nat Commun* **7**, 12563 (2016).

127. Widder, K., Träger, J., Kerth, A., Harauz, G. & Hinderberger, D. Interaction of Myelin Basic Protein with Myelin-like Lipid Monolayers at Air–Water Interface. *Langmuir* **34**, 6095–6108 (2018).

128. Chadli, M. *et al.* New Tethered Phospholipid Bilayers Integrating Functional G-Protein-Coupled Receptor Membrane Proteins. *Langmuir* **33**, 10385–10401 (2017).

129. Tang, T. *et al.* Functional Infectious Nanoparticle Detector: Finding Viruses by Detecting Their Host Entry Functions Using Organic Bioelectronic Devices. *ACS Nano* **15**, 18142–18152 (2021).

130. Pappa, A.-M. *et al.* Optical and Electronic Ion Channel Monitoring from Native Human Membranes. *ACS Nano* (2020) doi:10.1021/acsnano.0c01330.

131. Uribe, J. *et al.* Dual Mode Sensing of Binding and Blocking of Cancer Exosomes to Biomimetic Human Primary Stem Cell Surfaces. *ACS Biomater. Sci. Eng.* (2021) doi:10.1021/acsbiomaterials.1c01056.

132. Tamm, L. K. & McConnell, H. M. Supported phospholipid bilayers. *Biophysical Journal* **47**, 105–113 (1985).

133. Jackman, J. A. & Cho, N.-J. Supported Lipid Bilayer Formation: Beyond Vesicle Fusion. *Langmuir* **36**, 1387–1400 (2020).

134. Hsia, C.-Y., J. Richards, M. & Daniel, S. A review of traditional and emerging methods to characterize lipid–protein interactions in biological membranes. *Analytical Methods* **7**, 7076–7094 (2015).

135. Liu, H.-Y., Chen, W.-L., Ober, C. K. & Daniel, S. Biologically Complex Planar Cell Plasma Membranes Supported on Polyelectrolyte Cushions Enhance Transmembrane Protein Mobility and Retain Native Orientation. *Langmuir* **34**, 1061–1072 (2018).

136. Diaz, A. J., Albertorio, F., Daniel, S. & Cremer, P. S. Double Cushions Preserve Transmembrane Protein Mobility in Supported Bilayer Systems. *Langmuir* **24**, 6820–6826 (2008).

137. Liu, H.-Y. *et al.* Self-assembly of mammalian cell membranes on bioelectronic devices with functional transmembrane proteins. *Langmuir* acs.langmuir.0c00804 (2020) doi:10.1021/acs.langmuir.0c00804.

138. Seddon, A. M., Curnow, P. & Booth, P. J. Membrane proteins, lipids and detergents: not just a soap opera. *Biochimica et Biophysica Acta (BBA) - Biomembranes* **1666**, 105–117 (2004).

139. Singh, R. R., Sangani, A. S., Daniel, S. & Koch, D. L. The combined hydrodynamic and thermodynamic effects of immobilized proteins on the diffusion of mobile transmembrane proteins. *Journal of Fluid Mechanics* **877**, 648–681 (2019).

140. Römer, W. & Steinem, C. Impedance Analysis and Single-Channel Recordings on Nano-Black Lipid Membranes Based on Porous Alumina. *Biophysical Journal* **86**, 955–965 (2004).

141. Andersson, J. & Köper, I. Tethered and Polymer Supported Bilayer Lipid Membranes: Structure and Function. *Membranes* **6**, 30 (2016).

142. Andersson, J., Köper, I. & Knoll, W. Tethered Membrane Architectures—Design and Applications. *Frontiers in Materials* **5**, (2018).

143. Pick, H., Alves, A. C. & Vogel, H. Single-Vesicle Assays Using Liposomes and Cell-Derived Vesicles: From Modeling Complex Membrane Processes to Synthetic Biology and Biomedical Applications. *Chem. Rev.* **118**, 8598–8654 (2018).

144. Liu, H.-Y. *et al.* Supported Planar Mammalian Membranes as Models of in Vivo Cell Surface Architectures. *ACS Appl. Mater. Interfaces* **9**, 35526–35538 (2017).

145. Richards, M. J. *et al.* Membrane Protein Mobility and Orientation Preserved in Supported Bilayers Created Directly from Cell Plasma Membrane Blebs. *Langmuir* **32**, 2963–2974 (2016).

146. Costello, D. A., Millet, J. K., Hsia, C.-Y., Whittaker, G. R. & Daniel, S. Single particle assay of coronavirus membrane fusion with proteinaceous receptor-embedded supported bilayers. *Biomaterials* **34**, 7895–7904 (2013).

147. Escribá, P. V. *et al.* Membranes: a meeting point for lipids, proteins and therapies. *Journal of Cellular and Molecular Medicine* **12**, 829–875 (2008).

148. van Meer, G., Voelker, D. R. & Feigenson, G. W. Membrane lipids: where they are and how they behave. *Nat Rev Mol Cell Biol* **9**, 112–124 (2008).

149. Selvaraj, V. *et al.* Mechanisms underlying the micron-scale segregation of sterols and GM1 in live mammalian sperm. *Journal of Cellular Physiology* **218**, 522–536 (2009).

150. Richter, R. P. & Brisson, A. R. Following the Formation of Supported Lipid Bilayers on Mica: A Study Combining AFM, QCM-D, and Ellipsometry. *Biophysical Journal* **88**, 3422–3433 (2005).

151. Briand, E., Zäch, M., Svedhem, S., Kasemo, B. & Petronis, S. Combined QCM-D and EIS study of supported lipid bilayer formation and interaction with pore -forming peptides. *Analyst* **135**, 343–350 (2010).

152. Bhattacharya, G. *et al.* X-ray Reflectivity Study of the Interaction of an Imidazolium-Based Ionic Liquid with a Soft Supported Lipid Membrane. *Langmuir* **33**, 1295–1304 (2017).

153. Soranzo, T., Martin, D. K., Lenormand, J.-L. & Watkins, E. B. Coupling neutron reflectivity with cell-free protein synthesis to probe membrane protein structure in supported bilayers. *Sci Rep* **7**, 3399 (2017).

154. Bruzas, I., Lum, W., Gorunmez, Z. & Sagle, L. Advances in surface-enhanced Raman spectroscopy (SERS) substrates for lipid and protein characterization: sensing and beyond. *Analyst* **143**, 3990–4008 (2018).

155. Kraft, M. L., Weber, P. K., Longo, M. L., Hutcheon, I. D. & Boxer, S. G. Phase Separation of Lipid Membranes Analyzed with High-Resolution Secondary Ion Mass Spectrometry. *Science* **313**, 1948–1951 (2006).

156. Pincet, F. *et al.* FRAP to Characterize Molecular Diffusion and Interaction in Various Membrane Environments. *PLOS ONE* **11**, e0158457 (2016).

157. Danial, J. S. H., Cronin, B., Mallik, C. & Walllace, M. I. On demand modulation of lipid composition in an individual bilayer. *Soft Matter* **13**, 1788–1793 (2017).

158. Kataoka-Hamai, C. & Yamazaki, T. Induced Rupture of Vesicles Adsorbed on Glass by Pore Formation at the Surface–Bilayer Interface. *Langmuir* **31**, 1312–1319 (2015).

159. Poltorak, L. *et al.* Lipid bilayers cushioned with polyelectrolyte-based films on doped silicon surfaces. *Biochimica et Biophysica Acta (BBA) - Biomembranes* **1860**, 2669–2680 (2018).

160. Largueze, J.-B., Kirat, K. E. & Morandat, S. Preparation of an electrochemical biosensor based on lipid membranes in nanoporous alumina. *Colloids and Surfaces B: Biointerfaces* **79**, 33–40 (2010).

161. Liu, Y., Chen, D., Zhang, W. & Zhang, Y. Mobile DNA tetrahedron on ultra-low adsorption lipid membrane for directional control of cell sensing. *Sensors and Actuators B: Chemical* **307**, 127570 (2020).

162. Saem, S. *et al.* Benchtop-fabricated lipid-based electrochemical sensing platform for the detection of membrane disrupting agents. *Sci Rep* **10**, 4595 (2020).

163. Hirtz, M. *et al.* Self-limiting multiplexed assembly of lipid membranes on large-area graphene sensor arrays. *Nanoscale* **8**, 15147–15151 (2016).

164. Kustanovich, K., Yantchev, V., Doosti, B. A., Gözen, I. & Jesorka, A. A microfluidics-integrated impedance/surface acoustic resonance tandem sensor. *Sensing and Bio-Sensing Research* **25**, 100291 (2019).

165. Cheng, Q., Zhu, S., Song, J. & Zhang, N. Functional lipid microstructures immobilized on a gold electrode for voltammetric biosensing of cholera toxin. *Analyst* **129**, 309–314 (2004).

166. Su, Z. *et al.* EIS and PM-IRRAS studies of alamethicin ion channels in a tethered lipid bilayer. *Journal of Electroanalytical Chemistry* **812**, 213–220 (2018).

167. Mazur, F., Bally, M., Städler, B. & Chandrawati, R. Liposomes and lipid bilayers in biosensors. *Advances in Colloid and Interface Science* **249**, 88–99 (2017).

168. Nishio, M., Teranishi, Y., Morioka, K., Yanagida, A. & Shoji, A. Real-time assay for exosome membrane fusion with an artificial lipid membrane based on enhancement of gramicidin A channel conductance. *Biosensors and Bioelectronics* **150**, 111918 (2020).

169. Perissinotto, F. *et al.* Structural insights into fusion mechanisms of small extracellular vesicles with model plasma membranes. *Nanoscale* **13**, 5224–5233 (2021).

170. Uribe, J. *et al.* Supported Membrane Platform to Assess Surface Interactions between Extracellular Vesicles and Stromal Cells. *ACS Biomater. Sci. Eng.* (2020) doi:10.1021/acsbiomaterials.0c00133.

171. Montis, C. *et al.* Biogenic Supported Lipid Bilayers from Nanosized Extracellular Vesicles. *Advanced Biosystems* **2**, 1700200 (2018).

172. Fernandez-Trillo, F., Grover, L. M., Stephenson-Brown, A., Harrison, P. & Mendes, P. M. Vesicles in Nature and the Laboratory: Elucidation of Their Biological Properties and Synthesis of Increasingly Complex Synthetic Vesicles. *Angewandte Chemie International Edition* **56**, 3142–3160 (2017).

173. Richards, M. J. *et al.* Membrane Protein Mobility and Orientation Preserved in Supported Bilayers Created Directly from Cell Plasma Membrane Blebs. *Langmuir* **32**, 2963–2974 (2016).

174. Montis, C. *et al.* Biogenic supported lipid bilayers as a tool to investigate nano-bio interfaces. *Journal of Colloid and Interface Science* **570**, 340–349 (2020).

175. Larios, J., Mercier, V., Roux, A. & Gruenberg, J. ALIX- and ESCRT-III–dependent sorting of tetraspanins to exosomes. *J Cell Biol* **219**, (2020).

176. Castellana, E. T. & Cremer, P. S. Solid supported lipid bilayers: From biophysical studies to sensor design. *Surface Science Reports* **61**, 429–444 (2006).

177. Khan, M. S., Dosoky, N. S. & Williams, J. D. Engineering Lipid Bilayer Membranes for Protein Studies. *International Journal of Molecular Sciences* **14**, 21561–21597 (2013).

178. Johnson, S. J. *et al.* Structure of an adsorbed dimyristoylphosphatidylcholine bilayer measured with specular reflection of neutrons. *Biophysical Journal* **59**, 289–294 (1991).

179. Koenig, B. W. *et al.* Neutron Reflectivity and Atomic Force Microscopy Studies of a Lipid Bilayer in Water Adsorbed to the Surface of a Silicon Single Crystal. *Langmuir* **12**, 1343–1350 (1996).

180. Diaz, A. J., Albertorio, F., Daniel, S. & Cremer, P. S. Double cushions preserve transmembrane protein mobility in supported bilayer systems. *Langmuir* **24**, 6820–6826 (2008).

181. Tanaka, M. & Sackmann, E. Polymer-supported membranes as models of the cell surface. *Nature* **437**, 656–663 (2005).

182. McCabe, I. P. & Forstner, M. B. Polymer Supported Lipid Bilayers. **2013**, (2013).

183. Rivnay, J., Owens, R. M. & Malliaras, G. G. The Rise of Organic Bioelectronics. *Chem. Mater.* **26**, 679–685 (2014).

184. Zhang, Y. *et al.* Supported Lipid Bilayer Assembly on PEDOT:PSS Films and Transistors. *Advanced Functional Materials* **26**, 7304–7313 (2016).

185. Perissinotto, F. *et al.* Structural Insights on Fusion Mechanisms of Extracellular Vesicles with Model Plasma Membrane. *bioRxiv* 2020.05.25.110601 (2020) doi:10.1101/2020.05.25.110601.

186. Rivnay, J., Owens, R. M. & Malliaras, G. G. The Rise of Organic Bioelectronics. *Chem. Mater.* **26**, 679–685 (2014).

187. Löffler, S., Libberton, B. & Richter-Dahlfors, A. Organic Bioelectronic Tools for Biomedical Applications. *Electronics* **4**, 879–908 (2015).

188. Simon, D. T., Gabrielsson, E. O., Tybrandt, K. & Berggren, M. Organic Bioelectronics: Bridging the Signaling Gap between Biology and Technology. *Chem. Rev.* **116**, 13009–13041 (2016).

189. Su, H. *et al.* Facile Generation of Biomimetic-Supported Lipid Bilayers on Conducting Polymer Surfaces for Membrane Biosensing. *ACS Appl. Mater. Interfaces* **11**, 43799–43810 (2019).

190. Strakosas, X., Bongo, M. & Owens, R. M. The organic electrochemical transistor for biological applications. *Journal of Applied Polymer Science* **132**, (2015).

191. Dijk, G., Rutz, A. L. & Malliaras, G. G. Stability of PEDOT:PSS-Coated Gold Electrodes in Cell Culture Conditions. *Advanced Materials Technologies* **5**, 1900662 (2020).

192. Proctor, C. M., Rivnay, J. & Malliaras, G. G. Understanding volumetric capacitance in conducting polymers. *Journal of Polymer Science Part B: Polymer Physics* **54**, 1433–1436 (2016).

193. Ohayon, D. *et al.* Laser Patterning of Self-Assembled Monolayers on PEDOT:PSS Films for Controlled Cell Adhesion. *Advanced Materials Interfaces* **4**, 1700191 (2017).

194. Ramuz, M., Hama, A., Rivnay, J., Leleux, P. & Owens, R. M. Monitoring of cell layer coverage and differentiation with the organic electrochemical transistor. *J. Mater. Chem. B* **3**, 5971–5977 (2015).

195. Zhang, Y. *et al.* Lipid bilayer formation on organic electronic materials. *J. Mater. Chem. C* **6**, 5218–5227 (2018).

196. Atanasov, V. *et al.* Membrane on a Chip: A Functional Tethered Lipid Bilayer Membrane on Silicon Oxide Surfaces. *Biophysical Journal* **89**, 1780–1788 (2005).

197. Skalová, Š., Vyskočil, V., Barek, J. & Navrátil, T. Model Biological Membranes and Possibilities of Application of Electrochemical Impedance Spectroscopy for their Characterization. *Electroanalysis* **30**, 207–219 (2018).

198. Rivnay, J. *et al.* Organic electrochemical transistors. *Nature Reviews Materials* **3**, 1–14 (2018).

199. Friedlein, J. T., McLeod, R. R. & Rivnay, J. Device physics of organic electrochemical transistors. *Organic Electronics* **63**, 398–414 (2018).

200. Bernards, D. A. & Malliaras, G. G. Steady-State and Transient Behavior of Organic Electrochemical Transistors. *Advanced Functional Materials* **17**, 3538–3544 (2007).

201. Rivnay, J. *et al.* High-performance transistors for bioelectronics through tuning of channel thickness. *Science Advances* **1**, e1400251 (2015).

202. Khodagholy, D. *et al.* High transconductance organic electrochemical transistors. *Nat Commun* **4**, 2133 (2013).

203. Ramuz, M. *et al.* Combined Optical and Electronic Sensing of Epithelial Cells Using Planar Organic Transistors. *Advanced Materials* **26**, 7083–7090 (2014).

204. Bernards, D. A., Malliaras, G. G., Toombes, G. E. S. & Gruner, S. M. Gating of an organic transistor through a bilayer lipid membrane with ion channels. *Appl. Phys. Lett.* **89**, 053505 (2006).

205. Ramuz, M. *et al.* Combined Optical and Electronic Sensing of Epithelial Cells Using Planar Organic Transistors. *Adv Mater* **26**, 7083–7090 (2014).

206. Ramuz, M., Hama, A., Rivnay, J., Leleux, P. & Owens, R. M. Monitoring of cell layer coverage and differentiation with the organic electrochemical transistor. *J. Mater. Chem. B* **3**, 5971–5977 (2015).

207. Brinkwirth, N. *et al.* Reliable identification of cardiac liability in drug discovery using automated patch clamp: Benchmarking best practices and calibration standards for improved proarrhythmic assessment. *Journal of Pharmacological and Toxicological Methods* **105**, 106884 (2020).

208. Bertholet, A. M. *et al.* Mitochondrial Patch Clamp of Beige Adipocytes Reveals UCP1-Positive and UCP1-Negative Cells Both Exhibiting Futile Creatine Cycling. *Cell Metabolism* **25**, 811-822.e4 (2017).

209. Velasco-Olmo, A., Ormaetxea Gisasola, J., Martinez Galvez, J. M., Vera Lillo, J. & Shnyrova, A. V. Combining patch-clamping and fluorescence microscopy for quantitative reconstitution of cellular membrane processes with Giant Suspended Bilayers. *Sci Rep* **9**, 7255 (2019).

210. Kamiya, K., Kawano, R., Osaki, T., Akiyoshi, K. & Takeuchi, S. Cell-sized asymmetric lipid vesicles facilitate the investigation of asymmetric membranes. *Nature Chem* **8**, 881–889 (2016).

211. Brosseau, C. & Sabri, E. Resistor–capacitor modeling of the cell membrane: A multiphysics analysis. *Journal of Applied Physics* **129**, 011101 (2021).

212. Curto, V. F. *et al.* Organic transistor platform with integrated microfluidics for in-line multi-parametric in vitro cell monitoring. *Microsystems & Nanoengineering* **3**, 17028 (2017).

213. Jimison, L. H. *et al.* Measurement of Barrier Tissue Integrity with an Organic Electrochemical Transistor. *Advanced Materials* **24**, 5919–5923 (2012).

214. Moysidou, C.-M. *et al.* 3D Bioelectronic Model of the Human Intestine. *Advanced Biology* **5**, 2000306 (2021).

215. Rivnay, J. *et al.* Organic electrochemical transistors for cell-based impedance sensing. *Appl. Phys. Lett.* **106**, 043301 (2015).

216. Inal, S. *et al.* Conducting Polymer Scaffolds for Hosting and Monitoring 3D Cell Culture. *Advanced Biosystems* **1**, 1700052 (2017).

217. Moysidou, C.-M. *et al.* 3D Bioelectronic Model of the Human Intestine. *Advanced Biology* **5**, 2000306 (2021).

218. Pitsalidis, C. *et al.* Transistor in a tube: A route to three-dimensional bioelectronics. *Science Advances* **4**, eaat4253 (2018).

219. Rivnay, J. *et al.* Using white noise to gate organic transistors for dynamic monitoring of cultured cell layers. *Sci Rep* **5**, 11613 (2015).

220. Fariat, G. C. *et al.* Organic electrochemical transistors as impedance biosensors. *MRS Communications* **4**, 189–194 (2014).

221. Huerta, M., Rivnay, J., Ramuz, M., Hama, A. & Owens, R. M. Early Detection of Nephrotoxicity In Vitro Using a Transparent Conducting Polymer Device. *Applied In Vitro Toxicology* **2**, 17–25 (2016).

222. Lieberth, K. *et al.* Monitoring Reversible Tight Junction Modulation with a Current-Driven Organic Electrochemical Transistor. *Advanced Materials Technologies* **6**, 2000940 (2021).

223. Yeung, S. Y., Gu, X., Tsang, C. M., Tsao, S. W. G. & Hsing, I. Organic electrochemical transistor array for monitoring barrier integrity of epithelial cells invaded by nasopharyngeal carcinoma. *Sensors and Actuators B: Chemical* **297**, 126761 (2019).

224. Ibsen, S. D. *et al.* Rapid Isolation and Detection of Exosomes and Associated Biomarkers from Plasma. *ACS Nano* **11**, 6641–6651 (2017).

225. Li, Q., Tofaris, G. K. & Davis, J. J. Concentration-Normalized Electroanalytical Assaying of Exosomal Markers. *Anal. Chem.* **89**, 3184–3190 (2017).

226. Kilic, T., Valinhas, A. T. D. S., Wall, I., Renaud, P. & Carrara, S. Label-free detection of hypoxia-induced extracellular vesicle secretion from MCF-7 cells. *Scientific Reports* **8**, 9402 (2018).

227. Mathew, D. G. *et al.* Electrochemical Detection of Tumor-Derived Extracellular Vesicles on Nanointerdigitated Electrodes. *Nano Lett.* **20**, 820–828 (2020).

228. Xu, L. *et al.* Optical, electrochemical and electrical (nano)biosensors for detection of exosomes: A comprehensive overview. *Biosensors and Bioelectronics* **161**, 112222 (2020).

229. Lubrano, C., Matrone, G. M., Iaconis, G. & Santoro, F. New Frontiers for Selective Biosensing with Biomembrane-Based Organic Transistors. *ACS Nano* **14**, 12271–12280 (2020).

230. Lubrano, C. *et al.* Towards biomimetic electronics that emulate cells. *MRS Communications* **10**, 398–412 (2020).

231. Szabó, G. T. *et al.* Critical role of extracellular vesicles in modulating the cellular effects of cytokines. *Cell. Mol. Life Sci.* **71**, 4055–4067 (2014).

232. Crescitelli, R. *et al.* Distinct RNA profiles in subpopulations of extracellular vesicles: apoptotic bodies, microvesicles and exosomes. *Journal of Extracellular Vesicles* **2**, 20677 (2013).

233. Caponnetto, F. *et al.* Size-dependent cellular uptake of exosomes. *Nanomedicine: Nanotechnology, Biology and Medicine* **13**, 1011–1020 (2017).

234. Van Deun, J. *et al.* EV-TRACK: transparent reporting and centralizing knowledge in extracellular vesicle research. *Nature Methods* **14**, 228–232 (2017).

235. Royo, F., Théry, C., Falcón-Pérez, J. M., Nieuwland, R. & Witwer, K. W. Methods for Separation and Characterization of Extracellular Vesicles: Results of a Worldwide Survey Performed by the ISEV Rigor and Standardization Subcommittee. *Cells* **9**, 1955 (2020).

236. Livshits, M. A. *et al.* Isolation of exosomes by differential centrifugation: Theoretical analysis of a commonly used protocol. *Scientific Reports* **5**, 17319 (2015).

237. Webber, J. & Clayton, A. How pure are your vesicles? *Journal of Extracellular Vesicles* **2**, 19861 (2013).

238. Linares, R., Tan, S., Gounou, C., Arraud, N. & Brisson, A. R. High-speed centrifugation induces aggregation of extracellular vesicles. *J Extracell Vesicles* **4**, (2015).

239. Witwer, K. W. *et al.* Standardization of sample collection, isolation and analysis methods in extracellular vesicle research. *Journal of Extracellular Vesicles* **2**, 20360 (2013).

240. Mol, E. A., Goumans, M.-J., Doevendans, P. A., Sluijter, J. P. G. & Vader, P. Higher functionality of extracellular vesicles isolated using size-exclusion chromatography compared to ultracentrifugation. *Nanomedicine: Nanotechnology, Biology and Medicine* **13**, 2061–2065 (2017).

241. Erdbrügger, U. & Lannigan, J. Analytical challenges of extracellular vesicle detection: A comparison of different techniques. *Cytometry Part A* **89**, 123–134 (2016).

242. Pol, E. van der *et al.* Particle size distribution of exosomes and microvesicles determined by transmission electron microscopy, flow cytometry, nanoparticle tracking analysis, and resistive pulse sensing. *Journal of Thrombosis and Haemostasis* **12**, 1182–1192 (2014).

243. Kowal, J. *et al.* Proteomic comparison defines novel markers to characterize heterogeneous populations of extracellular vesicle subtypes. *Proceedings of the National Academy of Sciences* **113**, E968–E977 (2016).

244. Lunavat, T. R. *et al.* Small RNA deep sequencing discriminates subsets of extracellular vesicles released by melanoma cells – Evidence of unique microRNA cargos. *RNA Biology* **12**, 810–823 (2015).

245. Zabeo, D. *et al.* Exosomes purified from a single cell type have diverse morphology. *Journal of Extracellular Vesicles* **6**, 1329476 (2017).

246. Pugholm, L. H., Revenfeld, A. L. S., Søndergaard, E. K. L. & Jørgensen, M. M. Antibody-Based Assays for Phenotyping of Extracellular Vesicles. *Biomed Res Int* **2015**, (2015).

247. Greening, D. W., Xu, R., Ji, H., Tauro, B. J. & Simpson, R. J. A Protocol for Exosome Isolation and Characterization: Evaluation of Ultracentrifugation, Density-Gradient Separation, and Immunoaffinity Capture Methods. in *Proteomic Profiling: Methods and Protocols* (ed. Posch, A.) 179–209 (Springer New York, 2015). doi:10.1007/978-1-4939-2550-6_15.

248. Lee, M., Ban, J.-J., Im, W. & Kim, M. Influence of storage condition on exosome recovery. *Biotechnol Bioproc E* **21**, 299–304 (2016).

249. Jung, M. K. & Mun, J. Y. Sample Preparation and Imaging of Exosomes by Transmission Electron Microscopy. *JoVE (Journal of Visualized Experiments)* e56482 (2018) doi:10.3791/56482.

250. Tauro, B. J. *et al.* Comparison of ultracentrifugation, density gradient separation, and immunoaffinity capture methods for isolating human colon cancer cell line LIM1863-derived exosomes. *Methods* **56**, 293–304 (2012).

251. Lee, D. W., Hsu, H.-L., Bacon, K. B. & Daniel, S. Image Restoration and Analysis of Influenza Virions Binding to Membrane Receptors Reveal Adhesion-Strengthening Kinetics. *PLOS ONE* **11**, e0163437 (2016).

252. Nathan, L. & Daniel, S. Single Virion Tracking Microscopy for the Study of Virus Entry Processes in Live Cells and Biomimetic Platforms. in *Physical Virology: Virus Structure and Mechanics* (ed. Greber, U. F.) 13–43 (Springer International Publishing, 2019). doi:10.1007/978-3-030-14741-9_2.

253. Kunze, A., Bally, M., Höök, F. & Larson, G. Equilibrium-fluctuation-analysis of single liposome binding events reveals how cholesterol and Ca2+ modulate glycosphingolipid trans-interactions. *Sci Rep* **3**, 1452 (2013).

254. Bally, M., Graule, M., Parra, F., Larson, G. & Höök, F. A virus biosensor with single virus-particle sensitivity based on fluorescent vesicle labels and equilibrium fluctuation analysis. *Biointerphases* **8**, 4 (2013).

255. Wallert, M. *et al.* Mucin-Inspired, High Molecular Weight Virus Binding Inhibitors Show Biphasic Binding Behavior to Influenza A Viruses. *Small* **16**, 2004635 (2020).

256. Peerboom, N. *et al.* Cell Membrane Derived Platform To Study Virus Binding Kinetics and Diffusion with Single Particle Sensitivity. *ACS Infect. Dis.* **4**, 944–953 (2018).

257. Burckhardt, C. J. & Greber, U. F. Virus Movements on the Plasma Membrane Support Infection and Transmission between Cells. *PLOS Pathogens* **5**, e1000621 (2009).

258. Jan Akhunzada, M. *et al.* Interplay between lipid lateral diffusion, dye concentration and membrane permeability unveiled by a combined spectroscopic and computational study of a model lipid bilayer. *Sci Rep* **9**, 1508 (2019).

259. Macháň, R. & Hof, M. Lipid diffusion in planar membranes investigated by fluorescence correlation spectroscopy. *Biochimica et Biophysica Acta (BBA) - Biomembranes* **1798**, 1377–1391 (2010).

260. Rose, M., Hirmiz, N., Moran-Mirabal, J. M. & Fradin, C. Lipid Diffusion in Supported Lipid Bilayers: A Comparison between Line-Scanning Fluorescence Correlation Spectroscopy and Single-Particle Tracking. *Membranes* **5**, 702–721 (2015).

261. Merminod, S., Edison, J. R., Fang, H., Hagan, M. F. & Rogers, W. B. Avidity and surface mobility in multivalent ligand–receptor binding. *Nanoscale* **13**, 12602–12612 (2021).

262. Jung, H., Robison, A. D. & Cremer, P. S. Multivalent ligand–receptor binding on supported lipid bilayers. *Journal of Structural Biology* **168**, 90–94 (2009).

263. White, J. M. & Whittaker, G. R. Fusion of Enveloped Viruses in Endosomes. *Traffic* **17**, 593–614 (2016).

264. White, J. M., Delos, S. E., Brecher, M. & Schornberg, K. Structures and Mechanisms of Viral Membrane Fusion Proteins: Multiple Variations on a Common Theme. *Critical Reviews in Biochemistry and Molecular Biology* **43**, 189–219 (2008).

265. Chernomordik, L. V. & Kozlov, M. M. Mechanics of membrane fusion. *Nat Struct Mol Biol* **15**, 675–683 (2008).

266. Carr, C. M. & Kim, P. S. A spring-loaded mechanism for the conformational change of influenza hemagglutinin. *Cell* **73**, 823–832 (1993).

267. Skehel, J. J. & Wiley, D. C. Receptor Binding and Membrane Fusion in Virus Entry: The Influenza Hemagglutinin. *Annual Review of Biochemistry* **69**, 531–569 (2000).

268. Costello, D. A., Whittaker, G. R. & Daniel, S. Variations in pH Sensitivity, Acid Stability, and Fusogenicity of Three Influenza Virus H3 Subtypes. *Journal of Virology* **89**, 350–360 (2015).

269. Hsu, H.-L., Millet, J. K., Costello, D. A., Whittaker, G. R. & Daniel, S. Viral fusion efficacy of specific H3N2 influenza virus reassortant combinations at single-particle level. *Scientific Reports* **6**, 35537 (2016).

270. Berquand, A. *et al.* Two-Step Formation of Streptavidin-Supported Lipid Bilayers by PEG-Triggered Vesicle Fusion. Fluorescence and Atomic Force Microscopy Characterization. *Langmuir* **19**, 1700–1707 (2003).

271. Outlaw, M. C. & Dimmock, N. J. IgG Neutralization of Type A Influenza Viruses and the Inhibition of the Endosomal Fusion Stage of the Infectious Pathway in BHK Cells. *Virology* **195**, 413–421 (1993).

272. Hsia, C.-Y., Chen, L., Singh, R. R., DeLisa, M. P. & Daniel, S. A Molecularly Complete Planar Bacterial Outer Membrane Platform. *Sci Rep* **6**, 32715 (2016).

273. Cui, Y., Wang, D. & Xie, M. Tumor-Derived Extracellular Vesicles Promote Activation of Carcinoma-Associated Fibroblasts and Facilitate Invasion and Metastasis of Ovarian Cancer by Carrying miR-630. *Frontiers in Cell and Developmental Biology* **9**, (2021).

274. Peng, J., Wang, W., Hua, S. & Liu, L. Roles of Extracellular Vesicles in Metastatic Breast Cancer. *Breast Cancer (Auckl)* **12**, 1178223418767666 (2018).

275. Becker, A. *et al.* Extracellular Vesicles in Cancer: Cell-to-Cell Mediators of Metastasis. *Cancer Cell* **30**, 836–848 (2016).

276. Grange, C. *et al.* Microvesicles Released from Human Renal Cancer Stem Cells Stimulate Angiogenesis and Formation of Lung Premetastatic Niche. *Cancer Research* **71**, 5346–5356 (2011).

277. Ortiz, A. Extracellular vesicles in cancer progression. *Seminars in Cancer Biology* **76**, 139–142 (2021).

278. Peinado, H. *et al.* Melanoma exosomes educate bone marrow progenitor cells toward a pro-metastatic phenotype through MET. *Nat Med* **18**, 883–891 (2012).

279. Cho, J. A., Park, H., Lim, E. H. & Lee, K. W. Exosomes from breast cancer cells can convert adipose tissue-derived mesenchymal stem cells into myofibroblast-like cells. *International Journal of Oncology* **40**, 130–138 (2012).

280. Song, Y. H. *et al.* Breast cancer-derived extracellular vesicles stimulate myofibroblast differentiation and pro-angiogenic behavior of adipose stem cells. *Matrix Biology* **60–61**, 190–205 (2017).

281. Eterno, V. *et al.* Adipose-derived mesenchymal stem cells (ASCs) may favour breast cancer recurrence via HGF/c-Met signaling. *Oncotarget* **5**, 613–633 (2013).

282. Scioli, M. G. *et al.* Adipose-Derived Stem Cells in Cancer Progression: New Perspectives and Opportunities. *International Journal of Molecular Sciences* **20**, 3296 (2019).

283. Freese, K. E. *et al.* Adipose-Derived Stems Cells and Their Role in Human Cancer Development, Growth, Progression, and Metastasis: A Systematic Review. *Cancer Research* **75**, 1161–1168 (2015).

284. Wang, M. *et al.* Role of tumor microenvironment in tumorigenesis. *J. Cancer* **8**, 761–773 (2017).

285. Chu, Y. *et al.* STAT3 activation by IL-6 from adipose-derived stem cells promotes endometrial carcinoma proliferation and metastasis. *Biochemical and Biophysical Research Communications* **500**, 626–631 (2018).

286. Prada, I. & Meldolesi, J. Binding and Fusion of Extracellular Vesicles to the Plasma Membrane of Their Cell Targets. *International Journal of Molecular Sciences* **17**, 1296 (2016).

287. French, K. C., Antonyak, M. A. & Cerione, R. A. Extracellular vesicle docking at the cellular port: Extracellular vesicle binding and uptake. *Seminars in Cell & Developmental Biology* **67**, 48–55 (2017).

288. Stranford, D. M., Hung, M. E., Gargus, E. S., Shah, R. N. & Leonard, J. N. A Systematic Evaluation of Factors Affecting Extracellular Vesicle Uptake by Breast Cancer Cells. *Tissue Engineering Part A* **23**, 1274–1282 (2017).

289. Mildmay-White, A. & Khan, W. Cell Surface Markers on Adipose-Derived Stem Cells: A Systematic Review. *Current Stem Cell Research & Therapy* **12**, 484–492.

290. Blandin, A.-F. *et al.* β1 Integrins as Therapeutic Targets to Disrupt Hallmarks of Cancer. *Frontiers in Pharmacology* **6**, (2015).

291. Kawan, M. *et al.* Monitoring supported lipid bilayers with n-type organic electrochemical transistors. *Mater. Horiz.* **7**, 2348–2358 (2020).

292. Moffat, J. G., Vincent, F., Lee, J. A., Eder, J. & Prunotto, M. Opportunities and challenges in phenotypic drug discovery: an industry perspective. *Nat Rev Drug Discov* **16**, 531–543 (2017).

293. McAleer, C. W. *et al.* On the potential of in vitro organ-chip models to define temporal pharmacokinetic-pharmacodynamic relationships. *Sci Rep* **9**, 9619 (2019).

294. Low, L. A., Mummery, C., Berridge, B. R., Austin, C. P. & Tagle, D. A. Organs-on-chips: into the next decade. *Nat Rev Drug Discov* **20**, 345–361 (2021).

295. Qu, Y. *et al.* Evaluation of MCF10A as a Reliable Model for Normal Human Mammary Epithelial Cells. *PLOS ONE* **10**, e0131285 (2015).

296. Puleo, J. & Polyak, K. The MCF10 Model of Breast Tumor Progression. *Cancer Research* **81**, 4183–4185 (2021).

297. Liu, K. *et al.* Evaluating cell lines as models for metastatic breast cancer through integrative analysis of genomic data. *Nat Commun* **10**, 2138 (2019).

298. Thiery, J. P., Acloque, H., Huang, R. Y. J. & Nieto, M. A. Epithelial-Mesenchymal Transitions in Development and Disease. *Cell* **139**, 871–890 (2009).

299. You, Y. *et al.* Matrix metalloproteinase 13-containing exosomes promote nasopharyngeal carcinoma metastasis. *Cancer Science* **106**, 1669–1677 (2015).

300. Cha, D. J. *et al.* KRAS-dependent sorting of miRNA to exosomes. *eLife* **4**, e07197 (2015).

301. Galindo-Hernandez, O., Serna-Marquez, N., Castillo-Sanchez, R. & Salazar, E. P. Extracellular vesicles from MDA-MB-231 breast cancer cells stimulated with linoleic acid promote an EMT-like process in MCF10A cells. *Prostaglandins, Leukotrienes and Essential Fatty Acids* **91**, 299–310 (2014).

302. Leal-Orta, E., Ramirez-Ricardo, J., Garcia-Hernandez, A., Cortes-Reynosa, P. & Salazar, E. P. Extracellular vesicles from MDA-MB-231 breast cancer cells stimulated with insulin-like growth factor 1 mediate an epithelial–mesenchymal transition process in MCF10A mammary epithelial cells. *J. Cell Commun. Signal.* (2021) doi:10.1007/s12079-021-00638-y.

303. Risha, Y., Minic, Z., Ghobadloo, S. M. & Berezovski, M. V. The proteomic analysis of breast cell line exosomes reveals disease patterns and potential biomarkers. *Sci Rep* **10**, 13572 (2020).

304. Mori, S. *et al.* Enhanced Expression of Integrin αvβ3 Induced by TGF-β Is Required for the Enhancing Effect of Fibroblast Growth Factor 1 (FGF1) in TGF-β-Induced Epithelial-Mesenchymal Transition (EMT) in Mammary Epithelial Cells. *PLOS ONE* **10**, e0137486 (2015).

305. Otero-Ortega, L. *et al.* Low dose of extracellular vesicles identified that promote recovery after ischemic stroke. *Stem Cell Research & Therapy* **11**, 70 (2020).

306. Yin, Y., Shelke, G. V., Lässer, C., Brismar, H. & Lötvall, J. Extracellular vesicles from mast cells induce mesenchymal transition in airway epithelial cells. *Respiratory Research* **21**, 101 (2020).

307. Brown, K. A. *et al.* Induction by transforming growth factor-β1 of epithelial to mesenchymal transition is a rare event in vitro. *Breast Cancer Research* **6**, R215 (2004).

308. Pell, T. J. *et al.* Epithelial Barrier Integrity Profiling: Combined Approach Using Cellular Junctional Complex Imaging and Transepithelial Electrical Resistance. *SLAS Discovery* **26**, 909–921 (2021).

309. Atai, N. A. *et al.* Heparin blocks transfer of extracellular vesicles between donor and recipient cells. *J Neurooncol* **115**, 343–351 (2013).

310. Jeppesen, D. K. *et al.* Reassessment of Exosome Composition. *Cell* **177**, 428-445.e18 (2019).

311. Melo, S. A. *et al.* Glypican-1 identifies cancer exosomes and detects early pancreatic cancer. *Nature* **523**, 177–182 (2015).

312. Szczepanski, M. J., Szajnik, M., Welsh, A., Whiteside, T. L. & Boyiadzis, M. Blast-derived microvesicles in sera from patients with acute myeloid leukemia suppress natural killer cell function via membrane-associated transforming growth factor-β1. *Haematologica* **96**, 1302–1309 (2011).

313. King, H. W., Michael, M. Z. & Gleadle, J. M. Hypoxic enhancement of exosome release by breast cancer cells. *BMC Cancer* **12**, 421 (2012).

314. Kowal, E. J. K., Ter-Ovanesyan, D., Regev, A. & Church, G. M. Extracellular Vesicle Isolation and Analysis by Western Blotting. in *Extracellular Vesicles: Methods and Protocols* (eds. Kuo, W. P. & Jia, S.) 143–152 (Springer, 2017). doi:10.1007/978-1-4939-7253-1_12.

315. Srinivasan, B. *et al.* TEER measurement techniques for in vitro barrier model systems. *J Lab Autom* **20**, 107–126 (2015).

316. Shintani, Y., Maeda, M., Chaika, N., Johnson, K. R. & Wheelock, M. J. Collagen I Promotes Epithelial-to-Mesenchymal Transition in Lung Cancer Cells via Transforming Growth Factor–β Signaling. *Am J Respir Cell Mol Biol* **38**, 95–104 (2008).

317. Vellinga, T. T. *et al.* Collagen-rich stroma in aggressive colon tumors induces mesenchymal gene expression and tumor cell invasion. *Oncogene* **35**, 5263–5271 (2016).

318. Kaiser, J.-P. *et al.* Cytotoxic effects of nanosilver are highly dependent on the chloride concentration and the presence of organic compounds in the cell culture media. *J Nanobiotechnology* **15**, 5 (2017).

319. Kolli, R., Kaivosoja, E. & Levon, K. Choice of Reference Electrode is Critical for Potentiometric Whole Cell-based Sensor. *Electroanalysis* **27**, 1636–1641 (2015).

320. Tria, S. A. *et al.* Dynamic Monitoring of Salmonella typhimurium Infection of Polarized Epithelia Using Organic Transistors. *Advanced Healthcare Materials* **3**, 1053–1060 (2014).

321. Xu, J., Lamouille, S. & Derynck, R. TGF-β-induced epithelial to mesenchymal transition. *Cell Res* **19**, 156–172 (2009).

322. Yang, J. *et al.* Guidelines and definitions for research on epithelial–mesenchymal transition. *Nat Rev Mol Cell Biol* **21**, 341–352 (2020).

323. Grände, M. *et al.* Transforming growth factor-β and epidermal growth factor synergistically stimulate epithelial to mesenchymal transition (EMT) through a MEK-dependent mechanism in primary cultured pig thyrocytes. *Journal of Cell Science* **115**, 4227–4236 (2002).

324. He, P., Qiu, K. & Jia, Y. Modeling of mesenchymal hybrid epithelial state and phenotypic transitions in EMT and MET processes of cancer cells. *Sci Rep* **8**, 14323 (2018).

325. Verma, R. Fibronectin. in *Encyclopedia of Cancer* (ed. Schwab, M.) 1399–1402 (Springer, 2011). doi:10.1007/978-3-642-16483-5_2182.

326. Reyngold, M. *et al.* Remodeling of the Methylation Landscape in Breast Cancer Metastasis. *PLOS ONE* **9**, e103896 (2014).

327. Chimonidou, M. *et al.* DNA Methylation of Tumor Suppressor and Metastasis Suppressor Genes in Circulating Tumor Cells. *Clinical Chemistry* **57**, 1169–1177 (2011).

328. Baylin, S. B. & Jones, P. A. A decade of exploring the cancer epigenome — biological and translational implications. *Nat Rev Cancer* **11**, 726–734 (2011).

329. Cheng, Y. *et al.* Targeting epigenetic regulators for cancer therapy: mechanisms and advances in clinical trials. *Sig Transduct Target Ther* **4**, 1–39 (2019).

330. Zhu, X. *et al.* BCR-ABL1–positive microvesicles transform normal hematopoietic transplants through genomic instability: implications for donor cell leukemia. *Leukemia* **28**, 1666–1675 (2014).

331. Zhao, D. *et al.* TFPI2 suppresses breast cancer progression through inhibiting TWIST-integrin α5 pathway. *Molecular Medicine* **26**, 27 (2020).

332. Guo, H. *et al.* Tissue factor pathway inhibitor-2 was repressed by CpG hypermethylation through inhibition of KLF6 binding in highly invasive breast cancer cells. *BMC Molecular Biology* **8**, 110 (2007).

333. Eads, C. A. *et al.* MethyLight: a high-throughput assay to measure DNA methylation. *Nucleic Acids Research* **28**, e32-00 (2000).

334. Chettouh, H. *et al.* Methylation panel is a diagnostic biomarker for Barrett's oesophagus in endoscopic biopsies and non-endoscopic cytology specimens. *Gut* **67**, 1942–1949 (2018).

335. Nairismägi, M.-L. *et al.* Translational control of TWIST1 expression in MCF-10A cell lines recapitulating breast cancer progression. *Oncogene* **31**, 4960–4966 (2012).

336. Zhan, Y. *et al.* Carcinoma-associated fibroblasts derived exosomes modulate breast cancer cell stemness through exonic circHIF1A by miR-580-5p in hypoxic stress. *Cell Death Discov.* **7**, 1–15 (2021).

337. Tan, E.-J. *et al.* Regulation of transcription factor Twist expression by the DNA architectural protein high mobility group A2 during epithelial-to-mesenchymal transition. *J Biol Chem* **287**, 7134–7145 (2012).

338. Ramesh, V., Brabletz, T. & Ceppi, P. Targeting EMT in Cancer with Repurposed Metabolic Inhibitors. *Trends in Cancer* **6**, 942–950 (2020).

339. Jonckheere, S. *et al.* Epithelial-Mesenchymal Transition (EMT) as a Therapeutic Target. *CTO* **211**, 157–182 (2022).

340. Dudás, J., Ladányi, A., Ingruber, J., Steinbichler, T. B. & Riechelmann, H. Epithelial to Mesenchymal Transition: A Mechanism that Fuels Cancer Radio/Chemoresistance. *Cells* **9**, 428 (2020).

341. Garcia, E. *et al.* Inhibition of triple negative breast cancer metastasis and invasiveness by novel drugs that target epithelial to mesenchymal transition. *Sci Rep* **11**, 11757 (2021).

342. Saxena, M., Stephens, M. A., Pathak, H. & Rangarajan, A. Transcription factors that mediate epithelial–mesenchymal transition lead to multidrug resistance by upregulating ABC transporters. *Cell Death Dis* **2**, e179–e179 (2011).

343. Pattabiraman, D. R. *et al.* Activation of PKA leads to mesenchymal-to-epithelial transition and loss of tumor-initiating ability. *Science* **351**, aad3680 (2016).

344. Van Noorden, C. J. F., van Sluis, G. L. & Spek, C. A. Experimental and clinical effects of anticoagulants on cancer progression. *Thrombosis Research* **125**, S77–S79 (2010).

345. Gerotziafas, G. T., Papageorgiou, C., Hatmi, M., Samama, M.-M. & Elalamy, I. Clinical Studies with Anticoagulants to Improve Survival in Cancer Patients. *PHT* **36**, 204–211 (2007).

346. Alyahya, R., Sudha, T., Racz, M., Stain, S. C. & Mousa, S. A. Anti-metastasis efficacy and safety of non-anticoagulant heparin derivative versus low molecular weight heparin in surgical pancreatic cancer models. *International Journal of Oncology* **46**, 1225–1231 (2015).

347. Niers, T. M. H. *et al.* Mechanisms of heparin induced anti-cancer activity in experimental cancer models. *Critical Reviews in Oncology/Hematology* **61**, 195–207 (2007).

348. Borsig, L. *et al.* Heparin and cancer revisited: Mechanistic connections involving platelets, P-selectin, carcinoma mucins, and tumor metastasis. *Proceedings of the National Academy of Sciences* **98**, 3352–3357 (2001).

349. Mei, L. *et al.* Antitumor and Antimetastasis Activities of Heparin-based Micelle Served As Both Carrier and Drug. *ACS Appl. Mater. Interfaces* **8**, 9577–9589 (2016).

350. Franzen, C. A. *et al.* Characterization of Uptake and Internalization of Exosomes by Bladder Cancer Cells. *BioMed Research International* **2014**, e619829 (2014).

351. Sento, S., Sasabe, E. & Yamamoto, T. Application of a Persistent Heparin Treatment Inhibits the Malignant Potential of Oral Squamous Carcinoma Cells Induced by Tumor Cell-Derived Exosomes. *PLOS ONE* **11**, e0148454 (2016).

352. Prada, I. *et al.* A new approach to follow a single extracellular vesicle—cell interaction using optical tweezers. *BioTechniques* **60**, 35 (2016).

353. Mondal, A., Ashiq, K. A., Phulpagar, P., Singh, D. K. & Shiras, A. Effective Visualization and Easy Tracking of Extracellular Vesicles in Glioma Cells. *Biol Proced Online* **21**, (2019).

354. Derendorf, H. *et al.* Pharmacokinetic/pharmacodynamic modeling in drug research and development. *J Clin Pharmacol* **40**, 1399–1418 (2000).

355. Soumpasis, D. M. Theoretical analysis of fluorescence photobleaching recovery experiments. *Biophysical Journal* **41**, 95–97 (1983).

356. Lu, B. & Maharbiz, M. M. Germanium as a scalable sacrificial layer for nanoscale protein patterning. *PLOS ONE* **13**, e0195062 (2018).

357. Wustoni, S., Savva, A., Sun, R., Bihar, E. & Inal, S. Enzyme-Free Detection of Glucose with a Hybrid Conductive Gel Electrode. *Advanced Materials Interfaces* **6**, 1800928 (2019).

358. Ohayon, D. *et al.* Biofuel powered glucose detection in bodily fluids with an n-type conjugated polymer. *Nat. Mater.* **19**, 456–463 (2020).

359. Nakagawa, T. *et al.* TGF-β induces proangiogenic and antiangiogenic factorsvia parallel but distinct Smad pathways1. *Kidney International* **66**, 605–613 (2004).

360. Rodríguez, T. M. *et al.* Effect of TGF-β1 Stimulation on the Secretome of Human Adipose-Derived Mesenchymal Stromal Cells. *Stem Cells Translational Medicine* **4**, 894–898 (2015).

361. Jarad, M., Kuczynski, E. A., Morrison, J., Viloria-Petit, A. M. & Coomber, B. L. Release of endothelial cell associated VEGFR2 during TGF-β modulated angiogenesis in vitro. *BMC Cell Biology* **18**, 10 (2017).

362. Aga, M. *et al.* Exosomal HIF1α supports invasive potential of nasopharyngeal carcinoma-associated LMP1-positive exosomes. *Oncogene* **33**, 4613–4622 (2014).

363. Ramteke, A. *et al.* Exosomes secreted under hypoxia enhance invasiveness and stemness of prostate cancer cells by targeting adherens junction molecules. *Molecular Carcinogenesis* **54**, 554–565 (2015).

364. Chen, Y. *et al.* Aberrant low expression of p85α in stromal fibroblasts promotes breast cancer cell metastasis through exosome-mediated paracrine Wnt10b. *Oncogene* **36**, 4692–4705 (2017).

365. Ozawa, P. M. M. *et al.* Extracellular vesicles from triple-negative breast cancer cells promote proliferation and drug resistance in non-tumorigenic breast cells. *Breast Cancer Res Treat* **172**, 713–723 (2018).

366. Jordan, K. R. *et al.* Extracellular vesicles from young women's breast cancer patients drive increased invasion of non-malignant cells via the Focal Adhesion Kinase pathway: a proteomic approach. *Breast Cancer Research* **22**, 128 (2020).

367. Sarrió, D. *et al.* Epithelial-Mesenchymal Transition in Breast Cancer Relates to the Basal-like Phenotype. *Cancer Research* **68**, 989–997 (2008).

368. Goh, C. Y. *et al.* Exosomes in triple negative breast cancer: Garbage disposals or Trojan horses? *Cancer Letters* **473**, 90–97 (2020).

369. Bauer, K. R., Brown, M., Cress, R. D., Parise, C. A. & Caggiano, V. Descriptive analysis of estrogen receptor (ER)-negative, progesterone receptor (PR)-negative, and HER2-negative

invasive breast cancer, the so-called triple-negative phenotype. *Cancer* **109**, 1721–1728 (2007).

370. Fulford, L. G. *et al.* Basal-like grade III invasive ductal carcinoma of the breast: patterns of metastasis and long-term survival. *Breast Cancer Research* **9**, R4 (2007).
371. Yao, H. *et al.* Triple-negative breast cancer: is there a treatment on the horizon? *Oncotarget* **8**, 1913–1924 (2016).
372. Santner, S. J. *et al.* Malignant MCF10CA1 Cell Lines Derived from Premalignant Human Breast Epithelial MCF10AT Cells. *Breast Cancer Res Treat* **65**, 101–110 (2001).
373. Cichon, M. A., Degnim, A. C., Visscher, D. W. & Radisky, D. C. Microenvironmental Influences that Drive Progression from Benign Breast Disease to Invasive Breast Cancer. *J Mammary Gland Biol Neoplasia* **15**, 389–397 (2010).
374. Bertolini, I., Perego, M., Ghosh, J. C., Kossenkov, A. V. & Altieri, D. C. NFκB activation by hypoxic small extracellular vesicles drives oncogenic reprogramming in a breast cancer microenvironment. *Oncogene* **41**, 2520–2525 (2022).
375. Lai, X. *et al.* Epithelial-Mesenchymal Transition and Metabolic Switching in Cancer: Lessons From Somatic Cell Reprogramming. *Frontiers in Cell and Developmental Biology* **8**, (2020).
376. Zhang, Y. & Weinberg, R. A. Epithelial-to-mesenchymal transition in cancer: complexity and opportunities. *Front. Med.* **12**, 361–373 (2018).
377. Jolly, M. K., Ware, K. E., Gilja, S., Somarelli, J. A. & Levine, H. EMT and MET: necessary or permissive for metastasis? *Molecular Oncology* **11**, 755–769 (2017).
378. Hiew, M. S. Y. *et al.* Incomplete cellular reprogramming of colorectal cancer cells elicits an epithelial/mesenchymal hybrid phenotype. *Journal of Biomedical Science* **25**, 57 (2018).
379. Bronsert, P. *et al.* Cancer cell invasion and EMT marker expression: a three-dimensional study of the human cancer–host interface. *The Journal of Pathology* **234**, 410–422 (2014).

380. Sampson, V. B. *et al.* Wilms' Tumor Protein Induces an Epithelial-Mesenchymal Hybrid Differentiation State in Clear Cell Renal Cell Carcinoma. *PLOS ONE* **9**, e102041 (2014).

381. Schliekelman, M. J. *et al.* Molecular Portraits of Epithelial, Mesenchymal, and Hybrid States in Lung Adenocarcinoma and Their Relevance to Survival. *Cancer Research* **75**, 1789–1800 (2015).

382. Wrenn, E. D. *et al.* Regulation of Collective Metastasis by Nanolumenal Signaling. *Cell* **183**, 395-410.e19 (2020).

383. Barrios-Rodiles, M. *et al.* High-Throughput Mapping of a Dynamic Signaling Network in Mammalian Cells. *Science* **307**, 1621–1625 (2005).

384. Haynes, J., Srivastava, J., Madson, N., Wittmann, T. & Barber, D. L. Dynamic actin remodeling during epithelial–mesenchymal transition depends on increased moesin expression. *Mol Biol Cell* **22**, 4750–4764 (2011).

385. Liu, C.-Y., Lin, H.-H., Tang, M.-J. & Wang, Y.-K. Vimentin contributes to epithelial-mesenchymal transition cancer cell mechanics by mediating cytoskeletal organization and focal adhesion maturation. *Oncotarget* **6**, 15966–15983 (2015).

8 APPENDICES

Appendix A: Materials and methods

8.1 Cell culture

8.1.1 HEK-293 and HEK-TREK cells

Human embryonic kidney 293 cells (HEK-293; kind gift from Marc Borsotto, Université de Nice Sophia Antipolis, France) were cultured in 75 cm^2 flasks with advanced Dulbecco's modified Eagle medium (DMEM; Thermo Fisher Scientific, TFS) with the addition of 10% foetal bovine serum (Merck), 50 U/mL penicillin and 50 μg/mL streptomycin (TFS), 1% (v/v) GlutaMax (TFS), and 50 μg/mL gentamicin (TFS). HEK-293 cells transfected overexpressing TREK-1 (potassium channel subfamily K member 2; KCNK2) protein (HEK-TREK-1; kind gift from Marc Borsotto, Université de Nice Sophia Antipolis, France) were similarly cultured in 75 cm^2 flasks with the same media as HEK supplemented with 500 μg/mL G 418 disulfate salt solution (Merck). Cells were cultured until 80–90% confluent before passaging, and cells were cultured until P60 and P30 for HEK-293 and HEK-TREK-1, respectively.

8.1.2 Vero and BHK cells

Vero E6 (Vero) cells (accession no. CRL-1586, ATCC) were cultured in 75 cm^2 flasks with Dulbecco's modified Eagle medium (DMEM; Sigma-Aldrich) supplemented with 10% foetal bovine serum (Sigma-Aldrich), 2 mM GlutaMax (Gibco), and 1% (v/v) penicillin-streptomycin (Gibco). Baby hamster kidney cells (BHK) were similarly cultured in the same media as Vero cells. Cells were maintained at 37 °C, 5% CO_2, and passaged when reaching 80–90% confluency using Dulbecco's phosphate-buffered saline (DPBS) and Trypsin EDTA (Cellgro).

8.1.3 ADSCs

StemPro Human ADSCs were obtained from ThermoFisher Scientific (Rochester, NY) and cultured in ADSC growth medium kit purchased from Lonza (Walkersville, MD). Experiments were performed with cells between passages 1 and 6. All cell cultures were maintained at 37 °C and 5% CO_2, and the media were changed every 2–3 days as recommended by manufacturers.

8.1.4 MDA-MB-231 cells

MDA-MB-231 epithelial breast cancer cells (ATCC HTB-26) were cultured according to supplier's instructions with Dulbecco's Modified Eagle Medium (DMEM; Thermo Fisher Scientific, TFS) and supplemented with 10% (v/v) foetal bovine serum (FBS; Merck), 50 U/mL

penicillin, 50 μg/mL streptomycin, and 1% (v/v) GlutaMAX (TFS). MDA-MB-231 (ATCC HTB-26) cells were cultured to 80% confluency before passaging and did not exceed 15 passages.

8.1.5 MCF10A cells

MCF10A human mammary epithelial cells (ATCC CRL-10317) were cultured with Mammary Epithelial Cell Growth Medium Basal Medium (CC-3151; Lonza) and supplemented with growth supplements BPE, 2 ml; hEGF, 0.5 ml; Hydrocortisone, 0.5 ml; and insulin, 0.5 ml from MEGM SingleQuots Supplement Pack (CC-4136; Lonza) and 100 ng/ml cholera toxin (Sigma Aldrich). MCF10A were cultured to 70-80% confluency before passaging and did not exceed 10 passages. Trypsin neutralising solution (TFS) was used during subculturing. All cell lines were incubated at 37 °C with 5% CO_2.

8.2 EV characterisation

8.2.1 Dynamic light scattering (DLS)

EV samples were analysed by dynamic light scattering using a Zetasizer Nano S90 (Malvern Panalytical) configured with a 633 nm laser and a 90-degree scattering optic. DLS measures the correlation function of intensity fluctuations and mathematically converts this into an intensity size distribution using the Stokes-Einstein relationship. The Malvern Zetasizer software was set to automatically determine the adequate number of runs per measurement. All measurements were carried out at 25 °C using disposable plastic cuvettes.

8.2.2 Nanoparticle tracking analysis (NTA)

NTA was used to determine the size and particle concentration of EVs. Samples were diluted 100-fold in PBS and tracked on a Nanosight NS500 (Malvern) configured with a 532 nm laser and an Electron Multiplication Charge-Couple Device Camera (EMCCD). Each sample was diluted in particle-free PBS to concentrations of 10^8-10^9 particles/mL and introduced manually. At least 3 x 60 s videos were recorded per sample. Particle concentration and size distribution was determined using NTA 3.2 software. Detection threshold was set to 8. All measurements were carried out at 18-19 °C. NTA measures nanoparticles in suspension by analysing Brownian motion and finding the size of the translational diffusion diameter (hydrodynamic diameter) of each sphere/nanoparticle. The lower resolution limit of NTA depends on the scattered intensity of the particle and the sensitivity of the camera. Biological particles such as EVs have a refractive index of about 1.37-1.45 giving a lower limit of detection of around 30 nm.

8.2.3 Zeta potential measurements

Zeta potential was determined using a folded capillary zeta cell (DTS1070, Malvern) and a Zetasizer Nano ZSP (Malvern). Samples were dispersed in PBS (pH 7.4) and the Smoluchowski model was applied.

8.2.4 Protein quantification

The total protein content of intact EVs was quantified using a Qubit 4 Fluorometer (TFS) and a bicinchoninic acid assay (BCA) Gold kit (TFS) as per manufacturer's instructions.

8.2.5 Transmission electron microscopy (TEM)

EV samples were visualized by TEM using negative staining method. 10 µl sample was applied on glow-discharged carbon-coated copper grids for 2 min, washed twice in Milli-Q water for 30 seconds each, and stained with 1% (w/v) water solution of uranyl acetate for 2 min at RT. Imaging was performed on a FEI Tecnai G20 electron microscope, operating at 200 kV, 20-micron objective aperture, and images were recorded with an AMT camera.

8.2.6 Immunogold labelling

TEVs from MDA-MB-231 cells were incubated with mouse anti-CD63 (TFS, 1:5 000) followed by anti-Ms conjugated with 20 nm gold nanoparticle (1: 5 000; TFS) for 2 hrs. TEVs were spun through a G25 column (Cytiva) after each incubation step and imaged using TEM.

8.3 Immunoblot analysis

To extract protein from EVs, pellets from UC were resuspended in the supplemented RIPA buffer, or already solubilised samples were mixed with RIPA buffer at a 1:1 ratio under agitation. Protein content was quantified as described previously and samples were stored at -80 °C pending further analysis.

EV lysates were diluted in lithium dodecyl sulfate (LDS) sample buffer (4X Bolt; Invitrogen), denatured by heating for 10 min at 70 °C, and subjected to electrophoresis using precast NuPAGE Novex 4-12% Bis-Tris Proteins Gels (Invitrogen) in NuPAGE MES SDS Running Buffer (Invitrogen) under non-reducing conditions at constant 200 V for 30 min. The same amount of protein (between 10-25 µg) from each sample was loaded into the gel wells. Proteins were electrotransferred onto PVDF Transfer Membranes (TFS) using NuPAGE Transfer Buffer (Invitrogen). Membranes were blocked with 5% (w/v) BSA in PBS (TFS, Oxoid) with 0.1% (v/v) Tween-20 (PBST; TFS) for 1 h. Membranes were probed with mouse anti-CD9 (Invitrogen; 1:5 000), mouse anti-CD63 (TFS, 1:5 000), mouse anti-annexin A1 (TFS; 1:5 000), and/or rabbit anti-calreticulin (abcam; 1:5 000) monoclonal primary antibodies for 1 h in PBST.

This was followed by incubation with HRP-conjugated anti-mouse IgG H&L (Invitrogen; 1:10 000) and anti-rabbit IgG H&L (abcam; 1:10 000) secondary antibodies in PBST for 1 h. All incubations were carried out on a shaker at RT or 4 °C. Western blots were washed 3-5 times in PBST for 5 min after each incubation step and were visualised using Pierce enhanced chemiluminescence (ECL) Western Blotting Substrate (TFS) on a G:BOX Chemi XX6 (Syngene).

8.4 Formation of supported lipid bilayers from liposomes and blebs

8.4.1 Preparation of glass coverslips

Glass microscope coverslips (25 mm × 25 mm; no. 1.5, VWR) were cleaned in piranha solution (45 mL 50% hydrogen peroxide (Sigma) and 105 ml of sulfuric acid (BDH)) for 10 min and rinsed with DI water for 30 min. Glass coverslips were subjected to oxygen plasma treatment (Harrick Plasma Cleaner) at a pressure of 750 mTorr on the high setting for 2 min prior to PEDOT:PSS spin-coating.

8.4.2 Cell blebbing

This protocol has been described in previous literature.[130,135,173] Briefly, 9×10^5 cells were seeded in 10 cm culture dishes (Corning) supplemented with 6 mL of culture media and grown for 24–72 h until 90% confluent in a 37 °C, 5% CO_2 incubator. Cells were washed with GPMV buffer (2 mM $CaCl_2$, 10 mM HEPES, 150 mM NaCl at pH 7.4), and then incubated in 4 mL of vesiculation buffer (GPMV buffer supplemented with 25 mM formaldehyde (FA; Sigma-Aldrich) and 2 mM dithiothreitol (DTT; Sigma-Aldrich)) to induce bleb formation. Cells were incubated at 37 °C for 1 h (**ADSCs**), 1 h 30 min (**BHK**), and 3 h (**Vero**). The cell supernatant, containing the blebs, was settled on ice for 15-25 min, to separate the cell debris from the blebs. Cell blebs were subsequently collected from the supernatant. The cell blebs were stored at 2-8 °C for up to 2 weeks.

8.4.3 Fluorescent labelling of liposomes, blebs, and EVs

To label the SLB, 1 μL of 0.36 mM octadecyl rhodamine B chloride (R18, Molecular Probes) fluorophore, a membrane-intercalating fluorophore, was added to 200 μL of bleb solution in a sonication bath for 15 min. The excess of fluorophore was removed by using a G25 spin column (GE Healthcare). Starting from the labelled blebs/liposomes, supported lipid bilayers were assembled as described in the previous section.

8.4.4 Fluorescence recovery after photobleaching (FRAP)

FRAP experiments were performed on an inverted Zeiss LSM800 confocal microscope (Zeiss Germany) with a 10× objective. A 150 mW 561 nm optically pumped semiconductor laser (Coherent, Inc.) was used to photobleach a 20 μm diameter spot in the supported lipid bilayer, and its fluorescence intensity recovery was monitored up to 20 min. The fluorescence intensity change over time was fit using a Bessel function, following the method of Soumpasis et al.[355] The diffusion coefficient was calculated with equation 6:

$$D = w^2/4t_{1/2} \quad (6)$$

where w is the radius of the photobleached spot and $t_{1/2}$ is the time required to achieve half of the maximum recovery intensity. The mobile fraction was determined by the final intensity over the initial intensity of the bleached area.

8.4.5 Preparing lipid vesicles from liposomes

The lipids 1,2-Dioleoyl-sn-glycero-3-phosphocholine (DOPC; 10 mg/mL) and 1,2-dioleoyl-3-trimethylammonium-propane (chloride salt) (DOTAP; 25 mg/ml) (Avanti Polar Lipids) were combined at a 4:1 ratio. The organic solvent in which there were dispersed was evaporated using a desiccator and the liposomes were resuspended in PBS to a final concentration of 2-4 mg/L. Large, unilamellar vesicles were prepared by extrusion using a 0.2 μm polycarbonate membrane (Avanti Polar Lipids) and the solution was stored at 2-8 °C for up to 2 weeks.

8.5 Organic electronic devices

8.5.1 PEDOT:PSS preparation and coating

The PEDOT:PSS solution contained 95% v/v Clevios PH 1000 (Heraeus), 5% v/v ethylene glycol (Sigma-Aldrich), 0.002% v/v 4-dodecylbenzenesulfonic acid (Sigma-Aldrich), and 1% v/v (3-glycidyloxypropyl) trimethoxysilane (Sigma-Aldrich). The solution was sonicated after every step and made fresh prior to spin-coating.[201] The complete solution was filtered through a 0.8 μm filter. PEDOT:PSS was spin coated onto MEAs (dried under nitrogen and treated with oxygen plasma for 2 min just prior to use) at 2,500-3,000 rpm for 35 s, baked at 140 °C for 1 h, and then immersed in DI water for 4 h. Prior to use, PEDOT:PSS coated slides and devices were washed gently in 70 % ethanol, kept in DI water overnight, dried using N_2 gas, and O_2 plasma treated.

8.5.2 Electronic device fabrication (chapter 3)*

PEDOT:PSS electrodes and OECTs were fabricated using a process developed specifically for patterning delicate materials.[356] Glass wafers were cleaned for 20 min in a 9:1 sulfuric acid/hydrogen peroxide solution heated at 120 °C. E-beam evaporation was used to deposit Ti (5 nm)/Au (50 nm)/Ti (5 nm) on top of a photoresist/lift-off resist bilayer prepatterned by photolithography, followed by lift off in solvent. The two thin Ti layers act as adhesion layers between Au and the substrate and top insulator. Plasma-enhanced chemical vapor deposition was used to coat the SiO_2 (100 nm) insulation layer and Au contacts were exposed using photolithography and etched with CHF3 reactive ion etching. A PEDOT:PSS (Clevios PH1000) solution containing 5 vol% ethylene glycol and 1 vol% (3-glycidyloxypropyl)trimethyoxysilane was spin-coated at 2000 rpm, baked on a hot plate at 120 °C for 20 min, and immersed in methanol for 5 min, followed by rinsing in deionized water. The polymer was then protected by a sacrificial layer of Ge (100 nm) deposited using e-beam evaporation. Photolithography followed by reactive ion etching with CF4 and O_2 were used to etch through the Ge and PEDOT:PSS layers, respectively. The Ge sacrificial layer was removed by immersing the chips in deionized water overnight.

8.5.3 Multielectrode array fabrication (chapter 4)†

Multielectrode arrays (MEAs) were fabricated using an established photolithography process on 4 in. glass wafers. The wafers were cleaned using a piranha (H_2O_2/H_2SO_4, ratio 1:3–4) bath, washed with water, and cleaned with O_2 plasma (Nanoplas DSB 6000). The electrode areas were defined using standard photolithography steps. To perform the lift-off step, the wafers were coated with a photoresist bilayer consisting of LOR 5B (Microchem) and S1813 (Shipley), exposed to UV light using the EVG 6200 mask alignment system and developed using a MF319 developer. A 10 nm layer of Cr and a 100 nm layer of Au were deposited using magnetron sputtering

* Electronic devices were provided by colleagues from the Salleo Research Group at Department of Materials Science and Engineering, Stanford University, USA

† Electronic devices were provided by Victor Druet (Organic Bioelectronics Laboratory, KAUST)

(Equipment Support Company Ltd. ESCRD4) and lifted using appropriate solvents. After the lift-off step, the first parylene C layer was vaporized to a thickness of 1.7 μm using an SCS Labcoter 2 with silane as an adhesion promoter. A second Parylene C layer was vaporized to act as the sacrificial layer for polymer film patterning. A layer of AZ9260 was spun cast and developed using an AZ developer as a mask for reactive ion etching (Oxford Instruments PlasmaLab 100-ICP 380), which was used to expose the device channels and pads for polymer deposition. Each chip consists of four circular electrodes of 500 μm in diameter (0.00196 cm^2).

8.5.4 Fabrication of OECTs (chapter 5)‡

OECTs were microfabricated on glass substrates based on established protocols using standard photolithography and parylene C peel-off techniques.[357,358] The process starts with the first layer of photoresist (AZ5214) being spin coated and exposed to ultraviolet light using contact aligner to create Au electrodes and interconnection pads. The photoresist patterns were generated with AZ 726 MIF developer, followed by metal sputtering of 10 nm Cr and 100 nm Au and a standard lift-off process using hot dimethyl sulfoxide. Next, we coated the second layer of photoresist AZ9260 on the substrates and developed them using AZ developer. A parylene C layer was deposited to insulate the gold interconnects. The OECT channel and gate were patterned by reactive ion etching, using a second layer of parylene C, which was peeled off to yield a channel length and width of 50 μm or 100 μm and a gate dimension of 500 x 500 μm^2.

8.6 Electrical Measurements

8.6.1 Electrochemical impedance spectroscopy (EIS)

A potentiostat (Autolab PGSTAT128N) equipped with a frequency response analysis module was used to record the impedance spectra in the frequency range between 100 KHz and 0.1 Hz. Commercially available Ag/AgCl and a platinum mesh were used as reference and counter electrodes, respectively. The PEDOT:PSS-coated Au MEAs were used as the working electrodes.

‡ Electronic devices were provided by Victor Druet from the Organic Bioelectronics Laboratory at KAUST, SA

A glass cloning cylinder was glued onto the MEA using PDMS to act as a well. The electrodes were circular, 500 μm in diameter, and thus the active electrochemical area was 0.00196 cm^2. The applied AC voltage was 0.01 V, and the DC voltage was 0 V versus open circuit potential. All measurements were taken in 1 × PBS buffer contained in a glass well attached to the MEAs.

8.6.2 Organic electrochemical transistor measurements

OECTs were characterized using a dual-channel source-meter unit (NI-PXI) with custom-written control code in LabVIEW. All measurements were performed using a Ag/AgCl pellet (D = 2 mm × H = 2 mm – Warner instruments) as the gate electrode. The channels studied were 50 μm in length and 50 μm in width. The devices were placed under the confocal microscope on top of a 1.2 mm-thick supporting glass slide. FRAP measurements were performed with a 10× magnification objective and at the same time a drain voltage −0.5 V was continuously applied. The OECT response time was calculated by applying square shaped pulses at the gate electrode, 0.5 V in magnitude and 5 ms in width.

8.7 Assessment of VEGF secretion by ADSCs[§]

ADSCs were seeded on a Millicell EZ-slide (Millipore, Burlington, MA) at a density of 8 × 10^4 cells/well. After 48 h, ADSCs were changed to 2% FBS media to slow down cell proliferation and incubated overnight at 37 °C and 5% CO_2. Each well had a different treatment as follows: negative control with no treatment (NT), ADSCs treated with 40 μg of cEXOs, ADSCs incubated with 20 μg/mL of anti-integrin β1/CD29 antibody (MAB 2253Z, Millipore, Burlington, MA) for 2 h at 37 °C, followed by addition of 40 μg of cEXOs, and ADSCs treated with 10 ng/ml of TGFβ1 (ThemoFisher Scientific, Waltham, MA). Cell media were changed every other day along each of the treatments. In addition, 100 μL of media from each well were removed on days 0, 2, and 5 and stored at −20 °C for the VEGF-ELISA assay. As a measure of proangiogenic activity, VEGF secretion by ADSCs under all mentioned conditions was assessed using a Human VEGF DuoSet ELISA kit (R&D Systems, Minneapolis, MN) following the manufacturer's protocol. The VEGF

[§] Work by Uribe

concentration was normalized by the number of alive cells under each condition. The number of alive cells was assessed for each well/treatment on days 2 and 5 by staining cells' nuclei using Hoechst (ThermoFisher Scientific, Waltham, MA) and getting the average number of cells in 30 frames per well in images acquired using an inverted Zeiss Axio Observer Z1 microscope with α Plan-Apochromat objectives, a Hamamatsu EM-CCD camera, Image EM, model C9100-13 (Bridgewater, NJ), and an X-Cite 120 microscope light source, Lumen Dynamics Group Inc. (Ontario, Canada). Four independent replicates of the experiment were performed.

Appendix B: Supplementary Information

8.8 Characterisation of SLBs on PEDOT:PSS substrates and electronic devices

Most recently, the integration of 'authentic' cell membranes on chip have been successfully used for ion channel activity studies, preserving orientation and function of the ion channels as demonstrated both optically and electrically, providing a viable alternative to patch clamp whole-cell experiments.[137] In a follow-up study, the effect of two pharmacological compounds on the K^+ ion channel, TREK-1, was assessed electrically on native plasma membranes derived from human embryonic kidney cells.[130] The results were confirmed using two types of electrical measurement, EIS and transistor-based, while simultaneously performing optical studies on the same devices. To successfully form the natively-derived, mobile membranes on PEDOT:PSS electronic devices used in the studies above, SLBs were formed on PEDOT:PSS coated glass substrates and OECTs and characterised by FRAP.

Optically, one figure of merit to evaluate quality is the lateral mobility (fluidity) of the lipids within the membrane plane, which can be assessed using FRAP. Since OECT channels are transparent, they are compatible with FRAP. For these tests, lipids were labelled with a lipophilic fluorescent molecule, R18, prior to their rupture. If the SLB forms after liposome rupture, the fluorophore is then free to diffuse in the two-dimensional plane of the bilayer; upon photobleaching, intensity recovers as unbleached R18 molecules exchange with bleached ones in the photobleached areas. If the liposomes do not rupture, then there will be no recovery after photobleaching. SLB quality is quantitatively assessed by calculating the diffusion coefficient (*D*) and mobile fraction (*MF*) from the kinetics of fluorescence recovery in this photobleached area. As PEDOT:PSS electrodes have opaque gold films beneath, they do not facilitate direct optical measurements and SLBs must therefore be characterised on PEDOT:PSS-coated glass instead. Vero and BHK + POPC SLBs were formed on glass and OECTs to compare the extracted *D* and *MF* values (**Figure S8.1**).

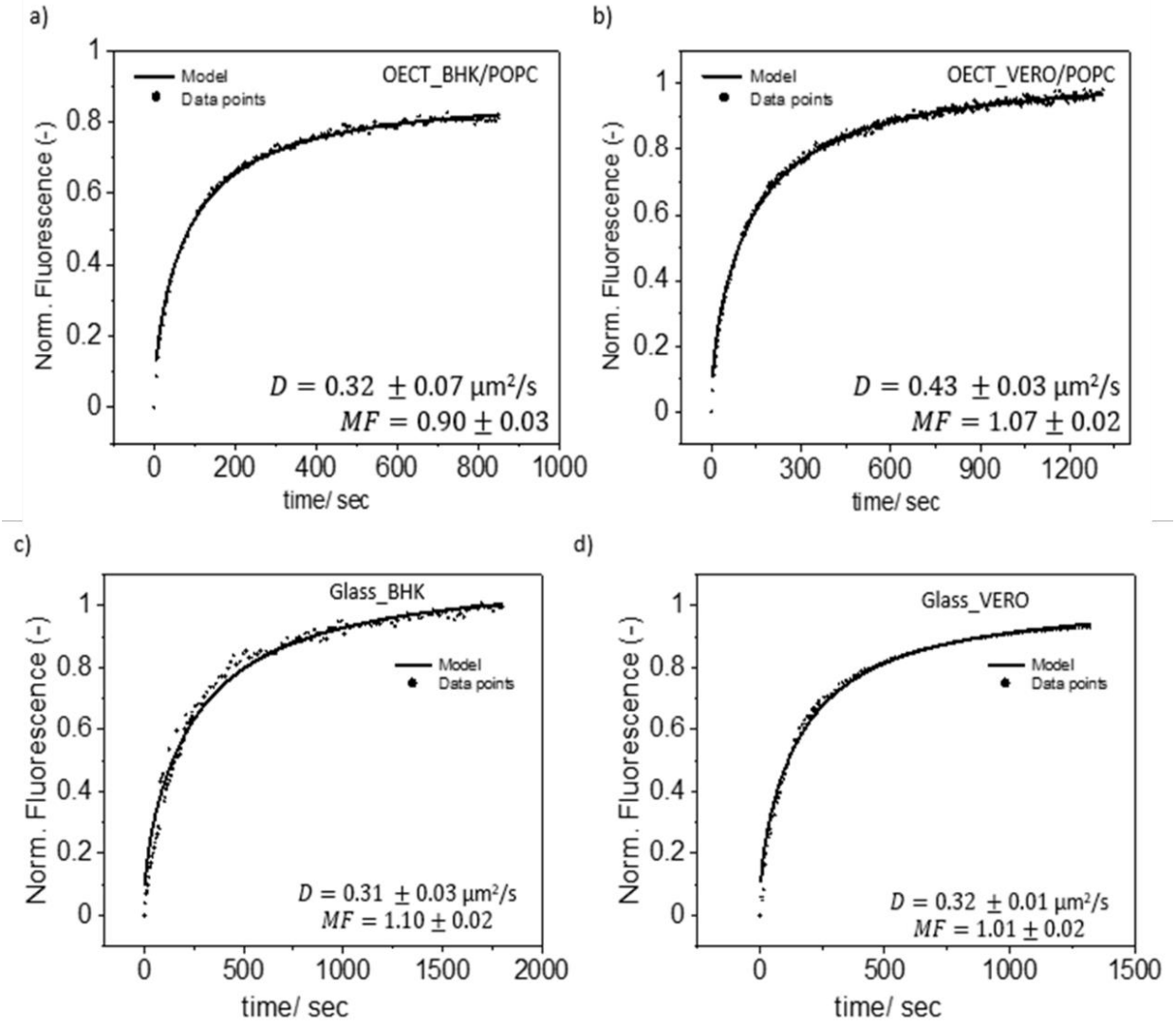

Figure S8.1: Comparing membrane mobility on PEDOT:PSS and glass substrates. FRAP measurements of (a) BHK SLBs and (b) Vero SLBs formed on the PEDOT:PSS-based OECT channels and FRAP measurements on the same SLBs formed on bare glass: (c) BHK and (d) Vero.

The transparency of PEDOT:PSS films in the OECT is a major advantage compared to the electrodes. Placing the OECT devices under a confocal microscope, while the three terminals of the device are connected, enables simultaneous electrical and optical monitoring of the SLBs formed on the channels of the OECT (Figure S8.6).

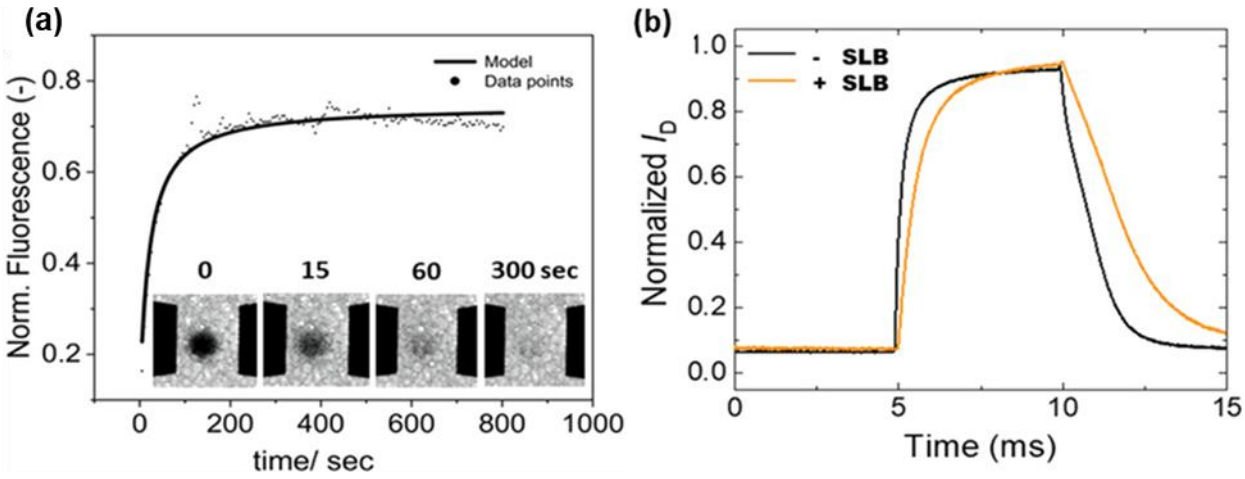

Figure S8.2: Simultaneous optical and electrical characterisation of HEK-TREK-derived SLB on PEDOT:PSS OECTs. (a) (FRAP measurements performed simultaneously with the electrical measurements from the same PEDOT:PSS-OECT channel (50 μm × 50 μm) shown in b of HEK-TREK-derived SLB. Inset images depicting (from left to right) photobleached, initial recovery, partial recovery, and complete recovery, with D = 1.50 μm^2/s and MF = 0.75. n=1. Black boxes are source and drain electrodes with the PEDOT:PSS channel in between. (b) Temporal response of the drain current. A 0.5 V pulse was applied at the gate, while the drain voltage was −0.5 V. The speed of the device response (τ) to a square gate pulse increases by the presence of a HEK-TREK membrane.[130]

Here, a HEK-TREK-derived SLB formed on an OECT was probed by dual optical and electrical readouts. The FRAP measurements were carried out at the same time as the OECT response was measured to confirm the quality of the membrane formed on the device. The optical characterization of the membrane is in agreement with the electrical data recorded simultaneously. These results demonstrate the ability to form synthetic SLBs and native biomembranes on CP-coated substrates and bioelectronic devices using the vesicle fusion method for sensing applications.

8.9 Supplementary Information for Chapter 2

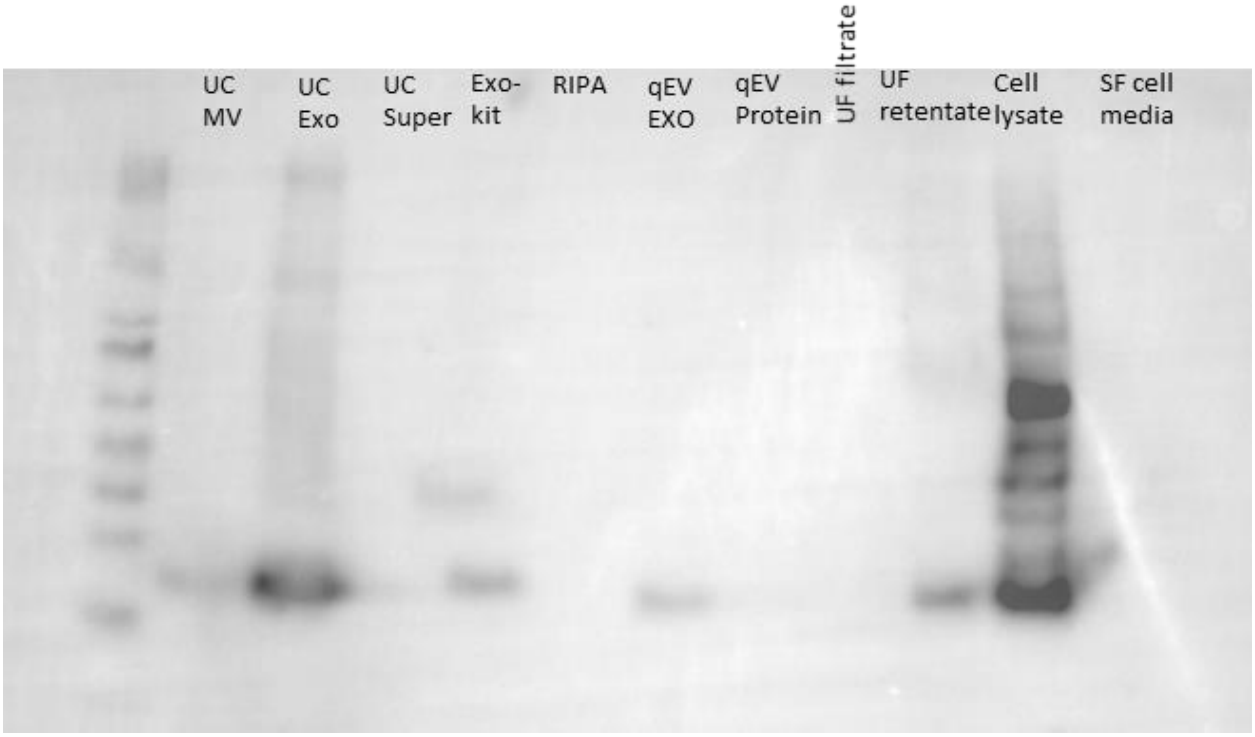

Figure S8.3: Western blot against EV biomarker CD9

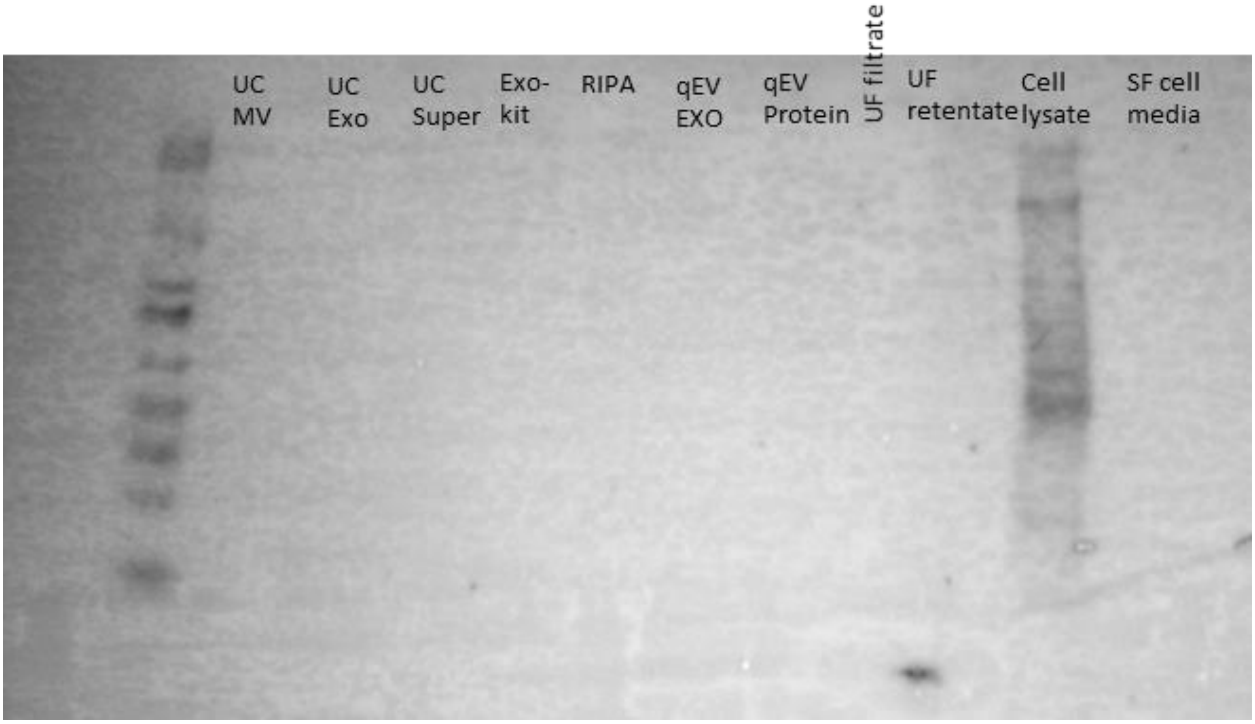

Figure S8.4: Western blot against ER marker calreticulin

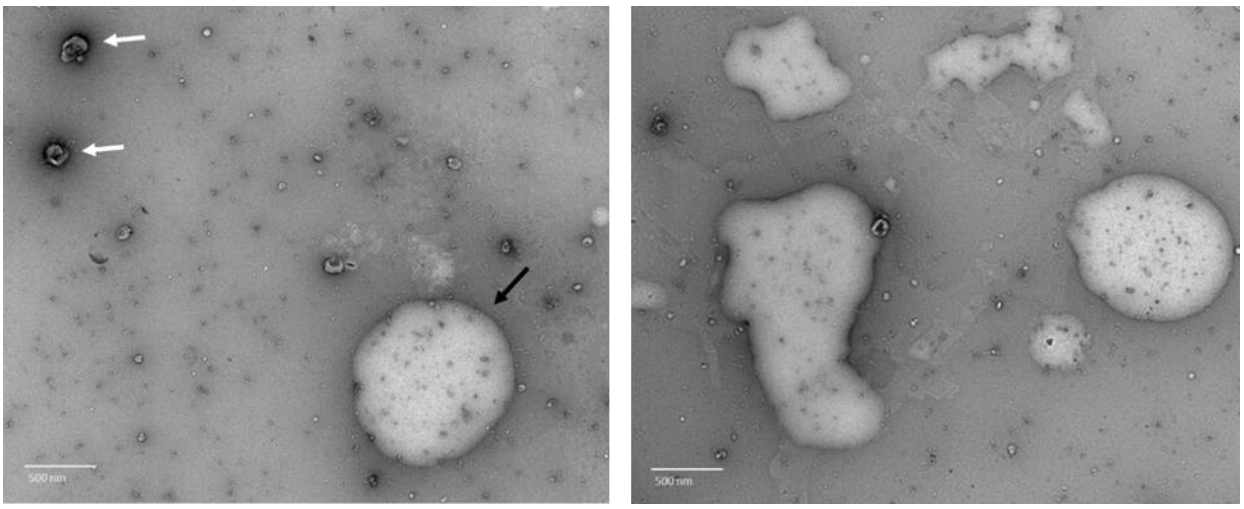

Figure S8.5: TEM images from SEC EV isolates. **LHS**: Exosome-sized particles with cup shaped morphology (white arrows) and large vesicle, potentially a liposome (black arrow). **RHS**: These irregular shaped vesicles are most likely fragments from the cell membrane that carried over.

8.10 Supplementary Information for Chapter 3

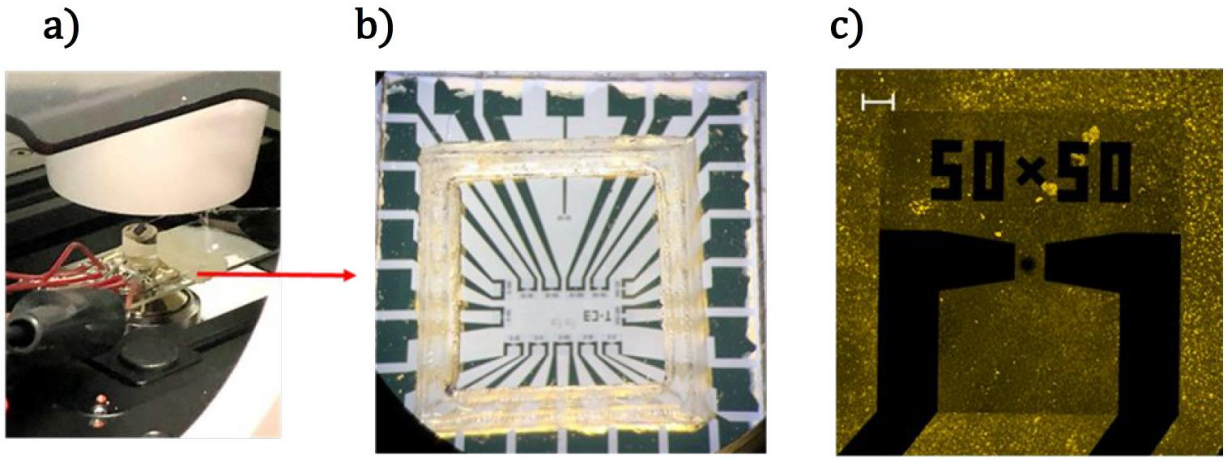

Figure S8.6: Simultaneous optical and electronic measurements on the channel of OECTs. (a-c) Experimental setup used for the simultaneous optical and electrical measurements using OECT devices. The OECT devices were secured on the confocal platform (a) with wired connections to the dual-channel source-meter unit (NI-PXI) for simultaneous optical and electrical measurements. (b) a well on an array of devices. The array shown is approximately 1 cm x 1cm. (c) 10x magnification of 50x50 µm OECT channel with R18 stained HEK-TREK-1 derived SLB captured immediately after photobleaching. Scale bar is 50µm.[129]

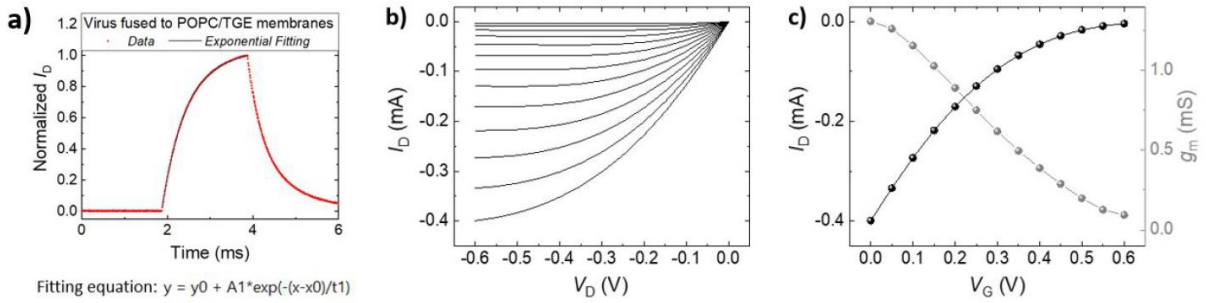

Figure S8.7: Fitting the response time of OECTs. Fitting the evolution of the drain current after a short voltage pulse at the gate with an exponential function to determine τ, i.e. the response time of OECTs (t1 in the fitting equation). b) representative output curves and c) representative transfer and transconductance curves at VD= -0.6 V of the PEDOT:PSS-based OECT channels used in this study with dimensions: Width = Length = 50 µm.

8.11 Supplementary Information for Chapter 4

8.11.1 Characterisation of ADSCs blebs and cEXOs*

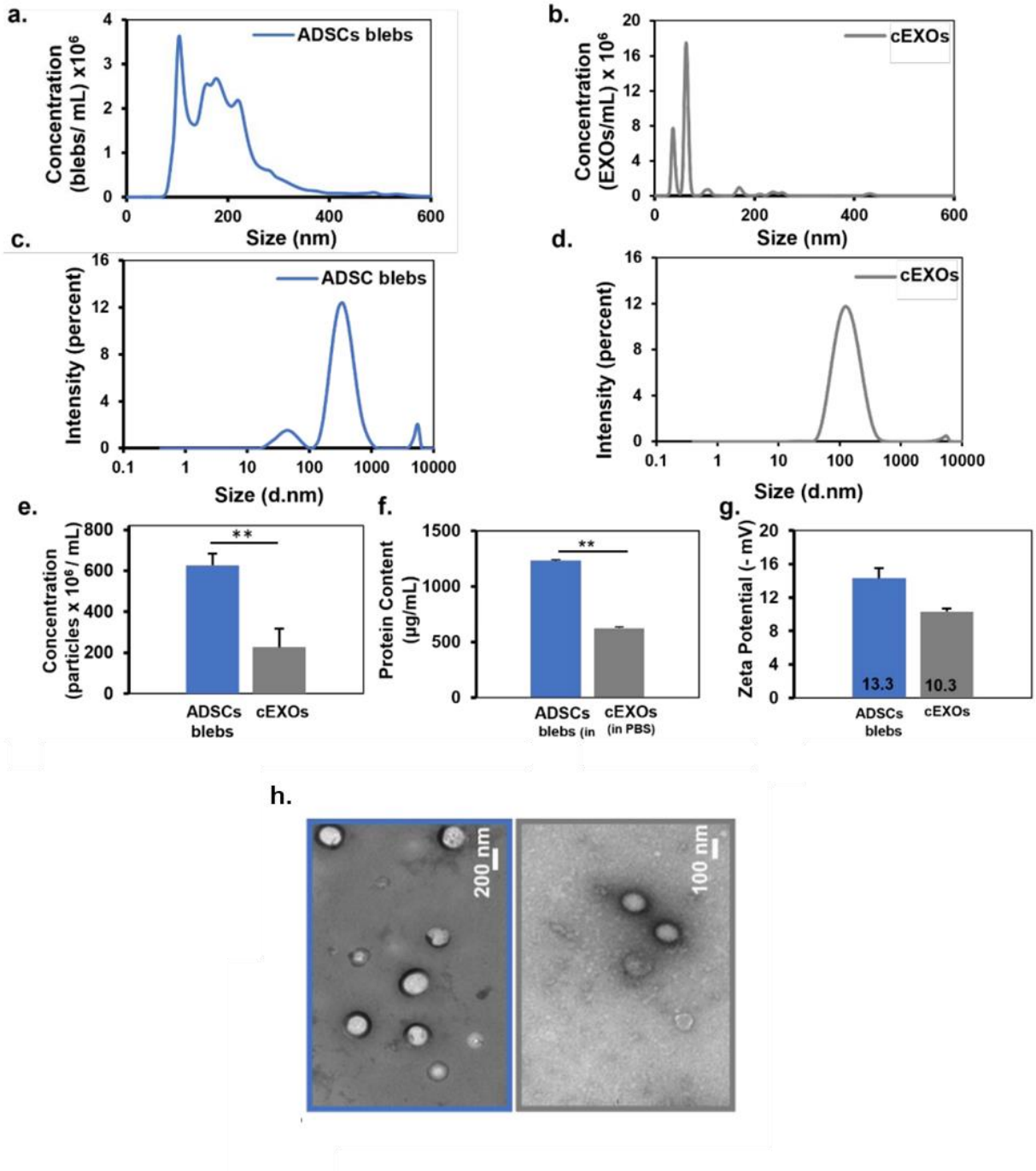

Figure S8.8: Characterization of ADSCs blebs and cEXOs. Size distribution of ADSCs membrane blebs by (**a**) NTA and by (**c**) DLS. Size distribution of cEXOs by (**b**) NTA and by (**d**) DLS. Particle concentration of ADSCs blebs and cEXOs by (**e**) NTA and protein concentration by (**f**) BCA. (**g**) Zeta potential of ADSCs blebs and cEXOs using laser Doppler electrophoresis. (**i**) TEM images of ADSCs cell blebs (LHS) and cEXOs (RHS).

8.11.2 EIS of antibody binding to SLB

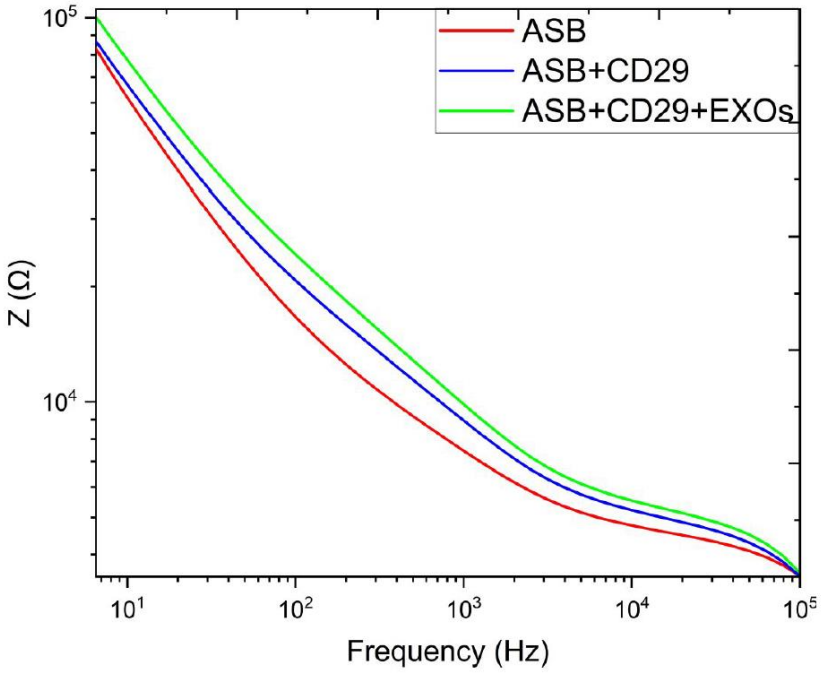

Figure S8.9: Treatment of the ASB with anti-CD29 antibody resulted in a small change in membrane resistance. Antibody binding to the ASB causes a small increase in membrane resistance.

8.11.3 Blocking of integrin β1 decreases cell proliferation and VEGF secretion by ADSCs in culture[†]

We previously used an in vitro cEXO-membrane platform (EVSB) to isolate interactions between the cEXO surface and ADSCs and found proangiogenic markers including upregulation of VEGF and cell proliferation to be a direct outcome.[170] Therefore, to validate the mediating role of integrin β1 in cEXO–ASDC binding, we investigated its influence on VEGF and cell proliferation upregulation, as binding outcomes. Toward this end, we conducted an *in vitro* assay to assess the number of live cells and the concentration of VEGF secreted by ADSCs treated with

[*] Data acquired by Uribe

[†] Data acquired by Uribe

cEXOs in the presence and absence of CD29 Ab, as a blocking treatment for integrin β1, in ADSCs.

ADSCs grown to 80% confluency were treated for 5 days under four conditions: 40 μg of cEXOs (cEXOs), CD29 Ab followed by cEXOs (CD29), transforming growth factor beta (TGFβ) as a positive control, and no treatment (NT) as a negative control (**Figure S8.10**). ADSCs with no treatment (NT) were expected to secrete less VEGF than the treated counterparts.[170,279] Conversely, ADSCs treated with TGFβ were expected to show increased VEGF secretion because TGFβ plays a key role in VEGF regulation and induction of proangiogenic factors.[359–361] Secreted VEGF concentration per cell for all conditions was assessed via ELISA at days 2 and 5 of treatment. For easier data interpretation, the results represent VEGF secretion per cell for all conditions normalized by the no treatment (NT_2) values on day 2. Therefore, NT_2 values were used as a baseline to analyse the VEGF concentration by ADSCs.

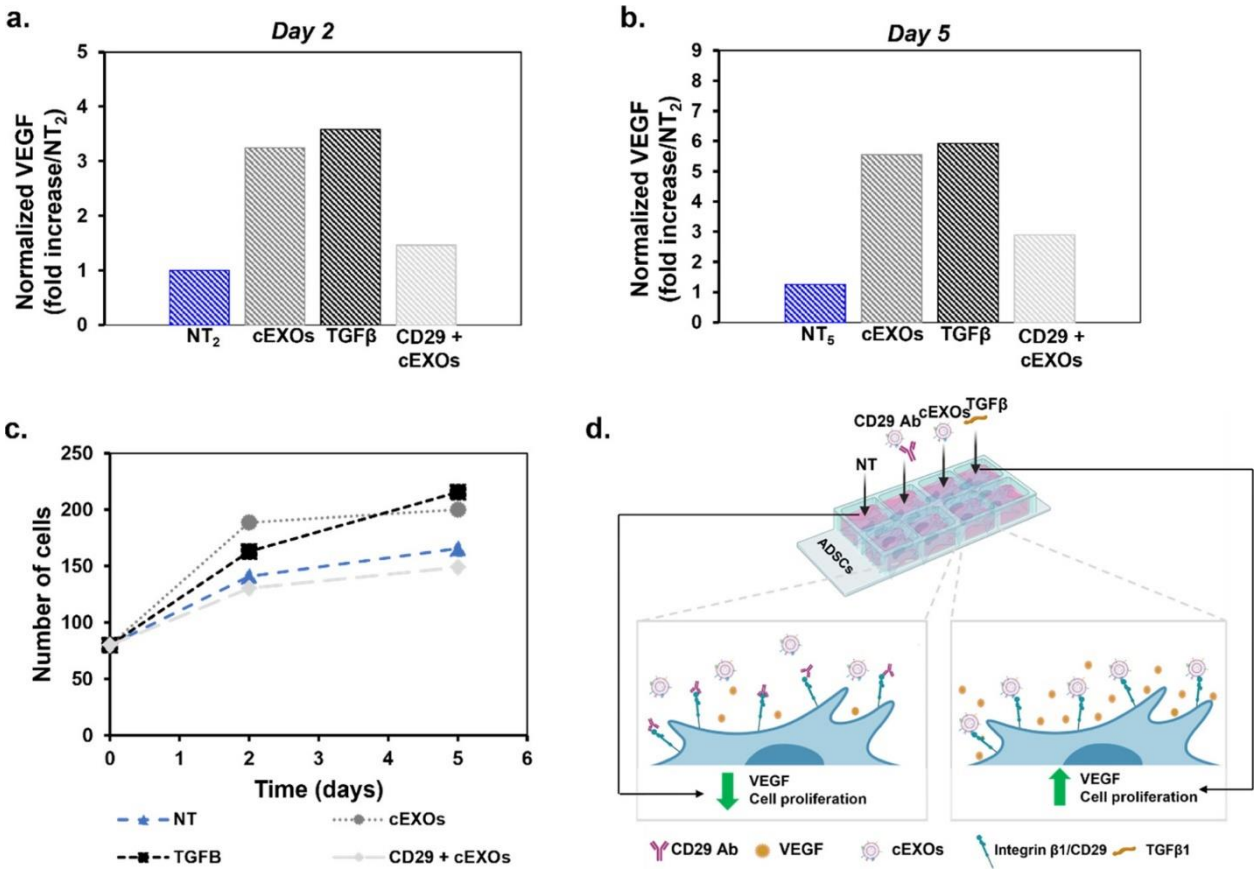

Figure S8.10: Blocking of integrin β1/CD29 decreases the cell number and VEGF secretion by ADSCs treated with cEXOs.

(a) Normalized secreted VEGF concentration by ADSCs for all four conditions: NT, CD29 Ab + cEXOs, cEXOs, and TGFβ on day 2 and (b) on day 5 of treatment. VEGF secretion for all conditions was normalized by the VEGF concentration at no treatment (NT_2) on day 2. (c) Number of alive ADSCs at days 0, 2, and 5 of treatment for the same conditions as in (a). (d) Schematic representation of experiment showing ADSC–cEXOs treatment leads to

the upregulation of VEGF secretion and cell proliferation in ADSCs; and inhibition of ASDC–cEXO binding and decrease in those outcomes by blocking integrin β1 with CD29 Ab. Created with Biorender.com. n=3.[131]

As expected, VEGF secretion is significantly upregulated in ADSCs treated with cEXOs and with TGFβ compared to the NT counterparts for both days. The results displayed in **Figure S8.10a** show that cells treated with cEXOs and TGFβ for 2 days secreted approximately 3 and 4 times more VEGF than NT_2 cells. Interestingly, ADSCs treated with CD29 Ab, before cEXO addition, secreted a similar VEGF concentration to NT_2 cells. The same behaviour was observed on day 5 of treatment, where cells treated with cEXOs and TGFβ secreted around 6 times more VEGF than NT_2 and NT_5 cells, and cells treated with CD29 Ab secreted just 2 times more VEGF than N_2 and N_5 cells. As expected, the VEGF quantity was slightly higher on day 5 than on day 2, for all conditions as shown in **Figure S8.10b**. These results indicate that blocking integrin β1 in ADSCs prevents the proangiogenic activity.

Because cell proliferation is also influenced by cEXO binding to ADSCs, we counted the number of alive cells under the same conditions. As seen in **Figure S8.10c**, treating ADSCs with cEXOs and TGFβ leads to a higher number of live cells than NT, as we have previously reported. Conversely, a decrease in the cell number was observed with CD29 Ab treatment before cEXO addition. Given these results, it suggests that integrin β1 plays an important role in cEXO–ADSC binding and blocking it is a strategy with therapeutic potential to decrease proangiogenic activity that occurs from VEGF upregulation and proliferation of ADSCs in the TME.

8.12 Supplementary Information for Chapter 5

Supplementary Discussion 1: A model to recapitulate TEV-driven invasive ductal carcinoma.

It is now well established that TEVs provide autocrine and paracrine signals within the tumour ecosystem to activate an EMT programme in neoplastic epithelial cells.[10,362] This endows the recipient cells with the ability to invade the tissue surrounding the primary tumour, intravasate, and enter the circulation.[7] TEVs accomplish this by transferring functional cargo comprising transcriptional regulators,[9] EMT drivers,[299,362] and signalling molecules[363] that influences signalling pathways, such as the canonical Wnt/β-catenin pathway,[364] and alters the transcriptome and proteome of recipient cells, thereby inducing a change in cell phenotype.[364] TEVs derived from TNBC cells were reported to promote proliferation and drug resistance in non-tumourigenic breast cells,[365] and TEVs from young women's breast cancer patients were found to drive increased invasion of non-malignant cells.[366] In breast carcinomas, the proclivity for mesenchymal transition may be related to the high aggressiveness and characteristic metastatic spread of these tumours.[367] TNBC is a particularly aggressive and invasive breast cancer subtype[368] with metastases frequently

occurring in the first 3 years following surgery and a very low 5-year survival rate for afflicted patients (77% compared to 93% for other breast cancer subtypes[369]). The higher mortality is partly due to a disproportionate number of metastatic disease cases.[370] Treatment of TNBC has been limited due to the lack of well-defined therapeutic targets[371] and the scarcity of effective targeted therapies is in part to blame for a poorer prognosis and treatment outcome for TBNC than other types of breast cancer.[368] Studies of progression from ductal carcinoma *in situ* to invasive disease have been facilitated by the use of the MCF10A series,[9,372] which have intrinsic phenotypic plasticity for mesenchymal transition[367] and are widely used for investigating EMT in premalignant cells.[295,296] MCF10A cells display characteristics of luminal ductal cells but not of myoepithelial cells and they make up the mammary ductal microenvironment of the terminal ductal lobular unit, which is the origin of most pathologic breast lesions.[373] By contrast, MDA-MB-231 is a cancerous epithelial cell line isolated from a patient with metastatic mammary adenocarcinoma; a type of cancer that begins in the glandular tissue of breast lobules and ducts. Therefore, inducing EMT in MCF10A cells by exposure to MDA-MB-231-derived TEVs (MDA-TEVs) represents a highly relevant disease model for investigating the lesions preceding invasive breast cancer. There is ample precedent for using it, as TEVs derived from MDA-MB-231 cells stimulated with linoleic acid[301] or insulin-like growth factor-1[302] were found to mediate EMT in MCF10A cells, as did hypoxic small EVs derived from the same cell line.[374]

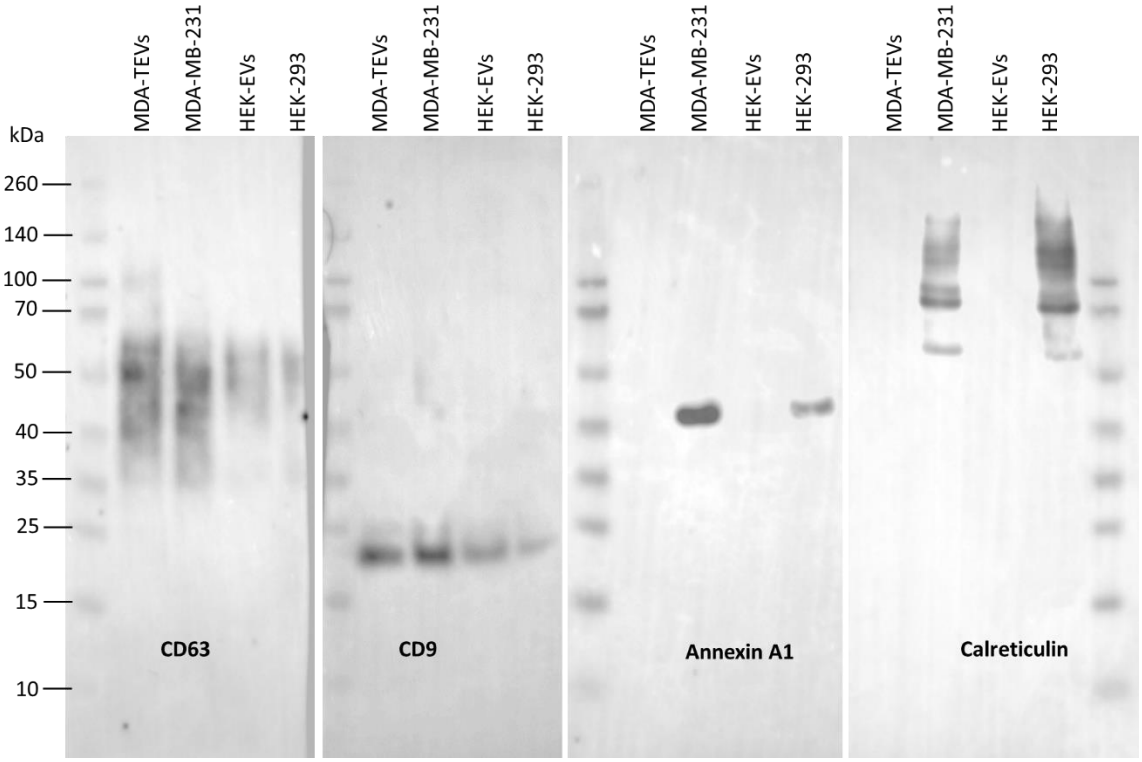

Figure S8.11: Unedited Western blots for EV characterisation. Samples probed for EV markers CD63 and CD9, microvesicle marker annexin A1, and negative marker calreticulin.

Supplementary Discussion 2: Investigating EMT requires high temporal resolution and functional readouts

Our platform aims to address the limitations of current sensing technologies in metastasis research. Namely, the inability to monitor the transient state of a dynamic biological system and produce quantitative, time-series data relevant to the biology at play. EMT is a transient process and one of the difficulties in its study arises because the transitions between epithelial and mesenchymal states are not binary.[375] Carcinoma cells often exhibit a spectrum of epithelial-mesenchymal characteristics[376,377] and studies have shown that cancer cells, including breast cancers, express both epithelial and mesenchymal markers.[378,379] As such, the existence of hybrid EMT states or phenotypes (partial EMT) have been suggested to describe a tumour cell differentiation state in which cancer cells keep both EMT and mesenchymal-to-epithelial transition (MET; reverse-EMT) characteristics. This may promote tumour cell plasticity and tumour progression[378,380,381] and is thus an important feature to capture during phenotype screening. Moreover, migration of cells does not necessarily require the cells to lose all epithelial features, as epithelial cells can migrate as single cells or collectively, while attached with one another via weakened cell-cell interactions.[382] This indicates that the migratory and invasive capacity of cells undergoing EMT is not accurately represented by the simple expression, or lack of expression, of selected (mesenchymal) markers. As such, functional changes in the biological properties of cells must be assessed as well.[322]

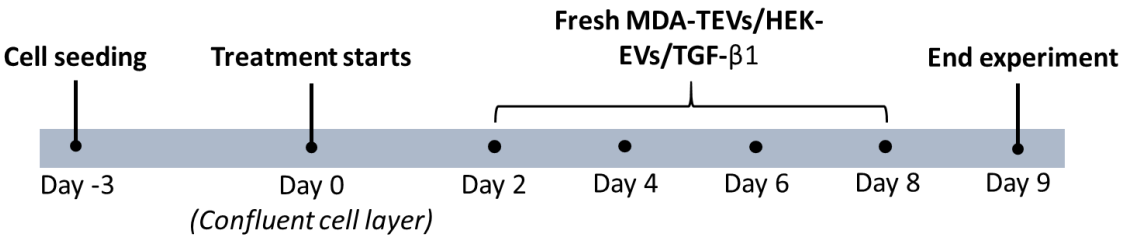

Schematic S1: Experimental overview and treatment exposure schedule

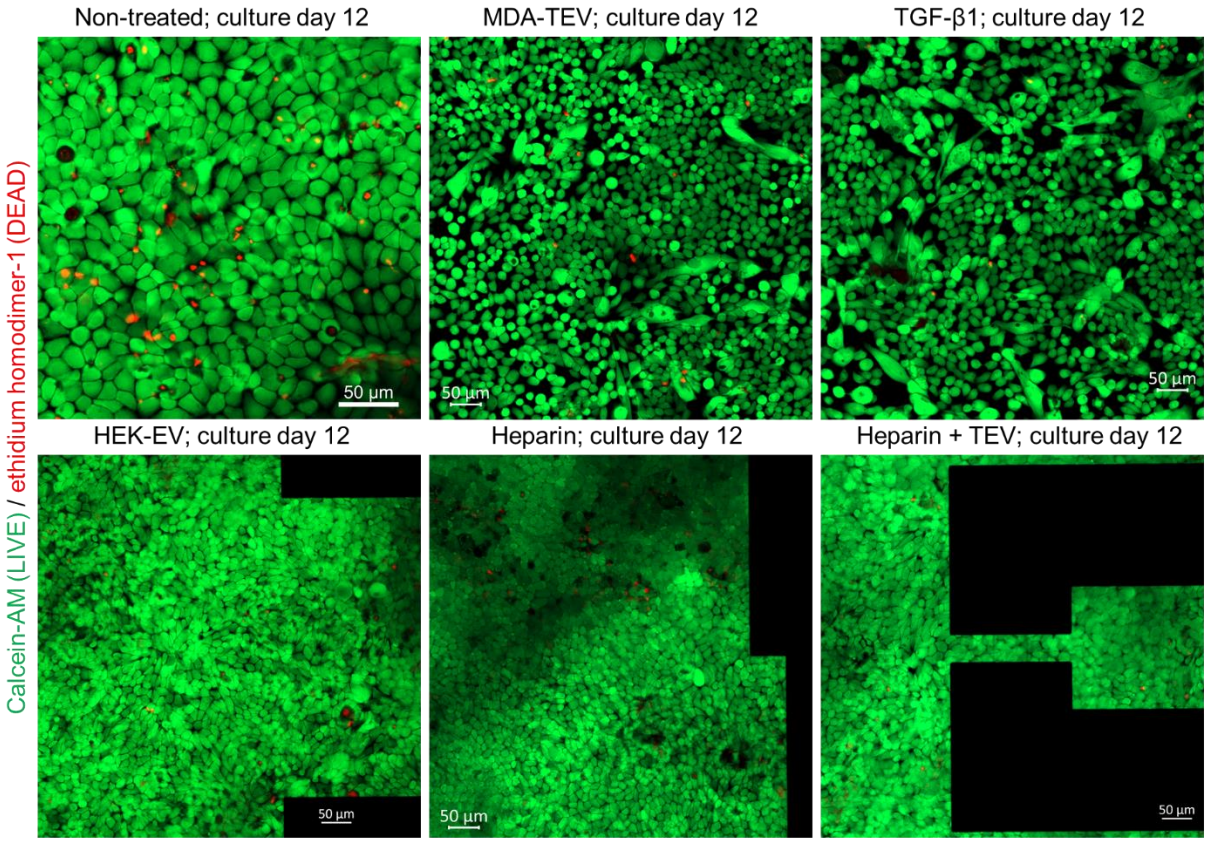

Figure S8.12: Cell viability.

Cells cultured for 12 days on OECTs stained with viability/cytotoxicity kit probes (green-LIVE: Calcein AM; red-DEAD: ethidium homodimer-1).

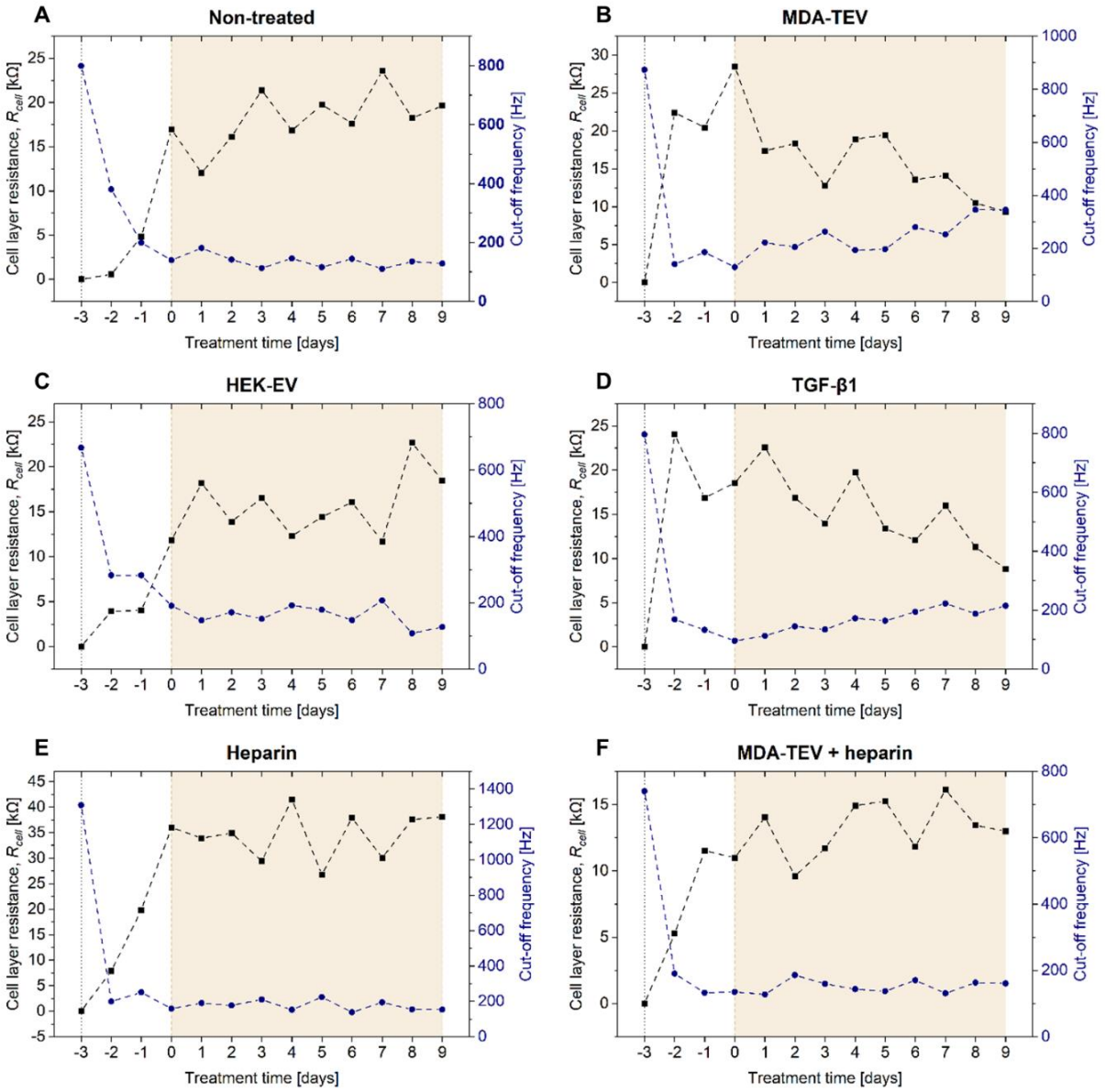

Figure S8.13: Representative cut-off frequency and cell layer resistance, $\boldsymbol{R_{cell}}$, vs time plots for all conditions tested. (**A**) Non-treated. (**B**) MDA-TEV treated. (**C**) HEK-EV treated. (**D**) TGF-β1 treated. (**E**) Heparin treated. (**F**) MDA-TEV + heparin treated.

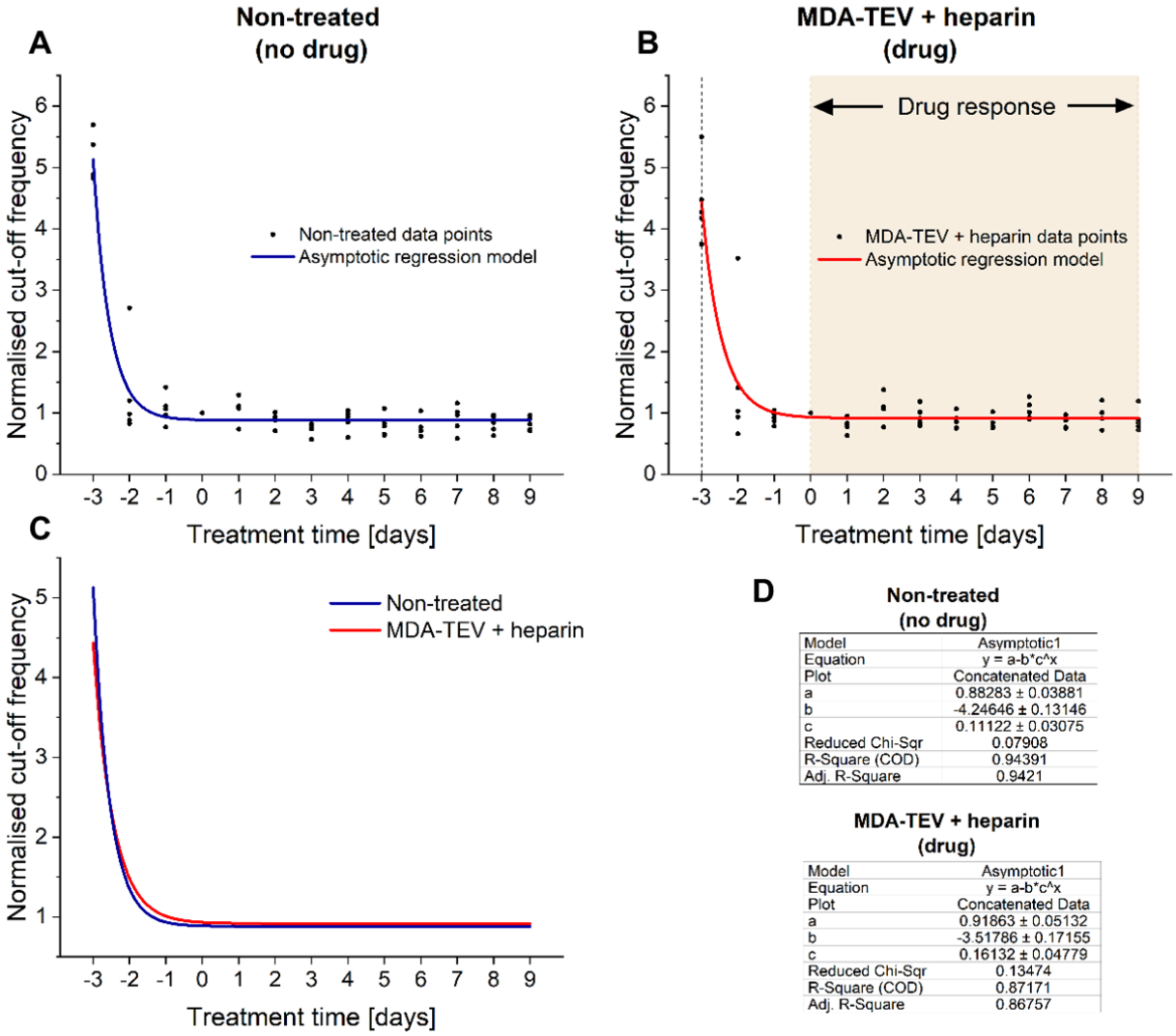

Figure S 8.14: Modelling the transient drug response using electrical measurements. Asymptotic regression of non-treated (A) and MDA-TEV + heparin treated (B) MCF10A cells, demonstrating that the normalised cut-off frequency tends towards 0.88 ± 0.034 and 0.92 ± 0.051, respectively. (C, D) The two models are very similar, indicating that heparin treatment of cells exposed to MDA-TEVs block any malignant transformation.

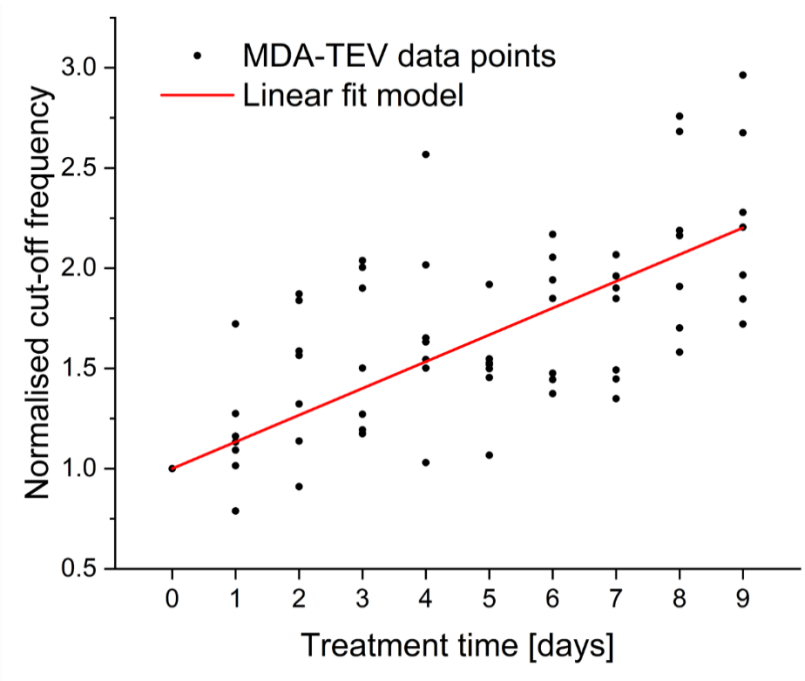

Figure S8.15: Linear regression of MDA-TEV treatment condition.

Supplementary Discussion 3: Molecular mechanisms of EMT and determining its occurrence

EMT status is typically defined by changes in cellular properties together with a set of molecular markers.[322] Epithelial cells are connected to one another via a variety of epithelial cell junctions that help maintain epithelial polarity, while mesenchymal cells do not contain functional epithelial junctions and present a back-front polarity in their actin stress fibres, characteristic of a migrating cell.[322] During EMT, epithelial cells lose their apical-basal polarity and lateral cell–cell adhesion and gain migratory and invasive properties. Loss of apico-basal polarity leads to destabilisation of adhesion complexes, such as tight junctions and adherens junctions at the lateral membrane,[383] and is preceded by reorganisation of filamentous actin (F-actin). Actin filaments in mesenchymal cells are bundled into thick contractile stress fibres that increase cellular contractability for migration.[384] Vimentin, a type III intermediate filament found in mesenchymal cells, mediates cytoskeletal organisation and focal adhesion maturation, which the migrating cells utilise to attach to the ECM.[385] Previous studies using the same MDA-TEV-EMT model[301,302] assessed transcript and protein expression using RT-qPCR and Western blot and demonstrated that MDA-TEVs induced down-regulation of E-cadherin (epithelial marker) expression and upregulation of Twist-related protein 1 (TWIST1) transcripts, as well as vimentin and N-cadherin (mesenchymal markers) expression in MCF10A cells. TWIST1 is an E-cadherin transcriptional repressors that bind to promoter E-boxes on E-cadherin to repress transcription and they are part of the canonical Wnt/β-catenin pathway, indicating that TEVs (and their cargo) modulate this EMT pathway. Functionally, TEVs promoted migration and invasion in MCF10A cells, as measured by migration/wound-healing and Boyden chamber assays.[301,302]

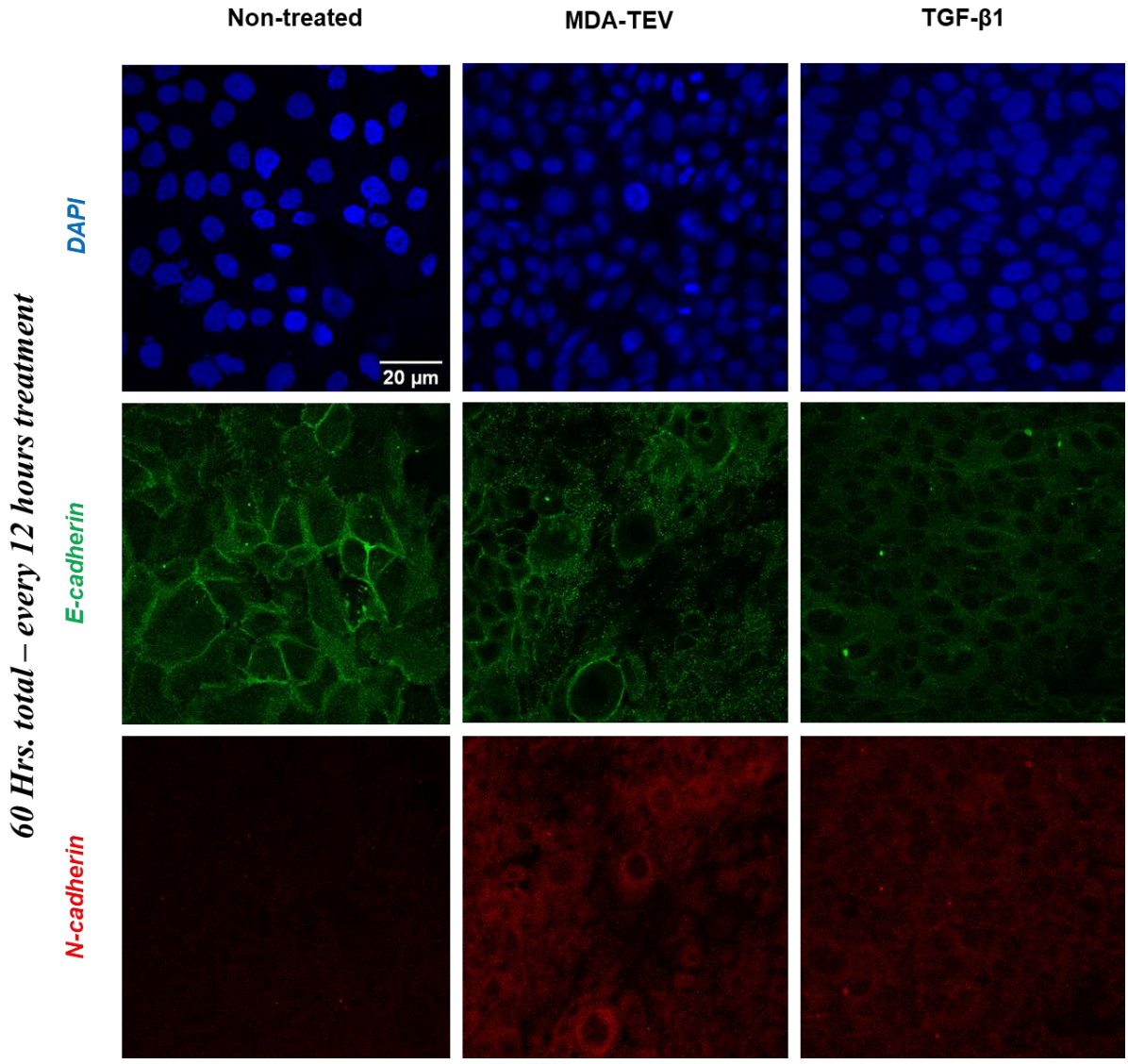

Figure S8.16:IF imaging of MDA-TEV and TGF-β1 treated MCF10A cells. E-cadherin (green), N-cadherin (red), and nuclei (blue) on MCF10A monolayer with no treatment (left column), treated with 50 µg of MDA-TEVs (middle column), or with 10 ng/mL TGFβ (right column) every 12 hours for 60 hours.

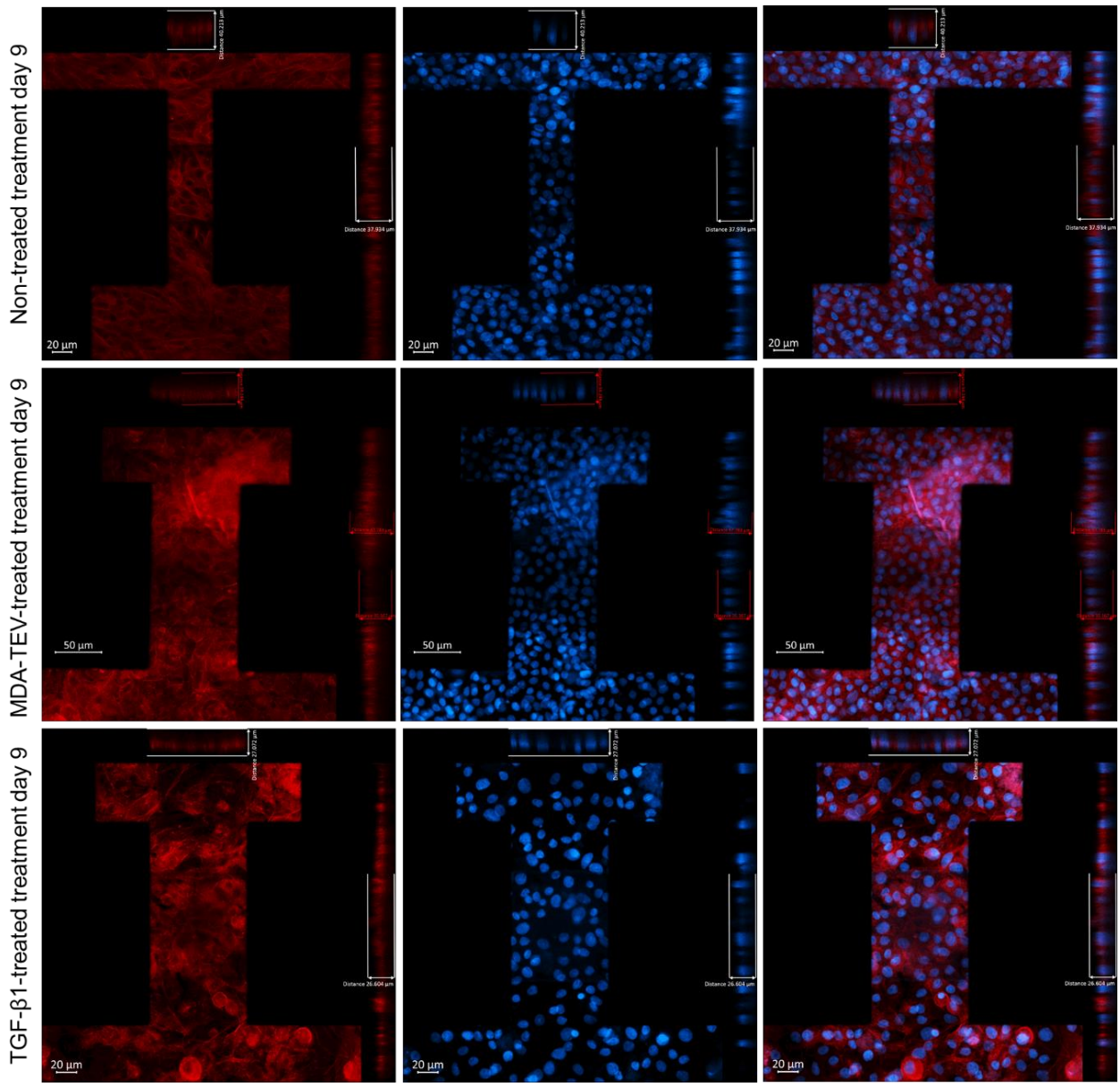

Figure S8.17: Unedited x/z and y/z orthogonal views of each cell layer in the OECT channel.

Imaging performed on treatment day 9 and obtained by z-stacked confocal images. Cell height was calculated using the built-in tools in the Zen software, as shown in the images.

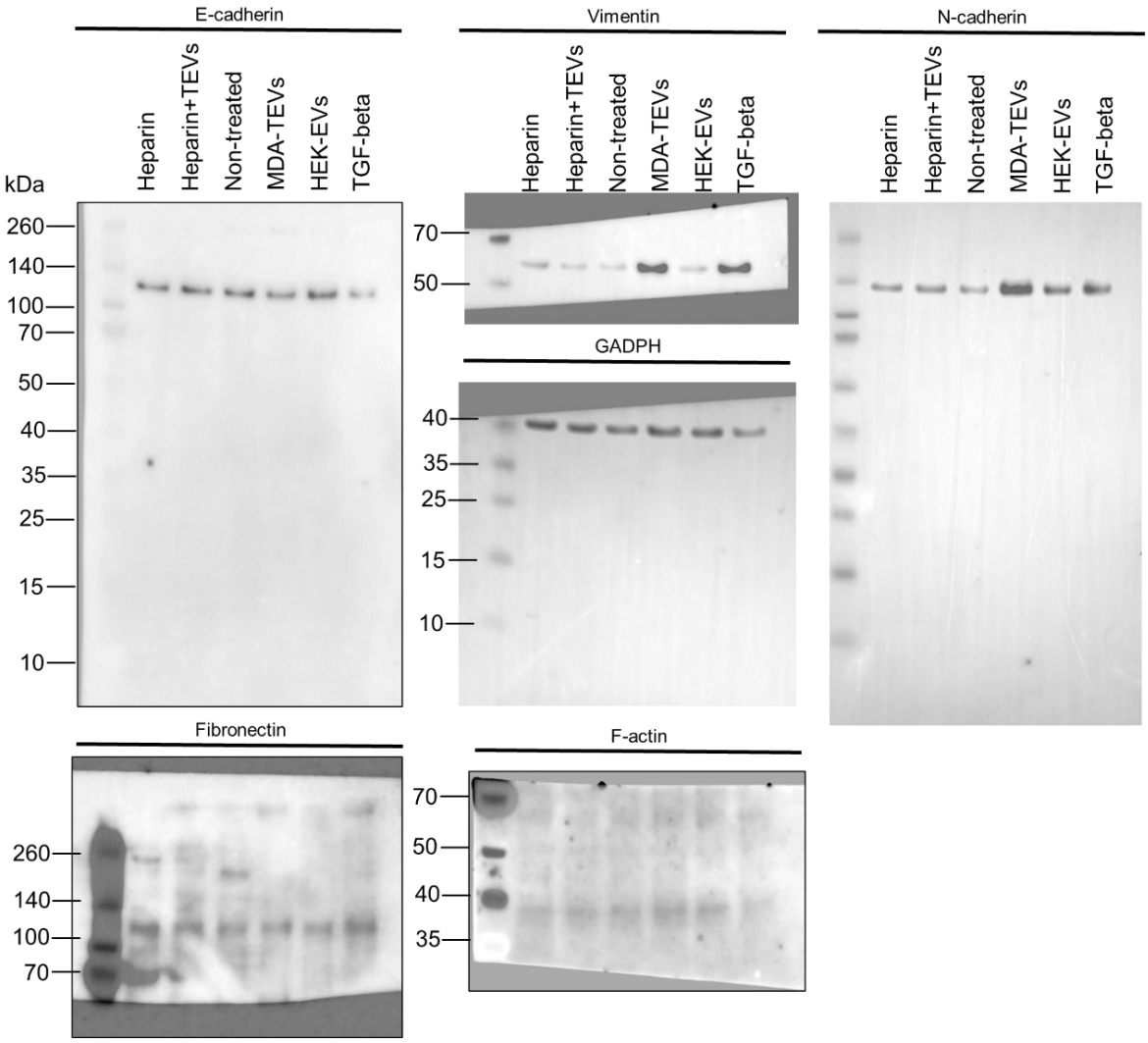

Figure S8.18: Unedited immunoblots of whole-cell lysates collected on treatment day 9 against EMT markers. Equal quantities of protein were separated on SDS-PAGE gels and membranes were blotted with indicated antibodies. Vimentin, predicted: 54-75 kDa; E-cadherin, predicted: 97 kDa; N-cadherin, predicted: 125-135 kDa; fibronectin (slightly smeared due to glycosylation[325] and shows multiple bands with lower MW;), predicted: 262-285 kDa; and F-actin (band at ~70 kDa may indicate presence of dimers), predicted 42 kDa. The presence of multiple bands is also indicated on antibody product page (abcam).

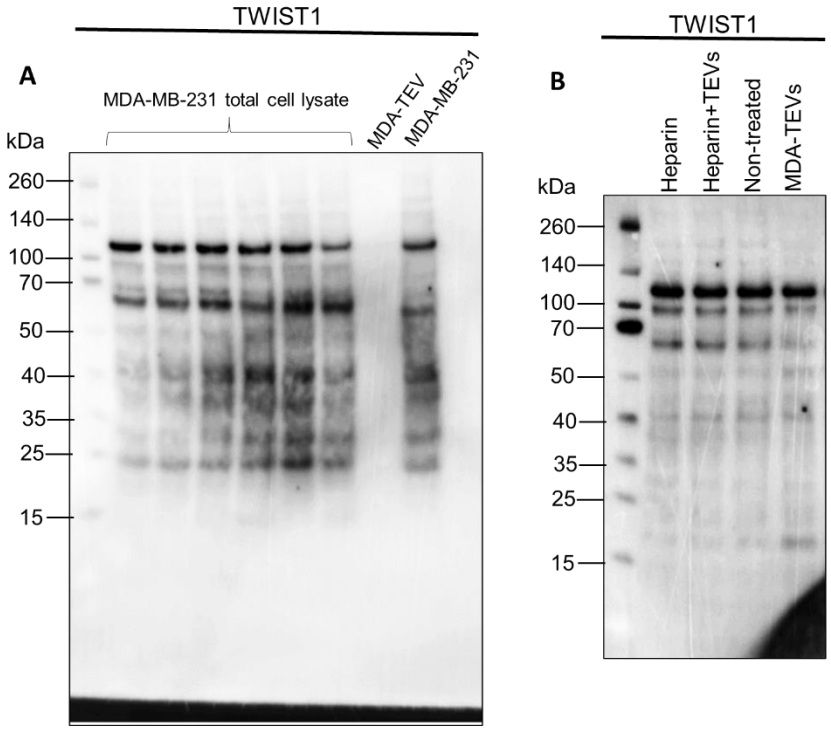

Figure S8.19: Unedited immunoblots of TWIST1 protein abundance.

(**A**) MDA-MB-231 total cell lysate and MDA-TEVs. (**B**) MCF10A cells treated under conditions indicated. TWIST1 has a predicted molecular weight of 21 kDa. The presence of multiple bands is also indicated on antibody product page (abcam).

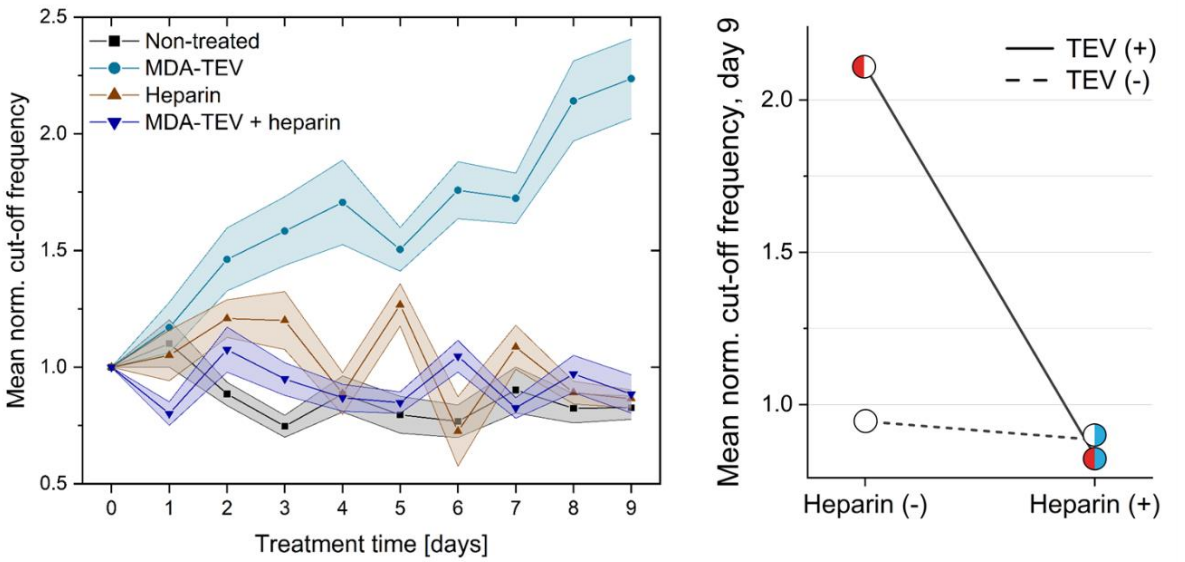

Figure S8.20: OECT-based measurements of heparin treatment. LHS: Cut-off frequency normalised to day 0 (treatment start day) over time for the four drug treatment conditions: non-treated; 200 µg MDA-TEVs; 10 µg/ml heparin; and 200 µg MDA-TEVs + 10 µg/ml heparin, (mean ± s.e.m.; s.e.m. indicated by lightly coloured areas; n=3). Data points before treatment day 0 are omitted for clarity. RHS: Interaction plot illustrating the relationship between MDA-TEV and heparin treatment (mean; n=3).

"The whole world is a series of miracles, but we're so used to them, we call them ordinary things."

— *Hans Christian Andersen*